SILESIAN UNIVERSITY OF TECHNOLOGY

FACULTY OF CHEMISTRY

DEPARTMENT OF ORGANIC CHEMISTRY, BIOORGANIC CHEMISTRY AND BIOTECHNOLOGY

GRZEGORZ STANDO, MSc

Doctoral dissertation

Development of high-performance composites based on non-functionalized carbon nanostructures

Supervisor: Dawid Janas, Ph.D. DSc

GLIWICE 2023

POLITECHNIKA ŚLĄSKA

WYDZIAŁ CHEMICZNY

KATEDRA CHEMII ORGANICZNEJ, BIOORGANICZNEJ I BIOTECHNOLOGII

Mgr inż. GRZEGORZ STANDO

Rozprawa doktorska

Opracowanie wysokiej klasy kompozytów na bazie nanostruktur węglowych bez konieczności destruktywnej modyfikacji chemicznej

Promotor: dr hab. inż. Dawid Janas, Prof. PŚ

GLIWICE 2023

I would like to thank:

My family, mom, dad, brother, and wife for supporting me and always giving a hand during my Ph.D. course.

Prof. Haitao Liu and Prof Lei Li, and their scientific groups, especially: Dr. Nathan Tolman, Jason Smith, and Fan Yang, for exchanging knowledge and hosting at the University of Pittsburgh.

Dr. Pyry-Mikko Hannula, Prof. Mari Lundström, and her research group for the opportunity to work with amazing people and learn about the use of waste as a raw material and team-work.

Dr. Pavel Chulkin and Mr. Paweł Stando for help and guidance about the synthesis of a part of composites of polyaniline and nanocarbon.

Current and past members of Functional Nanomaterial groups, mainly the students with whom I worked and helped start their scientific carrier.

My supervisor Prof. Dawid Janas for sharing the knowledge and experiments which allowed me to gain financial support and start my career in science.

The work was founded mainly by the Polish Ministry of Education and Science ("Diamond Grant" program, grant agreement 0036/DIA/201948), and Polish National Agency for Academic Exchange (under the Iwanowska program, grant agreement PPN/IWA/2019/1/00017/UO/00001)

Tables of contents

Abstract in English

Carbon nanostructures were discovered at the end of the last century, and despite the passage of time, they are still a hot topic. Especially carbon nanotubes and graphene are the objects of both basic research and R&D. A single carbon nanotube or graphene flake has magnificent mechanical, electrical, and thermal properties compared to conventional materials such as copper and steel. However, macroscopic objects from carbon nanomaterials do not retain these unique properties. The connection of carbon nanomaterials with polymers, metals, or ceramics is one of the solutions to keep some of the nanostructure properties presented by individual building blocks by facilitating stress or charge transfer. It is commonly believed that the surface of nanotubes, graphene, and fullerenes is hydrophobic, which unfortunately limits their application in composites. The most popular answer to this problem is destructive chemical functionalization by inserting hydrophilic functional groups. Obtaining a hydrophilic surface of carbon nanomaterial increases its compatibility with other materials, such as polymers or metals. However, this functionalization often deteriorates the primary structure of carbon nanomaterials and changes their properties.

The scientific goal of this dissertation was to test the hypothesis that carbon nanostructures (fullerene C_{60}, carbon nanotubes, graphene) may, under certain conditions, exhibit hydrophilic character and the reason for their hydrophobic surface in the ambient is the adsorption of aromatic hydrocarbons present in the air. In parallel, the aim was to produce high-performance composites based on non-functionalized carbon nanostructures and to investigate their potential applications.

The first part of this work proved that to make the surface of nanocarbon hydrophilic, and it is enough to subject them to annealing that desorbs surface contaminations. Secondly, a general mechanism of the observed phenomenon – changing the surface character of carbon nanostructures from hydrophilic to hydrophobic, was developed using spectroscopic studies and selected theoretical models. Lastly, to prove that non-functionalized carbon nanostructures can be interfaced well with polymers and metals, such composites were made and characterized. Their electrical, mechanical, thermal, and thermoelectric properties were determined, and their potential application areas were indicated.

Streszczenie w języku polskim

Nanostruktury węglowe zostały odkryte pod koniec poprzedniego wieku i mimo upływu lat dalej cieszą się one dużą popularnością. W szczególności nanorurki węglowe, a także grafen są obiektami badań zarówno podstawowych jak prac badawczo-rozwojowych. Pojedyncza nanorurka węglowa czy płatek grafenowy mają niesamowite właściwości mechaniczne, elektryczne oraz termiczne, przewyższające konwencjonalne materiały takie jak miedź i stal. Jednakże, obiekty makroskopowe wykonane wyłącznie z nanomateriałów węglowych nie zachowują tych unikalnych właściwości. Utworzenie kompozytów nanomateriałów węglowych z polimerami, metalami lub ceramiką to jeden ze sposobów na zachowanie części właściwości charakterystycznych dla nanowęgla dzięki usprawnieniu transferu obciążenia bądź ładunku. Powszechnie uważa się, że powierzchnia nanorurek, grafenu oraz fulerenów jest hydrofobowa co niestety limituje ich zastosowanie. Najpopularniejszym rozwiązaniem tego problemu jest destruktywna funkcjonalizacja chemiczna poprzez wszczepienie hydrofilowych grup funkcyjnych. Uzyskanie hydrofilowej powierzchni nanomateriału węglowego zwiększa jego kompatybilność z innymi materiałami takimi jak polimery czy metale. Jednakże funkcjonalizacja ta często niszczy pierwotną strukturę nanomateriałów węglowych i zmienia ich właściwości.

Celem niniejszej rozprawy było przetestowanie hipotezy, że nanostruktury węglowe (fuleren C_{60}, nanorurki węglowe, grafen) mają w określonych warunkach charakter hydrofilowy, a przyczyną ich hydrofobowej powierzchni w warunkach naturalnych są zaadsorbowane węglowodory aromatyczne na ich powierzchni obecne w powietrzu. Równoległym, celem było wytworzenie wysokiej klasy kompozytów na bazie niefunkcjonalizowanych nanostruktur węglowych i zbadaniu ich potencjalnych zastosowań.

W ramach pierwszej części pracy udowodniono, że w celu hydrofilizacji powierzchni nanorurek wystarczy poddać je wygrzewaniu aby desorbować zanieczyszczenia powierzchniowe. Następnie, opracowano ogólny mechanizm zjawiska zmiany charakteru powierzchni nanostruktur węglowych z hydrofilowego na hydrofobowy, co potwierdzono badaniami spektroskopowymi oraz stosując wybrane modele teoretyczne. Na koniec, by zweryfikować, że niefunkcjonalizowane nanomateriały węglowe mogą dobrze przylegać do polimerów i metali, wytworzono i scharakteryzowano takie kompozyty. Określono ich właściwości elektryczne, mechaniczne, termiczne i termoelektryczne, a także wskazano potencjalne obszary ich zastosowań.

Abbreviations

10% Graphene –	Graphene combined with single-walled carbon nanotubes (proportion 1:9 by mass)
10% N-MWCNTs –	N-doped in-house made multi-walled carbon nanotubes combined with single-walled carbon nanotubes (proportion 1:9 by mass)
10% O-MWCNTs –	Oxidized in-house made multi-walled carbon nanotubes combined with single-walled carbon nanotubes (proportion 1:9 by mass)
25% Graphene –	Graphene combined with single-walled carbon nanotubes (proportion 1:3 by mass)
25% N-MWCNTs –	N-doped in-house made multi-walled carbon nanotubes combined with single-walled carbon nanotubes (proportion 1:3 by mass)
25% O-MWCNTs –	Oxidized in-house made multi-walled carbon nanotubes combined with single-walled carbon nanotubes (proportion 1:3 by mass)
50% N-MWCNTs –	N-doped in-house made multi-walled carbon nanotubes combined with single-walled carbon nanotubes (proportion 1:1 by mass)
50% O-MWCNTs –	Oxidized in-house made multi-walled carbon nanotubes combined with single-walled carbon nanotubes (proportion 1:1 by mass)
AFM –	Atomic force microscopy
CA –	Contact angle
CNTs –	Carbon nanotubes
CVD –	Chemical vapor deposition
c-CVD –	Catalytic chemical vapor deposition
Cu+10% Graphene –	Composite of graphene combined with single-walled carbon nanotubes (proportion 1:9 by mass) with deposited copper
Cu+10% N-MWCNTs –	Composite of N-doped in-house made multi-walled carbon nanotubes combined with single-walled carbon nanotubes (proportion 1:9 by mass) with deposited copper
Cu+10% O-MWCNTs –	Composite of oxidized in-house made multi-walled carbon nanotubes combined with single-walled carbon nanotubes (proportion 1:9 by mass) with deposited copper
Cu+25% Graphene –	Composite of graphene combined with single-walled carbon nanotubes (proportion 1:3 by mass) with deposited copper

Cu+25% N-MWCNTs –	Composite of N-doped in-house made multi-walled carbon nanotubes combined with single-walled carbon nanotubes (proportion 1:3 by mass) with deposited copper
Cu+25% O-MWCNTs –	Composite of oxidized in-house made multi-walled carbon nanotubes combined with single-walled carbon nanotubes (proportion 1:3 by mass) with deposited copper
Cu+50% N-MWCNTs –	Composite of N-doped in-house made multi-walled carbon nanotubes combined with single-walled carbon nanotubes (proportion 1:1 by mass) with deposited copper
Cu+50% O-MWCNTs –	Composite of oxidized in-house made multi-walled carbon nanotubes combined with single-walled carbon nanotubes (proportion 1:1 by mass) with deposited copper
Cu+MWCNTs –	In-house made multi-walled carbon nanotubes with deposited copper
Cu+NC-MWCNTs –	Commercial multi-walled carbon nanotubes with deposited copper
Cu+SWCNTs –	Composites of single-walled carbon nanotubes with deposited copper
C_xH_y –	Hydrocarbons
DF –	Film from dispersion method (dispersion film)
DFE –	Film from dispersion method used as an electrode (dispersion film electrode)
EB –	Emeraldine base
EB+SWCNTs –	Composite of emeraldine base with single-walled carbon nanotubes
ES –	Emeraldine salt
ES+G+SWCNTs –	Composite of emeraldine salt with graphene nanoplatelets 120-150 m^2/g combined with single-walled carbon nanotubes (proportion 1:1 by mass)
ES+O-SWCNTs –	Composite of emeraldine salt with oxidized single-walled carbon nanotubes
ES+SWCNTs –	Composite of emeraldine salt with single-walled carbon nanotubes
ES+SWCNTs unwashed –	Composite of emeraldine salt with single-walled carbon nanotubes without washing by H_2O
ES+SWCNTs washed –	Composite of emeraldine salt with single-walled carbon nanotubes washed for 1 minute in H_2O
FTIR –	Fourier-transform infrared spectroscopy

G+SWCNTs 1:1 –	Composite of graphene nanoplatelets 120-150 m^2/g with single-walled carbon nanotubes (proportion 1:1 by mass)
G+SWCNTs 1:3 –	Composite of graphene nanoplatelets 120-150 m^2/g with single-walled carbon nanotubes (proportion 1:3 by mass)
G+SWCNTs 1:9 –	Composite of graphene nanoplatelets 120-150 m^2/g with single-walled carbon nanotubes (proportion 1:9 by mass)
HOPG –	Highly oriented pyrolytic graphite
LB –	Leucoemeraldine base
LB+SWCNTs –	Composite of leucoemeraldine base with single-walled carbon nanotubes
MWCNTs –	In-house made multi-walled carbon nanotubes
NC-MWCNTs –	Commercial multi-walled carbon nanotubes
O-SWCNTs –	Oxidized single-walled carbon nanotubes
PANI –	Polyaniline
PB –	Pernigraline base
PB+SWCNTs –	Composite of pernigraline base with single-walled carbon nanotubes
PMMA –	Poly(methyl methacrylate)
PMMA+SWCNTs –	Composites of polymethyl methacrylate and single-walled carbon nanotubes
PTFE –	Polytetrafluoroethylene
SEM –	Scanning electron microscopy
SLG –	Single layer graphene
SWCNTs –	Single-walled carbon nanotubes
WCA –	Water contact angle
VFF –	Film from vacuum filtration (vacuum filtration film)
XPS –	X-ray photoelectron spectroscopy

1. Aims and scope

This scientific work aimed to verify the hypothesis "pure nanocarbon surface is wettable with water and aromatic hydrocarbons are the reason for their apparent hydrophobicity". The doctoral dissertation results from initial research, which started in 2017. The results of these studies were as follows: thermally annealed carbon nanotubes exhibit surprisingly high wettability with water[1] and deposition and deposition of (at this point unspecific) hydrocarbons can render the surface apparently hydrophobic[2]. In addition, earlier literature studies conducted by scientific groups of Prof. Lei Li and Prof. Haitao Liu from the University of Pittsburgh in the United States discovered that graphene and graphite are also strongly hydrophilic upon purification. However, to this date, the group of hydrocarbons responsible for the phenomenon remains unknown in the literature (especially for 0D and 1D nanocarbon). What is more, the mechanism of hydrophobization of nanocarbon surface has not been proposed. Other research groups observed the analogous impact of impurities on the wettability of 2D materials such as hexagonal MoS_2 and BN, supporting the central hypothesis of the thesis. To understand the mentioned phenomenon, three carbon nanomaterials and one material have been chosen: **0D fullerene C_{60}**, **1D – single-walled carbon nanotubes** (SWCNTs), **2D – single layer graphene** (SLG), and **3D – highly oriented pyrolytic graphite** (to analyze the impact of a number of graphene layers) (HOPG). Both experimental results and theoretical models were engaged to fill this research gap.

The second hypothesis of the dissertation is the implication of the first one: "Functionalization of carbon nanostructure is not always needed to manufacture high-performance composites with other materials since they can be made hydrophilic by thermal annealing without change to the structure or composition of the material". Without hydrophilic functional groups on the nanocarbon surface composites should have much better properties, and it would improve the application potential of the material as thermoelectric generators, supercapacitors, or membranes.

Part of the dissertation is already published[3–6]. One more article is currently under preparation for submission to peer-review evaluation.

2.Introduction

2.1 Nanocarbon materials – overview

2.1.1 History, properties and applications

In 1959, during his now-famous lecture, Richard Feynman said that “there is plenty of room at the bottom”[7]. This visionary sentence formally started the history of nanoscience more than sixty years ago. Since this time, the field has developed at an unprecedented pace. Nowadays, scientists worldwide study this matter in various forms, such as: nanoparticles, nanorods, nanowires, nanotubes, nanodots, or nanohorns[8]. However, it is not the peculiar architecture per se that draws attention but the broad spectrum of unique properties these materials offer. Thanks to appreciable electrical[9], mechanical[9], thermal[10], and optical[11] characteristics, they are envisioned to succeed in many traditional materials that we currently use daily.

In 1985, three scientists, Sir Harold Kroto, Robert Curl, and Richard Smalley published an article about the new allotropic form of carbon – fullerenes[12]. It was a breakthrough that changed thinking about carbon materials and created a new subgroup – nanocarbon structures. Moreover, the scientific community appreciated these materials by awarding the Nobel Prize in chemistry in 1996 for discovering fullerenes. Not long after, Sumio Iijima described carbon nanotubes (CNTs) in 1991[13] and nowadays, he is recognized as the one who discovered carbon nanotubes. However, Soviet scientists observed that carbon nanotube structures could be found in products of the thermal decomposition of carbon monoxide and published the results in 1952. They did not name the structures and the language of publication was Russian, thus it had a limited impact on world science[14]. Furthermore, Andre Geim and Konstantin Novoselov demonstrated graphene to the world in 2004 and received Nobel Prize in physics in 2010 for this achievement[15]. After all these years, many news types of carbon nanostructures have been discovered, such as: carbon nanoonions[16], carbon quantum dots[17], nanodiamonds[18], carbon nanohors[19], and carbon nanofibers[20]. However, the most popular ones are fullerenes (0D material), carbon nanotubes (1D material), and graphene (2D material) (Figure 1).

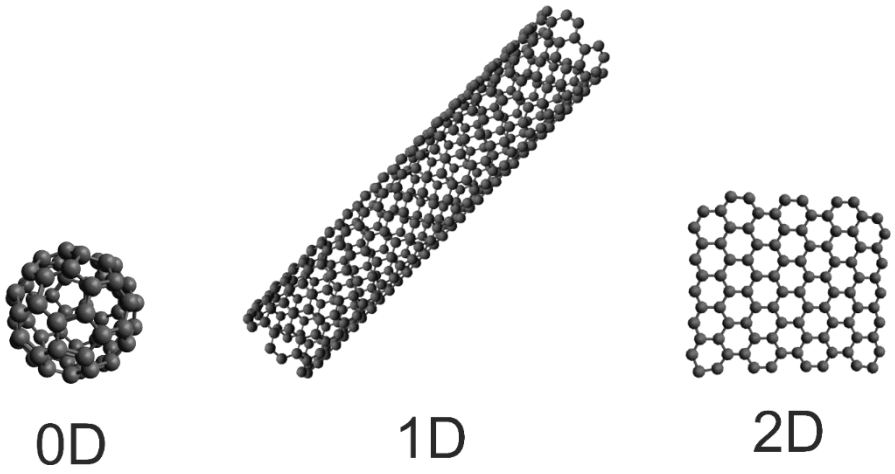

Figure 1 Carbon nanostructures: 0D – fullerene C_{60}, 1D – single-walled carbon nanotube, 2D – single layer graphene.

The total number of publications about one of these three nanomaterials is nearly 400 000 (based on the Scopus database, years 1985-2022, key words "Carbon nanotubes" or “fullerenes” or "graphene") and this number is still growing. The reasons scientists worldwide research these low-dimensions materials are mainly their unique properties: mechanical[21], chemical[22], electrical[23], optical[24], and thermal[25]. For example, Young’s modulus for individual carbon nanotubes can achieve 810 GPa[26], while for graphene Young’s modulus of 1 TPa was recorded[27]. However, the properties of macroscopic objects from nanocarbon materials are not appreciable. For example, the electrical properties of such ensembles are much lower than building blocks[28].

The most popular solution to this problem is adding doping agents (salts, Brønsted acids, base, etc.) and manufacturing composites with other materials like polymers, metals, or ceramics. It is also possible to combine these two methods. The doping effect is now intensively researched by scientists worldwide. Many substances can be used as doping agents: amines[29], inorganic oxygen acids ($HClO_4$, H_2SO_4, HNO_3)[30] or even guano[31]. As a result of these intensive works, S. G. Kim et al. synthesized fibers from carbon nanotubes (1D macroscopic object) doped by chlorosulfonic acid, and their electrical conductivity was 11.2 MS/m, Young modulus 300 GPA, tensile strength 5GPa, which is the highest published conductivity and is the important step to achieve better properties than traditional materials: copper, steel, and silver[32].

The other strategy is to combine polymer, metal, and ceramics with nanocarbon structures to create materials with improved properties. This connection allows for making new kinds of materials. Thanks to the properties of carbon nanotubes or graphene, even small addition thereof allowed the creation of conductive paths in non-conductive substances such as concrete[33] or basalt[34]. Furthermore, the use of such materials in composites typically improves strength. As a consequence, nanocarbon-containing composites have many potential applications. More description about them is given in the section *Composites based on nanocarbon materials – manufactures methods and properties*.

All the mentioned advantages of carbon nanomaterials caused two of them – carbon nanotubes and graphene - to be produced on an industrial scale. However, nomenclature is problematic for graphene materials. Many companies sell reduced graphene oxide as graphene or graphite oxide as graphene oxide because of the lack of standardization[35]. According to Yano Research Institute Ltd, the production of CNTs was 2255.8 metric tons in 2018[36]. The main applications of CNTs are as a part of composite materials with polymers (about 60%). Another two main fields are: energy storage and electronics[37,38]. The primary production method is chemical vapor deposition and its modifications[39]. The total graphene production is hard to estimate, but it may be a few hundred tons. The application areas typically overlap with those of CNTs[40]. However, unlike CNTs, electronics is its main area of application, then composite materials and energy storage[41].

2.1.2 Oxidized nanocarbon materials

As mentioned in the previous chapter, carbon nanomaterials' main application is connecting with other materials. Unfortunately, due to the underlying chemistry and physics, the mentioned compounds usually integrate poorly with nanocarbon, which results in inefficient energy transfer (thermal, electrical, mechanical). To reduce this problem, functionalization is commonly conducted, which improves the material compatibility by making it more hydrophilic due to the introduction of functional groups[42,43].

Partial oxidization of carbon nanostructures is the most typical way of functionalization. A mixture of two acids HNO_3 and H_2SO_4[44–46], $KMnO_4$[47], H_2O_2[48,49], O_3[50], piranha solution[1], concentrated[51], or fuming nitric acid[52] are a few examples of oxidizing agents that can be used. The substrates (oxidizing agents and used carbon nanomaterials) and parameters affect the primary product and its quality[53]. Such treatment may, for instance, impact the product's electrical conductivity. Oxidized samples had much different conductivity

values compared to the reference sample, which was made up of unoxidized MWCNTs: As compared to films made of pristine MWCNTs, the resistance of films made from oxidized multi-walled carbon nanotubes (O-MWCNTs) produced using fuming acid was nearly two times lower. The resistance of films made from O-MWCNTs by piranha solution increased 1.47 times compared to refence sample, and the resistance value for oxidation was 10.34 times (O_3 – low concentration)[50] and 12.98 times higher (higher concentration). The qualities of products are also influenced by reaction time. Various functional groups, including carboxyl, formyl, hydroxyl, ether, ester (lactones), carbonyl, and acid anhydride, are formed as oxygen atoms are inserted into the carbon nanostructure throughout the reaction. The effect of the time parameter on the ratio between different oxygen groups has been demonstrated by Gerber et al. (Table 1). The amount of carbonyl and hydroxyl groups rapidly increased in the oxidation reaction's early stages using HNO_3 (temperature was 120 ºC), reaching a maximum after 1 hour and progressively declining due to additional oxidation to carboxylic groups. The scientists noticed the development of lactones, acid anhydrides, and carboxylic acid on the surface of the CNTs after the reaction had been going on for two hours. The final ratio between functional groups is: 4.17 -COOH: 6.25 -OH: 2.42 $(-CO)_2O$: 3.75 >C=O: 1 -COO-[54] after the reaction (8 hours). The fact that an increase in temperature leads to an increase in the number of oxygen groups is well known and has been documented in numerous scientific articles[1,44,51,54–56].

Table 1 Evolution of the proportion between functional groups in time. "*Ratio"* was calculated as follows: chosen concertation of groups and ester groups at chosen unite of time [54]

Groups	**Ratio at 0 hours**	**Ratio at 1 hour**	**Ratio at 2 hours**	**Ratio at 4 hours**	**Ratio at 8 hours**
Carbonyl	20.00	90.00	3.75	3.45	3.75
Anhydride	2.00	1.00	1.50	1.91	2.42
Carboxyl	1.00	1.00	2.38	3.36	4.17
Hydroxyl	10.00	21.00	8.88	5.91	6.25
Ester (from lactones)	1.00	1.00	1.00	1.00	1.00

In the case of MWCNTs, this reaction also reduces the number of walls while damaging the nanotube's structure and producing new defects[57,58]. Additionally, the unzipping of the nanotube and formation of graphene oxide nanoribbons can result from the oxidation of MWCNTs by a potent oxidizing agent. That phenomenon was seen in MWCNTs, which were

oxidized by $KMnO_4$[59], by Kosynkin et al. As a result, numerous publications about "oxidative unzipping" began to appear[60–63]. The initial step for oxidation is to create structural defects in the case of an ideal carbon nanotube – without any defects. These defects may be introduced during the synthesis of CNTs or by oxidizing agents during the oxidation of nanomaterial[64,65]. Then, oxidation progresses in the vicinity of these defects. According to Dimiev and coworkers, the ratio of MWCNTs to $KMnO_4$ is crucial for both oxidizing and unzipping nanotubes. MWCNTs/$KMnO_4$ ratios of 1/0.06 and 1/0.12 did not result in a successful reaction. MWCNT oxidation was accomplished at ratios of 0.5 and 1 of $KMnO_4$. When the amount of $KMnO_4$ was three times larger than the MWCNTs, oxidative unzipping was seen[62]. Cataldo and co-workers demonstrated that a solution of HNO_3 and H_2SO_4 may be used to create graphene oxide nanoribbons from SWCNTs[63].

Interestingly, Brønsted acids (H_2SO_4, $HClO_4$, and HNO_3), when used under mild conditions and at low concentrations, can also dope CNTs[30]. Sustaining SWCNT film in an HNO3 solution has been claimed to enhance electrical conductivity. It has been claimed that submerging SWCNT film in an HNO_3 solution enhances electrical conductivity. When the film was submerged in a 69.7% HNO_3 azeotropic solution for three hours at room temperature, Pareth and his co-workers noticed a 33% drop in resistance[66]. Moreover, SWCNT film resistance was 40% lower than pristine film after 12 M HNO_3 60 minutes (room temperature), according to measurements made by Geng et al.[67].

Nowadays, through oxidation, other carbon nanostructures such as graphene oxide (GO) flakes are produced using Hummers[68], Hofmann[69], Brodie[70], and Staudenmaier[71] protocols. Originally, these methods were applied to synthesize oxidized graphite. Later modifications enabled the exfoliation of graphite oxide to GO[72,73]. Besides the Brodie, which is based on photocatalyst reaction with organic compounds, most of these methods are based on aqueous solutions of inorganics acids (H_2SO_4 and HNO_3) and salts (NaCl, $KClO_4$ and $KMnO_4$). Beyond doubt, the modified Hummers' method is the most popular way to synthesize GO due to its lower cost compared to others.

GO is an electrical insulator, thus, to make its electrical conductor, it is necessary to remove oxygen groups, which gives reduced graphene oxide (rGO). The reduction can be made in different ways, such as: thermal annealing[74], microwave[75], chemical reductions (H_2[76], $NaBH_4$[77], N_2H_4[78], Vitamin C[77], etc.). All present methods allow nanomaterial synthesis with different residual oxygen content and properties. For example, hydrazine (N_2H_4) not only reduces GO, but also dopes it, thereby increasing the electrical conductivity of the synthesized

product. rGO is not graphene because of residue functional groups and high defect numbers (Figure 2). However, it is possible to improve the quality of rGO by CVD-Assisted Annealing[79], but it is still low quality compared to graphene synthesized from CVD. However, the chemical method enables the production of much larger amounts of rGO than pristine graphene, which explains its popularity.

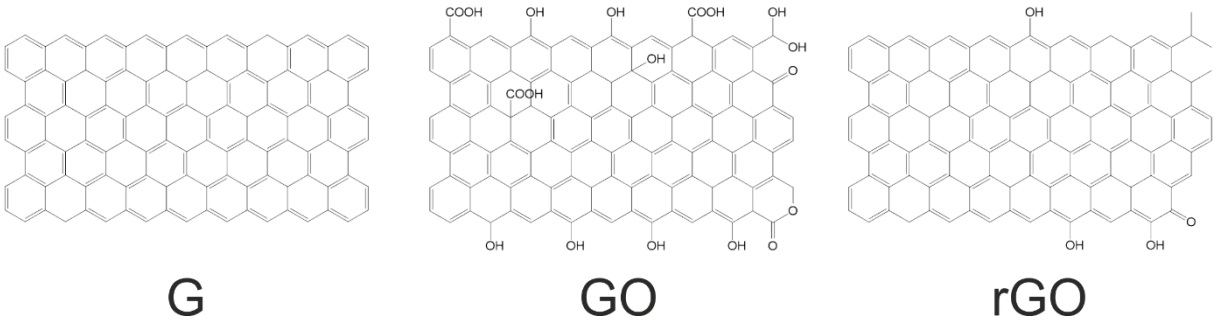

Figure 2 Structure of graphene – G, graphene oxide – GO, and reduced graphene oxide – rGO.

To sum up, functionalization affects the primary structure by inserting oxygen functional groups, which modifies the material's properties. It is conducted to improve the connection between nanocarbon and other materials as it makes nanocarbon more hydrophilic.

2.2 Wettability of nanomaterials

2.2.1 Contact angle and surface characters

Wettability is one of the most crucial surface parameters, significantly impacting material physical properties and integration degree with other materials. The contact angle is defined as the angle where a liquid–vapor interface meets a solid surface (Figure 3).

Figure 3 Schematic diagram of the contact angle (θ).

By studying contact angle, one may monitor the deposition of impurities[80], physical processes (adsorption of hydrocarbons and other impurities)[81], and chemical reactions (corrosion, oxidation, reduction)[5,82]. Water is the most popular used liquid to gauge contact angle because the studied materials are most commonly interfaced with hydrophilic materials. Figure 4 presents the most popular water contact angle (WCA) notations for a given surface to

determine its character[83]: superhydrophilic, hydrophilic, hydrophobic, and superhydrophobic. Thus, WCA is the angle between the pure solid surface, water and vapor without any additional substances in the ideal model. As mentioned previously, in real-life situations, plenty of factors can affect its value, especially adsorbed surface contaminants.

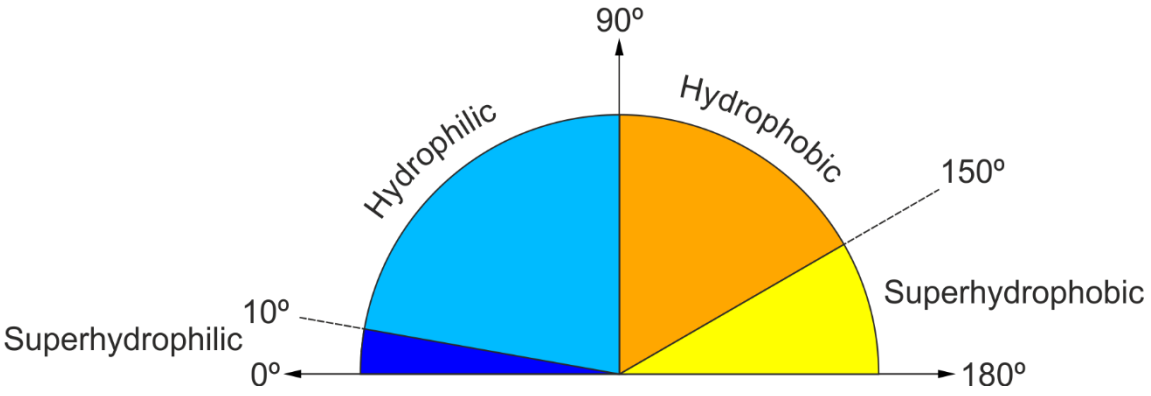

Figure 4 Diagram a value of WCA and the surface character.

Contact angle measurements are divided into two groups (Figure 5): static by taking an image and dynamic by recording the movie. The most commonly used is static contact angle (Figure 5a) – in literature, it usually could be a simple *"contact angle*" due to its popularly. Dynamic allows recording the evolution of contact angle value in time, which might inform us about surface properties. From advancing (θ_{adv}) and receding contact angle (θ_{rec}), it is possible to calculate the contact angle hysteresis (θ_{hys}), which gives us information about the homogeneity of the surface in terms of topography and chemical composition. It can be calculated as follow[84]:

$$\theta_{hys} = \theta_{adv} - \theta_{rec}$$

Where:

θ_{hys} – contact angle hysteresis

θ_{adv} – advancing contact angle

θ_{rec} – receding contact angle

Figure 5b depicts how to register advancing and receding WCAs by the tilting base method. This method is based on gravity force, so the size of the droplet will affect measurements and the size should be the same or similar. It is also possible to obtain the value of θ_{adv} more straightforwardly by adding the liquid volume to the deposited drop (Figure 5c).

Removing part of the chosen liquid and reducing the drop size allows us to measure θ_{rec} (Figure 5d). Additionally, it is possible to make the contact angle measurement under liquid by creating vapor bubbles under the liquid (Figure 5e), which may be useful in understanding the wettability of thin materials[84].

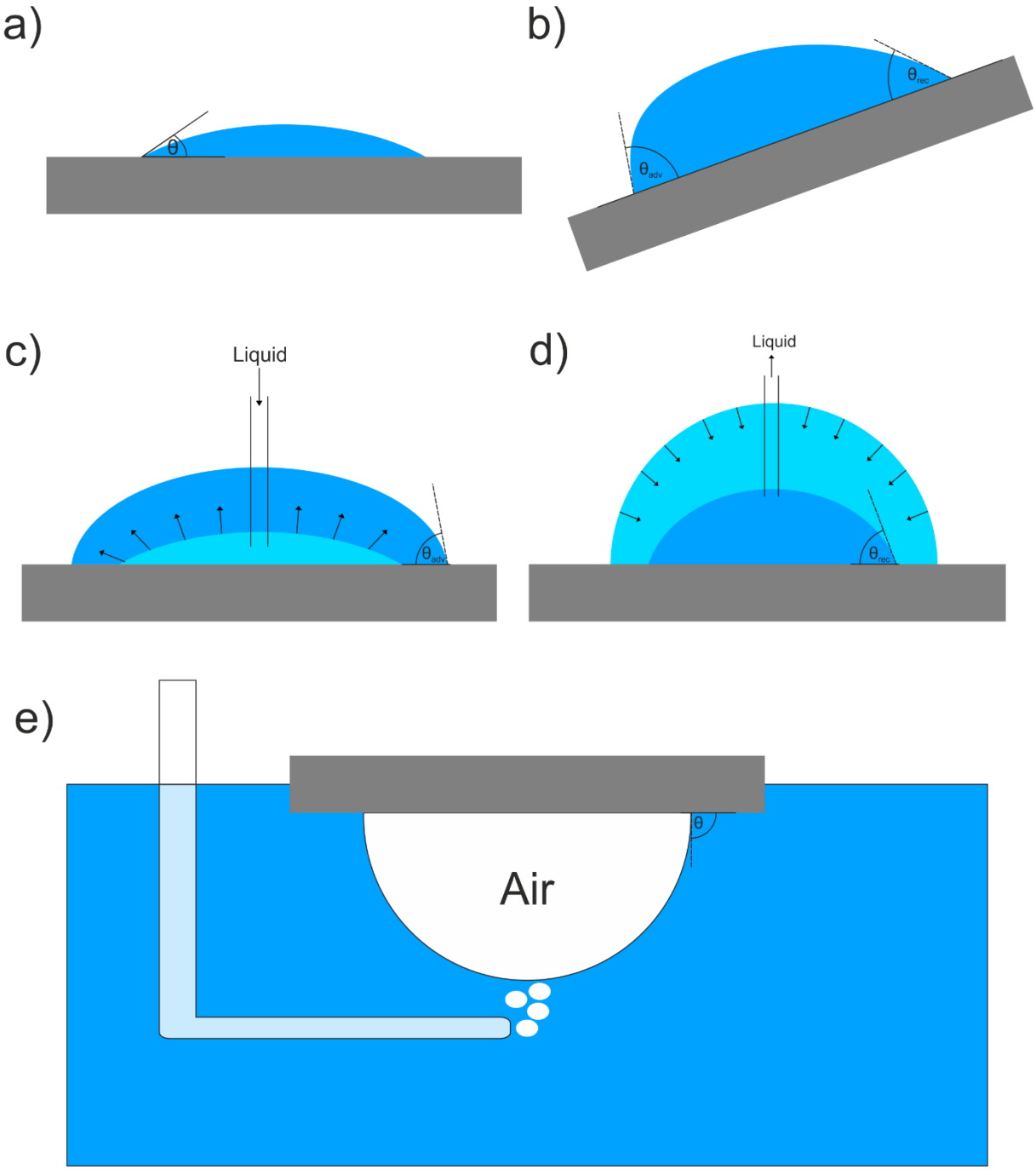

Figure 5 a) static contact angle, b) tilting base method, c) measurement method of θ_{adv} by addition of liquid, d) determination of θ_{rec} by removing the liquid, e) under the liquid method of measurement contact angle.

2.2.2 Surface character of nanocarbon materials and other 2D materials

The scientific community considers carbon nanomaterials as hydrophobic: fullerenes[85], carbon nanotubes[86], and graphite[87], or slightly hydrophilic – graphene[88]. However, there are reports suggesting that their hydrophobicity is caused by airborne contaminants (hydrocarbons), which may conceal their hydrophilic nature[1,80,89–91]. What is more, the values measured for these materials can be from superhydrophilic to superhydrophobic (Table 2). In most references, the researchers do not consider the effect of roughness on the water contact angle measurements, especially for 0D and 1D materials. The impact of roughness on WCA will be presented in this work. In the case of 1D materials – carbon nanotubes, it was demonstrated that after annealing, they are superhydrophilic without any functionalization and exposition for air[1]. In the case of hexagonal 2D materials, after synthesis, they are hydrophilic, but they become more and more hydrophobic in the air[5]. In both cases, authors claimed that airborne contaminants (hydrocarbons) are the reason for hydrophobization. On the other hand, Kuziel et al. claimed in their works that carbon nanotubes and graphene flakes have amphipathic nature – oxygen functional groups on the edges of nanostructures are responsible for hydrophilic behavior in dispersion solution type water/oil and body (sp^2 carbon) exhibits hydrophobic nature[92,93].

Table 2 Contact angles of different carbon nanomaterials.

Material	Contact angle [°]	Ref.
C_{60}	95	[85]
C_{60}	76±10	[94]
MWCNTs *annealed*	0	[1]
MWCNTs *aged*	40	
MWCNTs *long*	157	[92]
MWCNTs *short pristine*	140	
MWCNTs *short purified*	133	
Oxidized MWCNTs	108	
MWCNTs	80±4	[95]
MWCNTs *forest*	170	[96]
MWCNTs	91	[97]
MWCNTs *forest*	152.3±0.1	[98]
SWCNTs	161	[92]

SWCNTs	111	[97]
SWCNTs *annealed*	0	[2]
Graphene/water hydrogel	10±2	[99]
Graphene/ice	30±5	
Graphene/Cu	91±1	
Graphene/Si	88	[100]
Graphene/Au	79	[101]
Graphene/Cu *fresh*	44	[102]
Graphene/Cu *aged*	80	
Graphene/Ni *fresh*	80	
Graphene/Ni *aged*	60	
Graphene oxide	53±1.1	[103]
Reduced graphene oxide	97±2	
MoS_2 *fresh*	69	[90]
MoS_2 *aged*	91	
BN/Ni *fresh*	66	[80]
BN/Ni *aged*	88	
Free-standing graphene (measured by captive bubble method)	42±3	[104]
Graphite *exfoliated*	64±3	[87]
Graphite *aged*	95	

Fresh – contact angle measured immediately after synthesis, aged – contact angle measured after prolonged exposition to air.

Before further analysis of this topic, it is necessary to define what can be found in the air. Many factors impact the composition of air impurities[105]. The primary cause of them is human activity, such as: using fossil fuels to heat homes, industrial activity, transportation, etc.[106,107]. Place, weather, and season affect how much each component is present[108]. The impurities can be classified as inorganic (for example, NH_3, H_2S, HCl, CS_2) and organic compounds (alkanes, alkenes, aromatic compounds, alcohols, ketones, aldehydes, etc.)[108–110]. For instance, toluene was detected in the air in many placed around the world: 131.3 μg/m^3 in Athens (Greece, Europe)[111], 177 μg/m^3 in Memphis (USA, North

America)[112], and 114 μg/m^3 Xinxiang (China, Asia)[110]. 178 μg/m^3 in Nairobi (Kenya, Africa)[109]. Thus, the concentration of airborne contaminants is relatively tiny. Although this concentration is not small as it can change the wettability of very sensitive surfaces like: graphene[90], graphite[113], mica[114], molybdenum disulfide[90], and hexagonal boron nitride[80]. Table 2 presents the WCA of hexagonal 2D materials: HOPG is 64°, SLG is 44°, and MoS_2 is 69°. They were exposed to ambient air for around 30 minutes when their WCAs quickly increased. Ellipsometry revealed that after around 30 minutes, a layer of hydrocarbon pollutants had accumulated with a thickness of between 0.5 and 0.6 nm[115,116]. The final WCA values for exposed samples were as follows: 80° for SLG, 91-96° for HOPG, 89°, and for MoS_2. According to the findings, 2D materials are first modestly hydrophilic before turning hydrophobic due to contamination with airborne hydrocarbons. The Fowkes model calculated the total surface energy based on the contact angles. The total surface energy was calculated to decrease with exposure duration as well: HOPG 54.5 mJ/m^2 →41.1 mJ/m^2, SLG 57.5 mJ/m^2→ 41.5 mJ/m^2, and MoS2 54.5 mJ/m^2 → 46.0 mJ/m^2. Interestingly, this drop was also discovered to be mostly caused by the modification of the polar component of surface energy, which accounts for the rise in WCA with exposure time (Table 3). The surface energy study revealed that the airborne hydrocarbon contamination on the surface of 2D materials is driven thermodynamically by a desire to decrease the overall surface energy.

Table 3 Surface free energy for pure (fresh) surface and after exposition to atmospheric air (aged), based on data from ref[5]

Material	**Contact angle**		**Surface free energy of a fresh sample**		**Surface free energy of an aged sample**		**Ref.**
	Fresh [°]	**After 30 min [°]**	**Non polar [mJ/m^2]**	**Polar [mJ/m^2]**	**Non polar [mJ/m^2]**	**Polar [mJ/m^2]**	
HOPG	64	91-96	46.5	8.0	41.0	0.1	[90,117]
Single-layer graphene (SLG)	44	80	43.5	14.0	37.9	3.6	[117]
MoS_2	69	89	49.0	5.5	45.4	0.6	[90]

Fresh – contact angle measured immediately after synthesis.

Li et al. also observed that water slows down the process of adsorption of hydrocarbons in low-temperature on the surface by adventitious hydrocarbons and does not impact the electrochemical properties of the material[118]. Moreover, the presence of hydrocarbon contaminants on the graphene surface has affected the heterogeneous electron transfer rate (electrochemical property) – the distance between the peaks in the CV curve rose from 59 mV to 177 mV[118]. Additionally, the capacity of supercapacitors or double-layer capacitors may come from the atmosphere or a solution. Hurst et al. reported that the capacity of the supercapacitor from the HOPG electrode was reduced by 70% after being exposed to ambient air for just ten minutes. Because of exposure to room-temperature ambient air, there was a noticeable drop in electrical current. The carbon electrodes were also contaminated when they were exposed to electrolyte solutions and even 'clean' water (such as deionized water from a Nanopure^{TM} water purification system)[115].

To sum up, hydrocarbon contaminants have a high impact on the wettability of materials and, due to it, on the electrochemical properties of the nanocarbon surface. Without considering the presence of these surface impurities, it is unlikely to understand the interaction between pure solid material and liquid.

As mentioned in the previous section, wettability significantly impacts electrochemical properties and can be used to monitor surface character evolution caused by environmental factors, but not only for them. It also influences a variety of other material characteristics: carrier mobility[119], charge doping[120], and integration with other materials[121,122]. The doping effect and wetting transparency have considerably impacted thin materials' contact angle (CA), such as monolayer graphene. Charge doping increases the hydrophilicity of graphene based on Si/SiO_2, according to Gou Hong et al. More hydrophilic values for the water contact angle (WCA) were p-type 60° n-type 78° (WCA for undoped is 88°)[100]. The substrate on which thin nanomaterial (graphene) is deposited is crucial for CA measurements. The WCA for a single layer of graphene (SLG) highly depends on the support character. It measured the WCA value can be: 77º for gold[123], 48º for glass[123], 33º silicon[123], 10º hydrogel[99], and 91º polydimethylsiloxane[99].

2.2.3 Theoretical models

Many theoretical models have been created recently to clarify material wettability while considering roughness's effect on CA. Each one begins with the basic Young equation[124],

which connects the forces in the three phases of the system (Figure 6a): atmosphere (vapor), selected liquid, and chosen solid phase. The equation is as follows:

$$\gamma^{sv} = \gamma^{sl} + \gamma^{lv} \cos\theta \quad (1)$$

Where:

θ – contact angle [º]

γ^{sl} – solid/liquid interfacial free energy [mJ/m^2]

γ^{sv}– solid surface free energy [mJ/m^2]

γ^{lv} – liquid surface free energy [mJ/m^2]

As indicated above, an important factor to consider is surface roughness. The Wenzel[125] and Cassie-Baxter[126] models have been developed to incorporate the influence of a rough surface for the value of contact angle in order to minimize it. They are currently the most well-liked and define two different wetting behaviors. Due to air trapped between grooves on a rough solid surface (Figure 6b), the contact angle measured by Cassie-Baxter (CA) is larger than the contact angle predicted by the model, creating a hydrophobic (solid/air) surface composition. The equation of Cassie-Baxter is:

$$\cos\theta_{CB} = f_1 \cos\theta_1 + f_1 \cos\theta_2$$

θ_{CB} –contact angle from Cassie-Baxter model [º]

f_1 – fraction of air gaps

θ_1 – contact angle of air gaps [º]

f_2 – fraction of solid surface

θ_2 – measured contact angle from experiments [º]

On the other hand, the Wenzel model makes the assumption that liquid permeates the grooves (Figure 6c), and CA may vary depending on the character surface. Compared to what can be seen from an image of a liquid drop on a solid surface, Wenzel CA for omniphilic surfaces will be higher and for omniphobic smaller[127]. Wenzel model is described by the following equation:

$$\cos\theta_{Wenzel} = r\cos\theta_m$$

θ_{Wenzel} –contact angle computed by Wenzel model [º]

r – factor roughness is defined as a ratio between the actual surface and the projected one for solid material

θ_m –contact angle obtained from experiments [º]

Computing free surface energy is the subsequent necessary step to comprehend surface behavior. The equation below compares the free surface energy to the polar and dispersion components.

$$\gamma^{total} = \gamma^d + \gamma^p$$

Where:

γ^{total}– total free surface energy [mJ/m^2]

γ^d – dispersive component of free surface energy [mJ/m^2]

γ^p – polar component of free surface energy [mJ/m^2]

This knowledge allows us to understand surface behavior better. The polar part is from the attraction of charge between the particles. The second part of total surface energy results from the dispersion of electron clouds in the particles on the material's surface.

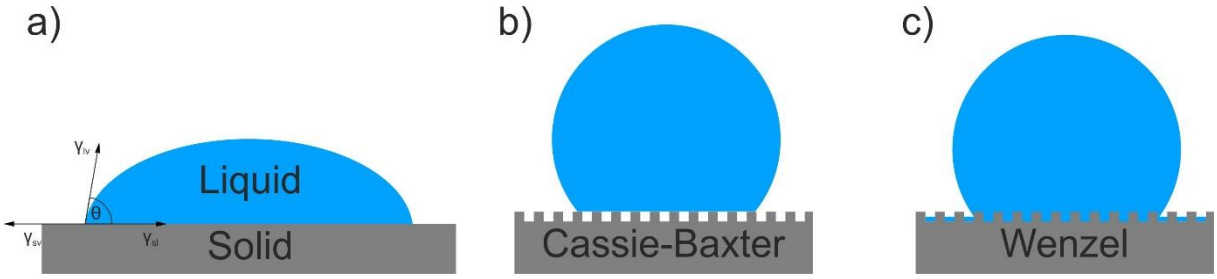

Figure 6 Schematic of: a) Drop of liquid interfaces between three faces described by the Young equation, b) Cassie-Baxter model, c) Wenzel model.

It can be calculated using many theoretical models. But among these, Neumann[128], Fowkes[129], and Owens-Wendt (Fowkes extended by Good's equation)[130] are the most widely used. The first one enables accurate total free surface energy computation. Although it is similar in composition to Fowkes and Owens-Wendt, it cannot be divided into its dispersive and polar components. We may understand the wetting behavior of the research surface under

investigation when we combine the models' results with characterization data obtained by other methods, such as microscopy and spectroscopy.

2.3 Composites based on nanocarbon materials – manufacturing methods and properties

Many techniques can produce composites based on carbon nanomaterial, but most need solvents, and according to green chemistry rules, the most preferred solvent is water. Some of these production methods are based on electrochemistry, for example: electropolymerization and electrodeposition. As mentioned before, the wettability of the substrate is a crucial parameter in electrochemical experiments, so one needs to ensure that nanocarbon is hydrophilic to make high-performance composites (many composite matrices are hydrophilic). Both materials must have the same surface character to achieve a good degree of integration. The next chapter will focus on the two types of composites: polymer and nanocarbon, as well as metal and nanocarbon[131–133].

2.3.1 Composites of carbon nanostructures with polymers

The connection of polymer and nanocarbon has better physical properties (compared to pristine macroscopic objects from nanocarbon materials), such as electrical conductivity[134], capacity[135], thermal conductivity[136], mechanical resistance[137], Seebeck coefficient[138]. What is more, many types of polymers have been used to connect with carbon nanomaterials, which have attractive properties, and due to them, they can be potentially applied as the material for: filtration[139], organic electronic[140], coatings for military[141], thermoelectric generators[138] or in energy storage systems[142]. For filtration, the most popular is a connection of graphene oxide with hydrophilic polymer to improve the mechanical properties of composites, ensuring the capability for separation of ions, for example: Mg^{2+} and Li^{+}, organics residues, and heavy metal ions from organic solvents[139]. The connection of conductive polymer with nanocarbon is very beneficial in the case of application in organic electronics. For instance, polyaniline (PANI), one of the earliest and most well-liked conductive polymers[143], is widely used because of its adaptable electrical properties[144,145], remarkable mechanical strength[146] and simple, inexpensive manufacturing process[147]. In total, there are three different base types (oxidation states) of PANI: pernigraniline (PB) is wholly oxidized (purple/red/black), emeraldine (EB) is slightly oxidized (blue/violet), whereas leucoemeraldine (LB) is completely reduced (yellow/colorless). These PANI forms vary in terms of their electrical and thermal properties[141,146,151]. However, they all have low electrical conductivity values[135,143,148]. Only emeraldine salt (ES) conducts well electric current and can achieve ~ 60 S/cm[149]. Figure 7 presents all described forms of PANI.

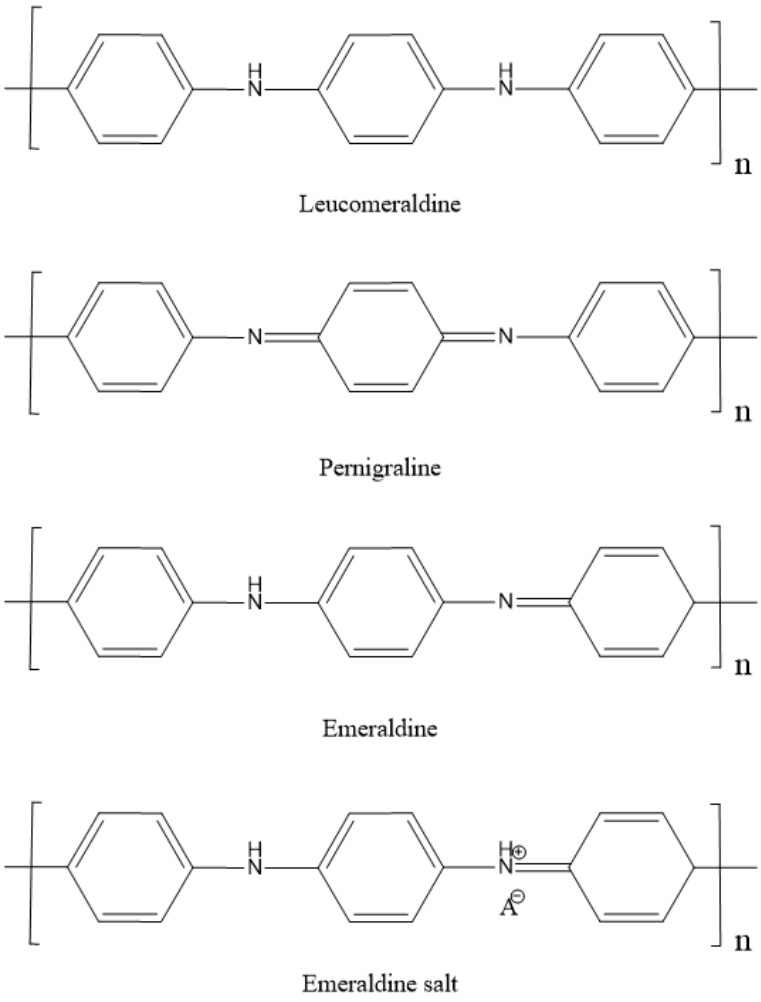

Figure 7 Various forms of PANI (A^- - anion).

R. Wu et al. demonstrated that the composite electrodes from SWCNTs and polyaniline (PANI) could achieve high electrical conductivity of 4 000 S/cm (4 MS/m) and a Seebeck coefficient of about ~23 μV/K[134]. Furthermore, such composites can be used to transform waste heat into electricity. Lu et al. demonstrated that such composites exhibited improved thermoelectric characteristics. Including conducting polymers into the nanocarbon network improved the Power Factor values from 65 $\mu W/mK^2$ to 83.2 $\mu W/mK^2$[150]. Incorporating tellurium nanorods, a material known for its thermoelectric capabilities, into SWCNTs/PEDOT: PSS composite gave even better results (104 $\mu W/mK^2$)[138].

The conductive-polymer composites can also serve as batteries and supercapacitors in electrical storage devices[137,151,152]. However, in order to increase the practicality of these applications, methods for creating high-performance composites with conductive polymers on a wide scale must be developed[153]. Moreover, the PANI-CNTs composites have a

pseudosupercapacitor behavior, and they can achieve high capacity 1266 F/g (PANI grafted to carbon nanotubes)[142], (PEDOT/PSS-SWCNT) 110 F/g[154] and PANI-oxidized SWCNTs 707 F/g[155]). The synthesis parameters and, more crucially, the kind of PANI produced significantly impact the characteristics of the formed PANI-nanocarbon composites[134]. According to reports, PANI/MWCNTs composites' capacitances depend on PANI form: 328 F/g for ES, 217 F/g for LB, and 139 F/g for PB[135]. Additionally, it has been demonstrated that the recorded electrical performance is significantly impacted by the PANI to nanocarbon ratio[134].

Many methods of manufacturing polymer-nanocarbon composites have been developed in recent years and they can be divided into two groups[156,157]:

a) Modification of nanocarbon with polymers by chemical reaction or mixing two materials. In the first group, a polymer is connected with the nanocarbon surface by chemical bonds: amide, ester, ether, carbon-carbon and many more[158]. The nanocarbon materials can be functionalized, but it is not necessary. In the case of functionalized materials, the most popular are amide[159] or ester[160] linkage by condensation. Non-functionalized material can be connected with polymer by cycloaddition[161] or sonochemical reaction[162]. One another strategy to synthesis modified material is to connect the monomer directly or by replacing the functional group with chosen nanocarbon material. The monomer can be polymerized in many ways, such as well-know from polymer chemistry, for example: free radical polymerization[163], reduction/oxidation polymerization[164], and atom transfer radical polymerization[165].
b) Composites processing without chemical connection of materials. One of the most important groups of methods is called “solution processing” or wet methods. They are based on achieving dispersion of nanocarbon or polymer/monomer. The next step is the formation of composites by: the membrane filtration method[134], dip-coating, spray-coating[166], spin-coating[167], in situ polymerization[165], and electropolymerization of dispersion[153] or polymerization onto nanocarbon electrodes[168]. Another group is based on achieving the powder by milling: balls[169], twin-roll masticator[170], and high-speed vibration[171]. The next step is the formation solid state by using high pressure. The powder nanocarbon can also be mixed with melted polymer and then compressed to create a film or fiber[172].

Depending on the intended use, the appropriate method is selected. For example, to achieve a high mechanical resistance composite, the best method is to use a solution and spin it through a spinneret[32]. To achieve good integration between the parts of composite materials via dip coating, spin coating and spray-coating, good penetration of the material by the selected solvent (low contact angle) is essential. Bartholome et al. reported that oxidized CNTs have a better integration degree with polyvinyl alcohol than pristine non-functionalized CNTs. To produce these composites, they used water dispersion of CNTs with the addition of surfactant (sodium dodecyl sulfate) and oxidized CNTs (without any additive). It was claimed that adsorbed sodium dodecyl sulfate caused worse thermal properties of composites containing CNTs and polyvinyl alcohol. However, the surfactant was necessary to achieve good dispersion in water[173]. It was stressed many times that the hydrophilicity of material is crucial for many electrochemical methods.

2.3.2 Composites of copper and carbon nanostructures

To enhance the electrical and mechanical properties of nanocarbon, one can combine them with other conductive materials[174,175]. A notable example of a synergistic effect of such an approach was shown by Subramaniam and co-workers, who demonstrated the properties of a CNT-Cu composite. The obtained material exhibited two orders of magnitude higher current carrying capacity[176] than a Cu standard. Numerous instances in the literature demonstrate the mechanical, electrical, and thermal advantages of contacting Cu with nanocarbon[177–180]. There is a vast spectrum of possible applications for such materials, which spans from supercapacitors[181,182], biosensors[183] to electrical conductors[184]. Composites are particularly promising for overhead transmission lines[184] and the automotive and aerospace industries[116] due to their low weight, high strength, and noteworthy electrical conductivity. Such a method may have a sustainable quality in addition to boosting the features of nanocarbon brought about by metal combinations.

There are many ways to produce this type of hybrid material. Depending on the copper and process character, they can be separated into four groups: powder processing, electroplating, electrodeposition (ED), and electroless deposition. In the first one, powders of nanocarbon and copper are mixed by using such techniques as ball/attrition milling[185–189], sonication[180,190,191], isostatic pressing[192,193], stirring[194] or vortex mixing[195], and then compacted. In this case, the process is straightforward and very scalable, so it can provide a large amount of composite[184,196]. The second one is electroplating, a well-known electrochemical process to make coatings on material surfaces. Electroplating is a simple

method of how these materials can be combined due to the fact that both of them are highly electrically conductive. In such an approach, two electrodes are employed: anode, the source of copper, and cathode, the nanocarbon material where the copper will be deposited. Driving electric current through an electrolyte gives rise to coating nanocarbon substrate with copper[197]. Alternatively, this goal can also be achieved by employing ED. In this approach, carbon nanomaterials such as film or coating networks are used as cathodes, while an inert metal is used as an anode (e.g., platinum). During the electrodeposition, the copper electrolyte is engaged, and its ions are deposited on the surface of carbon nanostructures as metallic copper. In four of them: electroplating, electrodeposition and electroless deposition, wettability is a key parameter that determines the connection between electrode materials and electrolytes (metal source).

One of the key benefits of these electrochemical approaches is that it is easy to conduct co-deposition of other metals by including them in the electrolyte solution[184,198,199]. Lastly, the composite can be made without employing an electric current. In electroless deposition, this can be accomplished by employing appropriate chemical reactions. For instance, to deposit copper onto carbon nanotubes, $CuSO_4$ aqueous solution can be used as a copper source, ethylenediaminetetraacetic acid (EDTA, an agent to complex metals ions) and glyoxylic acid as a reducing species to obtain metallic copper Cu[200]. Figure 8 demonstrates the strategies described above to produce copper-nanocarbon composites. In opposition to metal powder, Cu salts are toxic to the natural environment. The accepted upper limit of copper ions in water for humans is 10 mg/L, but the suggested safe level of Cu^{x+} in water for aquatic life should be lower than 2-4 ppb[201]. Thus, removing them from industrial wastewater is an essential task from the point of view of the circular economy and green chemistry.

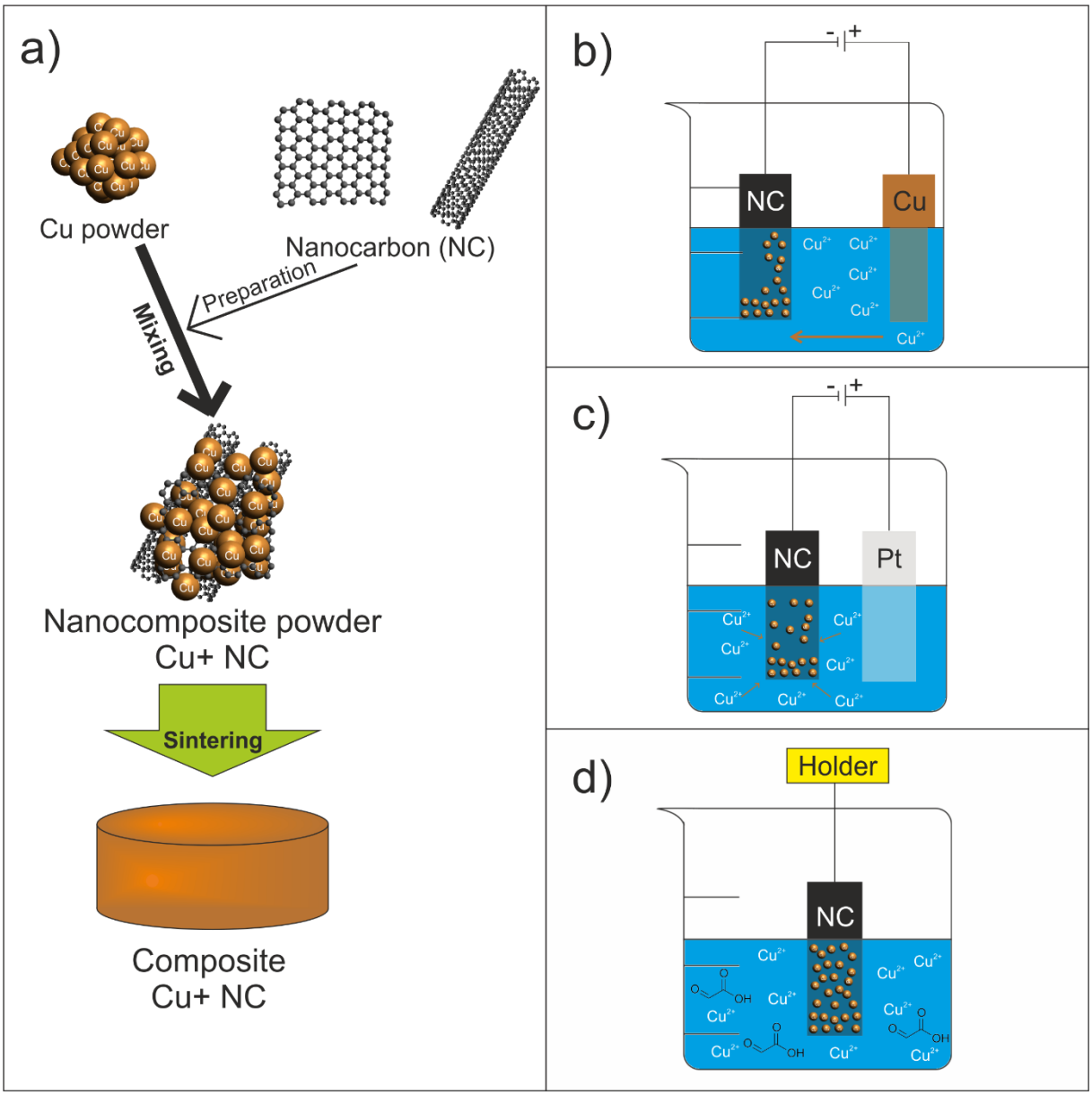

Figure 8 Schematics of four described methods of preparation of Cu-nanocarbon composites: a) powder processing, b) electroplating, c) electrodeposition, and d) electroless deposition.

3. Methodology

3.1 Materials

Table 4 List of used reagents

Name	Purity, Producer
Acetone	pure for analysis, Sigma Aldrich, USA
Aniline	pure for analysis, Sigma Aldrich, USA
Anthracene	≥99.0%, Fluka Analytical, USA
Argon	99.9999%, Matheson Gas, USA
Benzene	pure for analysis, Sigma Aldrich, USA
C_{60}	99.5% purity, Sigma-Aldrich, USA)
Copper foil, 25 µm thick	99.8%, Alfa Aesar, USA
Ethanol	pure for analysis, Chempur, Poland
Ethyl cellulose	pure, Acros Organics, USA
Graphene nanoplatelets, 5 µm particle size, surface area 120-150 m^2/g	99%+, XG Sciences, USA
Graphene nanoplatelets, surface area 300 m^2/g	pure, XG Sciences, USA
HOPG SPI-2 grade 10 × 10 × 1 mm – highly oriented pyrolytic graphite	pure, SPI Supplies, USA
Hydrochloric acid (HCl)	35-38%, Chempur, Poland
Hydrogen	99.9999%, Matheson Gas, USA
Hydrogen peroxide (H_2O_2)	30%, Chempur, Poland
Isopropanol	pure for analysis, Chempur, Poland
Li_2SO_4	(monohydrate, +99%, Acros Organics B.V.B. A., USA)
Mesitylene	pure for analysis, Sigma Aldrich, USA
Methanol	pure for analysis, Sigma Aldrich, USA
Naphthalene	reagent grade, Fisher Chemical, USA
NC7000™ – technical-grade multi-walled carbon nanotubes	Nanocyl, Belgium
O-xylene	pure for analysis, Sigma Aldrich, USA
Paraffine	pure, Polwax, Poland
Perchloric acid ($HClO_4$)	37% aqueous solution, pure for analysis, Avantor, Poland

Phosphoric acid (H_3PO_4)	85%, Chempur, Poland
Potassium permanganate ($KMnO_4$)	Pure, POCH, Poland
Sulfuric acid (H_2SO_4)	95%, Chempur, Poland
Toluene	pure for analysis, Sigma Aldrich, USA
Tuball™ – single-walled carbon nanotubes	80%+, OCSiAl, Luxembourg
Urea	pure, Sigma Aldrich, USA

3.2 General methodology employed to create macroscopic ensembles from nanocarbon materials

Synthesis of C_{60} is a multi-step reaction with a yield between 50-70%[202]. Thus, it was decided to use commercial material due to the high quality of such material and relatively low-cost compared to the costs of synthesis. The same situation was for SWCNTs.

The methods of manufacturing macroscopic objects from nanocarbon were as follows:

a) 0D – C_{60}: spray-coating;
b) 1D – single-walled carbon nanotubes;
   - filtration method to create VFF *(vacuum filtration film)*;
   - dispersion method to obtain DF (*dispersion film)*;
c) 2D – single-layer graphene: in situ synthesis on copper by chemical vapor deposition (CVD).

Using VFF allows understanding of the interaction between nanocarbon and airborne contaminants/polymers. However, VFF was unsuitable for application in electrochemical synthesis composites with polyaniline (PANI) and copper due to too small dimensions. Thus the DF was cut to small electrodes (DFEs) and used exclusively in electrochemical experiments. On the other hand, VFF was used to investigate the phenomenon of hydrophobization, deposition of vaporized hydrocarbons, and synthesis of composites with poly(methyl methacrylate). Figure 9 presents the employed approaches to create macroscopic objects from nanocarbon materials.

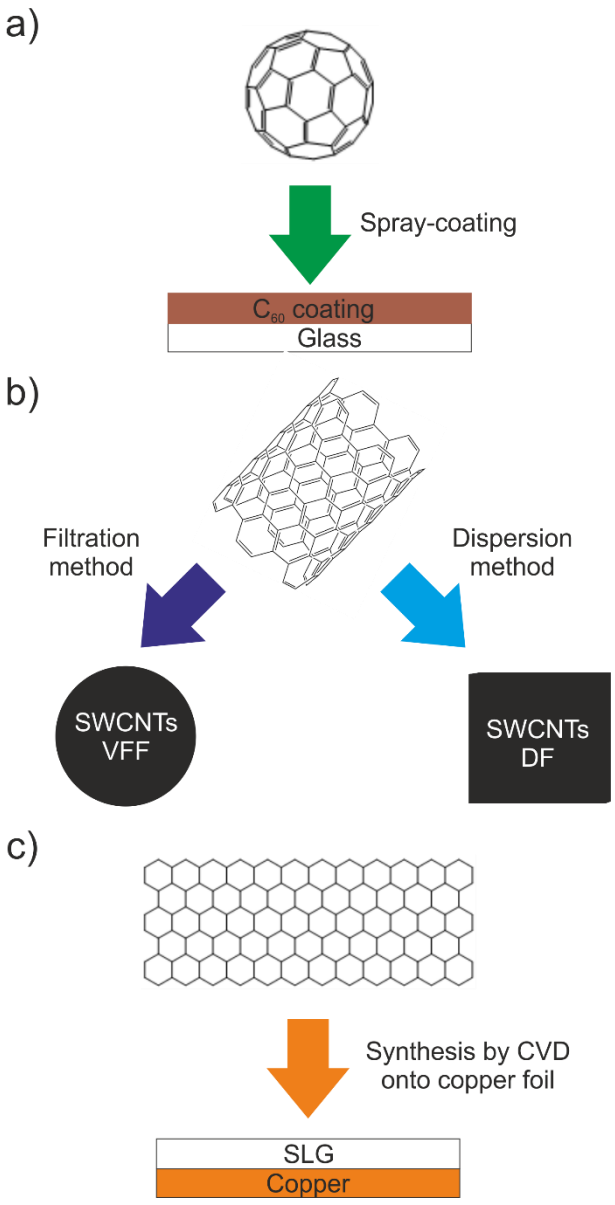

Figure 9 Schema of manufacture of macroscopic objects from: a) C_{60}, b) SWCNTs, and c) SLG.

3.3 Macroscopic objects from nanocarbon materials

3.3.1 C_{60}

C_{60} coating was applied on microscope glass slides using the spray-coating technique. 10 x 10 mm glass slides (total number 16) were put together next to each other to create an 80 mm x 20 mm rectangle secured on cardboard with double-sided tape. The cardboard was then placed in a custom-made glovebox to conduct the coating. 100 mg of C_{60} was dispersed in 15 mL of a 1:1 by mass solution of toluene and acetone. It was sonicated using a UP200St 200W Sonicator (Hielscher, Germany) for 30 minutes at 100% amplitude. The heat produced during the procedure was absorbed using an ice bath. Then, the dispersion was transferred to a spray-

coating gun. Subsequently, the dispersion was sprayed on glass slides attached to the cardboard under 2 bars of pressure. Compressed air was employed as the carrier gas.

3.3.2 SWCNTs

3.3.2.1 Purification

Prior to the production of VFFs and DFs, 3 g of SWCNTs were purified in the air flow for 1 hour at 500 ºC in a tube furnace (air mass flow was 600 sccm). In order to remove impurities produced during the synthesis of SWCNTs (the finished product includes less than 15% residual of catalyst based on iron), the acquired materials were placed in concentrated HCl at boiling point for two hours[203]. The SWCNTs were washed with 400 mL of deionized water and 250 mL of a 5% $NaHCO_3$ aqueous solution before filtering using PTFE membranes (φ = 40 mm, pore size 0.22 μm, Ahistrom, Germany). The product was then dried at 115 ºC during the following day to eliminate moisture.

3.3.2.2 Manufacture of VFFs

The filtration method was applied to create the SWCNTs VFF[3]. 80 mL of a 1:1 by mass solution of toluene/acetone was sonicated with 80 mg of SWCNTs in the ice bath. Sonication parameters were: 100% amplitude for 30 minutes (UP200St, 200W, Hielscher, Germany). The mixture was filtrated on a PTFE membrane (φ = 47 mm, pore size 0.22 μm, Ahistrom, Germany). After drying, the VFF was separated from the PTFE membrane.

3.3.2.3 Manufacture of DFs

500 mg of SWCNTs, 10 mg of ethyl cellulose (EC as the binder) and an 80 g of acetone/toluene mixture (1:1 by mass) were mixed and sonicated (Hielscher UP200St, Germany) at 100% amplitude over an ice bath until uniform dispersion was noticed. The dispersion was then deposited onto a 90 x 90 mm sheet of Nomex® using the drop-casting technique[204]. A DF was created after drying, and the EC binder was then eliminated from it by heat annealing in the air[1].

3.3.2.4 Oxidation of SWCNTs, O-SWCNT VFFs, and O-SWCNT DFs

SWCNTs (Tuball^{TM}, OCSiAl, Luxembourg) were oxidized[68,205] using a modified version of Hummers' technique. Time, temperature, and the quantity of $KMnO_4$ (POCH, Poland) oxidant were the three changed reaction parameters. Samples were taken for Raman spectroscopy at the following reaction periods: 0, 10, 20, 30, 40, 50, 60, 120, 180, 240, 300, and 420 minutes. The three selected reaction temperatures were 0 °C, 18 °C, and 40 °C.

SWCNTs were exposed to a solution of H_2SO_4 and H_3PO_4 and $KMnO_4$ at the following mass ratios: 0 (absence of oxidation agent), 0.15, 0.25, 0.45, 0.95, 1.9, 3.75, and 7.5.

12 mL of 85% H_3PO_4 and 120 mL of 95% H_2SO_4 (both from Chempur, Poland) were combined with 0.2 g of SWCNTs. The mixture was then mechanically stirred (OST Basic yellow, IKA Works, USA) for 30 minutes at 300 rpm. $KMnO_4$ was dosed continuously during this time. The times mentioned above, which were counted when the $KMnO_4$ addition was finished, are how long the reaction took to complete. The subsequent step was to pour the mixture into a glass beaker that held 400 mL of distilled water and 20 mL of 30% H_2O_2. Following that, the solid material was separated using PTFE membranes (diameter 47 mm, pore size 0.22 μm; Fisherbrand, Canada) and vacuum filtering. The crude product was purified using 100 mL of 10% HCl, 100 mL of distilled water, and 100 mL of methanol. The resultant material was dried at 80ºC overnight to eliminate moisture.

VFFs were formed using the same procedure as specified above for SWCNTs. The DFs were created from pristine SWCNTs as described in *3.3.2.3 Manufacture of DFs*. For O-SWCNTs, the method was modified as follows: mass ratio O-SWCNTs and binder (EC) was set to 1:1, and the components were mixed. The next steps remained the same as the procedure for SWCNTs[3].

3.3.3 Single-layer graphene

Single-layer graphene (SLG) was synthesized onto copper foil by chemical vapor deposition (CVD). The procedure was taken from the literature, and the only modification was: using 1% CH_4 in Ar instead of pure CH_4 and changing the mass flow of H_2[206]. As mentioned, the carbon source was methane, and the carrier gas was hydrogen and argon. The copper foil was cut into 70 x 10 mm rectangles. Before synthesis, it was electropolished for 30 seconds in a prepared solution (urea 5 g, isopropanol 50 mL, H_3PO_4 250 mL, ethanol 250 mL, deionized water 500 mL). The current used in the process was 0.5 A, electrodes (anode and cathode) were copper foils, but only the anode was used for synthesis. Deionized H_2O purified the Cu foil and then it was dried by N_2. Prepared foil was placed on a quartz boat and put inside of quartz tube. Then, after the pressure reduction to 45 mTorr, the H_2 flow and annealing were started. The flow was 20 sccm, and pressure returned to atmospheric value. The substrate was annealed for 1 hour. The process temperature was 1050 ºC. After this, the 1 sccm of 1% CH_4 in Ar was introduced to the tube reactor, and the growth step of graphene started. It lasted for 30 minutes. The last step was to finish the reaction by cooling it down rapidly to room temperature. The

flow of gases was flowing until room temperature was established. The gases were supplied by Matheson Gas (USA).

3.4 Annealing of nanocarbon surface and exfoliation of HOPG

The method was selected based on a literature review[1,5]. C_{60} coating's surface was annealed at 350 ºC and atmospheric pressure, with 90 sccm of Ar and 10 sccm of H_2 flowing through it for 4 hours (Figure 10). After completion of the annealing, the flow was continued until achieving room temperature. The tube was purged from the air for 30 minutes prior to heating. SWCNT VFFs were annealed the same way as SWCNT DFs during removing the binder[1]. SLG/Cu was annealed in a tube furnace as in the case of $C_{60,}$ but different parameters were used: 350 ºC, 2 hours, 100 sccm Ar and 10 sccm H_2. To remove surface contaminants from HOPG, a few graphene layers have been exfoliated with sticky tape until achieving a pure homogenous surface.

3.5 Deposition of hydrocarbons

Hydrocarbons were deposited by two saturation techniques: “flow” (SLG/Cu) and “static” (C_{60}, SWCNTs, HOPG). “Flow” used bubbling and flow of carrier gas via solubilized benzene and PAH powder to transfer hydrocarbons onto the freshly annealed SLG surface (Figure 10). After the finishing of the deposition, the material was immediately characterized. This method allows for reducing the impact of environmental factors like airborne contaminants. The static method was based on placing (immediately after surface purification) C_{60}, SWCNTs, and HOPG samples on the platform from glass slides inside a glass container filled with chosen hydrocarbon (Figure 11) to let saturated vapors deposit on the nanocarbon surface.

All glass used in the procedure was first purified by piranha solution at 60 ºC for 30 minutes, and after that, the glass was washed with deionized water. The quartz tube was annealed in air at 750 ºC for 4 hours to remove deposited C_xH_y.

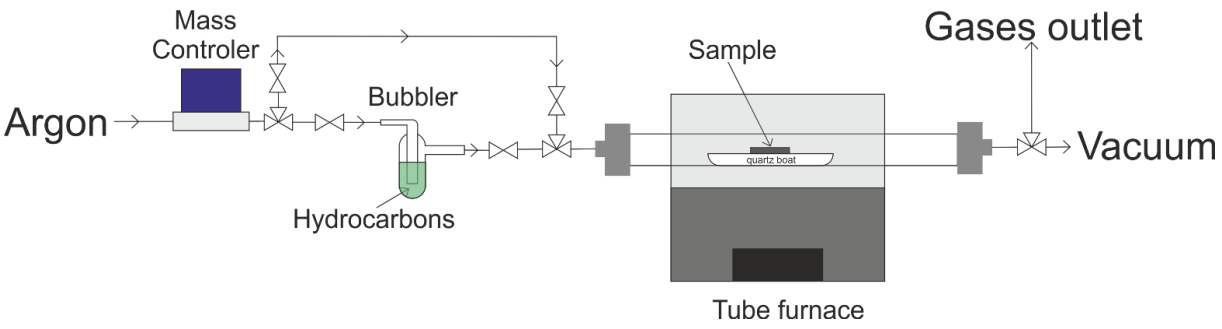

Figure 10 Setup used for annealing nanocarbon surface and dynamic deposition of hydrocarbons.

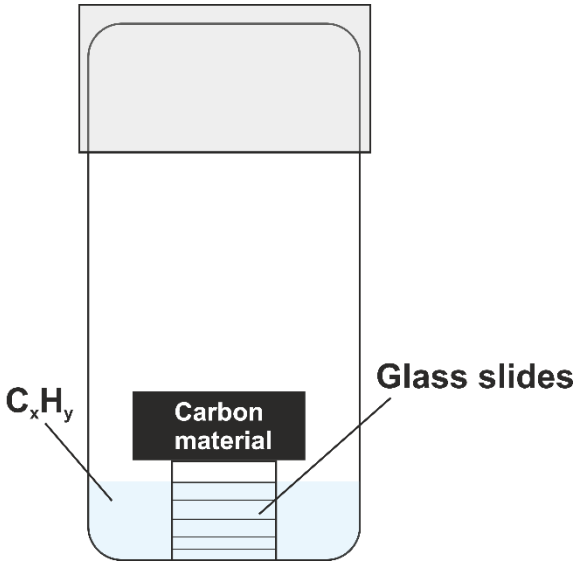

Figure 11 Chamber for static deposition of hydrocarbons.

3.6 Theoretical models

a) According to the Langmuir model, a monolayer of adsorbed molecules from the vapor phase covers the whole surface of solid material[207]. The Langmuir isotherm was used to compute the coverage of the adsorbent by monolayer degree:

$$\theta_{Lan} = \frac{K_{Ad/De} p_A}{1 + K_{Ad/De} p_A}$$

Where:

θ_{Lan} – coverage degree of adsorbent by monolayer adsorbate

$K_{Ad/De}$ – adsorption-desorption equilibrium [1/Pa]

p_A – partial pressure of adsorbate [Pa]

b) The Wenzel model reduces the impact of roughness on the contact angle value. As it was mentioned previously, it assumes that liquid drop permeates the grooves of the rough surface.

$$\cos\theta_W = r\cos\theta_m$$

Where:

θ_w – Wenzel contact angle [rad]

r – the ratio of surface area to predicted area – roughness factor

θ_m – measured contact angle [rad]

c) The Fowkes model, which combines the Young, Young-Dupree, and the decomposition of the total surface energy into two compounds (dispersive (nonpolar) and polar) to calculate surface energy[129]:

$$\frac{(\gamma_l \cos\theta + 1)}{2} = \left(\gamma_l^d\right)^{\frac{1}{2}}\left(\gamma_s^d\right)^{\frac{1}{2}} + \left(\gamma_l^p\right)^{\frac{1}{2}}\left(\gamma_s^p\right)^{\frac{1}{2}} \quad (5)$$

Where:

θ – contact angle

γ_l^d – liquid dispersive (nonpolar) component [mJ/m^2]

γ_s^d – solid dispersive (nonpolar) component [mJ/m^2]

γ_l^p – liquid polar component [mJ/m^2]

γ_s^p – solid polar component [mJ/m^2]

3.7 Composites of polymer and nanocarbon – synthesis

3.7.1 Synthesis of the composite of CNTs with poly(methyl methacrylate)

VFFs from SWCNTs and O-SWCNTs were created the same way as it was presented in previous sections (*Section 3.3.2.2 Manufacture of VFFs and Section 3.3.2.4 Oxidation of SWCNTs, O-SWCNT VFFs, and O-SWCNT DFs)*. The SWCNT VFF after/before annealing and coming from O-SWCNTs prepared by Hummers method (time of reaction – 0 minutes, $KMnO_4$/SWCNTs mass ratio – 7.5 and temperature – 40 ºC) were immersed into acetone: 5% poly(methyl methacrylate) MW 996 000 g·mol^{-1} (PMMA) by A KSV-DCX2 dip-coater (Biolin Scientific, USA). The coating procedure was as follows: 10 immersions for 5 seconds with 3 seconds breaks for drying the composite.

3.7.2 Synthesis of nanocarbon and polyaniline composites

DFs from SWCNTs were previously described in section *3.3.2.3 Manufacture of DFs*. The elaborated methods have been modified to make composites of SWCNTs with graphene nanoplatelets 120-150 m^2/g. The procedure was as follows: SWCNTs were ground for 5 min before mixing with graphene and adding to organic solvents. 0.5 g of the mixture of SWCNTs and graphene combined with EC were put into 80 mL of an acetone/toluene solvent (1:1 by mass) and next, they were sonicated for 30 minutes at 100% amplitude in an ice bath with a 50:1 mass ratio of carbon nanomaterials to EC. Drop casting transferred the created dispersion from the glass beaker onto a NOMEX® sheet. Due to the limited adherence of the nanocarbon DF to the polyamide after solvent evaporation, it was delaminated and cut into smaller electrodes (DFEs): measuring 50 mm by 10 mm, and the binder was removed by annealing. Three mass ratios—1:9, 1:3, and 1:1—were used for the graphene nanoplatelets and SWCNTs (G+SWCNTs) composites.

DFEs from O-SWCNTs obtained by the Hummers method (procedure described in section *3.3.2.4 Oxidation of SWCNTs, O-SWCNT VFFs, and O-SWCNT DFs*) were produced in the same method as was described previously. Prior to the synthesis of the PANI+O-SWCNTs composites, the parameters of SWCNTs oxidation (temperature, $KMnO_4$/SWCNTs mass ratio, reaction time) were selected. Based on the results from section 4.2, two temperatures (0 ºC, 18 ºC) and three mass ratios (0.15, 0.45, 0.95) were selected and the reaction time was 0 minutes. This selection of parameters made it possible to study the effect of the amount of oxygen functional groups (I_D/I_G) on the PANI electropolymerization process. Table 5 summarizes the type and quantity of materials used to synthesize DFs from carbon nanomaterials.

Table 5 Amount of supplies required to prepare a 90 x 90 mm thin DFs

DFs	**Graphene [mg]**	**SWCNT [mg]**	**O-SWCNTs [mg]**	**EC [mg]**
SWCNTs	-	500	-	10
G+SWCNTs 1:9	50	450	-	
G+SWCNTs 1:3	125	375	-	
G+SWCNTs 1:1	250	250	-	
O-SWCNTs (0 ºC, 0.15 ratio)	-	-	500	
O-SWCNTs	-	-	500	

(0 ºC, 0.45 ratio)				
O-SWCNTs (0 ºC, 0.95 ratio)	-	-	500	
O-SWCNTs (18 ºC, 0.95 ratio)	-	-	500	

SWCNTs – single-walled carbon nanotubes; O-SWCNTs – oxidized SWCNTs; G – graphene nanoplatelets 120-150 m^2/g; EC- ethylcellulose

A description of the synthesis of PANI onto nanocarbon DFs is given in Supplement. In short, two DFs from nanocarbon materials as working and counter electrodes were used for PANI synthesis on nanocarbon materials. The reference electrode was Ag/AgCl. Aniline was dissolved in a water solution of $HClO_4$. The chosen range of electropolymerization (EP) was [(0V) – (1.2V)]. Figure 12 presents the setup for the synthesis of PANI-SWCNTs composites. To calculate the theoretical mass of deposited PANI and yield of synthesis, two equations were employed[208–211]:

$$m_t = \frac{q \cdot M}{F \cdot z}$$

Where:

m_t – PANI deposited mass on the working electrode calculated from the theoretical model [g]

q – complex impedance [A]

M – aniline molar mass 93.13 [g/mol]

F – Faraday constant: 96500 [A/mol]

z – the number of electrons in reaction (value is 2 for this case)

$$\eta = \frac{m_p}{m_t} \cdot 100\%$$

Where:

η – yield

m_p – purified product mass [mg]

m_t – the mass calculated from the previous equation (theoretical) [mg]

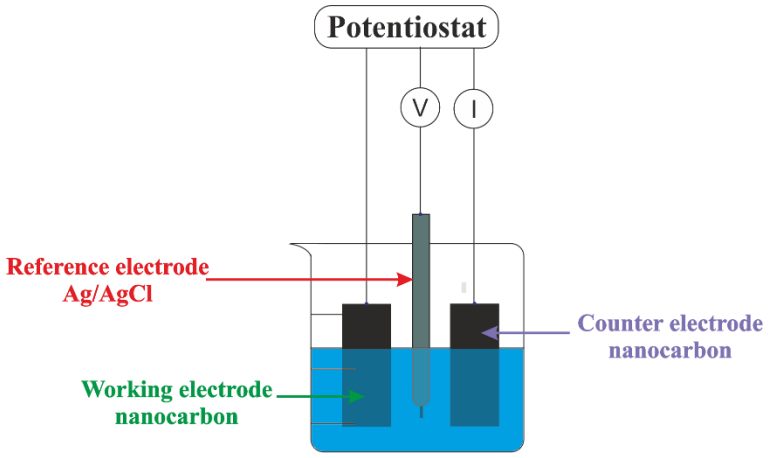

Figure 12 Setup used for electropolymerization of aniline onto nanocarbon materials.

3.8 Synthesis of Cu+nanocarbon composites

3.8.1 Carbon nanomaterials used for the synthesis of composites

Several nanocarbon materials were analyzed, some made internally and the rest obtained from commercial sources (where mentioned). MWCNTs and O-MWCNTs are the same materials as in the case of composites with PMMA described above.

SWCNTs (d=1.5 nm; Tuball^{TM}, OCSiAl, Luxembourg), NC-MWCNTs (d=10 nm; NC7000^{TM}, Nanocyl, Belgium), and graphene nanoplatelets 300 m^2/g (C-300, Sigma-Aldrich, USA) were employed as commercial materials in work. The company claims that the graphene substance is a few nanometers thick. The dissertation refers to these substances as SWCNTs, NC-MWCNTs, and G, respectively. With the exception of SWCNTs, the materials were used without any post-processing. Due to earlier discovery that the milling procedure boosts the electrical conductivity of the DFs created from them by inducing suitable deagglomeration[212], they were ground for 5 minutes.

Multi-walled CNTs (MWCNTs) were synthesized by using catalytic chemical vapor deposition (c-CVD). The procedure was the same as used in previously published works[213,214]. A furnace (Horizontal furnace Carbolite HST 12/900) was injected with a 5.5% wt. solution of ferrocene (p.a., Sigma-Aldrich, USA) in toluene (p.a., Chempur, Poland) at a rate of 5 mL/h while being kept under an argon flow (1.8 nL/min) at 800 °C for 4 hours. After that, the dosing was stopped, and flow was running until the furnace had room temperature.

MWCNTs were oxidized to examine the effects of oxidation. They received treatment using a 3:1 (V/V) mixture of HNO_3 (65% Chempur, Poland) and H_2SO_4 (95% Chempur, Poland). The procedure was carried out for three hours at 140 °C. After the reaction, the system was cooled to room temperature, and the mixture was filtered through a polytetrafluoroethylene (PTFE) membrane filter with 0.22 μm pore size. To neutralize the pH of the product, it was first washed with a suitable quantity of 5% $NaHCO_3$ aqueous solution and then with distilled water. The product was then dried at 115 °C overnight.

3.8.2 Manufacture of nanocarbon DFEs

The same method was used to create composite DFs from two types of nanocarbon material, as in the case of SWCNT DFs: acetone/toluene (1:1, w/w) were combined with nanocarbon and ethyl cellulose (EC). With the exception of DFs produced from SWCNTs, for which it was selected a 50:1 ratio, it was the ratio of nanocarbon/EC 1:1 by mass in all the DFs. The materials were then sonicated over ice for the required amount of time using a Hielscher UP200St (Germany) at 100% amplitude. The dispersion was then applied on a Nomex® sheet (RP PRO, UK), from which dried nanocarbon sheets could be easily removed. Finally, EC was eliminated by annealing[166]. The DF size was 90 mm x 90 mm. To produce composite DFs materials, the following parameters were used: 80 mL mixture of acetone/toluene 1:1 mass, 0.5 g (for SWCNTs 0.01 g) ethyl cellulose and 0.5 g nanocarbon material. After delamination from the substrate, the composite containing 50% Graphene was corrugated and the surface was not homogeneous (holes in DFs). Due to the poor mechanical properties of the composite, they were not suitable for further research. Table 6 presents details about the preparations of DFs. Nanocarbon DFs were sliced into a rectangular electrodes (DFEs) form with dimensions 10 mm wide by 25 mm long for each electrochemical experiment.

Table 6 Information about preparation DFs for DFEs

Short Name	Materials used for DFs formation
SWCNTs	Single-walled carbon nanotubes
NC-MWCNTs	Commercial multi-walled carbon nanotubes
MWCNTs	In-house made multi-walled carbon nanotubes
10% O-MWCNTs	Oxidized in-house made multi-walled carbon nanotubes combined with single-walled carbon nanotubes proportion 1:9 by mass

25% O-MWCNTs	Oxidized in-house made multi-walled carbon nanotubes combined with single-walled carbon nanotubes proportion 1:3 by mass
50% O-MWCNTs	Oxidized in-house made multi-walled carbon nanotubes combined with single-walled carbon nanotubes 1:1 by mass
10% N-MWCNTs	*N*-doped in-house made multi-walled carbon nanotubes combined with single-walled carbon nanotubes proportion 1:9 by mass
25% N-MWCNTs	*N*-doped in-house made multi-walled carbon nanotubes combined with single-walled carbon nanotubes proportion 1:3 by mass
50% N-MWCNTs	*N*-doped in-house made multi-walled carbon nanotubes combined with single-walled carbon nanotubes proportion 1:1 by mass
10% Graphene	Graphene combined with single-walled carbon nanotubes proportion 1:9 by mass
25% Graphene	Graphene combined with single-walled carbon nanotubes proportion 1:3 by mass
50% Graphene	Graphene combined with single-walled carbon nanotubes proportion 1:1 by mass

3.8.3 Electrodeposition of copper onto nanocarbon DFEs

A synthetic Cu electrodeposition bath containing 40 g of Cu (0.63 mol/dm^3 Cu) and 100 g of H_2SO_4 per 1 L (1.02 mol/dm^3 H_2SO_4) was used to evaluate the electrochemical behavior of nanocarbon DFEs. The study also employed actual industrial process effluent. The Inductively Coupled Plasma - Optical Emission Spectrometer (ICP-OES) method was used to calculate the quantitative and qualitative composition of wastewater.

All electrochemical studies were conducted using a three-electrode cell with electrodes facing one another. The counter electrode was a platinum sheet with an order of magnitude larger surface area than the nanocarbon DFE sample employed as the working electrode. The nanocarbon DFE was 5 cm away from the platinum electrode. The stated current density values were estimated using the observed submerged geometrical area following the experiment utilizing the nanocarbon DFE sample that had been immersed about 1.5 cm into the fluid. The

reference electrode was a normal calomel electrode (SCE) positioned close to the nanocarbon DFE surface. As seen in the diagram below (Figure 13), the electrodes were attached to an IviumStat 24-bit CompactStat potentiostat (Ivium Technologies, Netherlands). The equilibrated open circuit potential of the electrodes was set to E = 0 V vs. SCE for cathodic polarization studies after the cathode's potential stabilized for 60 seconds. The voltage (E) was then swept at a rate of 20 mV/s from 0 V to -1 V. Cu was applied to the nanocarbon DFE by galvanostatic deposition, or chronoamperometry.

A modest amount of Cu was added to the nanocarbon DFE by a galvanostatic deposition pulse as distinct nuclei in order to examine variations in the surface activity of nanocarbon DFE. The deposition took place for 1 second at 0 V vs. SCE. All of the nanocarbon DFEs, both with and without the binder, were subjected to testing. Longer plating studies were also done to verify the application potential. It used the following parameters to recover Cu from wastewater: deposition voltage of -0.1 V vs. SCE for 3600 s. Six nanocarbon DFEs – SWCNTs, NC-MWCNTs, MWCNTs, 25% O-MWCNTs, 25% N-MWCNTs, and 25% Graphene – were employed in these investigations. All electrochemical operations were carried out a room temperature.

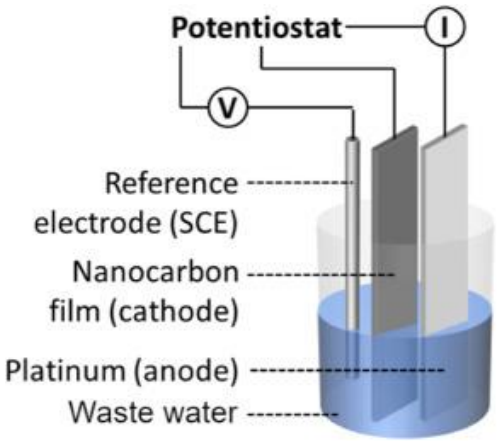

Figure 13 Three-electrode arrangement for Cu electrodeposition in a schematic. Reproduced with permission from ref. [4] © 2021 Grzegorz Stando, Pyry-Mikko Hannula, Bogumiła Kumanek, Mari Lundström, Dawid Janas. Published by Elsevier B.V.

3.9 Characterization of materials

3.9.1 C_{60}, SWCNTs, and SLG – powder and macroscopic objects

Surface morphology was examined using a scanning electron microscope (SEM) (SEM-JEOL-6390LV, Jeol, Japan) at 15 kV acceleration voltage and a 5000x magnification.

Roughness was defined using an atomic force microscope (AFM; Asylum MFP3D, Oxford Instruments, UK). At least four separate areas were subjected to tapping mode AFM scans. A minimum of two scans were taken from each location.

The Horiba Raman/AFM/TERS system (Horiba, UK) was used to create the Raman spectra. In each sample, the mapping mode acquired 50 spectra from 50 locations. 5 seconds were allotted for the exposure, the accumulation number was 10, and the gratings used were 1800 g/mm for the 437 nm laser and 2400 g/mm for the 638 nm laser. The software provided by the vendor was used to calculate the intensity ratio between the selected peaks (D, G, 2D, $A_g(2)$, $H_g(7)$, etc.). SLG required a laser at 473 nm and a power of 2.5 mW, while samples of C_{60} and SWCNTs required a laser at 638 nm and a power of 2.4 mW. SLG was transferred from copper foil to a SiO_2/Si wafer (Addison Engineering, USA) prior to measurements using a wet technique published in the literature[206]. Poly(methyl methacrylate, MW 996 000 $g \cdot mol^{-1}$ Aldrich) was spin-coated on top of SLG/Cu foil. The bottom side of graphene and copper were then eliminated by etching for 5 hours in a 0.1 M solution of aqueous ammonium persulfate (98%, Sigma-Aldrich). The PMMA-coated SLG was then transferred to a water bath using a microscope slide. After that, it was dried on a Si wafer. The PMMA was overnight dispersed in an acetone bath after drying. The samples were then dried and prepared for Raman analysis.

ESCALAB 250Xi XPS apparatus (Thermo Fisher, USA) was used to collect experimental samples' spectra. C_{60} samples were treated for 30 seconds by flood gun before collecting to surface charge compensation. Collection parameters were: $9 \cdot 10^{-9}$ Pa pressure in the analysis chamber, 10 scans in each chosen area, step size 0.1 eV, Al Kα (1486.6 eV) source gun, and plot size 650 µm. XPS was calibrated using pure silver wire.

By using a Bruker VERTEX-70LS FTIR (spectral range) with an accessory permitting attenuated total reflectance (ATR) measurements, FTIR spectra in the 4000-600 cm^{-1} range were acquired. Nitrogen was used to purge the device for 30 minutes prior to spectrum recording. A total of 64 scans with a resolution of 4 cm^{-1} were performed on each sample. Software from the vendor was utilized for analysis and to take the bands out of the backdrop.

In order to measure contact angles, both "side-view" and "top-view" methods were used:

- Side-view method

VCA Optima XE (AST products, USA) recorded the images of 2 μL drops placed on nanocarbon materials at a temperature of 20–22 °C and an average humidity of 30%. Each liquid under test had its specific syringe. After five seconds of deposition onto the surface, a picture of the contact angle was captured. Contact angles were calculated using vendor-supplied software, and their average value was based on 4–10 measurements.

- Top-view method

The drop had a 5 μL volume. Images were taken using a specially constructed setup that included a lifter, the smartphone camera (Samsung S10 mini, Korea), and a selfie stick (SPIGEN S540W, USA) with a Bluetooth controller. Like the "side-view" technique, the average temperature and average humidity were: 22 ºC and 30%. The drop was applied to a solid surface using an automatic pipette (Thermofisher, USA) that can dispense amounts of 1 to 10 μL. The values of the contact angle were calculated as follows[215].

Regarding omniphilic:

a) A specially constructed apparatus measured the drop's radius.

b) The following equation was used to calculate the drop's height:

$$\frac{1}{6}\pi h^3 + \frac{1}{6}\pi r_{cap}^2 h - V = 0$$

Where:

V – a volume of a drop [cm^3]

h – drop height [cm]

r_{cap} – radius of spherical cap [cm]

c) The following equation was used to compute the contact angle (θ):

$$\theta = 2\tan^{-1}\frac{h}{r_{cap}}$$

For omniphobic:

a) The h from the definition of spherical cap volume was calculated using the whole radius.

b) Equation below between the radius of the drop area (r_{cap}), the full radius, and the height of the drop was used to compute the r_{cap}:

$$r_{cap}^2 = 2rh - h^2$$

c) θ was calculated as follows:

$$\theta = 2\tan^{-1}\frac{h}{r_{cap}}$$

The two liquids: water and diiodomethane, were used to obtain contact angle values. Two ways of measuring contact angles were calibrated: "top-view" and "side-view." Both provided consistent WCA for polytetrafluoroethylene (PTFE), HOPG and SLG/Cu (Table 7). The top view technique enables collecting photos of drops on SLG/Cu samples as soon as annealing or deposition of C_xH_y is complete (less than 5 seconds), avoiding the need to carry samples unnecessarily to the contact angle goniometer. The reduction of airborne contaminant exposure time was essential: WCA values for SLG/Cu samples exposed for 5 and 15 seconds, respectively, are around 42º and 51º. Thus, top-view techniques reduced the time from 15 seconds to under 5 seconds, which is crucial for SLG/Cu measurements. Other materials: C_{60}, SWCNTs and HOPG the measured method did not have such a strong impact on WCA values after annealing or exfoliation (HOPG). Hydrophobization of materials was much slower than in the case of SLG/Cu.

Table 7 Measured WCA values by both methods

Material	Side-view WCA [º]	Top-view WCA [º]
PTFE	109.3±3.9	109.0±1.0
HOPG – aged	90.7±2.1	90.4±1.4
HOPG – exfoliated	63.5±3.9	63.0±1.3
HOPG – 30 minutes of benzene vapor deposition	82.5±4.1	82.2±4.8
SLG/Cu – 15 seconds air exposed	51.1±4.4	51.5±3.9
C_{60} coating annealed	0.0±0.0	0.0±0.0
SWCNTs annealed	0.0.±0.0	0±0.0

3.9.2 O-SWCNTs – powder, VFF, and DFs

Raman spectroscopy (Renishaw, Germany) was used to monitor the evolution of the intensity of peaks typical of nanocarbon materials and indicative of the chemical state of the SWCNT surface as the reaction progressed. To confirm the homogeneity of oxidation, the samples were assessed at 10 random locations using the following parameters: laser power of 5%, wavenumber 100-3000 cm^{-1}, magnification 20x, exposure time of 10 s, and 3 accumulations.

To describe the morphology of the products of SWCNTs oxidation (powder and DFs) high-resolution scanning electron microscopy (HR SEM, SUPRA 35 ZEISS, Germany) was employed. At 8 kV, the materials were examined.

Using a Keithley 2182A source meter (USA), the electrical conductivity of the reaction products' thin O-SWCNT DFs was measured using the 4-probe method. 100 mA of current was used during the measurement.

A specially constructed setup outfitted with a CMOS camera (Thorlabs, USA) was used to measure the water contact angles of VFFs. A camera image was captured after the 10 μL of demineralized water was applied to the chosen sample. During the measurements, the temperature was 21 °C, and the humidity was 53%. The contact angle plugin in ImageJ was utilized for the analysis.

A custom-made constructed thermopower setup (LBR CAMSEEB, Lublin, Poland) was used to determine Seebeck coefficients. The sample was heated from 25 °C to 100 °C while maintaining a 5 °C temperature difference between its hot and cold sides and a 5 °C temperature step between measurements. Due to resistance readings from a nanovoltmeter, the software calculated the value of the Seebeck coefficients.

ESCALAB 250Xi XPS apparatus (Thermo Fisher, USA) was used to collect experimental samples' spectra. C_{60} samples were treated for 30 seconds by flood gun before collecting to surface charge compensation. Collection parameters were: $9 \cdot 10^{-9}$ Pa pressure in the analysis chamber, 10 scans in each chosen area, step size 0.1 eV, Al Kα (1486.6 eV) source gun, and plot size 650 μm. XPS was calibrated using pure silver wire. Thermo Scientific Avantage software analyzed all spectra – to determine the bonds present on them. The components were fitted with the sum of Gauss (30%) and Lorentz (70%) functions. The background was created and subtracted by an automatic function (based on Shirley).

3.9.3 Characterization of polymer-nanocarbon composites

The surface area of the nanocarbon DFs was estimated using the Langmuir and Brunauer-Emmett-Teller (BET) models based on the results of nitrogen adsorption/desorption isotherms (ASAP 2420, Micromeritics, USA). The research was commissioned from the Center for Advanced Technologies of the Adam Mickiewicz University in Poland.

The values of water contact angles (WCA) for VFFs, DFs and composites were measured using a custom-made setup equipped with a CMOS camera (Thorlabs, USA). The same as in the case of O-SWCNTs described in section *3.9.2 O-SWCNTs – powder, VFF, and DFs*.

The materials were examined by a Raman spectrometer (made by Renishaw, Germany). The spectrometer's specifications were as follows: incoming light's wavelength was 514 nm; laser power was 5% (2.5 mW); exposure time was 10 s; accumulations were 4, and magnification was 20 times. The measurements were taken at three random locations to ensure the statistical significance of the collected data. By dividing the intensity of the D peak (sp^3 carbon atoms) by the intensity of the G peak (sp^2 carbon atoms) in the Raman spectrum, I_D/I_G for CNTs was calculated[216,217].

Scanning Electron Microscopy (SEM) combined with a dispersion X-ray energy detector (SEM+EDX) was used to examine the morphology of the samples for the reasons listed below: Working distance is 8 to 9 cm, and the current intensity is 5 kV. The magnifications that were used were 500x and 1000x, respectively. The analysis was commissioned from the Aalto University in Finland.

The PerkinElmer L160000A Fourier transform infrared spectrophotometer with attenuated total reflectance (Waltham, USA) was used to evaluate the composite samples. The wavelength range used for the spectra recording was 300 cm^{-1} to 4000 cm^{-1}. The analysis was commissioned from the Aalto University in Finland.

The ESCALAB 250Xi XPS instrument (Thermo Fisher, USA) was utilized to examine the chemical composition of the material's surface using X-ray photoelectron spectroscopy (XPS). Under 8.2 10^{-9} of lower pressure, scans were obtained. The gun type and plot size were the same as used in the section (*3.9.1 C_{60}, SWCNTs, and SLG – powder and macroscopic objects*). Five scans of the selected chemical elements were acquired at an energy pass of 50 eV (step size 0.100 eV). In the case of survey spectra, two scans were recorded. The generated data

were deconvoluted using Thermo Scientific Avantage software the same way as in the case of previous chapters: peaks shapes Gauss (30%) and Lorentz (70%) functions and the background by an automatic function (based on Shirley).

The mechanical tester ADMET eXpert series (ADMET, USA) was used to measure mechanical properties at a 10 mm per minute extension speed. The measurement samples were 40 x 10 mm in size, with the thickness varying depending on the type of composite being examined.

The 4-probe approach was used to measure the electrical properties using a Keithley 2182A source meter (Keithley, USA). The sample area was measured with an electronic caliper, and the thickness was determined with a micrometric screw. The measurements were made at least five times for each sample due to the thickness fluctuation.

With infrared thermography, the steady-state approach was used to measure thermal conductivity by IR thermal camera (FLIR ETS 320, Wilsonville, USA). The sample was measured by recording the temperature profile throughout its length as a direct current with predetermined parameters passed through it, the sample's temperature was measured as a function of its length, and it was modeled using the equation:

$$\kappa = \frac{U \cdot I \cdot 0.5L}{4 \cdot w \cdot d \cdot (T_m - T_o)}$$

Where:

κ – thermal conductivity [W/mK]

U – voltage [V]

I – current [A]

L – sample length [m]

w – sample width [m]

t – sample thickness [m]

T_m – the temperature in the middle of the sample (higher than either of the sample's ends) [K]

T_o – the temperature on the end of the sample [K]

A custom-made vacuum chamber was used for the measurements to eliminate environmental influences that would otherwise lead to heat convection to the environment.

Seebeck coefficients of synthesized composites were determined the same way as for O-SWCNTs.

The relation presented below was used to calculate the power factor:

$$Power\ Factor = \alpha^2\sigma$$

Where:

α – Seebeck coefficient [V/K]

σ – electrical conductivity [S/m]

The figure of Merit (zT) was computed by the equation:

$$zT = \frac{\alpha^2\sigma}{\kappa}T$$

Where:

zT – Figure of Merit [-]

α – Seebeck coefficient [V/K]

σ – electrical conductivity [S/m]

κ – thermal conductivity [W/m·K]

Using custom-made a designed Swagelok-type symmetrical coin cell configuration with three electrodes, as explained in ref.[218,219], the capacity of the supercapacitor was determined. Briefly stated, the reference electrode was Ag/AgCl (Accumet 13-620-53, Fisher, USA), the WE and CE were made of nanocarbon-based materials, the compression fittings were made of perfluoroalkoxy alkane with stainless steel flat ends, and the springs and coins were made of stainless steel. In an aqueous solution of 0.1 M Li_2SO_4, the CV ranged from 0 to 0.4 V vs. Ag/AgCl, a sweep of 50 mV/s, and an equilibrium duration of 60 s. The electrochemical data were analyzed with Gamry's Echem Analyst program. The following equation was used to determine capacitance:

$$C = \frac{1}{2w(\Delta V)} \int_{t1}^{t2} i(t)\, dt; dt = \frac{dV}{v}$$

Where:

C – capacitance [F/g]

w – the mass of the electrode [g]

V – potential [V]

i – current [A]

t – time of the CV [seconds]

t1 – initial time of the process

t2 – end time of the process

3.9.4 Characterization of synthesized copper-nanocarbon composites

The microstructure of the investigated nanocarbon DFEs was examined using scanning electron microscopy (SEM; JEOL JSM-7500FA). The materials were examined at a magnification of 2,200x for nanocarbon-Cu composites and 16,000x for powder samples under a 15 kV acceleration voltage. The surface composition of nanocarbon-Cu materials was examined using Energy-Dispersive X-ray Spectroscopy (EDX, JEOL JED-2300 Analysis Station) at a 15 kV acceleration voltage.

The parent nanocarbon materials' and the thin DFEs generated from them were evaluated using Raman spectroscopy (Renishaw, Germany). This technique was used to measure all of the powder and DFE samples. The following measurement parameters were used: a laser with a 514 nm wavelength, 5% power, a 20x objective, and a 10-second exposure time. To achieve statistical significance and reduce background noise, measurements were made at numerous locations on a sample at various accumulations.

The electrical conductivity of the DFEs was measured the same way as for DFs from SWCNTs and O-SWCNTs.

A specially constructed set-up using a CMOS camera (Thorlabs, USA) was used to measure water contact angles (WCA). Each time, 10 μL of water was placed on the DFE surface, and the contact angle value was calculated using an image taken with a camera with a macro lens. For WCA measurements, several droplets were put onto each type of DFE.

To determine the chemical composition of industrial wastewater, Inductively Coupled Plasma Optical Emission Spectroscopy (ICP-OES) was conducted (Perkin Elmer Optima 7100 DV, USA).

4. Results and Discussion

4.1 *Hydrophobic or Hydrophilic?* – understanding the wettability of nanocarbon materials and the phenomenon of their hydrophobization in the air

4.1.1 Investigation of the surface nature of nanocarbon structures

First, the water contact angles (WCAs) have been used to determine the surface character of the thin macroscopic objects made from C_{60}, SWCNTs, SLG/Cu, and HOPG (Figure 14). C_{60} (138.3±0.8º) and HOPG before exfoliation (exposed to airborne contaminants for more than 3 months) (96.9±2.9º) were hydrophobic in contrast with SLG/Cu's slightly hydrophilic character before annealing (also it was exposed to airborne contaminants for more than 3 months) (82.9±1.5º) nature. Figure 14 presents the WCA values for the top (facing air during drop casting, 81.3±3.5º) and bottom (facing the filter during drop casting, 109.7±5.8º) sides of the VFF from SWCNTs.

However, the two sides have varied roughness, which is the cause of the non-identical WCA value. According to the further examination performed by SEM and AFM (Figure 15), the top side is smoother. Top and bottom Wenzel roughness factors (r) are 1.11±0.01 and 1.49±0.08, respectively. After taking this issue into account, it can be concluded that both sides have comparable WCA of ca. 90º. All materials have hydrophilic or even superhydrophilic characteristics once the surface contaminants are removed by thermal annealing: C_{60} and SWCNTs (both sides) 0º, SLG 41.8±2.1º (compared to 42.0±1.3º measured immediately after synthesis) and HOPG 63.8±2.1º (after exfoliation). As it is less rough, the top side of SWCNTs' VFF was chosen for additional investigation.

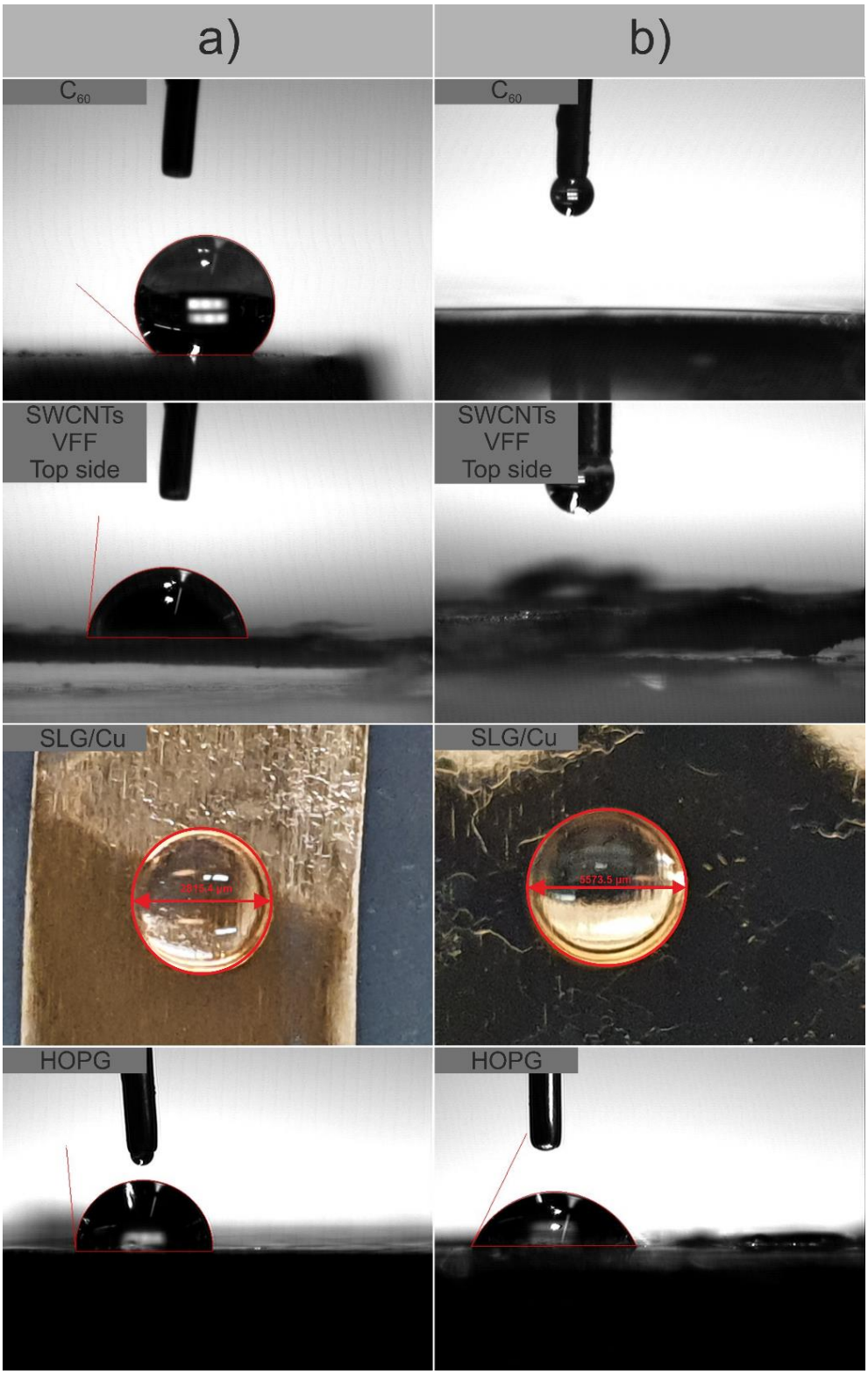

Figure 14 WCA measurements before (a) and after (b) the surface purification process: C_{60} and SLG/Cu were annealed in an atmosphere mixture of hydrogen and argon, SWCNT VFF were annealed in air, and HOPG was exfoliated.

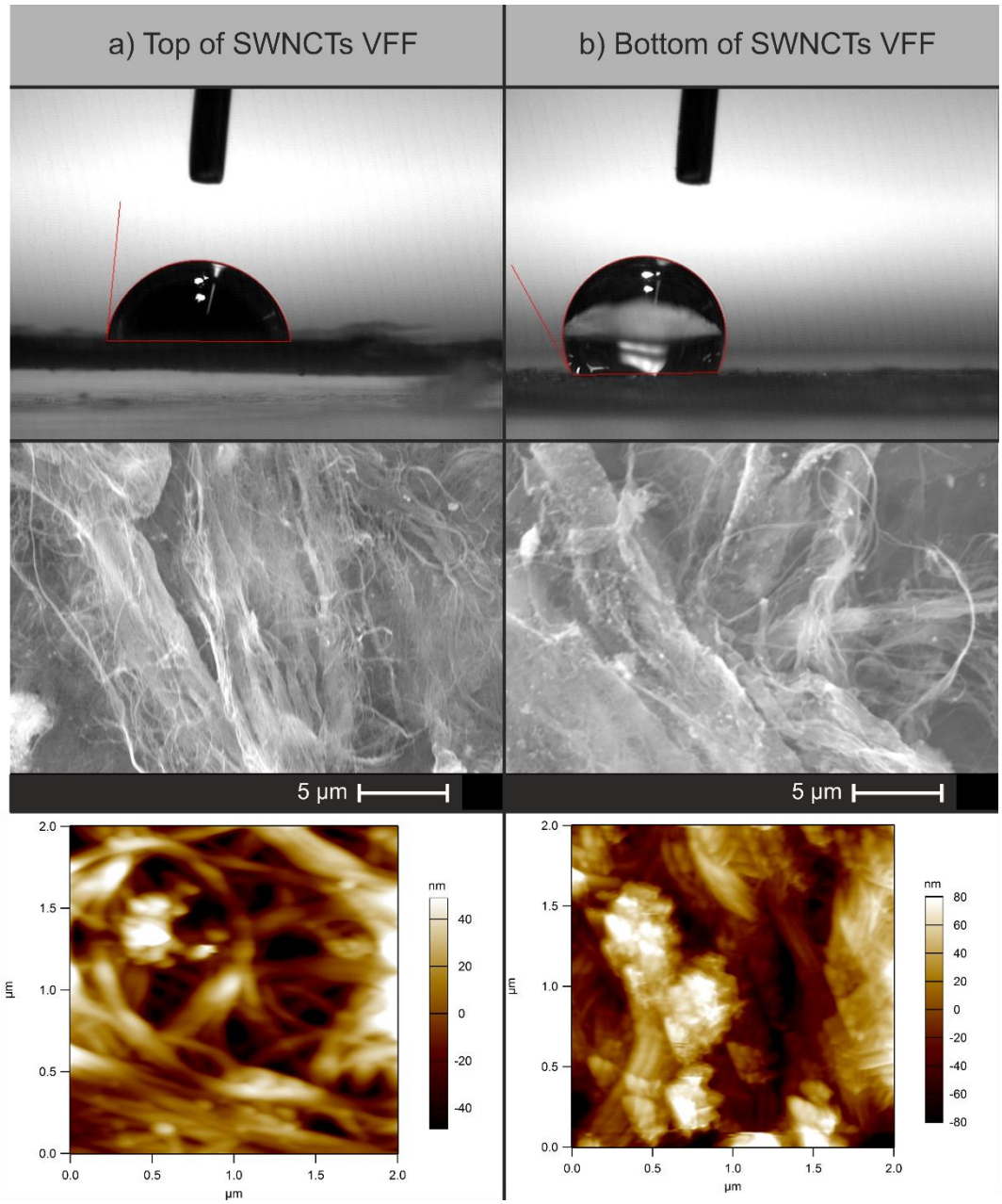

Figure 15 The WCA was measured on the top and bottom sides of the SWCNT VFF, surface analysis using scanning electron microscopy and atomic force microscopy.

Raman mapping was used to examine the surface of nanocarbon materials. Most significant peaks for C_{60} ($H_g(7)$, $A_g(2)$, and $H_g(7)$)[85], SWCNTs (RBM, D, G, 2D), and SLG (D, G, 2D)[216] were detected. No noticeable changes in peak intensity were observed after the annealing for C_{60}, SWCNTs and SLG/Cu. The proportion of bands from the 1460 cm^{-1} pentagonal pinch mode ($A_g(2)$) to 1416 cm^{-1} and 1564 cm^{-1} asymmetrical modes ($H_g(7)$ and $H_g(8)$) found at the C_{60} determine the impact of annealing[85,220]. The ratio of $A_g(2)/H_g(7)$ = 0.18±0.01 and $A_g(2)/H_g(8)$ = 0.17±0.01 for C_{60} before and after annealing is the same (Figure

16a). Regarding SWCNTs, RBM, 2D, G, and D peaks were unaffected by the treatment (Figure 16b). Prior to annealing, I_D/I_G^{SWCNTs} were 0.10±0.01 and after annealing, they were 0.10±0.02. Because there was no D peak in the spectra, the annealing procedure did no structural damage in SLG (I_D/I_G^{SLG} = 0) and I_{2D}/I_G^{SLG} were 1.88±0.07 and 1.87±0.06, respectively, which also proves no interference in graphene structures (Figure 16c). Examples of C_{60}, SWCNTs, and SLG Raman spectra are shown in Figure 16.

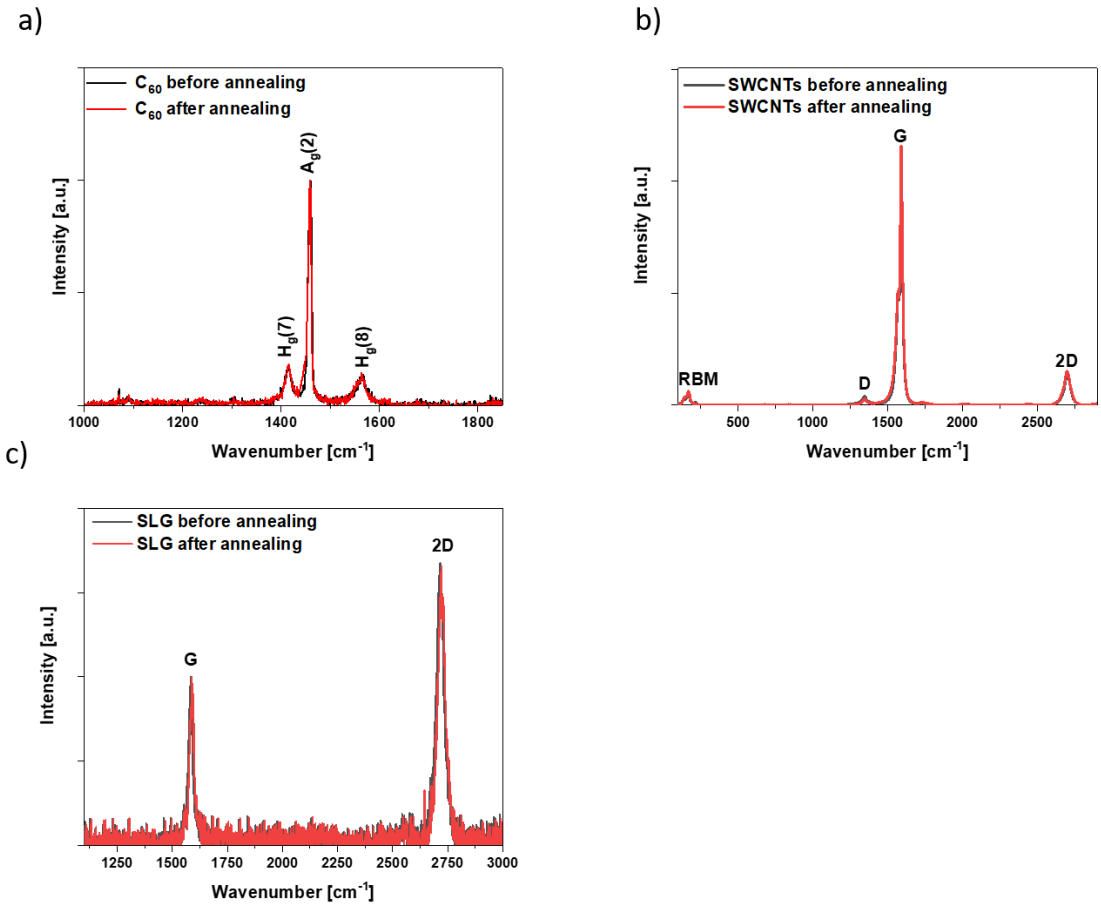

Figure 16 Raman spectra of a surface before and after annealing of C_{60}, SWCNTs, and SLG.

XPS spectroscopy was used to investigate the potential change in the chemical composition of the surface of macroscopic objects from carbon nanostructures before and after the annealing process (Figure 17). Additionally, XPS spectra of C_{60} and SWCNTs powders were used to check if there was any functionalization during the manufacturing of macroscopic objects. The C1s spectra of C_{60} coating before annealing had a different shape from C_{60} powder – form 284.6 to 289 eV spectrum had higher intensity (Figure 17a), which was caused by the presence of the bands from adsorbed hydrocarbons (toluene and acetone): C-C/C-H (284.8 eV) and C=O (288.5 eV)[221]. These organic solvents were used to manufacture C_{60} coating on

glass. After annealing, the spectra are nearly the same as pristine powder material, thus strongly suggesting that organic solvents are removed from the surface of C_{60} during the annealing. Regarding O1s spectra, it is visible that one single band at 532 eV from C=O (the chemical bonds are most likely from acetone molecules), adsorbed water and oxygen (Figure 17b, d and f)[221–223]. Thus it was hypothesized that similar intensity of O1s for C_{60} before and after annealing is caused by adsorbed water and oxygen form air, which replaces C=O from acetone. Furthermore, the recorded XPS spectrum of C_{60} powder was similar as observed by other scientists for non-functionalized material[224].

C1s spectra for SWCNTs (Figure 17c) before/after annealing and powder demonstrated that carbon nanomaterials were not damaged during film manufacture and annealing, which proves that lack of functionalization might cause the hydrophilization. The increasing intensity of the band in 532 eV (Figure 17d) was caused by the nanocarbon surface's adsorption of H_2O and O_2[221–223]. Results are coherent with the previous research, which demonstrated a lack of oxygen functional groups, which might be responsible for hydrophilization[1,3].

SLG/Cu C1s scan (Figure 17e) also presented a lack of significant change of chemical composition (no functionalization) and was similar to results recorded by other scientists. They showed a lack of insertion of oxygen functional groups onto the non-functionalized surface of SLG during the annealing process[116]. O1s scan of SLG/Cu (Figure 17f) presents the impact of support on XPS spectra as the band at 530.6 eV likely comes from CuO[225]. Copper as a hydrophilic material (measured WCA before graphene synthesis was 32.6±4.8º) definitely can easily adsorb water from the air[226], so the observed band increase at 532 eV may be due to the presence of Cu and give wrong conclusions as to the causes of the presence of water. Considering this statement, it was decided not to analyze the O1s scan in the case of SLG/Cu due to a potential misunderstanding of the results.

In light of the above interpretation, it was concluded that the nanocarbon materials do not undergo chemical functionalization during annealing.

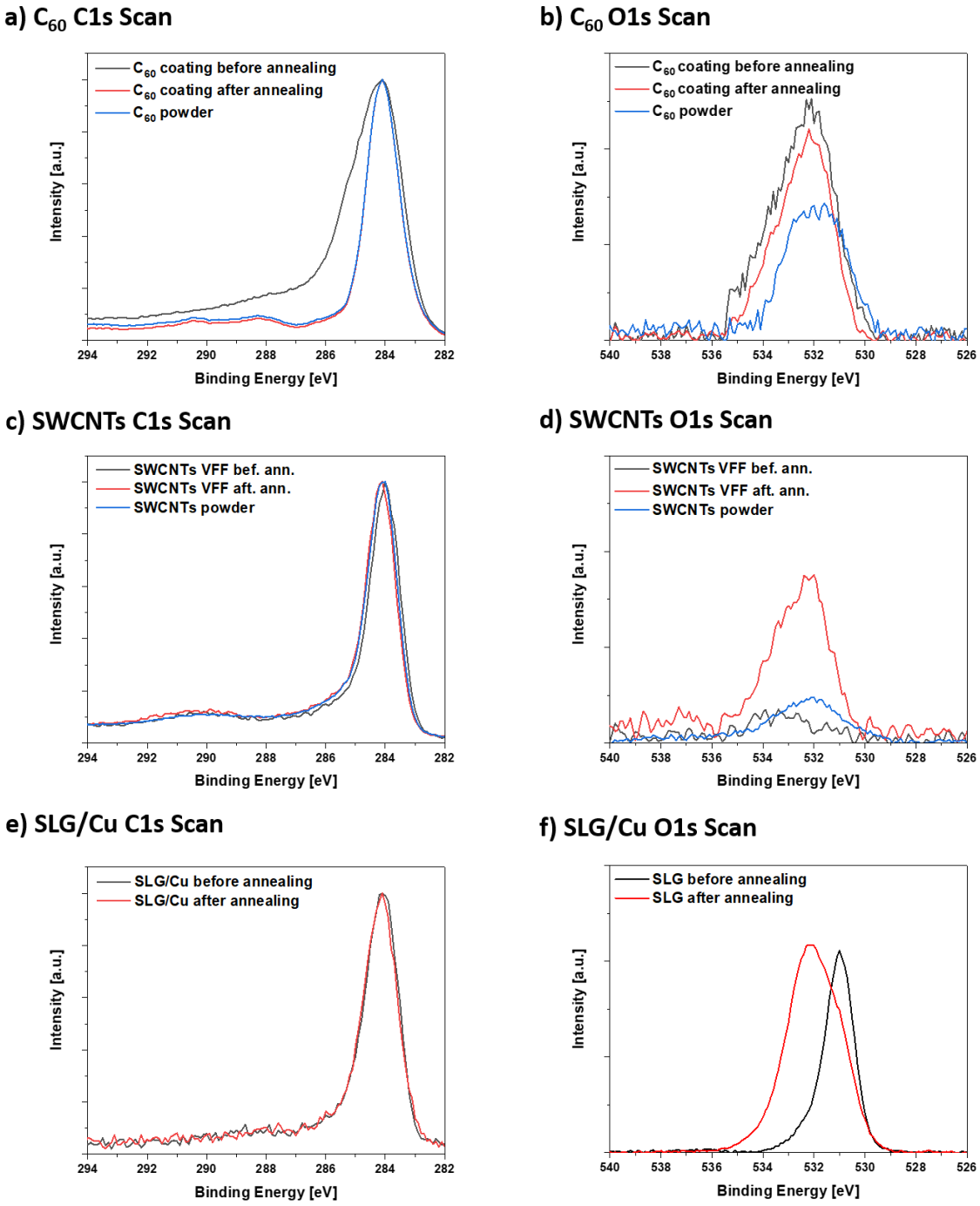

Figure 17 XPS spectra: C_{60} coatings before/after annealing and C_{60} powder used to manufacture coating – a) C1s scan and b) O1s scan, SWCNTs VFFs before/after annealing and SWCNTs powder used to create it – c) C1s scan and d) O1s scan, SLG/Cu before/after annealing – e) C1s scan and f) O1s scan.

4.1.2 Phenomenon of hydrophobization of nanocarbon surface

4.1.2.1 Impact of deposited hydrocarbons and airborne contaminants

Literature has shown that in the cases of the 1D material (SWCNTs), the 2D material (SLG), and the 3D material (HOPG), the hydrophobicity of carbon materials is caused by airborne pollutants (hydrocarbons)[1,2,116]. However, all papers for 1D materials have not considered the effect of roughness, the calculation of surface energy from theoretical models has not been conducted, and the observed phenomenon has not been fully explained. As a consequence, the mechanism of the phenomenon has not been proposed, and it is not known what kinds of hydrocarbons are responsible for this effect.

Thus, the analysis began with depositing two chemical compounds: cyclohexane (carbon atoms with hybridization sp^3) and benzene (sp^2 carbon atoms), on macroscopic objects: a) C_{60}, b) SWCNTs, c) SLG/Cu, and d) HOPG by vapor deposition to define the hydrocarbons that generate this phenomenon. The vapor pressure of these two C_xH_y is the same, which makes them perfect for defining which hydrocarbon is more preferred[227]. As the results show, investigated carbon nanomaterials favor the deposition of aromatic structures, which makes them more hydrophobic (Figure 18), according to the results. After one day of saturation, cyclohexane did not affect the WCA of the 0D nanomaterial (C_{60}). On the other hand, after 20 minutes, the benzene responded by raising the WCA value. Benzene caused a quicker transition in the surface character to hydrophobic for 1D, 2D, and 3D than cyclohexane did. It was noted that it takes 15 minutes to notice a more hydrophobic surface while using HOPG (3D material). This phenomenon will be described later part.

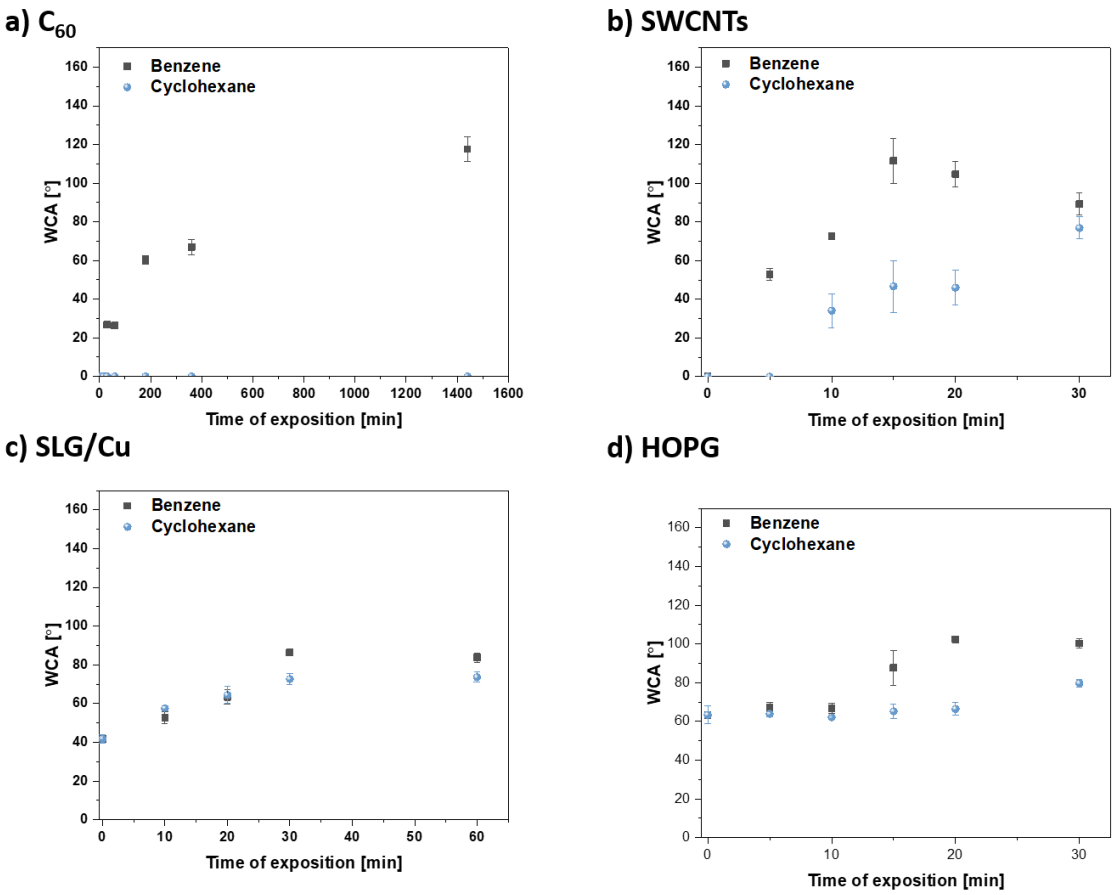

Figure 18 WCAs values of samples: a) C_{60}, b) SWCNTs, c) SLG/Cu, and d) HOPG, which were exposed to cyclohexane (sp^3) and benzene (sp^2) vapors (for the specified time), which have a similar vapor pressure.

According to the aforementioned observations, aromatic structures are preferred by carbon surfaces over sp^3 carbons. It is probably the result of favored interactions between the sp^2 carbon lattice and benzene's π-orbital system[228]. Additional aromatic compounds, including polycyclic aromatic hydrocarbons (PAHs) such as naphthalene, anthracene, and pyrene, as well as methyl derivatives of benzene (toluene, o-xylene, and mesitylene), were employed to purposefully contaminate the nanocarbon surfaces (C_{60}, SWCNTs, SLG/Cu, HOPG) in order to understand this interaction better. The coverage of various substances was calculated on the graphene surface using the Langmuir isotherm model, and the results show that each could cover the surface and form a monolayer (Table 8).

Table 8 Information from the literature was used to calculate the graphene surface's cover degree. During the experiments, the ambient temperature was 293 K (20 ºC) and the atmospheric pressure was 1008 hPa

C_xH_y	p_A [Pa]	$K_{Ad/De}$ (20 ºC)	θ_{Lan}	Adsorption to the surface	Ref.
Benzene	9619	$9.8 \cdot 10^{14}$	1	Parallel	[229]
Toluene	2828	$4.0 \cdot 10^{16}$	1	Parallel	
Naphthalene	12	$3.0 \cdot 10^{17}$	1	Parallel	[230,231]

p_A – vapor pressure, $K_{Ad/De}$ – equilibrium constant between adsorption and desorption on the graphene surface, θ_{Lan} – Langmuir cover degree of surface, adsorption on the surface – parallel or perpendicular

Due to the superhydrophilic surface of C_{60}, SWCNTs, and strongly hydrophilic copper foil (base for SLG, WCA^{Cu} = 32.6±4.8º), the Wenzel model was more suitable than Cassie-Baxter because it assumed that the water droplet should penetrate the rough surface[1,232]. AFM scans (Figure 19) were registered to measure the roughness. Wenzel roughness factor (r) reached the following values: r^{C60} = 1.39, r^{SWCNTs} = 1.11, $r^{SLG/Cu}$ = 1.00, and r^{HOPG} = 1.01. Therefore, roughness has a sizable impact on WCA for 0D and 1D materials (r >1), so the Wenzel model was used to reduce this impact. The results of roughness measurements for SLG/Cu and HOPG were coherent with research conducted by Kozbial et al.[233], who used similar materials. In the case of C_{60} and SWCNTs, no information was found about the impact of roughness on wettability in the literature about macroscopic objects made from the same materials and methods used in this dissertation. The surface roughness effect was not taken into account in the analysis data for SLG/Cu and HOPG since, according to the Wenzel model, it had no discernible influence on the WCA values of these samples.

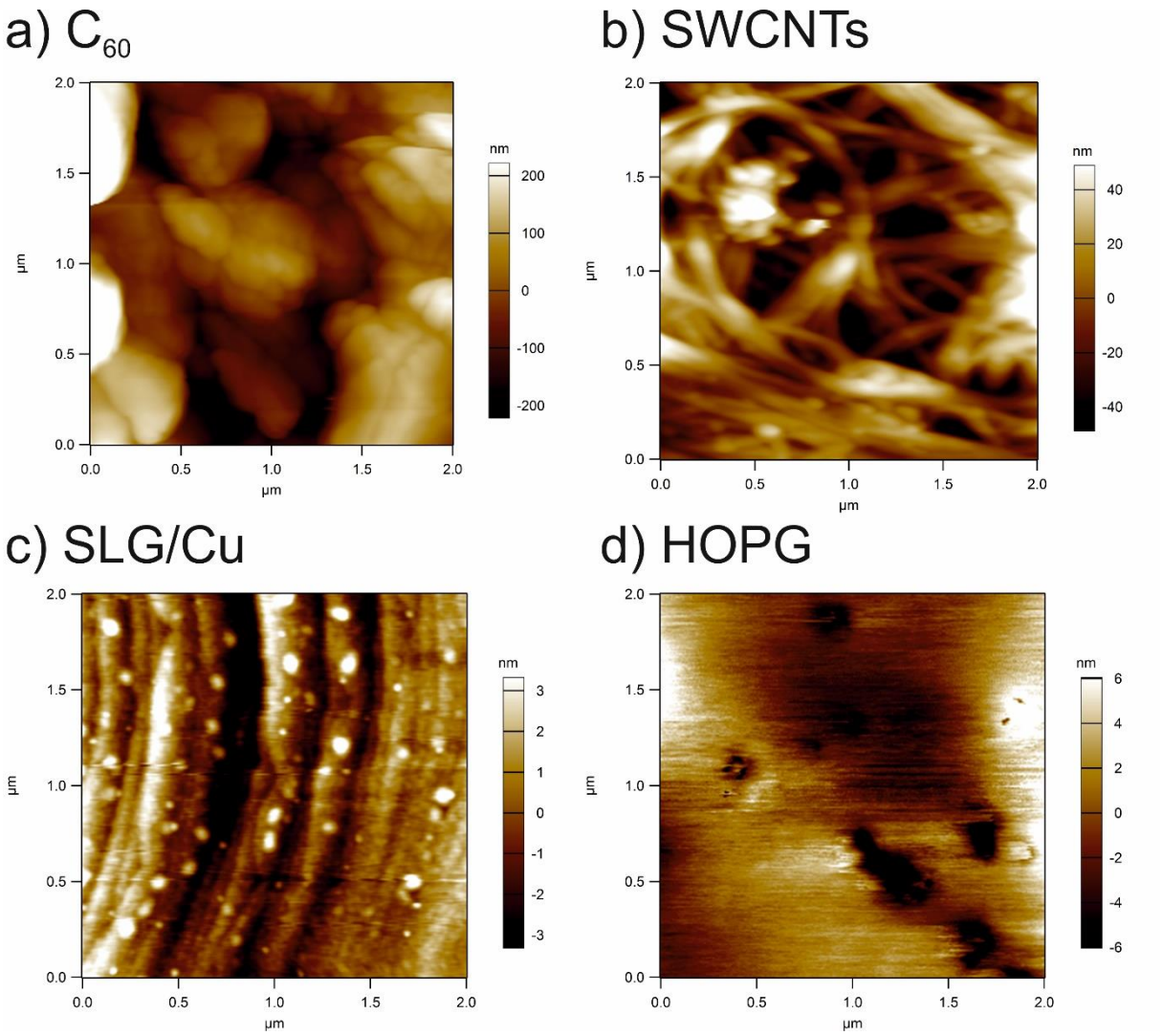

Figure 19 AFM surface scans which were obtained to a computer for: a) C_{60}, b) SWCNTs, c) SLG/Cu, and d) HOPG.

Only benzene and its methyl derivatives caused the change of WCA of C_{60} coating (one day of exposition of C_{60} coatings to PAH vapor did not affect their WCA). After 6 hours of exposure, it was discovered that depending on the number of methyl groups in the benzene ring, the wettability in the case of benzene derivatives affects the substrate differently (Figures 20a and b). Due to the hydrophobic nature of these groups and the geometry of 1D materials, SWCNTs become more hydrophobic as the number of methyl groups in the benzene ring increases (Figures 21a and b). The cylindrical shape of the SWCNTs might cause better exposure of the hydrophobic groups to water. What is more, it caused the surface of a macroscopic object to be rough because of agglomerations of carbon nanostructures. On the other hand, for SLG/Cu and HOPG, the presence of C_xH_y with methyl groups generally resulted in declining WCA compared to benzene (Figures 21c and d). Although the number of methyl

groups in the benzene ring had no discernible influence on WCA, the final value for SLG/Cu was 80±5º and HOPG was 90±5º. These findings imply that steric hindrance between the methyl groups onto the graphene surface may be in charge of the various behaviors. The hydrophobicity of 1D, 2D, and 3D materials decreases as the number of aromatic rings in the hydrocarbon molecules increases (Figures 22a, b, c, and d). The basic trends were unaffected by corrections based on the Wenzel model (Figures 20b, 21b and 22b). These observations are explained later in the section concerning surface free energy.

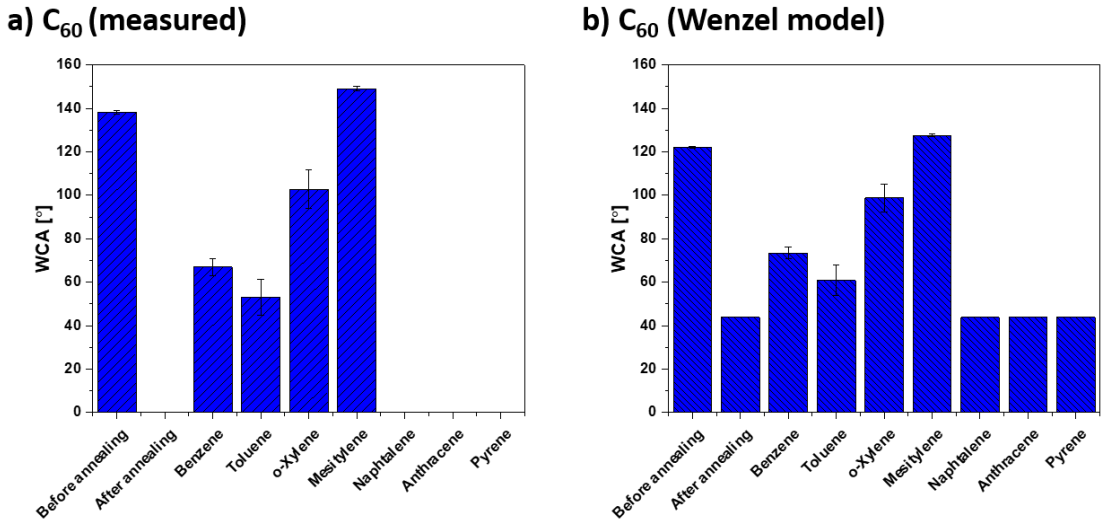

Figure 20 a) WCA for C_{60} samples C_xH_y without considering the impact of roughness, b) WCA computed from Wenzel model after 6 hours of deposition of specified compounds.

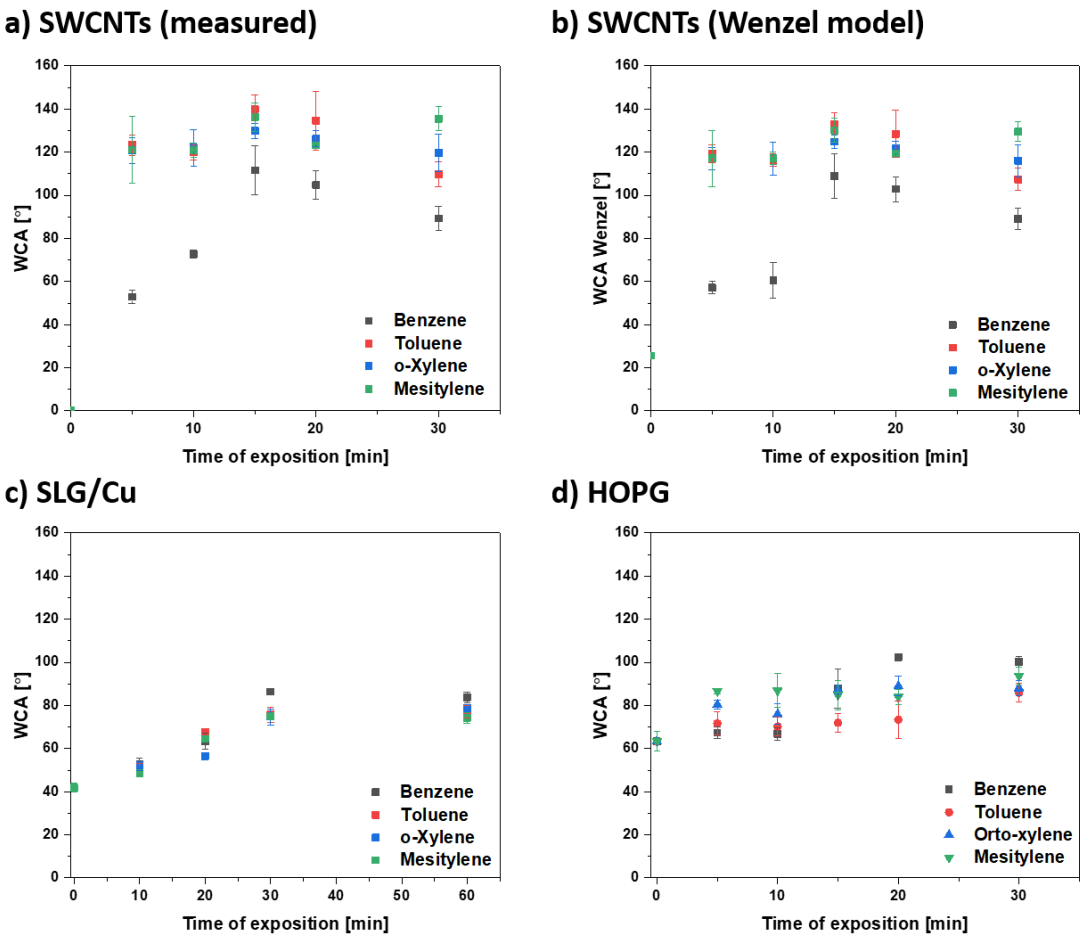

Figure 21 Evolution of the WCA value during exposure to methyl derivatives of benzene for: a) SWCNTs measured during experiments, b) SWCNTs recalculated using the Wenzel model, c) SLG/Cu, and d) HOPG.

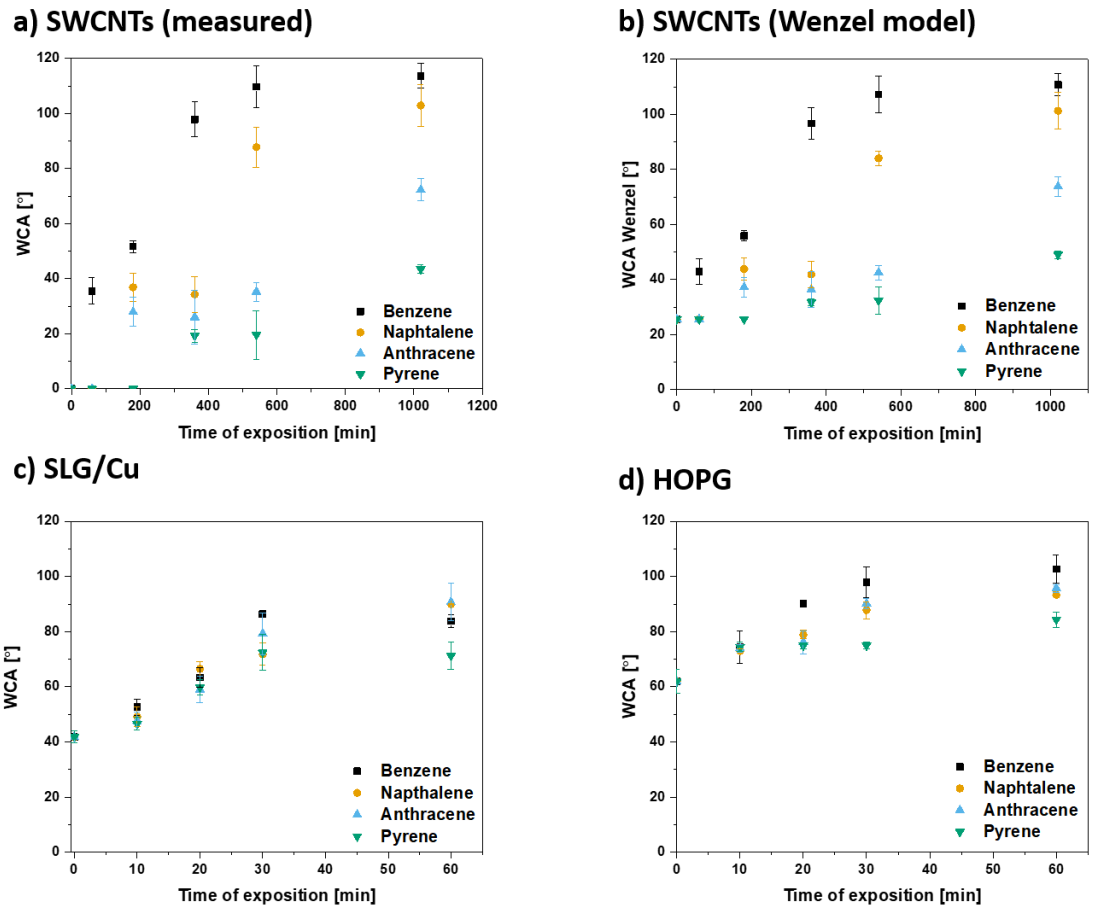

Figure 22 Evolution of the WCA value during exposure to PAHs for: a) SWCNT measured during experiments, b) SWCNTs recalculated using Wenzel model, c) SLG/Cu, and d) HOPG.

Aromatic hydrocarbons do not have any impact on Raman spectra – bands from C_{60} had a similar intensity to that of C_{60} coating after annealing (Figure 23). Therefore, XPS measurements were conducted to understand what caused the hydrophobization of the nanocarbon surface when it is saturated with vapor aromatic hydrocarbons. For C1s scans of C_{60} coatings (Figure 24a), the differences between the annealed coating and coatings with mesitylene were minor. For benzene and toluene, bands between 285 eV and 286 eV were observed to increase. WCAs after 6 hours of saturation vapor C_xH_y were still hydrophilic, which suggests that the adsorption process has not finished and during the transport, it might be adsorbed undefined airborne contaminates. On the other hand, after 6h C_{60} coating with deposited mesitylene was almost superhydrophobic (149.0±1.0º). O1s analysis (Figure 24b) demonstrated decreasing the intensity of the band at 532.5 eV from C=O, H_2O and O_2 caused by the C_xH_y deposit. Thus, the C_{60} surface preferred mesitylene (1,3,5-trimethylbenzene) over benzene derivatives with fewer methyl groups in the aromatic ring. C1s and O1s scan spectra

of C_{60} coating before annealing are different from those presented in Figure 24, and the reason is the presence of adsorption acetone on the surface, which caused the change in spectrum shape.

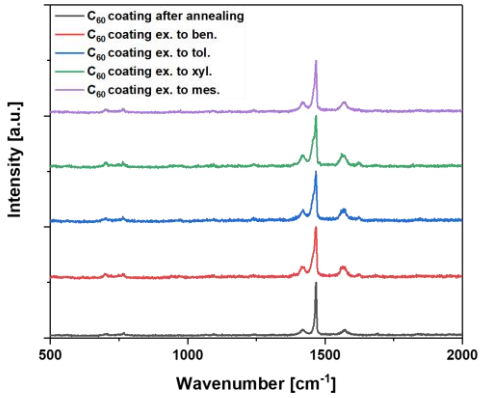

Figure 23 C_{60}'s Raman spectra with C_xH_y deposits: C_{60} coating after annealing, C_{60} coating exposed to vapor benzene (C_{60} coating ex. to ben.), C_{60} coating exposed to vapor toluene (C_{60} coating ex. to tol.), C_{60} coating exposed to vapor xylene (C_{60} coating ex. to xyl.), C_{60} coating exposed to vapor mesitylene (C_{60} coating ex. to mes.).

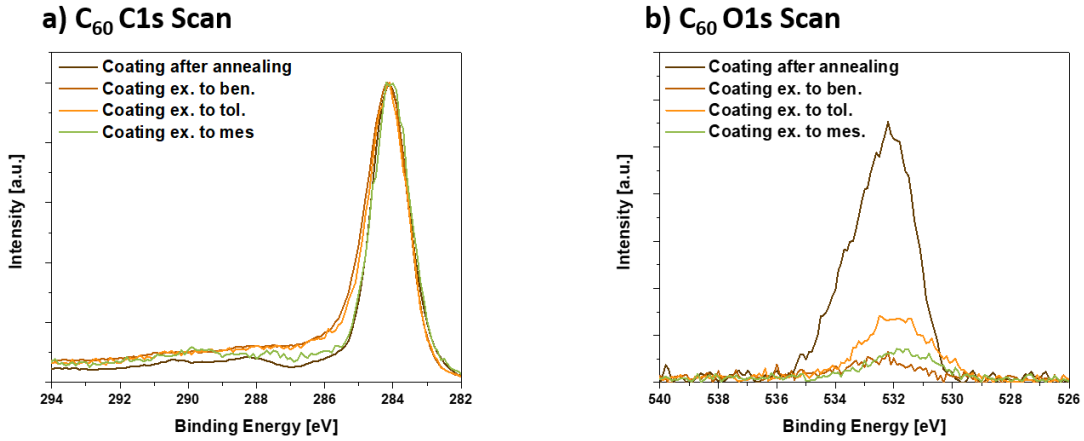

Figure 24 XPS spectra of C_{60} coatings with deposited C_xH_y on their surface after 6 hours of exposition to vapor: reference material – coating after annealing, C_{60} coating exposed to vapor benzene (C_{60} coating ex. to ben.), C_{60} coating exposed to vapor toluene (C_{60} coating ex. to tol.), and C_{60} coating exposed to vapor mesitylene (C_{60} coating ex. to mes.).

Then, SWCNTs samples with C_xH_y deposits were analyzed by Raman spectroscopy (Figure 25a) and the results were correlated with the electrical conductivity of these materials

(Figure 25b). Only in the case of mesitylene, the growth of I_D/I_G was observed in the Raman spectrum. I_D/I_G increased from 0.10 to 0.15 compared to pristine SWCNTs, but it is within the measurement error. Other hydrocarbons did not have a tangible impact on the intensity of the D band. Moreover, any C_xH_y deposited had no statistically important impact on the electrical conductivity of the SWCNTs VFFs (Figure 25b) either. Figure 26 presents the XPS spectra of chosen samples of SWCNTs and SLG/Cu with deposited aromatic hydrocarbons. Aromatic hydrocarbons did not influence the spectra of SWCNTs for C1s (Figure 26a), but they replaced adsorbed water – decreasing the intensity of the 532 eV band in the O1s spectra (Figure 26b). A slight change in the SLG/Cu spectra was observed, except for the SLG/Cu sample with the embedded spectrum of SLG with deposited mesitylene, where the intensity growth was noted in the range 284.6 – 286 eV. C-H bonds might cause this growth (Figure 26c).

To summarize this section, the C_{60} surface preferred benzene methyl derivatives with more alkyl groups than other arenes. It results that the C_{60} surface is quicker becoming hydrophobic using vapor xylene and mesitylene for deposition onto the surface than toluene. The SWCNTs and SLG/Cu did not have any preferences in the case of aromatic hydrocarbon chemical structure.

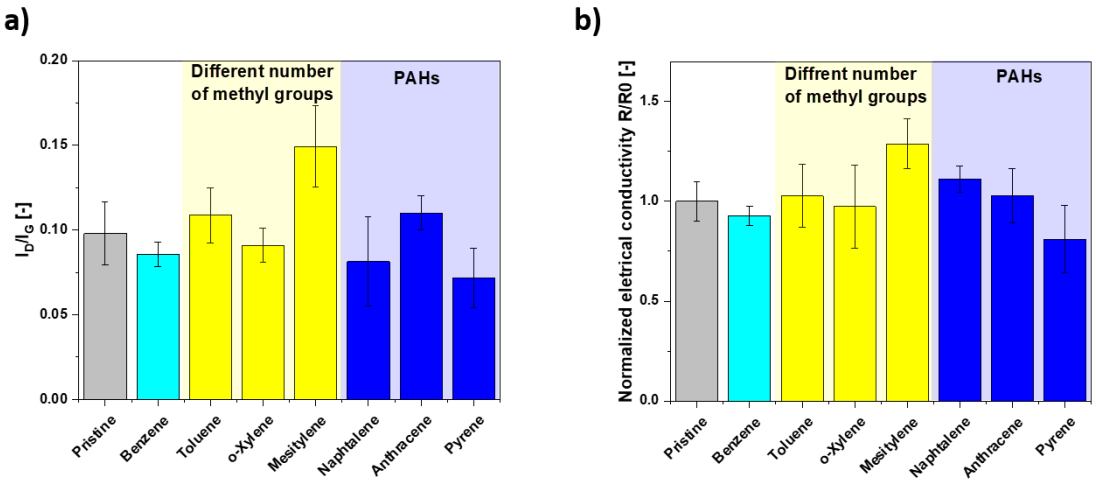

Figure 25 SWCNTs after deposition of C_xH_y: a) I_D/I_G calculated from Raman spectra and b) electrical conductivity normalized to pristine material.

Pristine – SWCNT VFF after annealing, Benzene – SWCNTsVFF after annealing exposed to benzene vapor, Toluene – SWCNT VFF after annealing exposed to toluene vapor, o-Xylene – SWCNT VFF after annealing exposed to o-xylene vapor, Mesitylene – SWCNT VFF after annealing exposed to mesitylene vapor, Naphthalene – SWCNT VFF after annealing exposed

to naphthalene vapor, Anthracene – SWCNT VFF after annealing exposed to anthracene vapor, Pyrene – SWCNT VFF after annealing exposed to pyrene vapor.

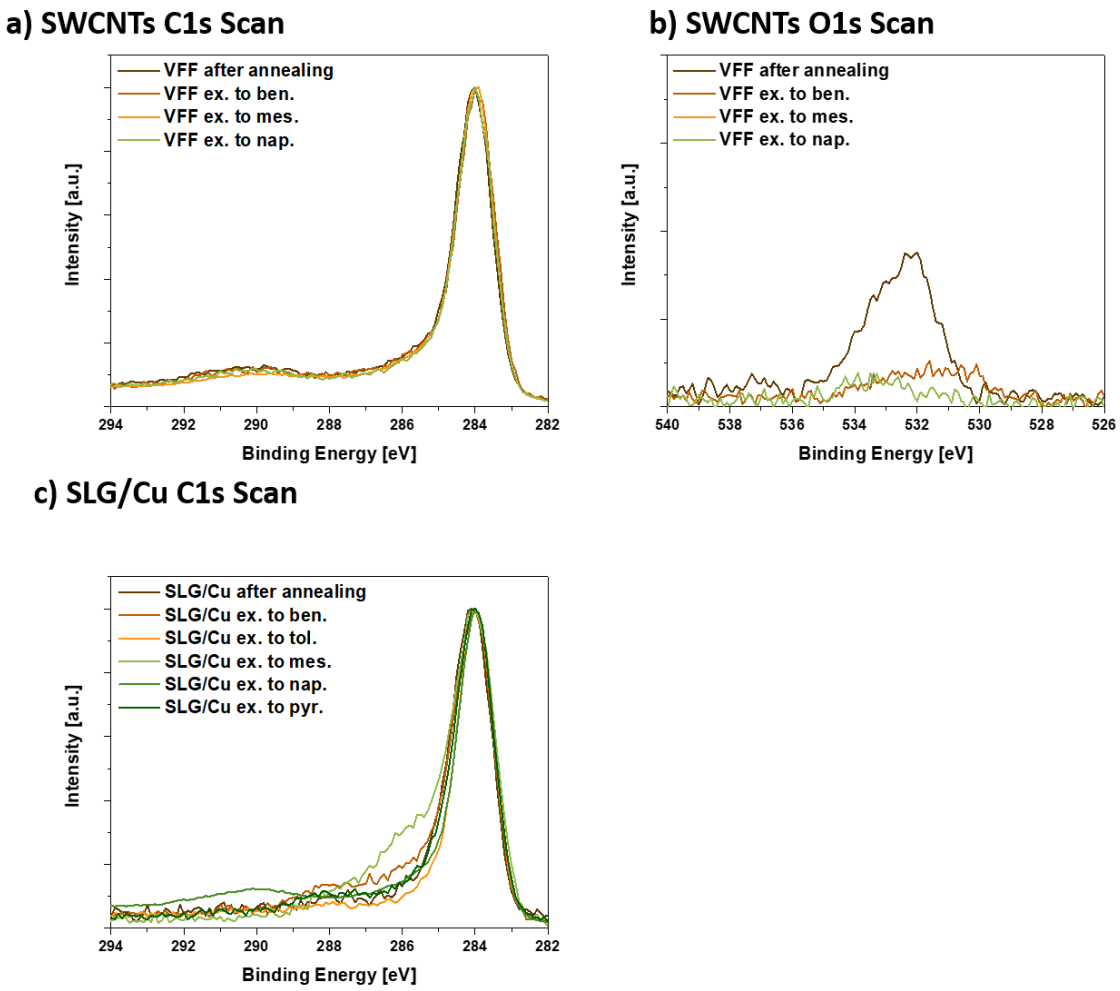

Figure 26 XPS spectra of chosen samples of SWCNTs with deposited C_xH_y a) C1s Scan and b) O1s Scan; SLG/Cu with deposited C_xH_y c) a) C1s Scan and d) O1s Scan.

The reactions of the annealed samples to prolonged atmospheric air exposure were also investigated (Figure 27). The C_{60} (0D) coating retained its superhydrophilic properties in air after annealing. The WCA rose for SWCNTs (1D), SLG (2D), and HOPG (3D) materials. For SWCNTs, the WCA value peaked at roughly 50º after reaching its maximum value of 50.7±2.5º after a week of air exposure. The highest value of WCA was seen for 2D and 3D carbon materials after one day, and afterward, there was a minor decline. According to Salim et al., minor fluctuations in the WCA may result from the dynamic replacement of surface pollutants, such as when greater molecular weight molecules replace lower molecular hydrocarbons[81].

In conclusion, it was found that the hydrophilic-to-hydrophobic transition of 0D and 1D nanomaterials occurred significantly more slowly than in the cases of flat and smooth 2D and 3D. It suggests that the geometry, surface area, and roughness of macroscopic objects from carbon materials may be involved. 0D and 1D objects tend to create an aggregation, which causes the roughness of surface macroscopic objects and high surface area[234,235].

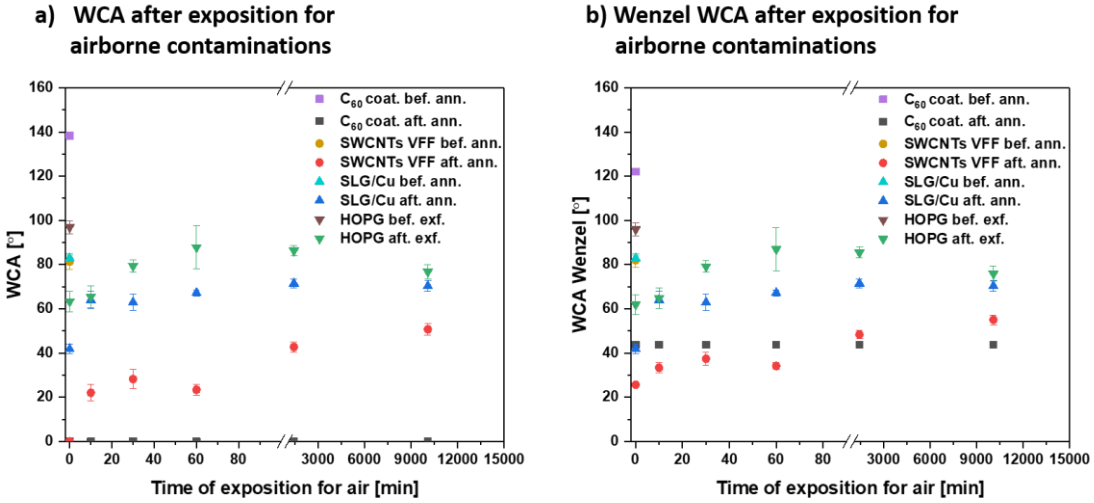

Figure 27 Measured evolution of WCA for carbon materials as a function of time of exposition to air a) and b) WCA computed by Wenzel model. C_{60} coat. bef. ann. – C_{60} coating before annealing exposed to atmospheric air for more than three months after manufactured coating, C_{60} coat. aft. ann. – C_{60} coating after annealing and then exposed to air, SWCNTs VFF bef. ann. – SWCNTs VFF before annealing exposed to atmospheric air for more than three months after manufactured VFF, SWCNTs VFF aft. ann. – SWCNTs VFF after annealing and then exposed to air, SLG/Cu bef. ann. – SLG/Cu before annealing, SLG/Cu aft. ann. – SLG/Cu after annealing and then exposed to air, HOPG bef. exf. – HOPG exposed to atmospheric air for more than three months after exfoliation, HOPG aft. exf. – HOPG after exfoliation and then exposed to air.

4.1.2.1 Mechanism of the phenomenon of hydrophobization of nanocarbon surface

For C_{60} and SWCNTs, ATR-FTIR results (Figure 28) present the following bands from adsorbed hydrocarbons before annealing: 1, 2, and 3 – C-H saturated (CH_3 and CH_2 groups) at 2904 cm^{-1} and 2972 cm^{-1} (C_{60} and SWCNTs), and 4, C=C aromatic/unsaturated at 3004 cm^{-1} (SWCNTs). The spectra of the annealed samples did not contain these bands. Also seen were the distinctive water bands (3100-3500 cm^{-1}). In conclusion, the evidence strongly suggests that the surface of an annealed nanocarbon (sp^2 carbon) initially absorbs water from the air before

it is replaced with hydrocarbons. The delayed variation of WCA in the case of HOPG exposed to benzene vapor is similarly explained by ATR-FTIR data (Figure 29). It was previously reported by Z. Li et al. that the surface contamination of the HOPG surface by airborne hydrocarbons is affected by both temperature and humidity[118]. It still detected H_2O peaks on the surface of HOPG 10 min after benzene vapor exposure. The peak vanished, though, after treating the air samples for a further 15 minutes. Furthermore, the peaks are substantially weaker in the spectra of HOPG treated with 15 minutes of saturation benzene vapor. The water is thus replaced by benzene on the graphite surface between 10 and 15 minutes. The speed of the process and the solubility of benzene (other used hydrocarbons are insoluble) in water are the causes of this peculiar behavior[236]. Additionally, the XPS O1s scan revealed the mechanism of the hydrophilic-to-hydrophobic transition for nanocarbon materials. In the case of C_{60} coating before annealing, it was observed high band from the band at 532 eV, C=O (acetone), H_2O, and O_2. The molecules were adsorbed during the process of manufacturing coating. After annealing, the data revealed an intensifying peak at around 532.5 eV from absorbed water (Figure 30). The strength of this peak waned after a month. It is hypothesized that water was initially adsorbable from the air after hydrocarbons subsequently replaced annealing. As was mentioned before, the presence of Cu has a significant impact on the spectra of SLG/Cu, so it was decided to use the HOPG as a model of the graphene surface. It was observed that the peak from the water had disappeared after 1 month of exposition of HOPG after exfoliation to air. The XPS data are coherent with ATR-FTIR spectra. The results of the XPS O1s scan for HOPG are also coherent with those recorded by Z. Li et al.[118], but this dissertation presents the mechanism of the observed phenomenon of hydrophobization nanocarbon surface. The adsorption of water onto the nanocarbon surface is the first step of the phenomenon and the hydrocarbons are replacing the water and causing the hydrophobicity of the surface.

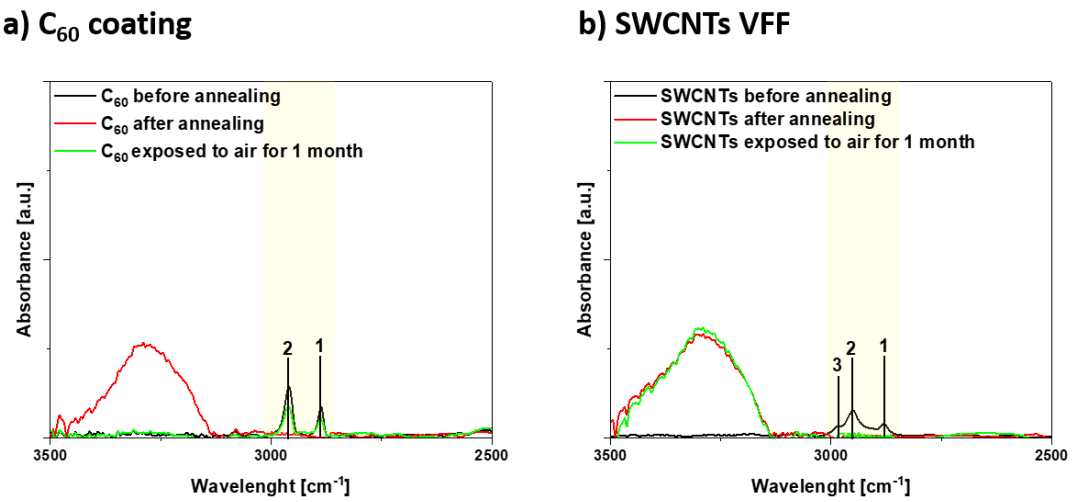

Figure 28 FTIR spectra of C_{60} and SWCNT samples: before/after annealing and exposed to air after annealing for 1 month.

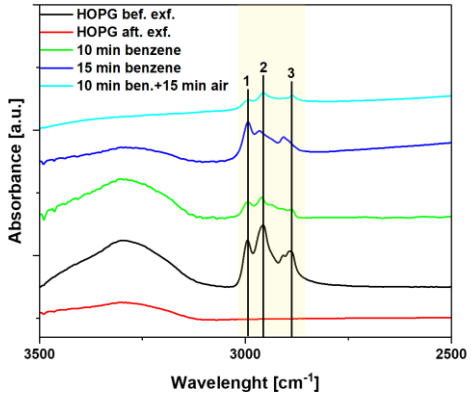

Figure 29 ATR – FTIR spectra of HOPG samples under various circumstances. HOPG bef. exf. – HOPG before exfoliation, HOPG aft. exf. – HOPG after exfoliation, 10 min benzene – samples exposed to benzene vapor for 10 minutes, 15 min benzene – samples exposed to benzene vapor for 15 minutes, 10 min ben.+15 min air – samples exposed to benzene vapor for 10 minutes and then 15 minutes to atmospheric air.

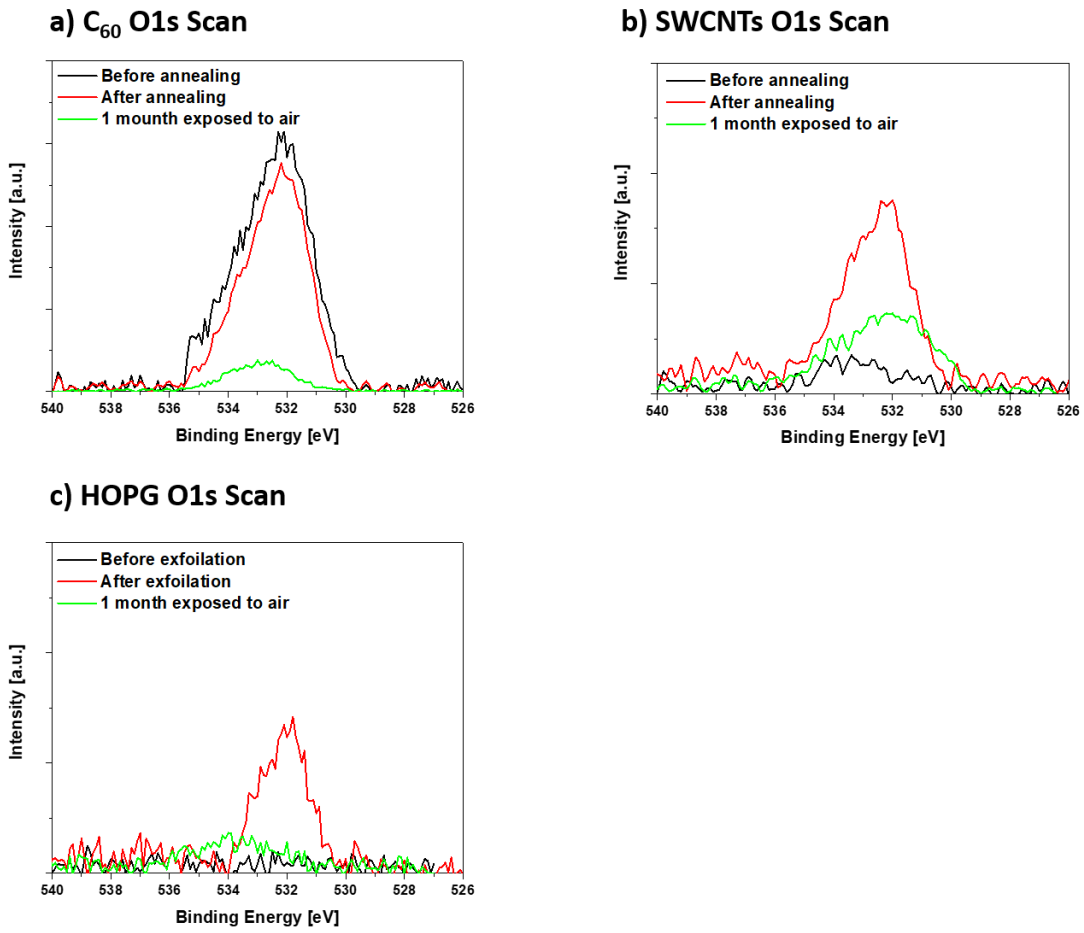

Figure 30 XPS O1s scans of a) C_{60}, b) SWCNTs, and c) HOPG.

Nanocarbon materials' surface-free energies were estimated to further understand the mechanism. Although several theoretical models for the calculation of surface free energy have been created, Neumann[128], Fowkes[129], and Owens-Wendt (Fowkes expanded by Good's equation)[130] are the three that are most widely used. The Fowkes and Owens-Wendt models provide dispersive and polar components, whereas the Neumann model enables calculating total surface free energy. The wetting behavior of the surfaces utilized in this work can be completely comprehended when the data from the models are combined with those from microscopy and spectroscopy. The surface free energy derived by the Fowkes model[129] is depicted in Figure 31 (data for the model are in Tables 9 and 10). The computation's output consistently shows a decrease in the polar component of the total surface free energy (γ^p) caused by deposited surface impurities. Additionally, it was observed that the dispersion part is reduced in the case of SLG/Cu, but the reduction in value γ^p is considerably greater. For all C_{60} and SWNCTs samples, the dispersion part (non-polar part) value is constant. C_{60} 30.6 mJ/m^2 (22.6 mJ/m^2 from the Wenzel model), SWCNTs 30.6 mJ/m^2 (27.7 mJ/m^2 from the Wenzel

model), and SLG 18.7 mJ/m^2 are all substantially more polar than the uncontaminated surface. The γ^p did not change for C_{60} after one day of exposure to the air, when the highest value of WCA was seen, but for SWCNTs and SLG, the values considerably were reduced. Wenzel's values were as follow: 30.6 mJ/m^2 → 17.4 mJ/m^2 (Wenzel 27.7 mJ/m^2 → 16.6 mJ/m^2) and 18.7 mJ/m^2 → 6.0 mJ/m^2. The drop in γ^p was caused by all hydrocarbons. Only for SLG/Cu samples did the dispersion part's value decrease. For various nanomaterials, the γ^p depends on the quantity of methyl groups in the benzene ring. The effect on 0D carbon is unclear. Increasing the methyl groups caused a clear increase of γ^p in the case of 1D carbon. The number of methyl groups does not affect the γ^p of 2D carbon. As mentioned previously, increasing the number of aromatic rings in the C_xH_y compound caused weaker hydrophobization of nanocarbon surface. Furthermore, nanocarbons with pyrene deposit has the highest value of polar energy. To explain this, thin coatings of the corresponding pure hydrocarbons on glass were created, and their contact angles were measured (Table 10). Naphthalene and anthracene have similar surface free energies, totaling 51.2 mJ/m^2 and 51.6 mJ/m^2, respectively, with polar parts of 0.4 mJ/m^2 and 0.8 mJ/m^2, respectively. On the other hand, the γ^p value for pyrene is substantially greater at 2.3 mJ/m^2, with a total surface energy of 53.1 mJ/m^2. Because pyrene is substantially more polar than the other selected PAHs, samples containing it are more hydrophilic than others. For all carbon nanomaterials, the free surface energy of benzene and naphthalene was found to be the lowest. They are among the most prevalent air contaminants[109]. XPS and FTIR studies, on the other hand, demonstrated that the alkyl group was present on the surface of nanocarbon materials that were exposed to air. Benzene and toluene are frequently the principal pollutants in these reports on the composition of air pollutants in industrialized and urban areas[109,110,112,237]. Other aromatic structures frequently have concentrations even 100 times smaller than theirs. All of these data leads to the conclusion that benzene and its alkyl derivatives are most likely the cause of hydrophobicity in common carbon materials, and the WCA value of nanocarbon materials relies on the composition of airborne contaminants. Figure 32 presents the proposed mechanism due to the results of this scientific work.

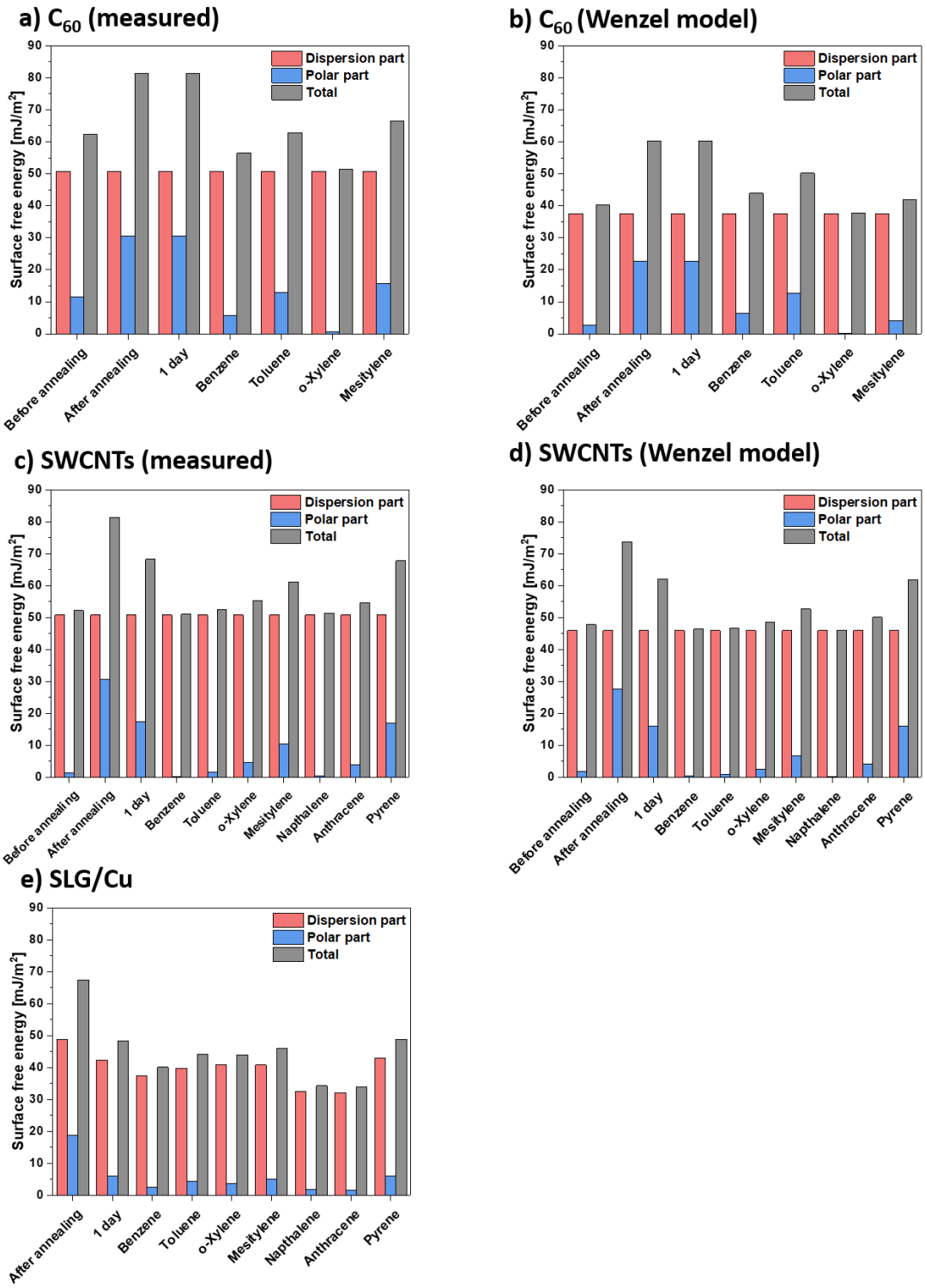

Figure 31 Surface free energy of prepared samples: WCAs of a) C_{60} measured from experiments, b) C_{60} coatings computed using contact angle calculated from the Wenzel model, c) SWCNTs VFFs measured from experiments, d) SWCNTs VFFs computed using contact angle calculated from the Wenzel model and e) SLG/Cu foil measured from experiments.

Table 9 Selected liquids and their surface free energy

Liquid	γ_l^d [mJ/m^2]	γ_l^p [mJ/m^2]	γ_l [mJ/m^2]	Ref.
Diiodomethane (DIM)	50.8	0.0	50.8	[238]
Water	72.8	51.0	21.8	[238]

Table 10 Information utilized by the Fowkes model to calculate the free surface energy

Material	Medium	Exposition time	θ_s water	θ_s DIM	r	θ_w water	θ_w DIM
C_{60}	Before annealing		138.3±0.8	0.0±0.0	1.39	122.1±0.5	43.8±0.0
	Air	After annealing (about 15 seconds)	0.0±0.0	0.0±0.0		43.8±0.0	43.8±0.0
		1 day	0.0±0.0	0.0±0.0		43.8±0.0	43.8±0.0
	Benzene	360 minutes	67.0±3.9	0.0±0.0		73.4±2.7	43.8±0.0
	Toluene	360 minutes	53.1±8.4	0.0±0.0		60.9±6.9	43.8±0.0
	o-Xylene	360 minutes	102.8±9.0	0.0±0.0		98.8±6.3	43.8±0.0
	Mesitylene	360 minutes	149.0±1.0	0.0±0.0		127.6±0.5	43.8±0.0
	Naphthalene	360 minutes	0.0±0.0	0.0±0.0		43.8±0.0	43.8±0.0
	Anthracene	360 minutes	0.0±0.0	0.0±0.0		43.8±0.0	43.8±0.0
	Pyrene	360 minutes	0.0±0.0	0.0±0.0		43.8±0.0	43.8±0.0
SWCNTs	Before annealing		81.3±3.5	0.0±0.0	1.11	81.8±3.1	43.8±0.0
	Air	After annealing (about 15 seconds)	0.0±0.0	0.0±0.0		25.6±0.0	25.6±0.0
		1 day	42.7±2.4	0.0±0.0		48.4±1.9	25.6±0.0
	Benzene	30 minutes	89.3±5.7	0.0±0.0		89.0±5.1	25.6±0.0
	Toluene	30 minutes	109.8±5.8	0.0±0.0		107.3±5.1	25.6±0.0
	o-Xylene	30 minutes	119.8±8.6	0.0±0.0		116.0±7.4	25.6±0.0
	Mesitylene	30 minutes	135.5±5.6	0.0±0.0		129.4±4.6	25.6±0.0
	Naphthalene	1020 minutes	103.7±7.5	0.0±0.0		101.3±6.7	25.6±0.0
	Anthracene	1020 minutes	72.3±4.0	0.0±0.0		73.9±3.5	25.6±0.0
	Pyrene	1020 minutes	43.5±1.6	0.0±0.0		49.0±1.3	25.6±0.0
SLG/Cu	Air	After annealing (about 5 seconds)	41.8±2.1	16.6±1.0	1.00	41.8±2.1	16.6±1.0
		1 day	71.5±2.0	34.2±2.2		71.5±2.0	34.2±2.2

	Benzene	60 minutes	83.8±2.4	44.0±2.7		83.8±2.4	44.0±2.7
	Toluene	60 minutes	77.1±2.8	39.4±3.1		77.1±2.8	39.4±3.1
	o-Xylene	60 minutes	78.7±1.8	38.5±2.1		78.7±1.8	38.5±2.1
	Mesitylene	60 minutes	74.3±2.5	37.4±1.3		74.3±2.5	37.4±1.3
	Naphthalene	60 minutes	90.0±0.3	52.9±4.1		90.0±0.3	52.9±4.1
	Anthracene	60 minutes	90.7±6.8	53.7±4.1		90.7±6.8	53.7±4.1
	Pyrene	60 minutes	71.2±4.9	32.9±1.5		71.2±4.9	32.5±1.5
Naphthalene	-	-	105.1±3.5	0.0±0.0	-	-	-
Anthracene	-	-	101.5±2.6	0.0±0.0	-	-	-
Pyrene	-	-	77.4±1.9	0.0±0.0	-	-	-

θ_s – static contact angle, r – Wenzel roughness factor, θ_w – Wenzel contact angle. The exposition time of vapor C_xH_y was selected by choosing the highest WCA value for samples.

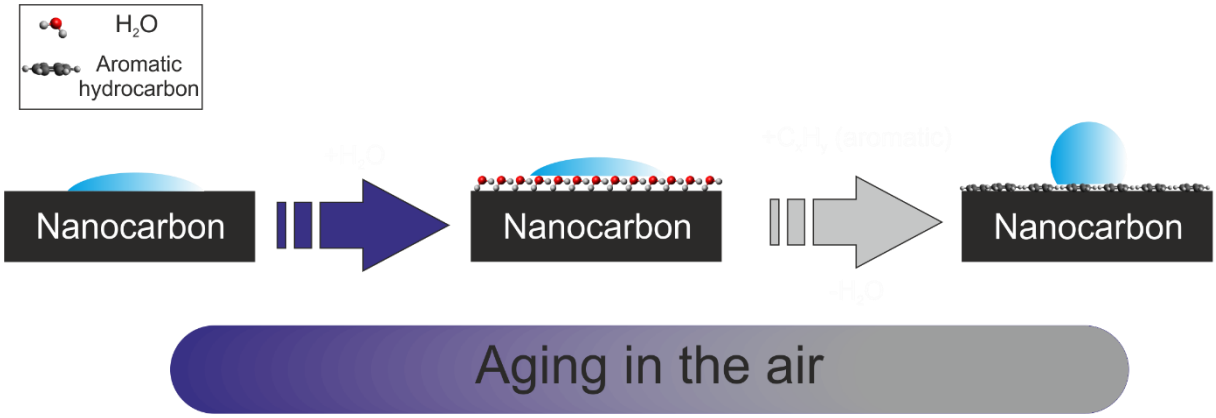

Figure 32 Mechanism of the phenomenon of hydrophobization of nanocarbon surface.

4.2. Oxidation of SWCNTs – synthesis, characterization and properties of DFs from O-SWCNTs

The next step was to synthesize functionalized nanomaterials to compare them with non-functionalized ones. Due to the good mechanical properties of the as-obtained SWCNTs VFF/DFs and lack of support (free-standing), they were chosen for functionalization to eliminate the impact of support, which would be present in case of C_{60} and SLG/Cu. The Hummers method was employed to oxidize the material. The impact of the oxidation conditions on the SWCNTs was measured using the I_D/I_G ratio measured using Raman spectroscopy. The amount of sp^3-hybridized carbon atoms and other defects is reflected in the intensity of the D band[239]. As a result of the increased defect content, one may anticipate an increase in the I_D/I_G ratio as oxidation advances. For three reaction temperatures 0 °C, 18 °C, and 40 °C, the

evolution of the D peak intensity was examined (Figure 33a). The $KMnO_4$/SWCNT mass ratio was maintained constant (7.5:1) throughout these studies. The strong crystallinity of pure SWCNT material was demonstrated by its low I_D/I_G value of 0.015±0.001 (Figure 33a). When oxidizing conditions were applied to the SWCNTs, a significant rise in the I_D/I_G ratios was seen after finishing the dosing of $KMnO_4$ (time of reaction t=0 min). While the treatment was at 0 °C the I_D/I_G ratio increased to just 0.069±0.012, but when the temperature was raised (the rest of the parameters were constant) to 18 °C – I_D/I_G was 0.624±0.061 and 40 °C, I_D/I_G – 0.853±0.034. An analysis of the kinetics revealed two different treatment routes for reactions that took place while the mixture was being cooled (0 °C) compared to 18 °C and 40 °C. In the first instance, the reaction continued steadily for the first 60 minutes before gradually slowing down compared to higher temperatures. The I_D/I_G ratio reached a value of 0.58±0.07 after 420 minutes at 0 °C, demonstrating a high level of disorder had been introduced to the SWCNTs. It is interesting to note that the procedure behaved differently for the treatments at higher temperatures.

At temperatures of 18 ºC and 40 ºC, the I_D/I_G ratio rapidly rose after finishing dosing, and then the I_D/I_G decreased value (Figure 33). After achieving the minimum I_D/I_G ratio grew again and was stable at a certain level. The degree of disorder in the system may initially diminish if the conversion rate of these CNTs species to CO_2 is faster than the rate of incorporation of the oxygen functional groups into the entire population of SWCNTs[64]. When these small-diameter SWCNTs were removed, only a rise in the I_D/I_G ratio was seen, a sign of the larger-diameter species' gradual functionalization. Relatively broad error bars on the I_D/I_G quotient values also served as a good indicator of the polydispersity of the SWCNTs used in the investigation. It is possible that the oxidation of the different SWCNT types did not proceed at the same rate since the material had a somewhat wide diameter distribution of 0.75 nm to 3 nm[240]. The final value of I_D/I_G for 18 °C and 40 °C after 420 minutes of oxidation SWCNTs achieved is as follows 0.73±0.10 and 0.90±0.05.

It was chosen to investigate how various ratios of $KMnO_4$ to SWCNTs impact the oxidation course to better understand the oxidation process via the Hummers method (Figure 33b). The notation of t=0 min indicates that the reaction was quenched immediately after the introduction of the oxidant was complete. At this point, the actual reaction time was 30 minutes because $KMnO_4$ was injected gradually in each case over the course of 30 minutes. Detailed information about the procedure of SWCNTs oxidation is provided in section *3.3.2.4 Oxidation of SWCNTs, O-SWCNTs VFFs, and O-SWCNTs DFs*. The kinetics of the process would be too

quick at 40 °C, hence the temperatures of 0 °C and 18 °C were used for this analysis. According to expectation, the more oxidant present, the more disorder was introduced into the material. At 0 °C, the amount of $KMnO_4$ had a negligible effect on the chemical modification. When the temperature was 0 °C and the ratio $KMnO_4$/SWCNTs=7.5, the I_D/I_G ratios only went up from 0.015±0.001 (pure SWCNTs) to 0.069±0.012. Therefore, although the oxidant was present in large quantities, it could not be effectively utilized when the process's time was short (t=0 min) and the temperature was low. On the other hand, even for the short reaction time, a rapid kinetics rise was seen when the process temperature was raised to 18 ºC. A significant number of functional groups containing oxygen were linked to the side walls of SWCNTs once the ratio of $KMnO_4$/SWCNTs=1.9 was attained (I_D/I_G=0.102±0.033). After this, the reaction advanced quickly before stabilizing at I_D/I_G=0.624±0.006 for $KMnO_4$/SWCNTs=7.5.

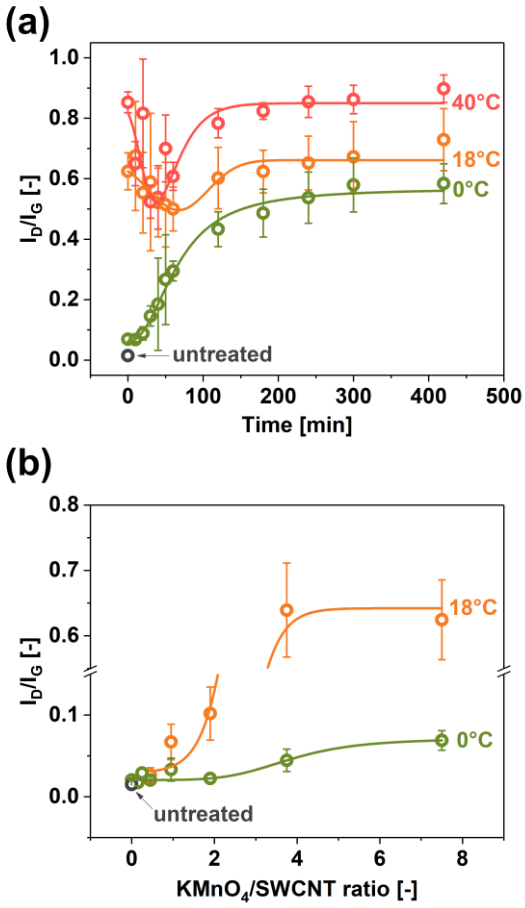

Figure 33 Results of investigation of the effect of SWCNT oxidation on the I_D/I_G ratio of the final product as a function of (a) time ($KMnO_4$/SWCNTs=7.5), and (b) $KMnO_4$/SWCNT ratio (t=0 min). Reproduced with permission from ref. [3] Copyright © 2022, Nature Publishing Group.

Figure 34 displays a Raman spectrum of the product produced under these circumstances ($KMnO_4$/SWCNTs=7.5, T=18 °C, t=0 min). The D and G peaks both exhibit significant broadening after oxidation. Bond heterogeneity and phonon lifespan shortening affect functional group grafting for the G band[241]. The FWHMs of the D and G bands increased significantly for highly functionalized SWCNTs to the point where these features began to converge. Additionally, the treatment had an impact on the G band, which had previously been split into G- and G+ components as a result of a symmetry breaking of the C-C bond stretching brought on by the influence of SWCNTs curvature[242]. These two features could no longer be recognized after oxidation, as in the earlier reported oxidation of SWCNTs[243].

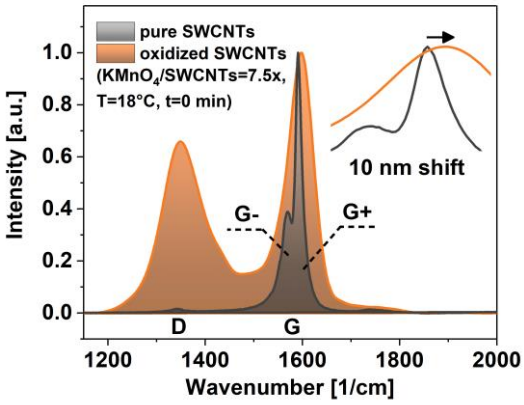

Figure 34 Comparison of Raman spectra substrate and product of oxidation SWCNTs in specified conditions. Reproduced with permission from ref. [3] Copyright © 2022, Nature Publishing Group.

Additionally, it was found that the G band maximum's location changed toward higher wavenumbers by as much as 10 nm. First, the simple interaction of SWCNTs with Brønsted acids causes the nanocarbon to be p-doped[30]. Mineral acids utilized in the study, such as H_2SO_4 and H_3PO_4, have the ability to remove electrons from the system, lowering its Fermi level[244]. Second, the presence of oxygen-containing functional groups like carboxyl and hydroxyl on the surface of SWCNTs reduces the electron density even more as a result of their ability to pull electrons[62,245]. Either of these modifications can explain the change mentioned above. As a result of the presence of oxygen in the air, SWCNTs are already p-doped, and the amount of the observed shift is significant[246]. Finally, the appearance of the D+D' characteristic from a two-phonon interband transition made possible by a high defect

concentration[216,241] was a sign of the material's significant functionalization (Figure 35). As can be seen for the samples made at 40 °C, as the D+D' peak's intensity increased, the 2D band's intensity steadily dropped as a result of damage to the SWCNT side wall.

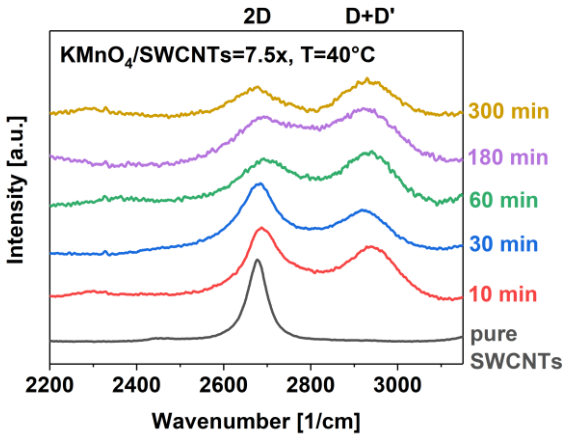

Figure 35 For pure SWCNTs and the end products of oxidation carried out under the prescribed conditions, the evolution of 2D and D+D' characteristics. Reproduced with permission from ref. [3] Copyright © 2022, Nature Publishing Group.

The alterations to the material's microstructure were shown using SEM (Figure 36). Once more, the sample processed at 40 °C was examined because this was the temperature where oxidation was most active. The SWCNT DFs were made of bundles of SWCNTs organized isotropically since horizontal alignment is not brought about by the ensemble production technique utilized, drop casting. The micrograph (Figure 36a) shows voids, which reduce the material's ability to transfer charge. However, the structure was significantly densified as soon as the SWCNT DFs came into contact with the extremely oxidizing and acidic media (Figure 36b). It was previously reported that porous CNTs films or fibers may condense when subjected to HCl, H_2SO_4, or HNO_3[247]. In addition to doping, the material's electrical conductivity rises as the individual CNTs and their bundles are packed closer together[248]. Additionally, the SWCNT DF's structure had become partially covered after 30 minutes of oxidation, which was not visible in the micrograph made after a longer oxidation period of 420 min (Figure 36c). It confirms our earlier theory that a portion of the substance (presumably defective and small-diameter SWCNTs) was initially highly oxidized. The more stable SWCNTs experienced gradual functionalization while these species were eliminated as the treatment continued.

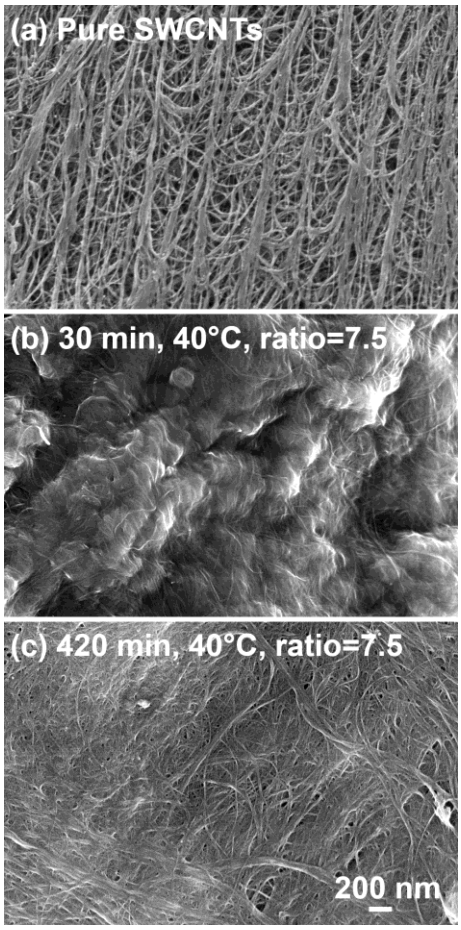

Figure 36 SEM micrographs for: parent material (pure SWCNTs) and oxidized products under chosen conditions. Reproduced with permission from ref.[3] Copyright © 2022, Nature Publishing Group.

After analysis of the SWCNT-based powders, their macroscopic networks were examined. Figure 37 shows the calculated I_D/I_G ratios for DFs formed from oxidized SWCNTs at various $KMnO_4$/SWCNTs ratios at 0 °C and 18 °C based on obtained Raman spectra. Similar to the base SWCNT powder utilized to create SWCNT networks, the level of disorder in the SWCNT ensembles rose with the amount of oxidant (Figure 36b). At 0 °C, the I_D/I_G ratio grew from 0.015±0.001 to just 0.108±0.018 at the $KMnO_4$/SWCNTs ratio of 7.5. however, at 18 °C, the I_D/I_G ratio increased to as high as 0.574±0.006. This result was anticipated because the higher the oxidation temperature, the more dynamic the insertion of functional groups into the SWCNTs. As one might expect, due to the effect of temperature on functional groups and EC (removing sp^3 carbon), the reported values for the DFs are slightly lower than for the obtained oxidized SWCNTs material utilized to manufacture the DFs. The employed high-temperature

annealing, which removes the EC binder, could also separate some functional groups from the SWCNT side wall[249], lowering the I_D/I_G ratios.

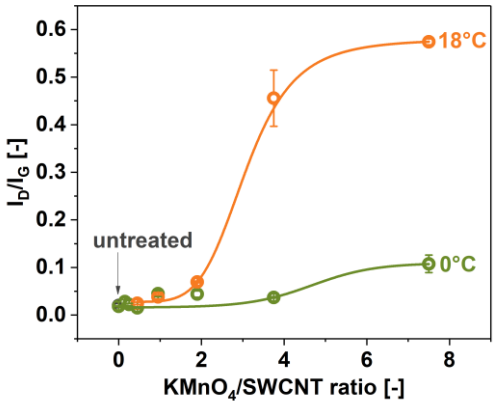

Figure 37 The impact of SWCNT oxidation on the I_D/I_G ratio of the DFs made from oxidized SWCNTs determined by Raman spectroscopy as a function of the $KMnO_4$/SWCNT ratio (t=0 min). Reproduced with permission from ref.[3] Copyright © 2022, Nature Publishing Group.

In addition, efforts were made to relate the conductivity of the material to the degree of structural disorder. Electrical conductivity was measured for samples of oxidized SWCNTs obtained at 0 °C and 18 °C (Figure 38). SWCNTs were submerged in the reaction mixture, and this resulted in a significant improvement in electrical conductivity. Due to the doping action of Brønsted acids (H_2SO_4 and H_3PO_4)[30], electrical conductivity values for low $KMnO_4$/SWCNTs ratios were greatly enhanced. The conductivity of the pure SWCNTs DFs was 283±32 S/cm, but it increased to 1321±95 and 1369±84 S/cm for the treatments at 18 °C and 0 °C. The addition of more $KMnO_4$ oxidants introduced disorder, which resulted in a rapid decline in the electrical conductivity of SWCNTs DFs.

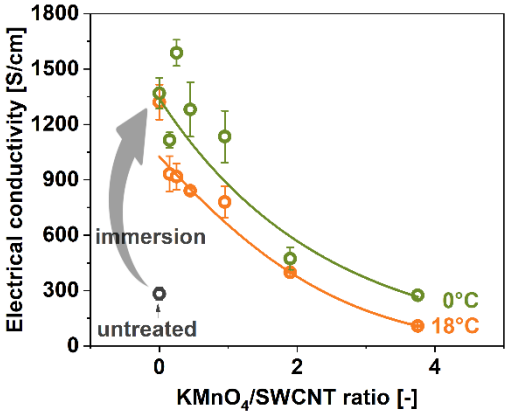

Figure 38 The impact of SWCNT oxidation on the electrical conductivity of the DFs made from oxidized SWCNTs as a function of the $KMnO_4$/SWCNT ratio (t=0 min). Reproduced with permission from ref. [3] Copyright © 2022, Nature Publishing Group.

The conditions for functionalization initiation were harsh as highly pure material was challenging to oxidize, however once defects were produced, as previously mentioned, the functionalization advanced. According to prior research, the unprocessed SWCNTs employed in this work easily tolerate oxidation even when exposed to concentrated HNO_3. The modified Hummers method's conditions were potent enough to affect the substance. According to research by Maciejewska et al., a defect (the conversion of methyl groups to formyl groups in (8,0) SWCNTs) can be oxidized with 0.62 eV. With the addition of 0.26 eV, the carboxyl group is formed. On the other hand, a far larger energy of 4.39 eV is required to directly implant this group into the CNT. Defect oxidation is therefore preferred over the creation of new ones[64]. According to the results above, adding a small amount of $KMnO_4$ did not significantly deteriorate the electrical conductivity. The functionalization, however, accelerated with more $KMnO_4$, which reduced the SWCNTs DFs' electrical conductivity. The electrical conductivity of the SWCNTs DFs only declined below the initial value for $KMnO_4$/SWCNTs ratios > 2. Due to the increased kinetics of the reaction, the oxidation was more dynamic when the reaction was conducted at 18 °C, as was expected.

Furthermore, the charge transport properties of the composite DFs made of oxidized SWCNTs and EC were investigated. It is interesting to note that the material's electrical conductivity dropped dramatically to 0.036±0.008 S/cm (4 orders of magnitude less than pure SWCNTs) when treated at a high temperature of 40 °C and a high ratio of $KMnO_4$ to SWCNTs (7.5). The Seebeck coefficient of this specimen was characterized, revealing significant

alterations to the electrical nature (Figure 39), reaching a very high absolute value of over -200 μV/K at 90 °C. Compared to the initial material, which had a Seebeck coefficient of about 48 μV/K, the changes seem significant. The change of sign also implies that electrons are now the main form of transport throughout the substance. The Seebeck coefficients of these materials were somewhat reduced to roughly 15 μV/K by simple immersion of SWCNTs in H_2SO_4/H_3PO_4 solution or brief exposure to oxidizing conditions (0 min, 0 °C, $KMnO_4$/SWCNTs=7.5). As previously indicated, mineral acids dope the system to alter its Fermi level, impacting charge carriers' mobility and density. While this makes the materials more electrically conductive, an excessive carrier density has a negative impact on the Seebeck coefficient[250]. In conclusion, the thermoelectric characterization findings show that the modified Hummers method can be used to choose the right oxidation conditions in order to modify the electronic properties of SWCNT DFs.

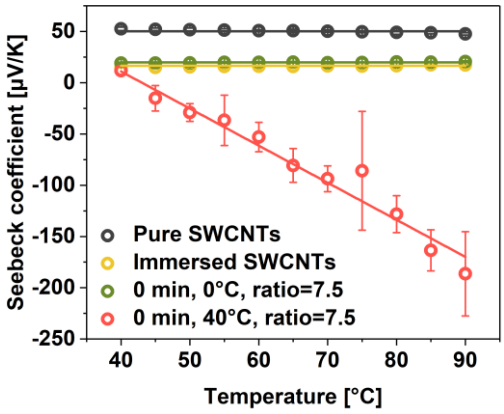

Figure 39 Seebeck coefficient of the SWCNT materials discussed in the text. Reproduced with permission from ref. [3] Copyright © 2022, Nature Publishing Group.

Finally, studies were carried out to evaluate this processing method's effect on the material's wettability. Previously, it was mentioned that annealing CNTs free-standing macroscopic object causes the desorption of impurities from the surface, which makes them hydrophilic[1,2]. As a result, it would be impossible to evaluate annealed DFs made from oxidized SWCNTs to determine the effect of oxidation because they would all be extremely hydrophilic. Additionally, some of the functional groups on the surface may be removed during the annealing process[245]. Considering each of these points, the filtration method was applied to create VFFs free from EC, thereby eliminating the need to anneal the material.

The effect of certain oxidation factors on the material's static WCA (γ) is shown in Figure 40. At 0 °C and at $KMnO_4$/SWCNT mass ratio of 7.5, the impact of reaction time was first investigated (Figure 40a). Raman spectra of O-SWCNTs results demonstrated that the radical decrease of WCA value from 71° (SWCNTs) to 27° (Figure 40a) was caused by increasing concentration of sp^3 carbon (Figure 33). Even at quick reaction times and 0 °C, WCA was reduced to 48°, demonstrating that the reaction is still in motion. Not many functional groups can be further integrated into the SWCNTs lattice because of the modest treatment conditions. Since $KMnO_4$ is ineffectively used during the 0 °C processing, it can be inferred that no more reactive oxygen species are available to alter the SWCNTs. What is more, as anticipated, an increase in the $KMnO_4$/SWCNTs ratio speeds up the oxidation process and increases the hydrophilicity of the VFFs (Figure 40b). Two conclusions can be drawn. Firstly, the WCA is unaffected by the immersion of SWCNTs VFFs in the acid mixture lacking the $KMnO_4$ oxidant. Secondly, equivalent WCA values to those obtained when the treatment is carried out at 0 °C for a lengthy period of 720 minutes (29° versus 27°) may be achieved at high $KMnO_4$ concentrations but with rapid reaction times. It is likely that using the modified Hummers approach would allow O-SWCNT VFFs to achieve a coherent final WCA value of ca. 28º. The effect of temperature on the WCA of the SWCNTs networks is compared in Figure 40c. Almost identical WCA values show this for the treatments at 18 °C and 40 °C (when the error bars are considered), thus maximum hydrophilicity was achieved for these nanomaterials. The modified Hummers method allows modeling the nature of the SWCNT surface by oxidation but at the expense of electrical conductivity and damage/destruction of the initial nanostructure.

If we correspond these results to non-functionalized materials, the WCA value of O-SWCNTs are higher than WCA annealed SWCNTs. However, the WCA of annealed SWCNTs increases due to the adsorption of hydrocarbons from the environment. The functionalization caused a loss of initial electrical properties. However, it is possible that after functionalization, the surface is resistant to the phenomenon of hydrophobization due to the presence of functional groups. The insertion of oxygen groups might prevent the creation of a hydrophobic C_xH_y monolayer by interfering in π-π stacking between the nanocarbon surface and aromatic hydrocarbons[251]. It might explain the observation of other scientists about dispersion in aqueous solutions of oxidized nanocarbon materials[173] that they were stable and did not need additional surfactants.

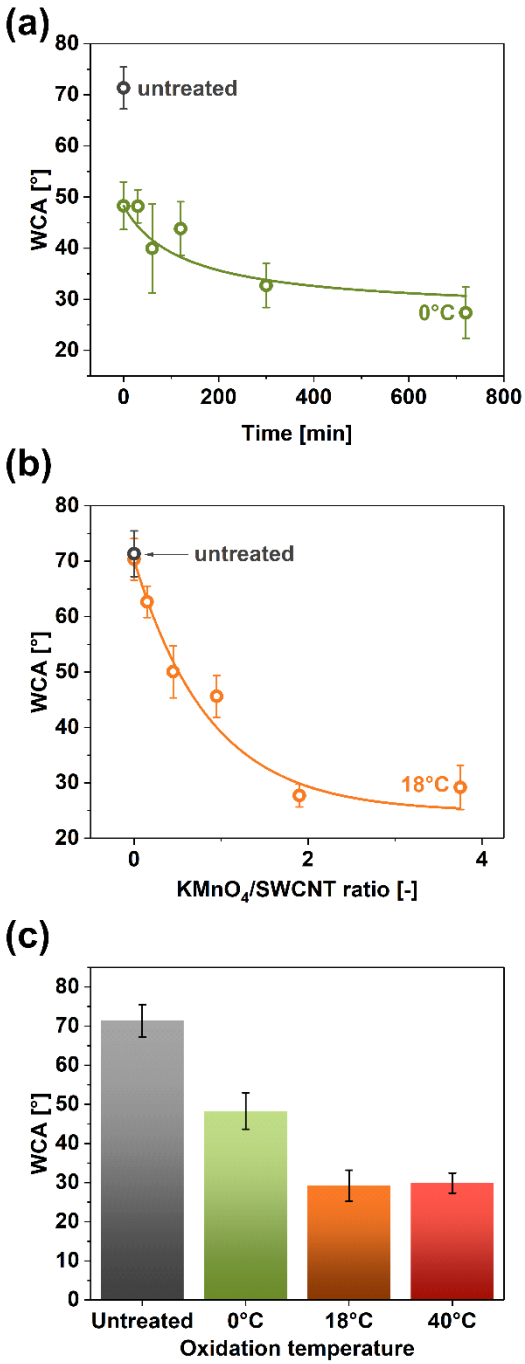

Figure 40 WCA as a function of (a) time (T=0 °C, $KMnO_4$/SWCNT=7.5), (b) $KMnO_4$/SWCNT ratio (T=18 °C, t=0 min), and (c) temperature ($KMnO_4$/SWCNT=7.5, t=0 min). Reproduced with permission from ref. [3] Copyright © 2022, Nature Publishing Group.

4.3 Composites – synthesis and properties

4.3.1 Introduction

This chapter will present the application of the phenomenon of hydrophilization of nanocarbon surfaces to manufacture high-performance composites based on nanocarbon materials. Three types of composites were made by connecting nanocarbon materials with: poly(methyl methacrylate) (PMMA), different kinds of polyaniline (PANI), and copper. In the case of PMMA, the VFFs from SWCNTs and O-SWCNTs were applied to understand the impact of adsorbed hydrocarbons on the nanocarbon surface and functionalization on manufacturing the composites.

The next part is devoted to the synthesis of PANI by electropolymerization onto DFEs from DFs: SWCNTs, O-SWCNTs and composites of SWCNTs with graphene nanoplatelets. It presents the role of wettability on electrochemical properties and the impact of PANI form on the physicochemical properties of composites. What is more, the role of the doping effect in the potential application of these materials as parts for supercapacitors and thermoelectric generators is presented.

Finally, the phenomenon was applied to synthesize composite nanocarbon materials with copper via electrodeposition and recovery of Cu from industrial wastewater. DFEs from pure CNTs: SWCNTs, synthesized multi-walled carbon nanotubes (MWCNTs), and commercial multi-walled carbon nanotubes (NC-MWCNTs) were used to deposit copper onto the nanocarbon surface. Additionally, composites: 10% O-MWCNTs, 25% O-MWCNTs, 50% O-MWCNTs, 10% N-MWCNTs, 25% N-MWCNTs, 50% N-MWCNTs, 10% Graphene and 25% Graphene were manufactured to investigate the effect of connection two nanocarbon structures on wettability and electrochemical properties. The results of the research work were the establishment of a method of selective copper recovery from industrial wastewater via electrodeposition onto nanocarbon DFEs.

4.3.2 Composites polymers and nanocarbon materials

4.3.2.1 Composites of nanocarbon with polymers containing hydrophilic groups

The impact of surface contaminants was measured by comparing the mass of deposit of poly(methyl methacrylate) PMMA on SWCNTs without annealing (growth of mass was 72%±2%) and annealed SWCNTs VFF (347%±15%). Without adsorbed hydrocarbon, the integration degree between nanocarbon and polymers molecules enhanced very much, leading

to 3.36 times higher deposition (by mass) of PMMA onto annealed SWCNTs VFF, compared with the starting material. SEM micrographs (Figure 41) did not demonstrate any morphological changes caused by annealing, thus the thin layer of hydrocarbons caused the lower integration degree between SWCNTs and chosen polymer before removing C_xH_y from SWCNTs surface. For O-SWCNTs (oxidation parameters: time of reaction – 0 minutes, $KMnO_4$/SWCNTs mass ratio – 7.5 and temperature – 40 ºC), mass growth due to PMMA adsorption was 22%±3% (Figure 42).

Figure 43 presents the mechanical test curves for synthesized materials. The fracture point of annealed SWCNTs VFFs was 3.99±0.01 MPa, and the Young modulus was 45.54±5.40 MPa. The oxidization of SWCNTs negatively affected the properties of pristine material. The fracture point for O-SWCNTs was less than 12.2 kPa±10.5 kPa (Young modulus 0.00122 MPa) - the VFFs broke soon after starting the mechanical tests. It might be caused by destroying the material's initial morphology and creating many defects (oxidation parameters: 40ºC, 0 minutes, and 7.5 ratio $KMnO_4$/SWCNTs). The presence of chosen polymer – PMMA increased the mechanical properties in both cases: PMMA+SWCNTs Young modulus 45.54±5.40 MPa → 102.41±5.91 MPa and fracture point 3.99±0.01 MPa→ 5.89±0.03 MPa for, analogously for PMMA+O-SWCNTs 61.56±2.41 MPa and 0.74±0.07 MPa. Figure 41 also presents the SEM images of pristine VFFs and composites with PMMA, and we can see that PMMA creates the layer on the VFF surface in both cases. This layer interconnecting SWCNTs is a reason for the enhancement of mechanical properties.[252,253] Thus, the surface impurities were the main barrier between achieving high-quality composite and inserting functional groups onto nanocarbon to reduce material properties (Figure 43). Highly O-SWCNTs have a much lower affinity to PMMA than SWCNTs, which suggests that besides functional groups, the quality of CNTs (number of structure defects) greatly impacts adsorption ability[251].

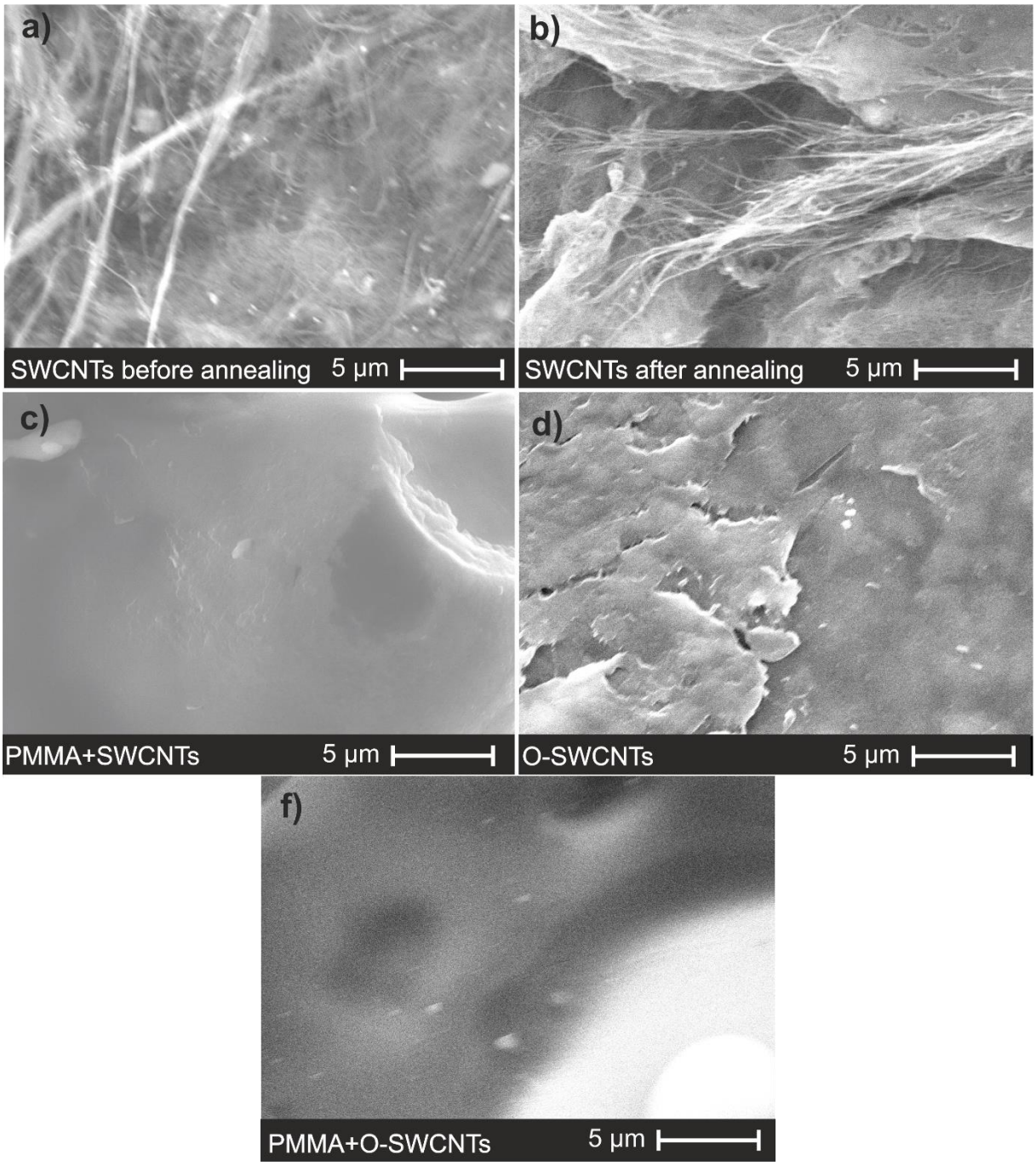

Figure 41 SEM micrographs: a) SWCNTs before annealing – SWCNT VFF before annealing, b) SWCNTs after annealing – SWCNT VFF after annealing, c) PMMA+SWCNTs – a composite of PMMA and SWCNT VFF after annealing, d) O-SWCNTs – VFF from oxidized SWCNTs, e) PMMA+O-SWCNTs – a composite of PMMA with O-SWCNT VFF.

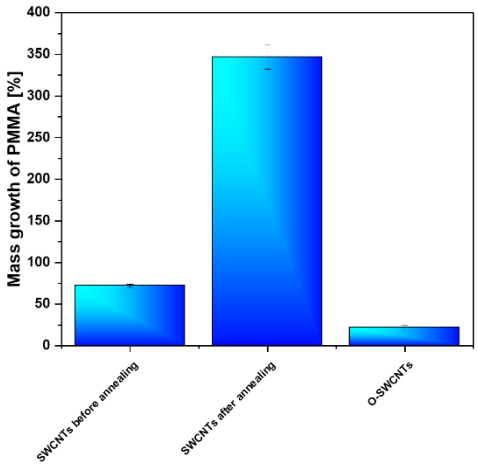

Figure 42 Mass growth of PMMA after dip-coating onto VFFs: SWCNTs before annealing – SWCNT VFF before annealing, SWCNTs after annealing – SWCNT VFF after annealing, O-SWCNTs – VFF from oxidized SWCNTs.

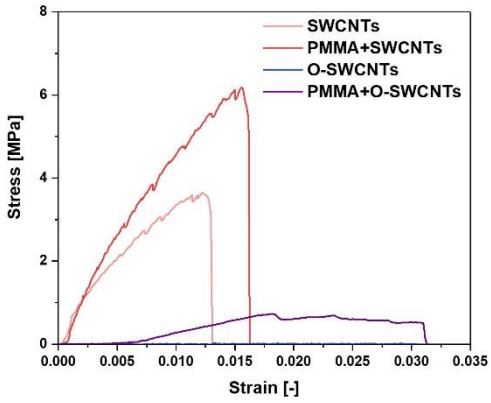

Figure 43 Mechanical tests of SWCNTs, PMMA+SWCNTs, O-SWCNTs and PMMA+O-SWCNTs.

4.3.2.2 Composites of nanocarbon with conductive polymers

4.3.2.2.1 Characterization of chosen DFs from nanocarbon materials and synthesis of PANI

The surface area of 723 m^2/g (calculated by BET model) or 1013 m^2/g (by Langmuir), the electrical conductivity of 1075.3±54.0 S/cm, and superhydrophilic character after annealing (WCA 0º) were all highly promising properties of manufactured SWCNT DFs. All of them allow applying the DFs as electrochemical applications. The high porosity of the materials (mostly micropores and mesopores) (Figure 44) is what caused the well-developed surface area[254]. Because of π-π stacking, such porosity encourages the adsorption of organic

molecules, particularly those with aromatic rings, when exposed to environmental conditions or when removed from a solution[228]. To capitalize on this observation, an attempt was made to create nanocarbon composites with conjugated polymers containing such groups. High surface area helps the initial step of the PANI electropolymerization (EP) process when the adsorption of aromatic water-soluble amine (aniline) happens on the surface of the nanocarbon. Simultaneously, the superhydrophilicity of the annealed DFEs provides good interaction with the electrolyte.

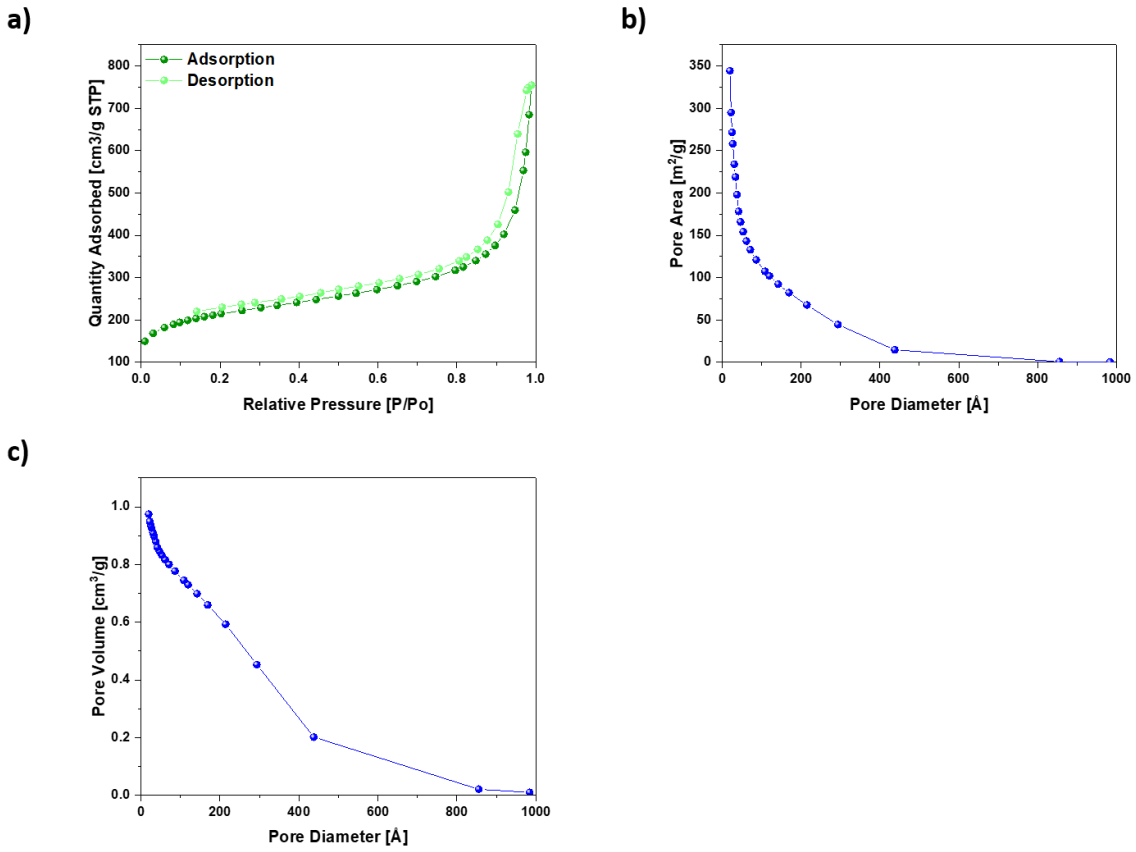

Figure 44 Results of N_2 adsorption and deposition experiments on SWCNT DFs: a) isotherm, b) pore area, and c) pore volume.

These characteristics aided in the electrochemical polymerization of PANI on nanocarbon DFEs. The objective was to evaluate whether a change in the nanocarbon DFEs' structure may impact the PANI deposition process. Due to the interaction between the electrons from the aromatic ring and the electrons delocalized in the nanocarbon surface at the start of polymerization, aniline was physically adsorbed on the SWCNT surface[151,255–257]. The electrical charge was then moved from the carbon nanostructures to the aniline, where EP and PANI chains formed, coating the nanocarbon surface in the process. Cyclic voltammetry (CV)

curves of polymerization aniline onto SWCNTs are shown in Figure 45. The chosen range [(0 V) - (1.2 V)] vs. Ag/AgCl allows to synthesize PANI onto SWCNTs with a yield of 88% (Figure 45a), and its content in composite was 60%. Due to the transport of the sample and the loss of deposited PANI caused by washing in demineralized water, the yield of the purification procedure was reduced[144,258]. Annealing was essential in the synthesis process since the PANI mass percent in the composite was decreased to 15% when the surface contaminants and dielectric binder (ethyl cellulose) were presented in DFE (Figure 45b). To prepare different types of PANI, the electrode potential was altered. The same number of oxidation and reduction cycles were used to produce emeraldine. The potential voltage was initially set to 0.4 V vs. Ag/AgCl, increased to 1.2 V vs. Ag/AgCl (oxidation voltage), and subsequently decreased to 0 V vs. Ag/AgCl (the reduction voltage). Thus, to create the emeraldine form (base/salt) (EB/ES), the final cycle must be terminated at 0 V vs. Ag/AgCl. Leucoemeraldine base (LB) was prepared on the working electrode by setting the electrode potential to 0 V vs. Ag/AgCl for 2 s. The electrode voltage was set to 1.2 V vs. Ag/AgCl for 2 s to oxidize the polymer in order to produce pernigraline base (PB) on the working electrode. The composites of PANI and SWCNTs during the process of EP (condition for emeraldine) gradually become more hydrophobic (Figure 45c) and it might be the reason why the CV curves have high resistance during the process – integration between electrode and electrolyte is weakening. WCA for composites after 50 cycles of EP is 55.1±4.9º, which is similar to the reported value of emeraldine salt with HCl (WCA = 50±10º in pH range 0-1)[259].

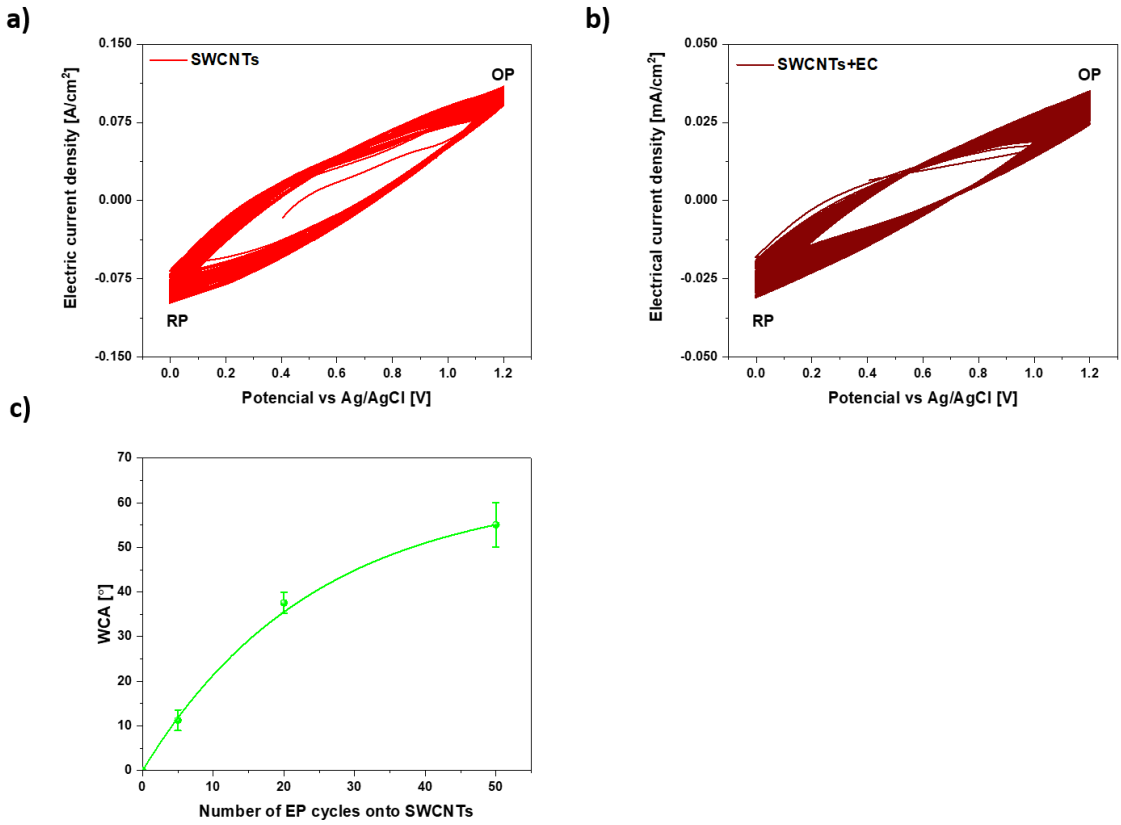

Figure 45 CV curves of aniline electropolymerizing process onto SWCNTs DFEs. Using different potential ranges, where has been marked reduction peak (RP) and oxidation peak (OP) [(0.0 V) – (1.2 V)]: a) SWCNTs and b) SWCNTs+EC. c) Evolution of WCA depending on the number of EP cycles onto SWCNTs. c) reproduced with permission from ref. [6] © 2023 Grzegorz Stando, Paweł Stando, Mika Sahlam, Mari Lundström, Haitao Liu Dawid Janas. Published by Elsevier B.V.

The same range was used for G+SWCNTs DFEs to compare their electrochemical properties with SWCNTs DFE. In comparison to 1:3 (51.2±0.5 mg) and 1:9 (46.1±0.5 mg), the ratio of 1:1 (graphene/SWCNTs) produced the most substantial amount of PANI deposit (143.4±0.5 mg). Compared to DFEs made from various ratios of graphene/SWCNTs, those made from composites with a graphene/SWCNTs ratio of 1:9 had a much lower electric current density (Figure 46). The composites with the 1:3 ratio could not be produced because of an unidentified surface process that interfered with the synthesis. In order to do additional research, a G+SWCNTs (1:1) composite was used.

Additionally, four types of O-SWCNT DFEs were used to investigate the impact of functionalized groups on electropolymerization. SWCNTs were oxidized under various

conditions to study the effects of destructive chemical functionalization: $KMnO_4$/SWCNTs ratio 0.95 at 18 ºC; 0.95, 0.45, and 0.15 at 0 ºC. Along with the peaks at around 0.6 V vs. Ag/AgCl from the synthesis of PANI (Figure 47) also showed peaks at this location from the oxidation and reduction of oxygen functional groups on SWCNTs[260] (OP2 and RP2 in Figure 47). As mentioned in the section about oxidation SWCNTs, the I_D/I_G ratio of O-SWCNTs shows the development of the oxidation process of the CNTs, and the rise in PANI mass on electrodes was correlated. The growth was seen to be 50% for $I_D/I_G^{0.95,18ºC}$ = 0.102±0.032, 55% for $I_D/I_G^{0.95,0ºC}$ = 0.033±0.014, 154% for $I_D/I_G^{0.45,0ºC}$ = 0.020±0.001 and 159% for $I_D/I_G^{0.15,0ºC}$ = 0.017±0.004. I_D/I_G was 0.018±0.002 for SWCNTs that were not functionalized. Functional groups were thus detrimental to the electropolymerization process. Oxygen groups and structural defects hindered the earliest synthesis stages, reducing the material's electrical conductivity and interfering with π-π monomer stacking onto SWCNTs.

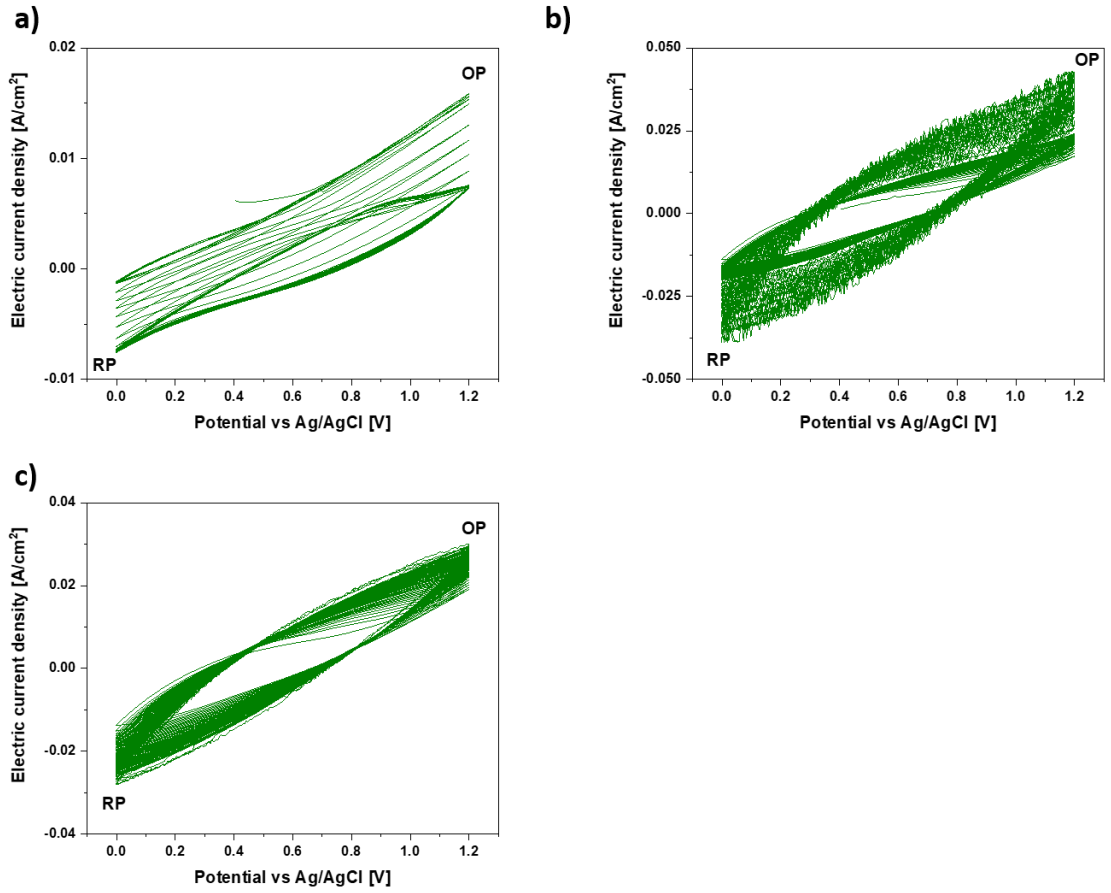

Figure 46 CV curves of PANI electropolymerized onto G+SWCNTs with mass ratios: a) 1:9, b) 1:3, and c) 1:1. Reproduced with permission from ref. [6]© 2023 Grzegorz Stando, Paweł Stando, Mika Sahlam, Mari Lundström, Haitao Liu Dawid Janas. Published by Elsevier B.V.

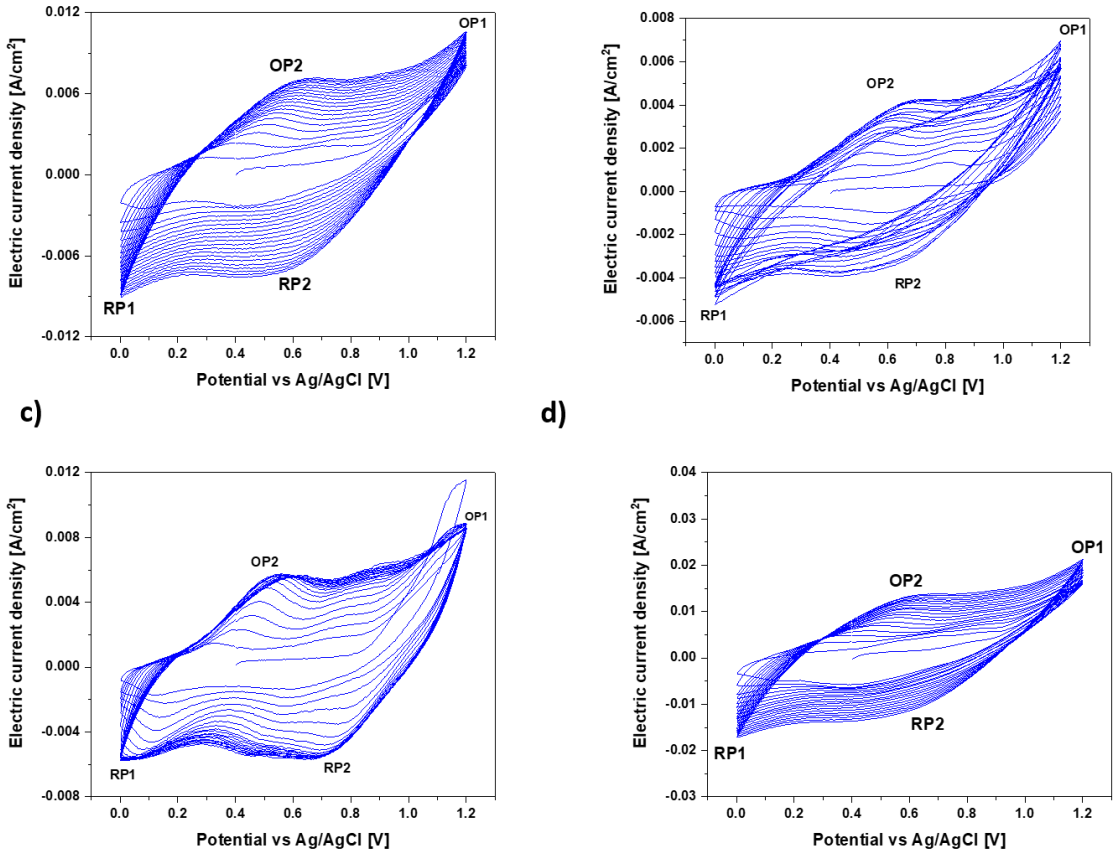

Figure 47 CV graphs of O-SWCNTs synthesized in different parameters, I_D/I_G was as follows: a) $I_D/I_G^{0.95,\ 18\ ^{\circ}C} = 0.102\pm0.032$, b) $I_D/I_G^{0.95,\ 0^{\circ}C} = 0.033\pm0.014$, c) $I_D/I_G^{0.45,\ 0\ ^{\circ}C} = 0.020\pm0.001$, d) $I_D/I_G^{0.15,\ 0\ ^{\circ}C} = 0.017\pm0.004$. Reproduced with permission from ref. [6]© 2023 Grzegorz Stando, Paweł Stando, Mika Sahlam, Mari Lundström, Haitao Liu Dawid Janas. Published by Elsevier B.V.

4.3.2.2.2 Characterization of PANI+SWCNTs composites

After 50 CV cycles of EP, three types of PANI were synthesized on SWCNTs DFEs, and the Raman spectra of each are shown in Figure 48a. These spectra were normalized to the maximum intensity of the 2D peak. The type of PANI greatly influenced the Raman spectra's shape. In the Raman spectra, PB and ES were not discernible (Figure 48a). Small bands near the D peak (associated with the polymer's oxidized unit at 1320–1400 cm^{-1}) $[-C_6H_4-N=C_6H_4=N-C_6H_4-]_n$)[261] were evident. From 0.018±0.002 (SWCNTs) to 0.114±0.034 (ES+SWCNTs) and 0.325±0.002 (PB+SWCNTs), the I_D/I_G ratio increased. The G+/G- ratio was altered by both types of PANI, and the G peak's location shifted (1 cm^{-1} for PB and 2 cm^{-1} for ES), indicating a doping effect[216]. The LB-related signals, on the other hand, were strong

and covered the spectrum's D and G peaks from SWCNTs. The reduced form of $[–C_6H_4\text{-}NH\text{-}C_6H_4\text{-}NH\text{-}C_6H_4–]_n$ is presented also on the spectrum (bands 995 cm^{-1}, 1193 cm^{-1}, and 1616 cm^{-1}). The salt was manufactured on the surface of SWCNTs, according to the XPS examination of ES+SWCNTs. In the N1s scan, -NH- (at 399 eV) and =N- (at 400.3 eV) from the reduced and oxidized units, respectively, were seen (Figure 48b; the ratio of -NH-/=N- intensity was 1.17:1). In addition, the nitrogen was present as the organic salt N+ (401.8 eV). The findings showed that 54% of the nitrogen bands detected were in this form[262,263]. Cl2p (Figure 48c) demonstrated chlorine was present as the counter ion, ClO_4^- anion (209.6 eV)[264], to the positively charged polymer. The XPS survey spectrum demonstrated the effective synthesis of composites, which exclusively revealed the four chemical elements carbon, oxygen, nitrogen, and chlorine (Figure 49). The PANI chain's approximately 1:1 ratio between an oxidized and reduced unit showed how emeraldine was prepared. All findings supported the findings in Figure 50 and demonstrated that the methods used allowed for the selective deposition of all forms of PANI on the nanocarbon surface[265,266]. The following chemical bonds were detected by the C1s and O1s scans (Figure 50): C=O, C=C, C-H, C-C, C-O, C-N, C=N, H-O, Cl-O, and O=C-O[263,267,268]. Thus, the results of the N1s and Cl2p scans, as well as the C1s and O1s scans, were in agreement. All of the observed linkages demonstrated that the ES with the ClO_4^- anion was created on the surface of the nanocarbon.

After 20 cycles of EP, electrical conductivity measurements were used to support the characterization of composites. The results are shown in Figure 49d, where LB and EB reduced the conductivity due to their non-conductive nature from 1075 S/cm to roughly 200 S/cm[143]. Because PB also functions as an insulator, its addition to SWCNTs resulted in a less pronounced reduction in conductivity, which came to 832.2±30.5 S/cm. It was hypothesized that "-N=N-" bonds, which display "π-π" interactions with the nanocarbon surface, might be the source of the less significant decrease in conductivity[151]. It is interesting to note that ES+SWCNTs composite had extremely high conductivity - 3031.2±113.5 S/cm - but this decreased to 1473.1±82.6 S/cm as a result of the partial elimination of $HClO_4$ by deionized water. This value, however, was still greater than that of the unprocessed SWCNT DFEs, both after annealing (1075.3±54.0 S/cm) and immersion in $HClO_4$ solution (1345.5±13.4 S/cm, Figure 49d). Both PANI and SWCNTs can be doped with $HClO_4$, according to the literature[30,269]. The obtained results demonstrated that the addition of $HClO_4$ to the composites increased their electrical conductivity. Emeraldine was dielectric in the absence of the doping agent, which reduced the conductivity of the composite. Additionally, research demonstrated that ES interacted with the

SWCNTs network rather than just pure PANI. The combination of Brønstead acid and PANI that forms the ES increases charge propagation through the SWCNT network (Figure 51)[256]. Additionally, the time of washing in demineralized water was selected to achieve the desired value for the material, reducing the amount of doping agents: 3031±113.5 S/cm (unwashed ES+SWCNTs), 1473.1±82.6 S/cm (washed 1 min, "washed" ES+SWCNTs), and 213±11.4 S/cm (washed 5 min, EB+SWCNTs). After a year of storage, it was discovered that the electrical conductivity of the composites made of ES+SWCNTs and EB+SWCNTs was unchanged.

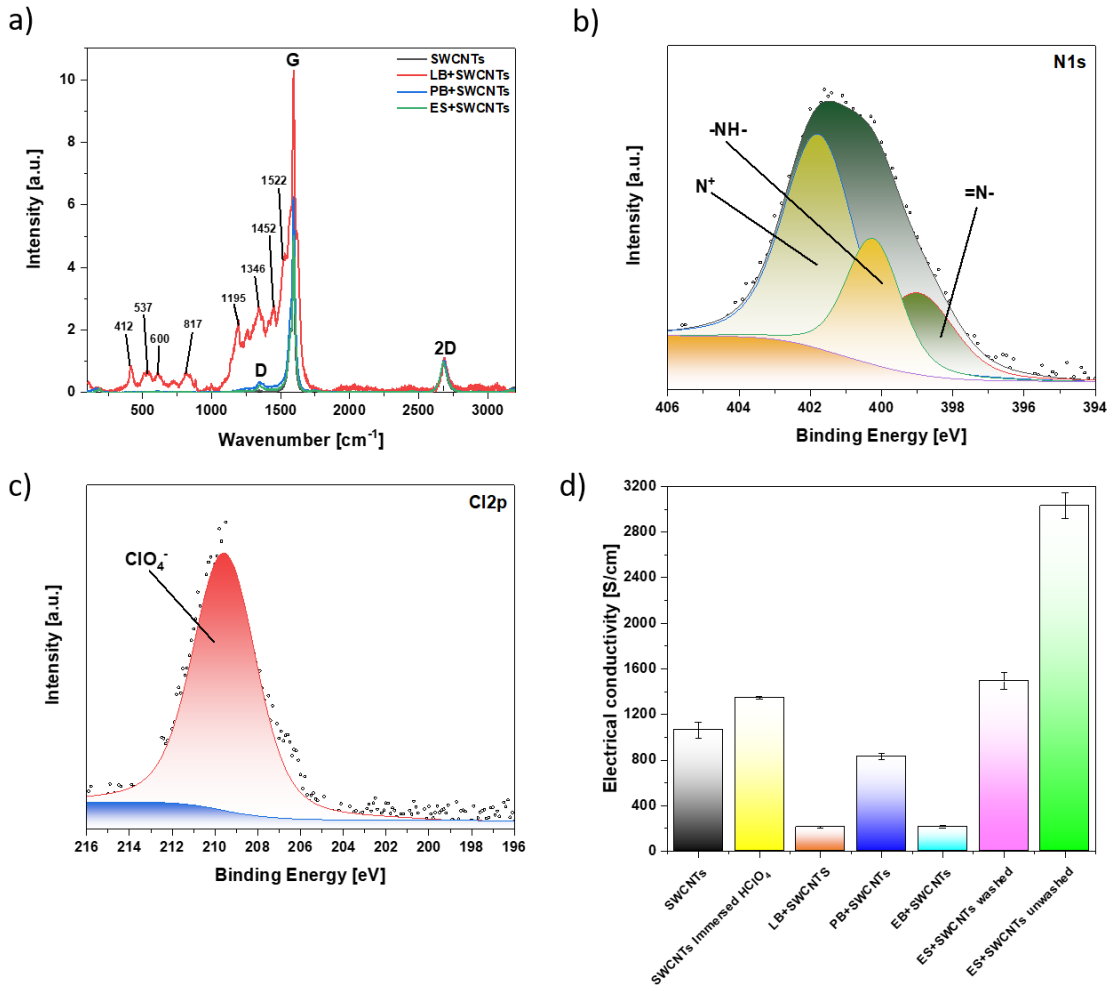

Figure 48 a) PANI+SWCNTs composites normalized to 2D, b) XPS spectrum in range N1s scan 20 cycles of EP ES+SWCNTs, c) XPS Cl2p scan of 20 EP cycles ES+SWCNTs composites, d) electrical conductivity of the synthesized composites. Reproduced with permission from ref. [6]© 2023 Grzegorz Stando, Paweł Stando, Mika Sahlam, Mari Lundström, Haitao Liu Dawid Janas. Published by Elsevier B.V.

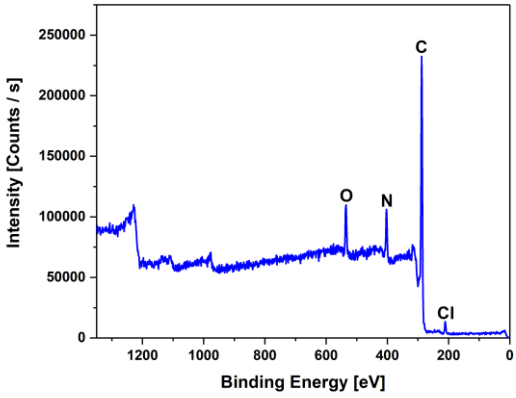

Figure 49 20 cycles of EP XPS survey. Reproduced with permission from ref. [6]© 2023 Grzegorz Stando, Paweł Stando, Mika Sahlam, Mari Lundström, Haitao Liu Dawid Janas. Published by Elsevier B.V.

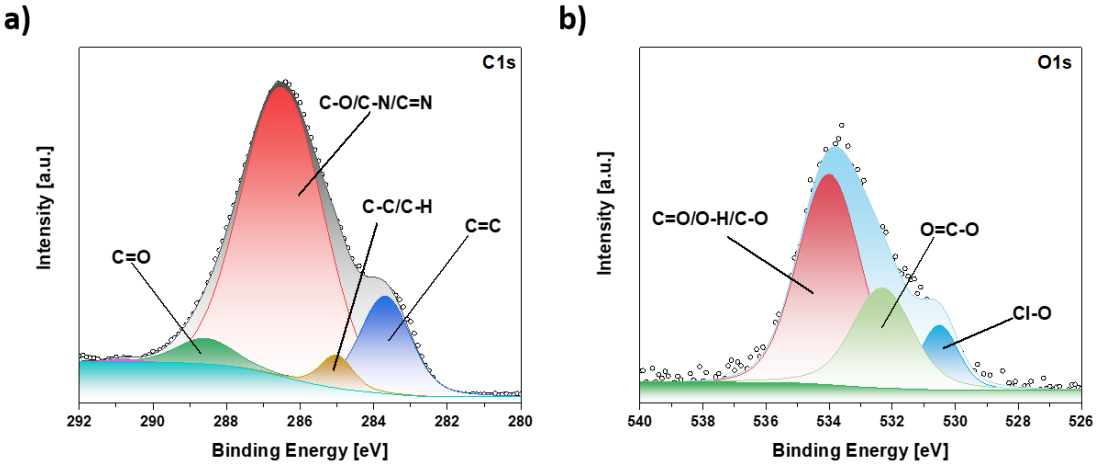

Figure 50 ES+SWCNTs XPS C1s (A) and O1s (B) scans following 20 cycles of EP of PANI. Reproduced with permission from ref. [6] © 2023 Grzegorz Stando, Paweł Stando, Mika Sahlam, Mari Lundström, Haitao Liu Dawid Janas. Published by Elsevier B.V.

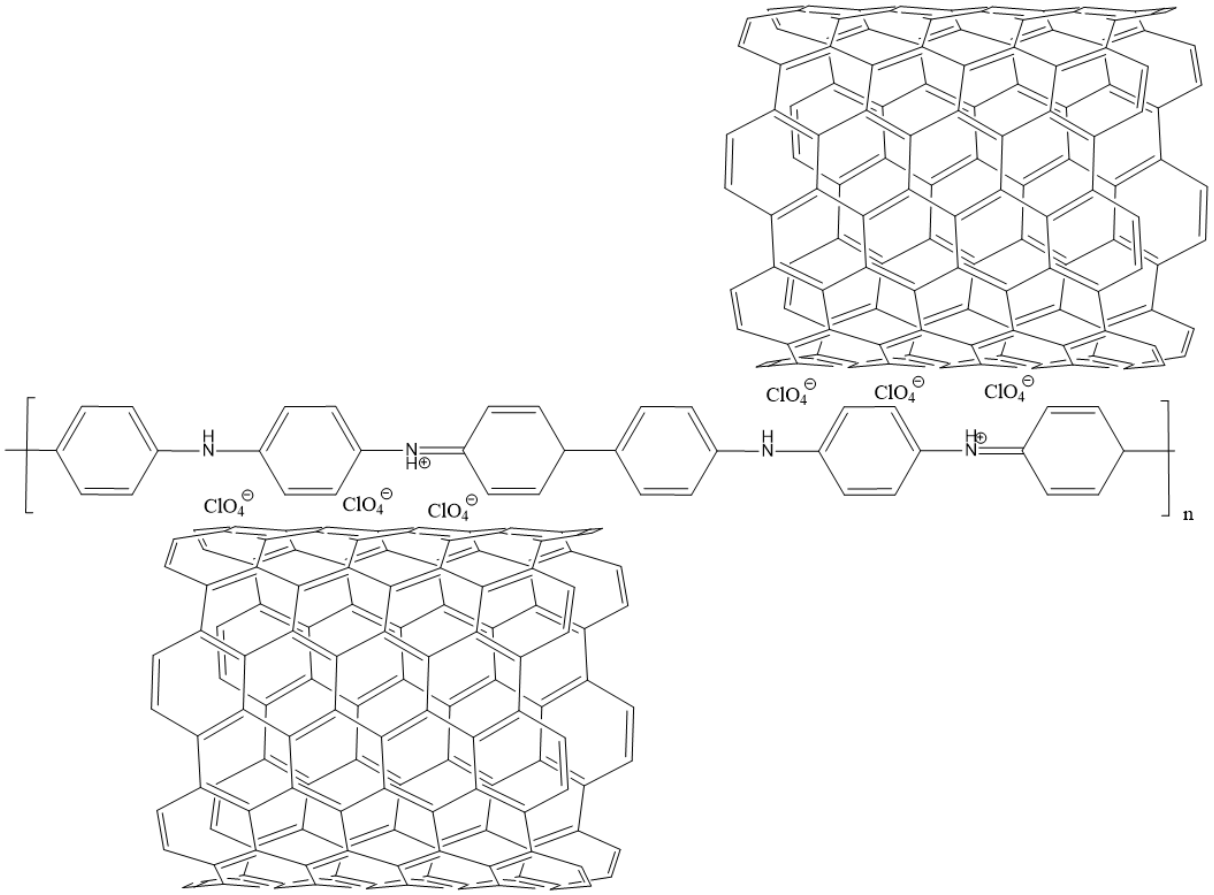

Figure 51 Proposition of SWCNTs and ES interactions. Reproduced with permission from ref. [6] © 2023 Grzegorz Stando, Paweł Stando, Mika Sahlam, Mari Lundström, Haitao Liu Dawid Janas. Published by Elsevier B.V.

The findings for the characteristics of ES+O-SWCNT composites revealed that the electrical conductivity decreased when the I_D/I_G of nanocarbon material grew (Figure 52). This result was in line with the findings of reduced PANI mass resulting from more structural defects. As a result, electrical conductivity was reduced compared to composites based on SWCNTs due to lower PANI salt content and DFEs with higher electrical conductivity values made from more oxidized CNTs[3].

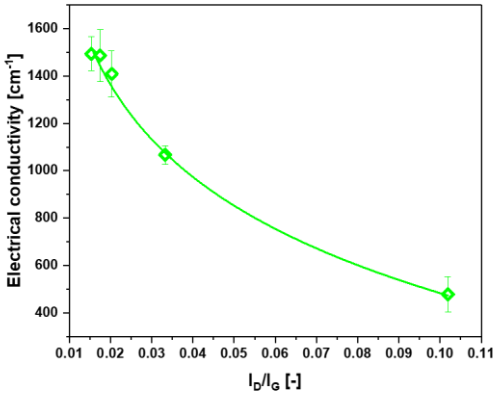

Figure 52 Raman spectroscopic analysis of the evolution of electrical conductivity as a function of I_D/I_G ratio. Reproduced with permission from ref. [6] © 2023 Grzegorz Stando, Paweł Stando, Mika Sahlam, Mari Lundström, Haitao Liu Dawid Janas. Published by Elsevier B.V.

The best outcomes in terms of prospective applications came from ES+SWCNTs. Investigations were done into how the amount of ES affected the form and characteristics of composites that contained nanocarbon. The Raman spectra (Figure 53), in which the bands associated with PANI were not found, were unaffected by the amount of ES on the surface of the SWCNTs, indicating that the ES coating did not interfere with the vibration of the SWCNTs[29,270].

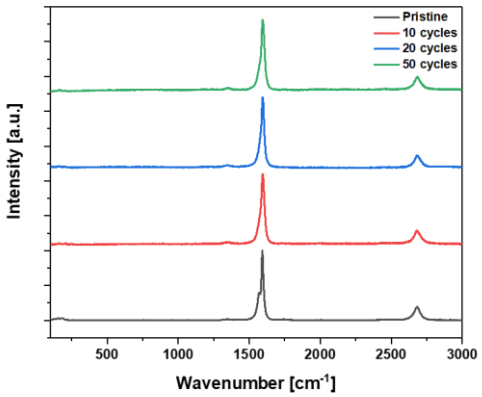

Figure 53 ES+SWCNTs composites Raman spectra. Reproduced with permission from ref. [6] © 2023 Grzegorz Stando, Paweł Stando, Mika Sahlam, Mari Lundström, Haitao Liu Dawid Janas. Published by Elsevier B.V.

However, the reduced [-C_6H_4-NH-C_6H_4-NH-C_6H_4-]$_n$ and oxidized [-C_6H_4-N=C_6H_4=N-C_6H_4-]$_n$ bands of the graphene-containing material ES+G+SWCNTs were discernible (Figure 54a). The band at 1193 cm^{-1} (from N,N'-diphenyl-p-phenylenediamine, reduced unit) and 1320 cm^{-1} (from N,N'-diphenyl-p-phenylenediimine, oxidized unit) were found in the spectrum after 5 cycles of EP. After another 15 cycles of EP, three new bands were observed at 1168 cm^{-1}, 1480 cm^{-1}, and 1525 cm^{-1}. The width of the G peak was the same for the composites after 5 and 20 cycles of EP, which suggested that the amount of ES was too small to disturb the vibration of SWCNTs. However, after 50 cycles of EP, the bands from ES dominated because the mass of PANI was 50.9% of the total mass of composites, which was not observed for 50 cycles of EP ES+SWCNTs with a similar ratio ES to nanocarbon. The interaction of 1D and 2D carbon nanomaterials with ES disrupted the SWCNT network's vibration, causing the formation of PANI's visible bands.

The Fourier-transform infrared spectroscopy (FTIR), as seen in Figures 54b and c, provided a thorough characterization of ES that was not feasible using Raman spectroscopy. As with SWCNTs DFEs, the spectra of high-quality, pristine nanocarbon materials typically do not show many IR bands due to their structure[271]. Thus, the PANI reaction product caused all of the composites' identified IR bands. The following peaks were observed (Figure 54b and c): C-H in aromatic connection 683 cm^{-1} and 742 cm^{-1} (out-of-plane bend), C-N 1018 cm^{-1}, 1055 cm^{-1}, and 1128 cm^{-1}, C=C 1485 cm^{-1} and 1600 cm^{-1}, N-H 1568 cm^{-1} (bending), C=C 3002 cm^{-1} (stretching), N-H 3113 cm^{-1}, and 3194 cm^{-1} (both are from stretching)[74]. The outcomes for the ES+G+SWCNTs samples were comparable. In order to deposit aniline onto nanocarbon DFEs, aniline was then polymerized[265,272]. The mass of ES in the composite did not directly correlate with the enhanced intensity of the chemical bonds such as: C-N, C=C, N-H, and C-H from ES. The best improvement was seen for 20 cycles of EP ES+SWCNTs in the case of electrical conductivity (Figure 54d) (SWCNT concentration was 60% of the composite mass, ratio 2:3 ES/SWCNTs by mass). Wu et al.'s research showed that a 2:3 ES/SWCNTs ratio was ideal for enhancing electrical conductivity[134]. The amount of ES was insufficient at 5 cycles of EP to generate conductive pathways in the composites. On the other hand, the matrix included an excessive amount of low-conductivity polymer for 50 cycles of EP. Due to the variable morphology of the material, ES+G+SWCNTs needed 50 cycles of EP to generate enough new connection routes to increase the charge transfer.

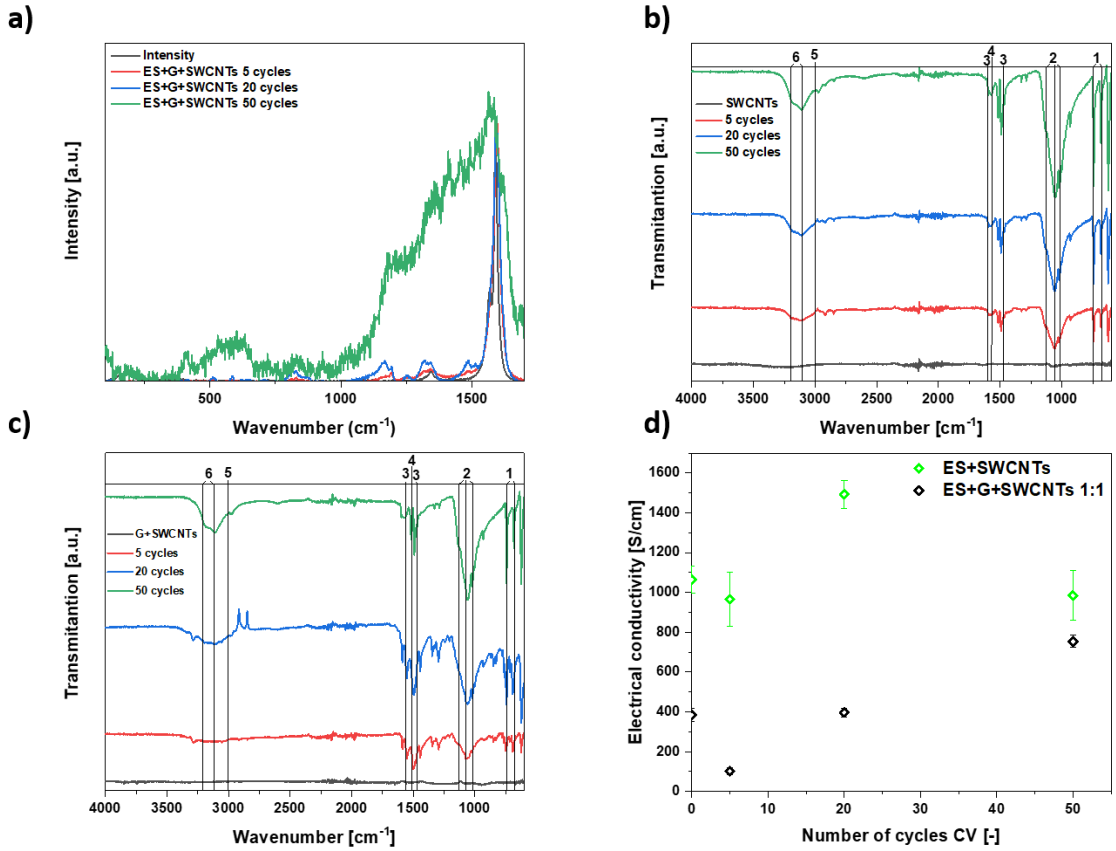

Figure 54 a) ES+G+SWCNTs composites, FTIR spectra of composites: b) ES+SWCNTs and c) ES+G+SWCNTs , where 1 – C-H in aromatic connection 683 cm^{-1} and 742 cm^{-1} (out-of-plane bend), 2 – C-N 1018 cm^{-1}, 1055 cm^{-1}, and 1128 cm^{-1}, 3 – C=C 1485 cm^{-1} and 1600 cm^{-1}, 4 – N-H 1568 cm^{-1} (bending), 5 – C=C 3002 cm^{-1} (stretching), 6 – N-H 3113 cm^{-1}, and 3194 cm^{-1} (both are from stretching), d) Effect of ES concentration on composites' electrical conductivity. Reproduced with permission from ref. [6] © 2023 Grzegorz Stando, Paweł Stando, Mika Sahlam, Mari Lundström, Haitao Liu Dawid Janas. Published by Elsevier B.V.

SEM micrographs (Figure 55a) show that after 5 cycles EP, the surfaces of SWCNTs and ES+SWCNTs were comparable, indicating that either the polymer was used insufficiently or the process took place uniformly on the surface. The surface got rougher as the number of CV cycles grew to 20 and 50, showing that PANI was produced unevenly on the DFEs. Similar outcomes were seen for composites made of G+SWCNTs (Figure 55b), however in this instance, the graphene nanoplatelet agglomerations could be seen on the surface. The two nanocarbon DFEs' different shapes most likely contributed to the increased roughness. The mechanism of the EP process[151], in which the composites were not one solid block but rather an accumulation of SWCNTs (and agglomerates of graphene in the case of G+SWCNTs),

situated in various regions, caused the roughness of the materials to change. In order to increase electrical conductivity, the polymer first filled in the spaces between the nanocarbon structures by forming new conductive channels. PANI agglomerates started to develop as the reaction went on, causing an uneven distribution on the surface.

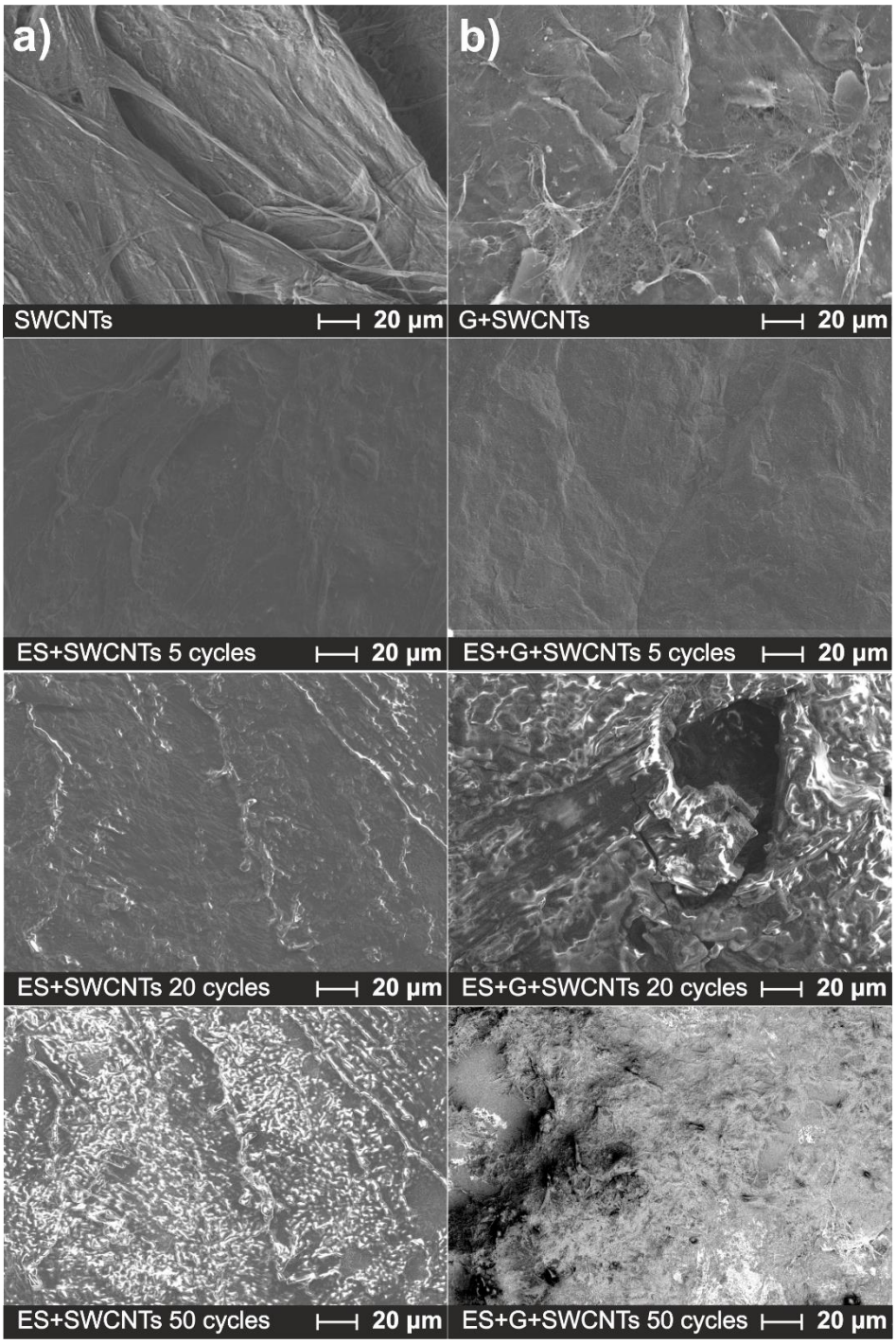

Figure 55 SEM images of electrodes made of SWCNTs and ES+SWCNTs after 5, 20, and 50 cycles of EP in a) and electrodes made of G+SWCNTs and ES+G+SWCNTs after 5, 20, and 50 cycles of EP in b). Reproduced and changed with permission from ref. [6]© 2023 Grzegorz Stando, Paweł Stando, Mika Sahlam, Mari Lundström, Haitao Liu Dawid Janas. Published by Elsevier B.V.

It was examined how the amount of ES in the composites affected their mechanical characteristics (Figure 56). Young modulus was found to be 45.53±5.40 MPa, and SWCNT DFEs were elastic in a narrow range of elongation from 0% to 0.7%. The DFE ruptured at 8% strain (fracture point: 3.99±0.01 MPa), and deformation took on a plastic character. Even while the Young modulus (20.76±0.76 MPa) and fracture point (1.27±0.01 MPa) values were lower, the material became more elastic across a wider range (to 6% strain) after the addition of graphene[273]. Young modulus increased to 102.41±5.91 MPa for 5 cycles of EP and 121.65±11.62 MPa for 20 cycles of EP due to the presence of ES in the SWCNTs network, while the fracture point was 5.89±0.03 MPa for 5 cycles of EP and 5.56±0.01 MPa for 20. The material demonstrated an ultimate strength of 8.44±0.02 MPa after 5 cycles of EP. Regression of the characteristics caused by more cycles of EP resulted in a change in the Young modulus from 45.53±5.40 MPa to 31.67±2.33 MPa and a change in the fracture point from 1.27±0.01 MPa to 0.93±0.01 MPa. The outcomes matched those of the electrical and SEM analyses. The elevated ES content of the composites for 50 cycles of EP caused the composites' structure to deteriorate.

Due to graphene nanoplates populating the gaps in the SWCNT network and changing the deformation character from elastic to plastic in the presence of ES, the characteristics of G+SWCNTs deteriorated. The Young modulus values dropped to 8.50±0.04 MPa and 14.08±0.05 MPa after 5 and 20 cycles of EP, respectively. This value climbed to 25.28±9.00 MPa after 50 cycles of EP. For 5 cycles of EP, the required strain rose from 8% to 28%, for 20 cycles of EP, from 22% to 3%, and for 50 cycles, of EP, from 3% to 2%. In only 20 cycles of EP, it was observed the increased of fracture point to 2.71±0.01 MPa. Moreover, the ultimate strength of all ES+G+SWCNT composites and ES+SWCNTs after 50 cycles of EP differed from the fracture point (ductile materials). For PANI composites including MWCNTs, a higher Young modulus of 9.0±0.2 GPa/(g/cm^3) was reported, although with a lower stated strength of 239 MPa/(g/cm^3)[151]. The top results of synthesized composites (Table 11) were 3.4±0.2 GPa/(g/cm^3) and 279±0.67 MPa/(g/cm^3). Compared to those examined in this research, the reported synthesized composites were more elastic and less resistant to stretching. As a result, ES enhanced the mechanical attributes of SWCNT DFEs. However, it transformed the deformation character of G+SWCNT composites from elastic to plastic, adversely affecting all research properties. Each composite showed an improvement in tensile strength.

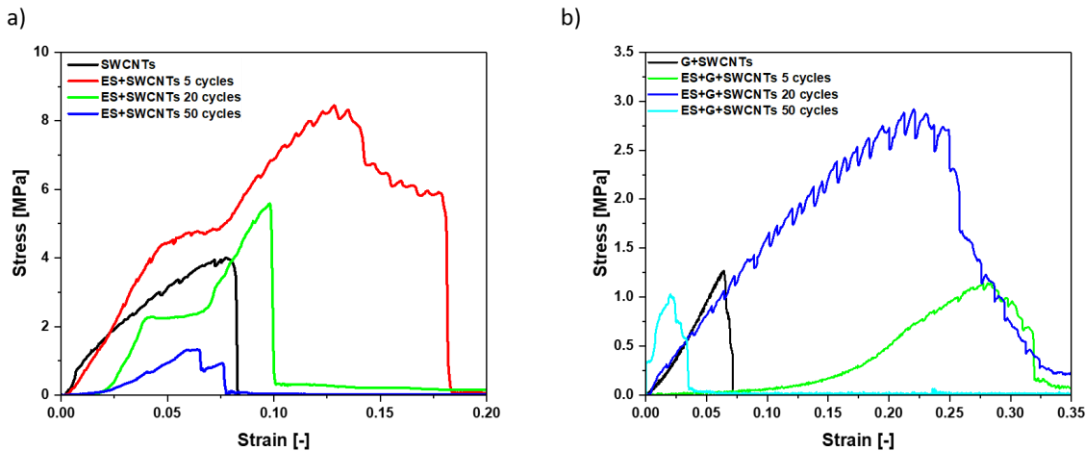

Figure 56 Stretching composites' stress evolution curves for a) ES+SWCNTs and b) ES+G+SWCNTs. Reproduced with permission from ref. [6]© 2023 Grzegorz Stando, Paweł Stando, Mika Sahlam, Mari Lundström, Haitao Liu Dawid Janas. Published by Elsevier B.V.

Table 11 Measured mechanical properties of composites

Sample	Young modulus [GPa/(g/cm^3)]	Ultimate strength [MPa/(g/cm^3)]	Fracture point [MPa/(g/cm^3)]
SWCNTs (pristine)	2.14±0.25	187.76±0.47 at 0.08 strain	187.76±0.47 at 0.08 strain
ES+SWCNTs (5 cycles of EP)	3.39±0.20	279.01±0.66 at 0.13 strain	194.71±0.99 at 0.18 strain
ES+SWCNTs (20 cycles of EP)	3.16±0.30	144.60±0.52 at 0.10 strain	144.60±0.47 at 0.10 strain
ES+SWCNTs (50 cycles of EP)	0.75±0.06	31.43±0.23 at 0.06 strain	22.14±0.24 at 0.08 strain
G+SWCNTs (pristine)	0.86±0.03	52.37±0.47 at 0.06 strain	52.37±0.47 at 0.06 strain
ES+G+SWCNTs (5 cycles of EP)	0.26±0.01	35.28±0.47 at 0.28 strain	18.09±0.30 at 0.31 strain
ES+G+SWCNTs (20 cycles of EP)	0.32±0.01	64.80±0.22 at 0.22 strain	60.76±0.22 at 0.22 strain
ES+G+SWCNTs (50 cycles of EP)	0.48±0.17	19.45±0.19 at 0.02 strain	10.58±0.19 at 0.03 strain

4.3.2.2.3 Potential applications of synthesized materials

As was already indicated, the synthesized composites had good electrical characteristics. Therefore double-layer capacitors constructed specifically for testing their use as supercapacitors were made. Figure 57 presents a CV analysis. SWCNTs have pseudo-supercapacitor properties, which allow them to be used as energy storage material[274]. The capacity Swagelok-type coin cell setup model from SWCNTs had a voltage range of 0-0.4 V and a 9.9±0.6 F/g capacity (Figure 57a). A capacitance of 3.4±0.1 F/g was found for the PB+SWCNT supercapacitor (Figure 57b). As was previously said, the connection between the PB and SWCNTs did not increase the electrical conductivity, which reduced capacity. ES+SWCNTs composites had capacities of 249.8±0.1 F/g and 103.0±0.1 F/g, respectively, following 5 and 20 cycles of EP (Figures 57c, d and e). The composites were thinner after five cycles (0.020±0.003 nm) than after twenty (0.050±0.005 nm). The electrolyte can penetrate the electrodes more easily thanks to the thinner layer, which also increases ion transport[275]. Additionally, as mentioned previously, material after 5 cycles of EP is more hydrophilic (11.3±2.3º) than after 20 cycles of EP (37.6±2.4º), which explains lower capacity – smaller electrode penetration. Xia et al. observed that the increasing sweep value changed the CV curve shape (starting from 10 mV/s) and increased the resistance of PANI-CNTs composites[276,277]. Yoon et al. also noted that when a normal three-electrode electrochemical cell setup was used, ES produced the best results from all oxidation states of PANI. However, due to variations in measurement technique, the difference between ES and pernigraline base was less significant (250 F/g for ES to 120 F/g for PB using MWCNTs, and a scan rate of 50 mV/s)[135]. The doping effect of the ES+SWCNT DFEs, which strengthened the electrical connection between ES and SWCNTs and led to a significantly greater conductivity and capacity than PB+SWCNTs, was responsible for the good electrical characteristics of ES+SWCNTs.

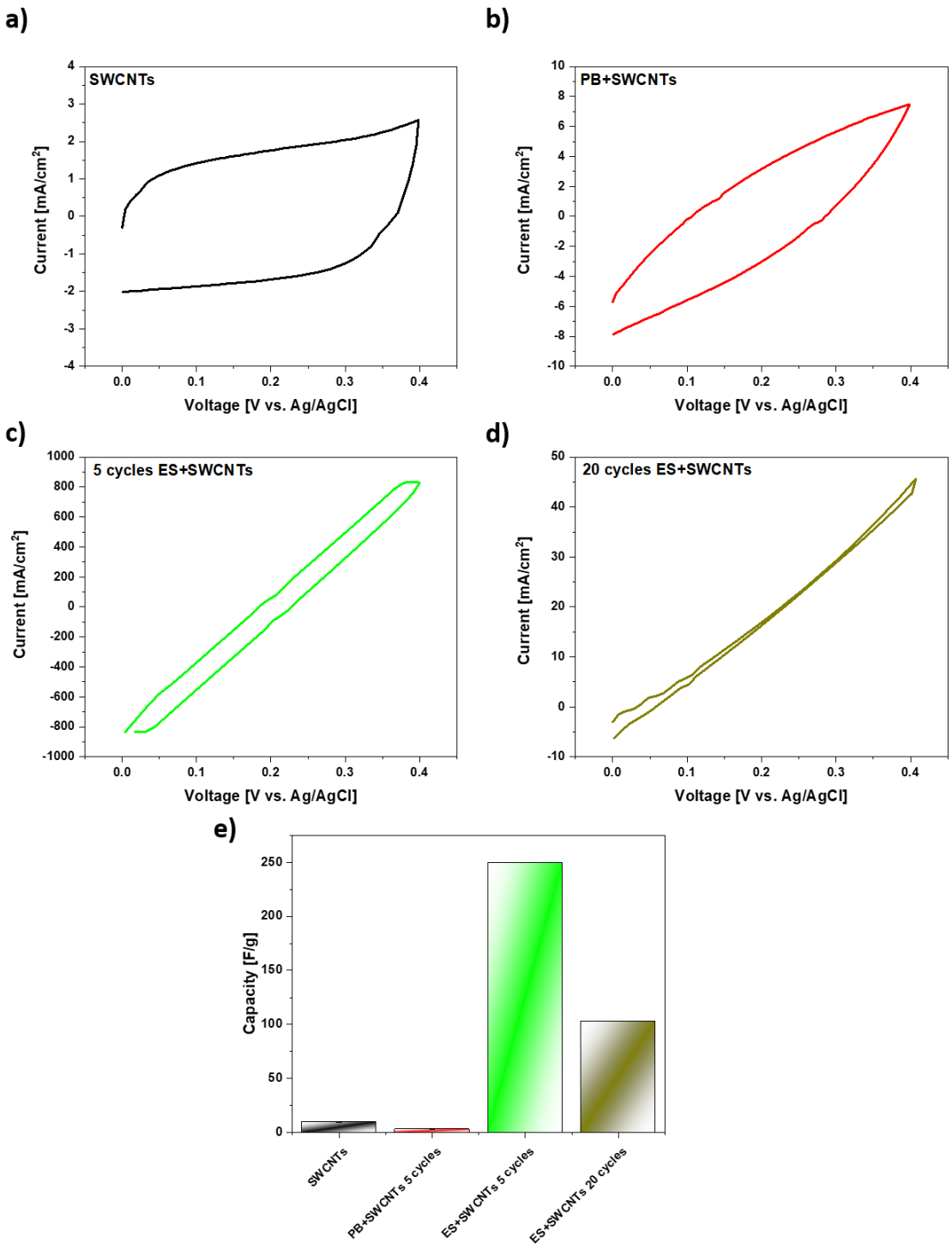

Figure 57 CV curves were employed for measuring: a) supercapacitor made of SWCNT DFEs; b) PB+SWCNTs for five cycles; c) ES+SWCNTs for five cycles; and d) ES+SWCNTs for twenty cycles, f) Capacities of manufactured supercapacitors. a), b), c) and d) were reproduced with permission from ref. [6]© 2023 Grzegorz Stando, Paweł Stando, Mika Sahlam, Mari Lundström, Haitao Liu Dawid Janas. Published by Elsevier B.V.

Figure 58a shows the calculated zT at 30 ºC for various kinds of composites. Each of the PANI forms had a different effect on the thermoelectric properties. It was found that only ES had a slightly positive influence on the thermoelectric properties at low-temperature zT $(73.8\pm20.0)\cdot10^{-6}$ (SWCNTs) → $(102.5\pm14.2)\cdot10^{-6}$ (ES+SWCNTs unwashed). It was mainly due to the increased electrical conductivity of ES+SWCNTs composites and a small decrease in the Seebeck coefficient, which was reported for Brønsted acid by Kumanek et al.[270]. Therefore, the amount of doping agent did not significantly impact the Seebeck coefficient value and composites' thermal properties. After the incorporation of sufficient doping agents, the value of Seebeck did not significantly decrease. Thus, the impact of the amount of doping agent was not negligible on the Seebeck coefficient (α) after a certain concentration. Before reaching this concentration maxima, the increase of the doping agent caused a decrease in α. Other scientific groups observed similar behavior for PEDOT-based materials, where reaching a certain dopant amount, the substance changed the electrical conductivity, but not α[278,279]. Teh et al. showed that in the presence of ES, the thermal conductivity remained unchanged, and the LB value slightly increased[280]. PB lowered the electrical conductivity by approx. 20%. Moreover, it increased the thermal conductivity of the composite to 868.8±48.7 W/mK from 601.64±41.7 W/mK and was the primary reason for the reduced zT value. It is the most stable form of PANI and has the best thermal properties, so this was a reason for the improvement of conductivity [280–284]. LB also increased the thermal transfer, but the observed increase was much smaller by 680±41.9 W/mK. Moreover, the value of other properties decreased due to the dielectric character of this form. The addition of ES diminished the thermoelectrical properties. In the case of composites based on G+SWCNTs, the zT value reduced from $(4.08\pm0.48)\cdot10^{-6}$ to $(2.37\pm0.69)\cdot10^{-6}$. The studied composites with three substances exhibited a much smaller potential for application as a material for thermogenerators than ES+SWCNTs.

The impact of temperature on the physical properties of SWCNTs and ES+SWCNTs unwashed was also examined. A significant improvement in the Power Factor occurred (Figure 58b). The highest value was determined at 90 ºC for ES+SWCNTs unwashed (at diagrams ES+SWCNTs): Power Factor 107.6±5.9 → 223.8±16.7 μW/mK^2. Heating of the samples improved the thermoelectric properties of the composite due to increased α and stable high electrical conductivity. However, the electrical resistance and α of SWCNTs DFE increased during heating, which was typical behavior for metallic character materials. This type of behavior was reported for DFs of CNTs by Kumanek et al.[270].

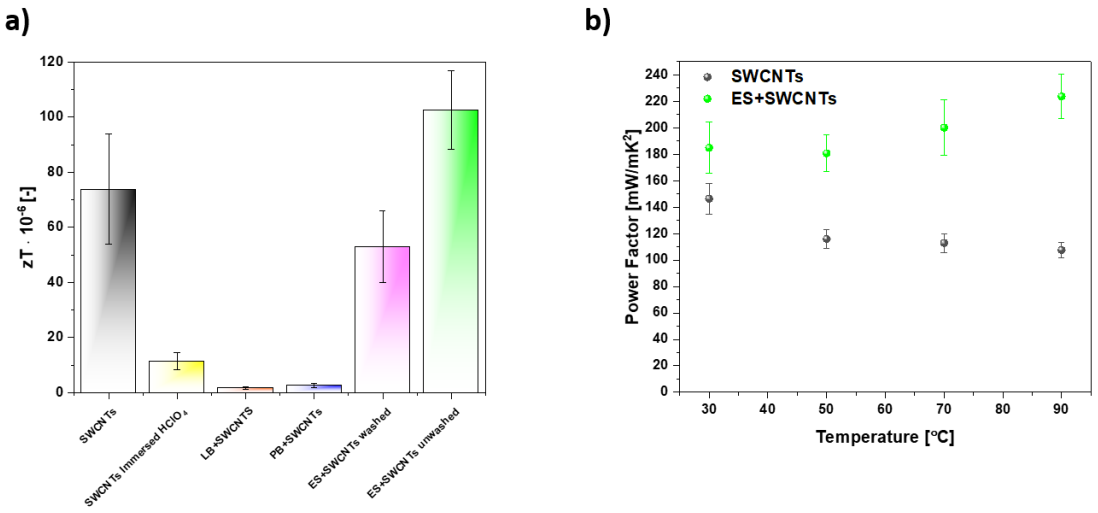

Figure 58 a) zT for nanomaterials produced at 30 ºC and b) temperature effects on the values of Power Factor.

4.3.3 Cu+nanocarbon composites

4.3.3.1 Short introduction to the synthesis of copper and nanocarbon composites

This chapter presented the application of the observed phenomenon of hydrophobization on air nanocarbon surface to the selective recovery of copper from industrial wastewater by electrodeposition. The different kind of carbon nanotubes (single-walled and multi-walled) was used to create DFEs from pure CNTs and composites DFEs composed of two types of nanocarbon material. Firstly, it established parameters for electrodeposition copper using the synthetic solution, and the DFEs were selected for Cu recovery. In the end, the chosen DFEs were used for the selective recovery of copper from wastewater.

4.3.3.2 Characterization of carbon nanomaterials and DFEs from them

Figure 59 presents the micrographs of the nanocarbon powders which were utilized to manufacture DFEs. The obtained micrographs clearly show that the diameter values of commercial nanomaterials (1.6±0.4 nm for SWCNTs and 9.0±2.0 nm for NC-MWCNTs - according to manufacturer information) are significantly less than those of in-house manufactured MWCNTs (115±34 nm). The diameter distribution of in-house produced MWCNTs reduced to 93±23 nm for O-MWCNTs after the oxidation reaction, which suggests that the functionalization procedure was successful[57]. Additionally, the diameter of N-MWCNTs was also lower (76±18 nm) than the diameter of MWCNTs produced under the same conditions without pyrazine. The longitudinal and radial growth of the material is

constrained because the synthesis of heteroatom-implanted MWCNTs typically occurs at a significantly slower rate than that of non-doped material[285,286]. The microstructure of graphene flakes also conforms to the topology predicted for such materials.

Raman spectroscopy examined the nanomaterials' structural perfection (Figure 60). By comparing the intensity of the defect-induced D-band, which is centered at about 1350 cm^{-1} (sp^3 carbon atoms), to the intensity of the feature of graphitic vibrations G, which is positioned at around 1580 cm^{-1} (sp^2 carbon atoms), it was possible to determine the crystallinity of the carbon lattice. The I_D/I_G ratios of the nanocarbon powders utilized to create DFs are first examined. Only SWCNTs showed a low D peak intensity (I_D/I_G=0.022) among all the assessed raw materials, demonstrating their high quality. CNTs materials' I_D/I_G ratios ranged from 0.276 to 1.292, showing high content of surface functional groups and various defects[287]. Compared to commercial technical-grade MWCNTs (NC-MWCNTs I_D/I_G=1.292±0.045), MWCNTs made in-house had a substantially lower level of contamination and distortion to the sp^2 carbon lattice (I_D/I_G=0.276±0.030).

The MWCNTs oxidation was successful, as shown by the acquired Raman spectra. After the treatment, the I_D/I_G for O-MWCNTs material increased from 0.276±0.030 to 0.434±0.019[239]. It was established that the nitrogen-doped (N-MWCNTs) D band intensity is almost twice as high as that for pristine MWCNTs produced under the same circumstances: 0.518±0.012 vs. 0.276±0.03. The I_D/I_G ratio of 0.620±0.006 in graphene nanoplatelets also demonstrated the presence of several unrelated species on its surface. Additionally, its I_{2D}/I_G ratio of 0.540±0.071 was noted, indicating the material's multilayer nature[288].

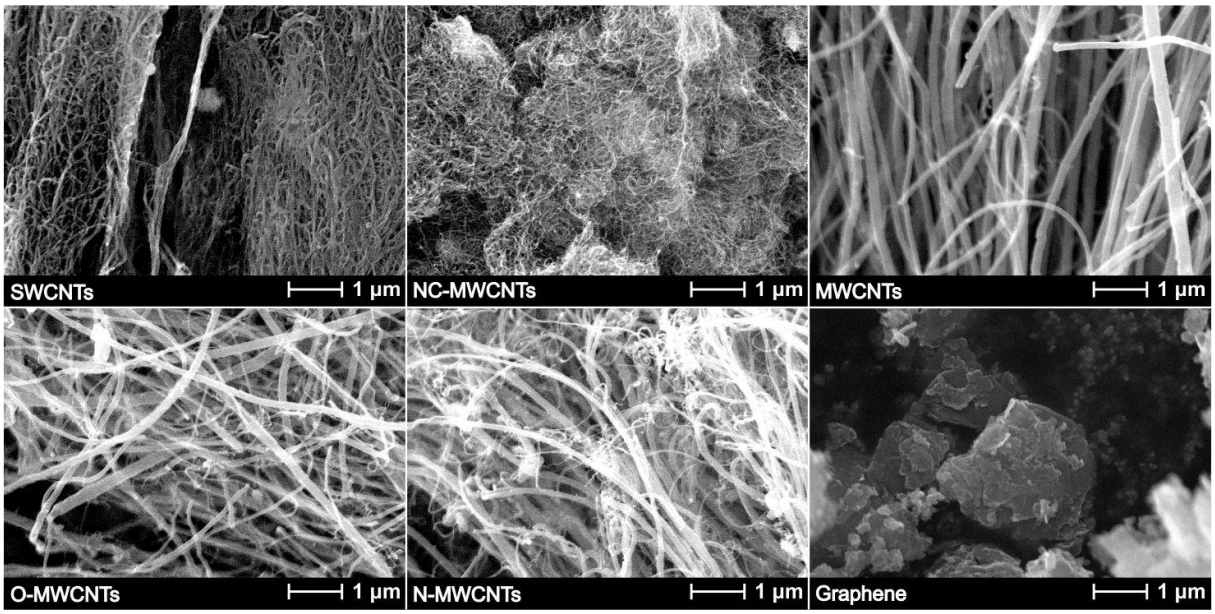

Figure 59 SEM micrographs of chosen nanocarbon, which was used to produce DFs Reproduced with permission from ref. [4] © 2021 Grzegorz Stando, Pyry-Mikko Hannula, Bogumiła Kumanek, Mari Lundström, Dawid Janas. Published by Elsevier B.V.

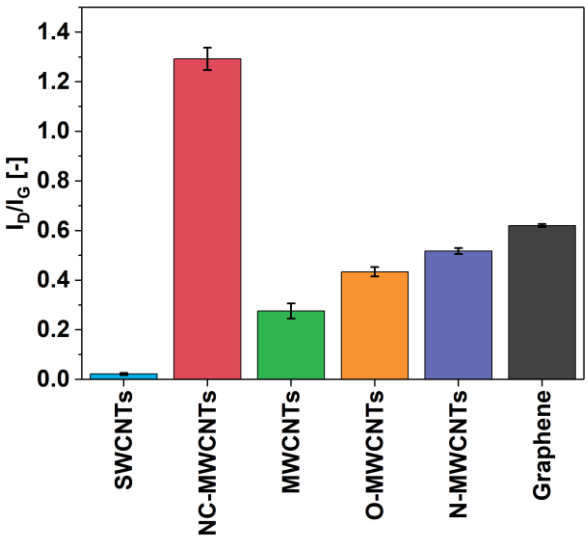

Figure 60 I_D/I_G calculated from Raman spectra of carbon nanomaterials. Reproduced with permission from ref. [4] © 2021 Grzegorz Stando, Pyry-Mikko Hannula,Bogumiła Kumanek, Mari Lundström, Dawid Janas. Published by Elsevier B.V.

The study of nanocarbon DFs generated from the aforementioned raw materials using Raman spectroscopy is shown in Figure 61 (both before and after the binder was removed). After annealing, the I_D/I_G ratios for the neat CNT materials (SWCNTs, NC-MWCNTs, and

MWCNTs) somewhat dropped. It is because annealing removes amorphous carbon, EC, and other forms of carbon, which lessens the intensity of the defect-induced D peak. However, the I_D/I_G ratios were significantly decreased when O-MWCNT materials were momentarily subjected to the effects of high temperature. In comparison to, a low concentration of O-MWCNTs (10%, I_D/I_G=0.018±0.001 → I_D/I_G=0.010±0.001) in the composite with SWCNTs, the effect was more pronounced at a high content of O-MWCNTs (50%, I_D/I_G=0.032±0.001 → I_D/I_G=0.017±0.001). During annealing, the most oxidized functionalized groups are detached, which would ultimately increase the material's average degree of structural perfection after annealing[189], which could be the cause of the drop in I_D/I_G at high O-MWCNT content. The I_D/I_G ratios for the N-doped samples were constant throughout annealing (10%, I_D/I_G=0.017±0.003 → I_D/I_G=0.013±0.003; 25%, I_D/I_G=0.014±0.002 → I_D/I_G=0.013±0.003; 50%, I_D/I_G=0.015±0.001 → I_D/I_G=0.013±0.001). Last but not least, the I_D/I_G ratios in the instance of mixing SWCNTs with graphene were unaffected by the thermal processing when the uncertainty values were taken into account. The signals from high-quality SWCNTs always predominate the spectra when they are used to create composites with other nanocarbon types, according to the analysis of the entire dataset. The resultant I_D/I_G ratio is low even though SWCNTs are mixed with materials that have high I_D/I_G ratios (e.g., 0.434, 0.518, and 0.620 for O-MWCNTs, N-MWCNTs, and graphene, respectively). Even when up to 1:1 w/w of functionalized nanocarbon is added to the SWCNTs matrix, it almost never rises above 0.02. Only a portion of the CNTs population is excited by resonant Raman scattering, which could bias data interpretation [289]. Because more SWCNTs are tuned to the chosen laser wavelength in this work, it appears that the signal intensity coming from SWCNTs surpasses that from MWCNTs.

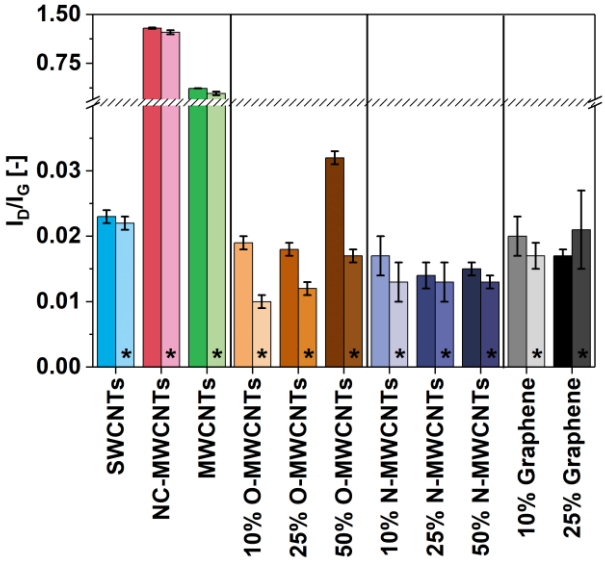

Figure 61 Nanocarbon DFs' I_D/I_G ratios before (without asterisk) and after (marked by an asterisk) removing the binder. Reproduced with permission from ref. [4] © 2021 Grzegorz Stando, Pyry-Mikko Hannula, Bogumiła Kumanek, Mari Lundström, Dawid Janas. Published by Elsevier B.V.

The suitable surface chemistry of the substrate, which ensures compatibility with the aqueous plating solution, is one of the crucial criteria for the electrodeposition process. The possibility of effectively plating Cu[290,291] onto the typically naturally hydrophobic nanocarbon DFEs increases with decreasing water contact angle (γ) values. The surface of the DFEs made from parent nanocarbon materials that contain the binder is comparatively hydrophobic (γ>90 degrees) (Figure 62). However, a drastic reduction in WCA was noticed for these samples after binder removal by annealing and exposure to atmospheric air for one day (SWCNTs: $\gamma^{\text{with EC}}$=113.6±5.6° → $\gamma^{\text{without EC}}$ =39.3±6.6°, NC-MWCNTs: $\gamma^{\text{with EC}}$ =111.6±4.8° → $\gamma^{\text{without EC}}$ =7.91.7°, and MWCNTs: $\gamma^{\text{with EC}}$ =95.42±8.2° → $\gamma^{\text{without EC}}$ = 9.0±2.4°). It was brought on by the thermal desorption of environmental contaminants, which hide the quasi-hydrophilic properties of the CNT surface[213,292]. The hydrophobic nature of the composite materials based on the SWCNT matrix, which contains N-MWCNTs, O-MWCNTs, and graphene, is also reduced (from about 70–80°). These filler materials have a higher disorder level than average, increasing their hydrophilicity. All of these materials have a WCA of up to about 20° after annealing. The observed values fall about in the middle of those of the MWCNT fillers and the SWCNT matrix, from which these composite materials are made[293,294].

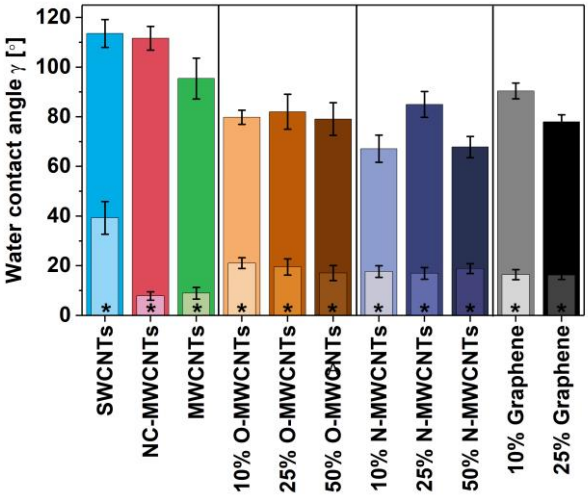

Figure 62 Value of WCAs before/after purification and removing EC from nanocarbon DFEs. Darker is the value before annealing, and lighter and marked with an asterisk is after annealing – WCA was measured after a one-day exposition of atmospheric air. Reproduced with permission from ref. [4] © 2021 Grzegorz Stando, Pyry-Mikko Hannula, Bogumiła Kumanek, Mari Lundström, Dawid Janas. Published by Elsevier B.V.

The electrochemical activity of nanocarbon DFEs is directly influenced by their electrical conductivity (Figure 63). The literature demonstrates that the pre-processing of the material and the presence of a binder or doping agents are important elements to take into account[212,214,295]. The high-quality SWCNT DFEs' electrical conductivity (1064.0±69.0 S/cm) was shown to be the greatest of all manufactured DFEs. On the other hand, technical grade (NC-MWCNTs) or in-house manufactured (MWCNTs). Samples had low electrical conductivity, measuring 36.8±0.5 S/cm for NC-MWCNTs and 123.9±18.3 S/cm for MWCNTs, respectively. The MWCNTs' profusion of defects brought this on and their fundamentally worse electrical conductivity than SWCNTs[296]. When O-MWCNTs, N-MWCNTs, or graphene, were combined with SWCNTs to create composite materials, and the electrical conductivity of the resulting hybrids was, on average, 6 times lower (by 5.4, 7.4, and 6.2 times, respectively). The Raman spectroscopy-detected considerable defect content in the mixed nanocarbon types can be used to explain the decline in electrical conductivity. Charge scattering is more noticeable because more defects are present, which raises the resistance. Unfortunately, due to the poor mechanical integrity of the DFEs made from O-MWCNTs, N-MWCNTs, or graphene, could not evaluate the electrical conductivity of DFEs generated purely from these materials. How the binder's removal affected the nanocarbon ensembles'

electrical conductivity was researched. SWCNTs, NC-MWCNTs, and MWCNTs' electrical conductivity did not appear to be affected by the annealing of the material, which was consistent with Raman spectroscopic characterization that showed no structural changes during thermal treatment[212,295]. Although, following annealing, the electrical conductivity of all SWCNT composites containing O-MWCNTs, N-MWCNTs, and graphene almost doubled (25% N-MWCNTs, $\sigma^{\text{without EC}}$=99.3±3.3 S/cm → $\sigma^{\text{without EC}}$ =148.7±8.5 S/cm or 50% O-MWCNTs, $\sigma^{\text{with EC}}$=82.7±15.3 S/cm → $\sigma^{\text{without EC}}$ =166.8±23.3 S/cm). After introducing O- and N-functionalities into these nanocarbon materials, the surface chemistry of CNTs becomes significantly more compatible with the EC structure. Therefore, it stands to reason that modified CNTs (O-MWCNTs and N-MWCNTs) interact particularly well with oxygen-rich EC binders. It could therefore result in the encapsulation of O-MWCNTs and N-MWCNTs by a dielectric binder, impeding the material's electrical conductivity. Consequently, the electrical conductivity increases because new percolation channels are created when the EC is eliminated by annealing. The Raman spectroscopy identified an abundance of defects in the graphene base material, which can be used to explain how SWCNTs/graphene composites have increased electrical conductivity after annealing, promoting their removal.

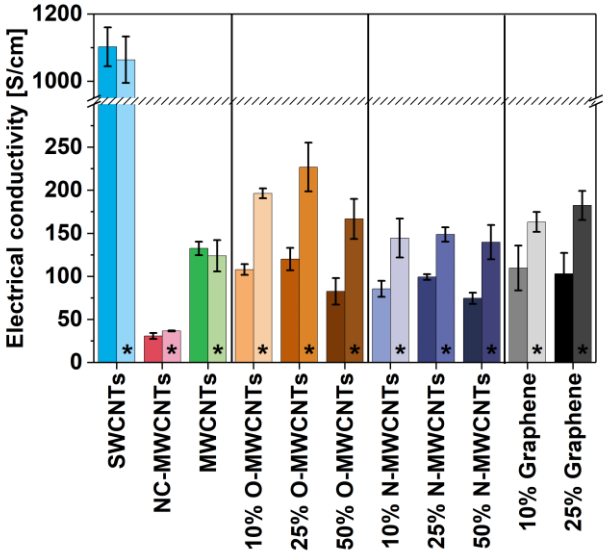

Figure 63 Before (without asterisk) and after (with asterisk) the binder was removed, the electrical conductivity values of nanocarbon DFEs. Reproduced with permission from ref. [4] © 2021 Grzegorz Stando, Pyry-Mikko Hannula, Bogumiła Kumanek, Mari Lundström, Dawid Janas. Published by Elsevier B.V.

4.3.3.3 Electrodeposition of copper and recovery copper from industrial wastewaters

Cathodic polarization curves were recorded for all samples in synthetic Cu electrolyte (Figure 64). The results showed typical characteristics of Cu electrodeposition from a high-concentration solution with some notable differences in deposition kinetics between various samples. Two distinctive sets of behaviors can be observed in all curves: (I) slow deposition kinetics for all samples containing binder and samples consisting purely of unfunctionalized MWCNTs and (II) fast deposition kinetics for all binder-free samples, including pure SWCNTs and their composites with functionalized MWCNTs.

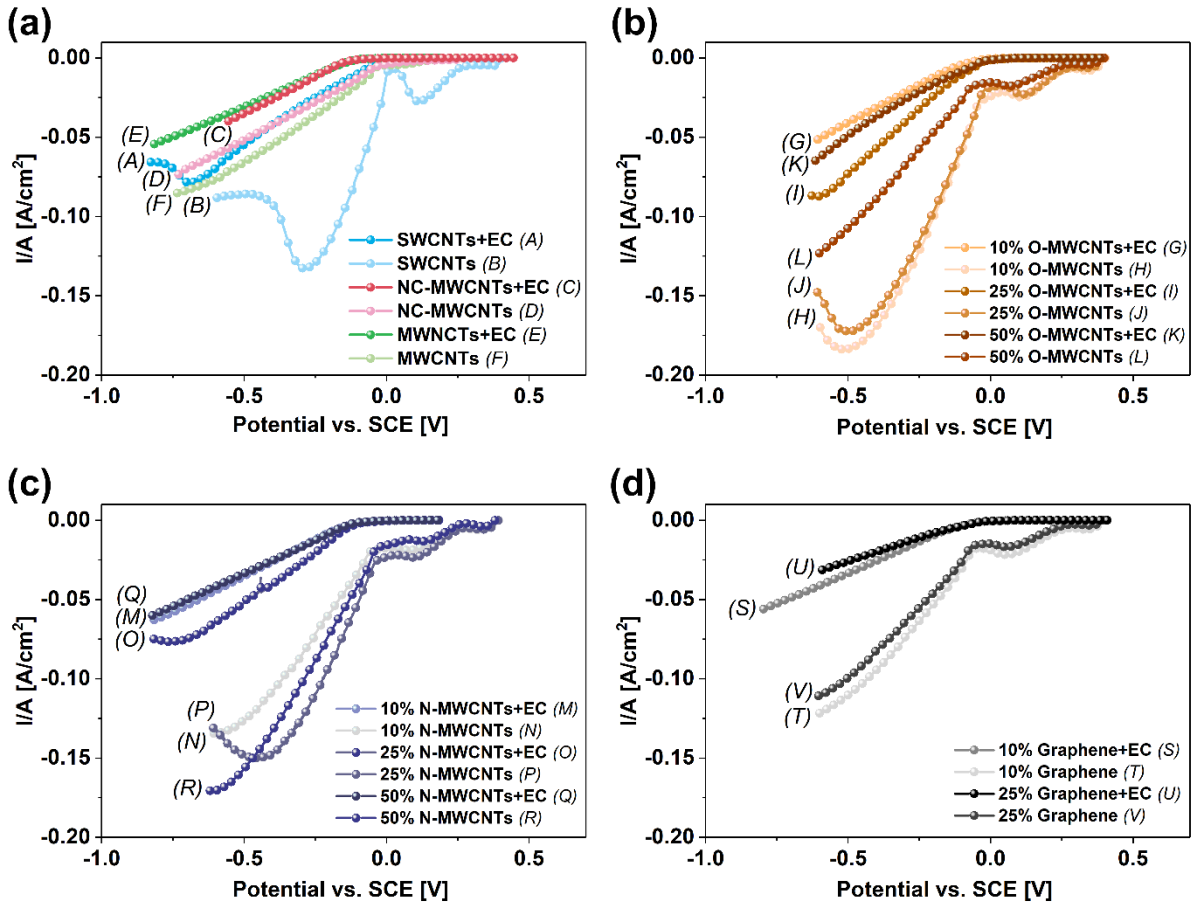

Figure 64 Cathodic polarization curves for (a) SWCNT DFEs, (b) composites O-MWCNT DFEs, (c) composites N-MWCNT, and (d) composites Graphene. Reproduced with permission from ref. [4] © 2021 Grzegorz Stando, Pyry-Mikko Hannula, Bogumiła Kumanek, Mari Lundström,Dawid Janas. Published by Elsevier B.V.

The pulse electrodeposition of Cu particles from the artificial electrolyte was researched in order to further evaluate the performance of various nanocarbon DFE materials. This

experiment used a single deposition pulse lasting 1 second at 0.0 V vs. SCE to electrodeposit copper onto the samples. In order to compare samples with various compositions as well as the impact of the binder on the initial nuclei developing in the early phases of Cu deposition, modest overvoltage was used for Cu deposition. The parent materials were looked at first (Figure 65). The outcomes demonstrated that clean SWCNTs are the best substrate for the pulse electrodeposition technique. The DFE's surface was covered in uniformly spaced round Cu clusters with a diameter of around 2 μm. The Cu deposition was also noticeable when the SWCNTs contained a binder (Figure 65), but the particles' size, shape, and distribution were less even. Thus, it was discovered that removing the binder was advantageous for the deposition of uniformly dispersed Cu nuclei, supporting the findings of the cathodic polarization studies.

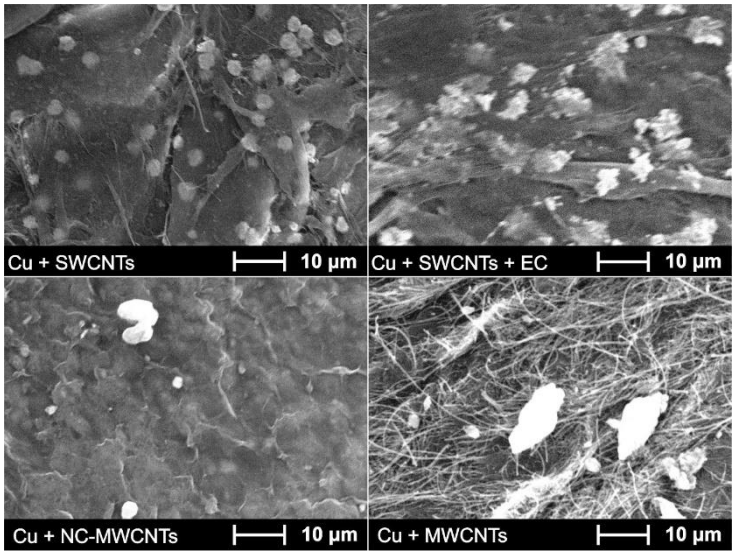

Figure 65 SEM micrographs of deposited copper onto SWCNTs, SWCNTs+EC, NC-MWCNTs, and MWCNTs. Reproduced with permission from ref. [4] © 2021 Grzegorz Stando, Pyry-Mikko Hannula, Bogumiła Kumanek, Mari Lundström, Dawid Janas. Published by Elsevier B.V.

On the other hand, when MWCNTs were employed, only scarce Cu clusters could be observed on the surface. The reason why the electrodeposition of Cu was inferior on these types of DFEs can be ascribed to the low electrical conductivity values and poor crystallinity (high I_D/I_G ratio, as shown in Figure 61 and electrical conductivity in Figure 63). NC-MWCNTs and MWCNTs have an order of magnitude lower electrical conductivity than SWCNTs and are characterized by an abundance of defects. Consequently, the DFEs made from them are more challenging to polarize, as shown in Figure 64, leading to reduced Cu deposition kinetics.

Hence, only a negligible amount of Cu on the surface could be observed after the deposition. Furthermore, the inhomogeneous distribution of Cu can be seen because Cu deposition is preferred for the defects which are prevalent in these materials. The next step was to determine how adding functionalized MWCNTs to the SWCNT matrix will impact the material's capacity to deposit copper (Figures 66 and 67). It has been demonstrated in the past that adding oxygen-containing functionalities to the surface of CNT DFEs enhances the electrochemical response for metal electrodeposition because these functional groups are more reactive than other functional groups, which results in a more uniform distribution of smaller metal nuclei[297]. A similar general pattern could be seen in this study to some extent, with smaller Cu nuclei up to 25% O-MWCNTs produced by increasing the proportion of functionalized MWCNTs while decreasing the proportion of SWCNTs. Only tiny Cu deposits with a maximum diameter of a few microns could be seen equally dispersed across the sample surface at 10% to 25% of O-MWCNTs (Figure 66). More oxidized MWCNTs produce sparsely distributed, 10 µm -sized Cu nuclei, which are identical to the pure MWCNT material. The outcomes are consistent with polarization investigations, which demonstrate that the deposition slope was comparable for samples containing only SWCNTs and for those comprising 10% and 25% O-MWCNTs. On the other hand, the cathodic slope clearly decreases at 50% O-MWCNTs, which is most likely due to the significant amount of less conductive MWCNTs that adversely affect polarization. As a result, compared to pure SWCNTs material, minor additions of functionalized CNTs were advantageous for depositing evenly distributed tiny Cu nuclei. The outcomes show that a simpler method can be used in place of oxidizing the bulk SWCNTs material. Here, the SWCNTs matrix is simply admixed with a few oxidized CNTs to speed up the process.

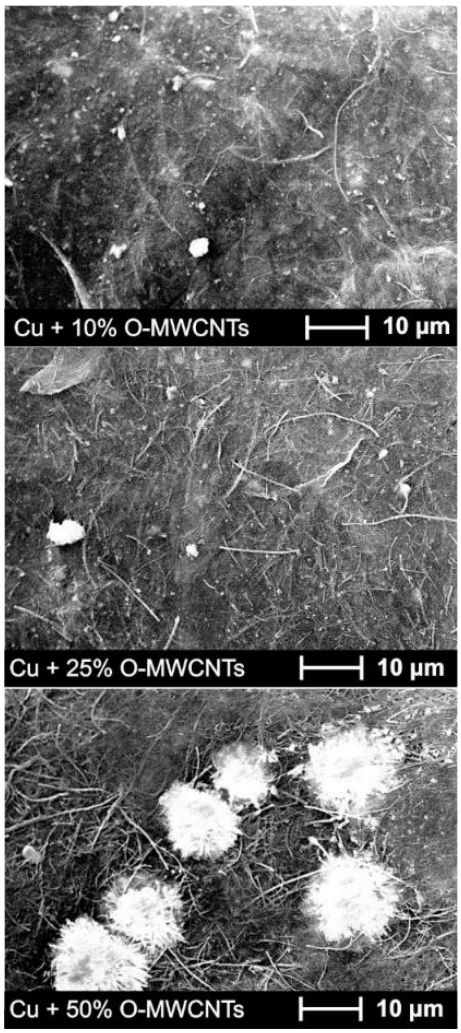

Figure 66 SEM micrographs of Cu deposit onto composites made from O-MWCNTs and SWCNTs. Reproduced with permission from ref. [4] © 2021 Grzegorz Stando, Pyry-Mikko Hannula, Bogumiła Kumanek, Mari Lundström, Dawid Janas. Published by Elsevier B.V.

Including N-MWCNT and graphene fillers in composite DFEs at a level of 25% in the SWCNT matrix did not encourage uniform Cu deposition (Figure 67). Both of these composite DFE types had scant deposition, extremely variable particle size and distribution, and no discernible pattern in the size of the Cu nuclei.

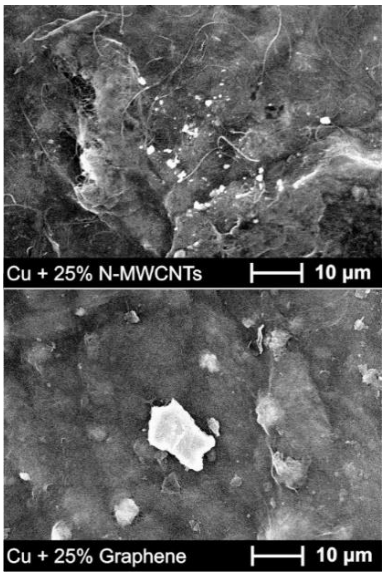

Figure 67 SEM micrographs of Cu deposited onto N-MWCNTs and Graphene composites. Reproduced with permission from ref. [4] © 2021 Grzegorz Stando, Pyry-Mikko Hannula, Bogumiła Kumanek, Mari Lundström, Dawid Janas. Published by Elsevier B.V.

Different types of DFEs were chosen for 1-hour electrodeposition at -0.1 V vs. SCE to investigate the viability of the nanocarbon composite DFEs for copper deposition from a real wastewater solution. This electrodeposition potential was chosen because it cannot deposit the less noble elements from the solution at a lower electrodeposition potential. It is thus possible to selectively deposit only Cu on the DFEs surface. Wastewater contains 100x less copper (428 ppm) than synthetic copper electrolytes. SEM micrographs display the morphology of the Cu particles that were deposited on different kinds of nanocarbon sheets (Figure 68). Copper deposits on DFEs have the following sizes: SWCNTs (1.5±0.3 µm), MWCNTs (4.3±0.5 µm), and 25% graphene (1.1±0.3 µm). The size distribution of the remaining materials was too uneven for a precise estimation of this value. As previously mentioned, the size of the Cu deposits generally follows the same pattern, with larger particles visible on the MWCNTs DFE. The lack of deposits on the NC-MWCNTs DFE was probably caused by its low conductivity, which could not allow deposition at such a high overvoltage. But the uniform size and distribution of the Cu deposits on the SWCNTs DFEs seemed hopeful, so it was analyzed more thoroughly.

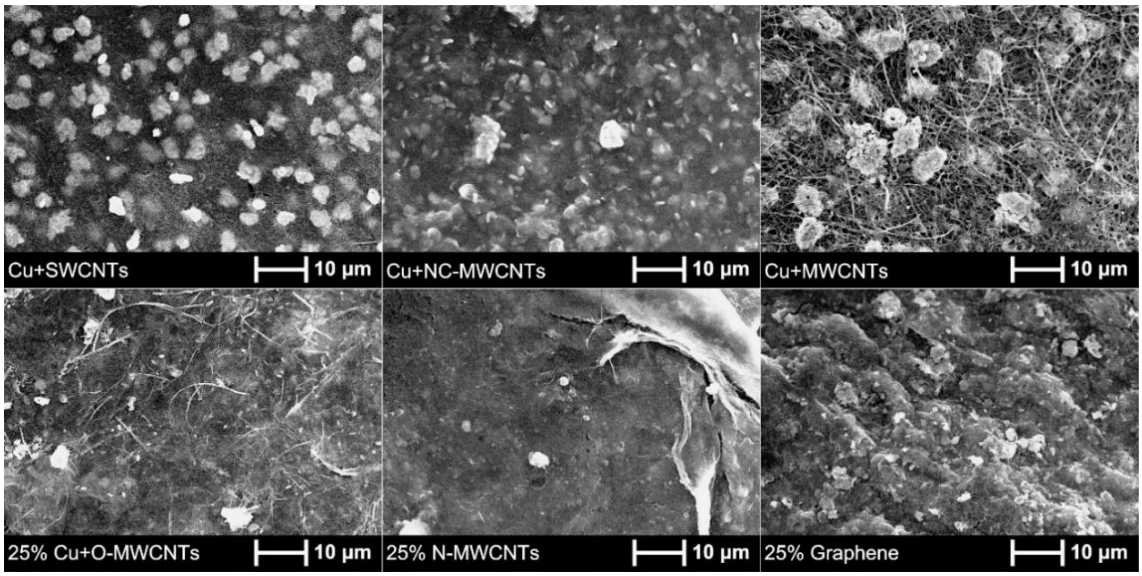

Figure 68 SEM micrographs of recovered copper deposit via electrodeposition on DFEs from nanocarbon materials. Reproduced with permission from ref. [4] © 2021 Grzegorz Stando, Pyry-Mikko Hannula, Bogumiła Kumanek, Mari Lundström, Dawid Janas. Published by Elsevier B.V.

The deposited particles' EDX mapping and spectrum analysis (Figure 69) showed that they were entirely composed of copper (>45 mass percent), with no other metallic components (Table 12). Additionally, oxygen (10 wt%) was found in the Cu-related regions, proving that these species are either partially oxidized or have oxygen-containing surface deposits. However, the absence of any other elements in the spectrum than carbon shows that, in addition to the Cu deposition being successful from a complex mixture of components, the process also exhibits selectivity when the right circumstances are applied. Findings demonstrate the suggested that the strategy for integration of Cu and nanocarbon selectivity and the ability to produce high-quality composites from waste materials is correct. Once more, hydrophilization was a key factor, allowing the improvement of the electrochemical properties using DFEs from nanocarbon materials. Hence, it is possible to obtain even better results by conducting thermal annealing rather than a chemical modification in the case of electrochemical applications (Figures 62, 63 and 64).

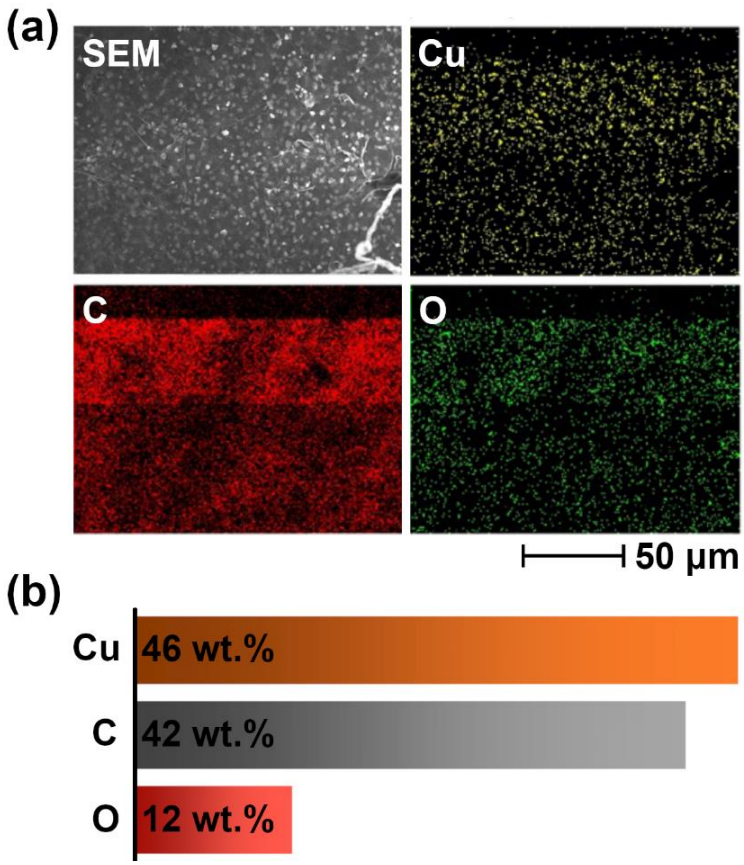

Figure 69 Cu-SWCNT composite EDX mapping in (a) and quantitative analysis in (b). Reproduced with permission from ref. [4] © 2021 Grzegorz Stando, Pyry-Mikko Hannula, Bogumiła Kumanek, Mari Lundström, Dawid Janas. Published by Elsevier B.V.

Table 12 Composition of used wastewaters for recovery copper via electrodeposition Reproduced with permission from ref. [4] © 2021 Grzegorz Stando, Pyry-Mikko Hannula, Bogumiła Kumanek, Mari Lundström, Dawid Janas. Published by Elsevier B.V.

Solution	Mg [mg/L]	Al [mg/L]	Fe [mg/L]	Ni [ppm]	Cu [ppm]	Zn [ppm]	As [ppm]	Sb [ppm]	Pb [ppm]
Synthetic solution	-	-	-	-	40.0×10^6	-	-	-	-
Industrial process wastewater	6600	1400	12500	13	428	100	52	-	4.5

5. Conclusions and outlook

Under specific conditions, i.e., in the absence of hydrocarbons, carbon nanostructures exhibit a strongly hydrophilic character. The small molecular aromatic hydrocarbons with alkyl groups greatly increase their hydrophobicity. The mechanism of this phenomenon seems to be as follows: polar nanocarbon surface adsorbs water from the air, which is then gradually replaced by methyl-benzene derivatives. Next, higher molecular weight might remove low-molecular aromatic C_xH_y and more polar aromatics compounds like pyrene. It could explain the decrease of the WCA in time for SLG/Cu and HOPG after achieving the maximum WCA value in the first minutes of the process. As a result, the WCA value of these materials highly depends on air composition and will evolve in time due to environmental factors. The π-π stacking interactions stabilize the connection between nanocarbon material and hydrocarbon, impeding integration with other materials like metals or polymers. The results of the thesis show that by removing the surface impurities, the connection between nanocarbon and hydrophilic materials may be enhanced. Therefore, the most popular method for hydrophilization of nanocarbon material – destructive chemical functionalization- appears unnecessary for all cases. Such processing causing the insertion of hydrophilic groups creates many defects in carbon nanostructures, which reduces its properties, for example, electrical conductivity. The composites manufactured from highly-functionalized carbon nanostructures have much worse electrical and mechanical properties than composites based on annealed non-functionalized nanocarbon materials.

This strategy allowed the creation of high-performance composites with polymers and metals. Furthermore, DFEs made from SWCNTs after annealing selectively recovered copper from industrial wastewater, wherein copper concentration was negligible in contrast to other metal ions. Moreover, other promising potential applications of synthesized composites were presented: as thermoelectric generators and supercapacitors. Future works should focus on investigating the phenomenon's application to real-life applications and finding new ways of surface purification. It gives new opportunities to create new generations of high-performance composites, free from the burden of destructive functionalization, which might be vital to achieving ambitious goals of the circle economy to establish groundbreaking green technologies.

The results of these scientific works should significantly impact two fields of science: chemistry and materials science, but it is hard to define directly how. In 2013, groups of Prof.

Liu and Lei from the University of Pittsburgh presented to the world how strong hydrophilic can be graphene and graphite, which unexpectedly started research on the effect of adsorbed airborne hydrocarbons on the wettability of 2D materials such as hexagonal MoS_2 and BN. Perhaps the same phenomenon is also valid for other 0D and 1D materials. Many factors have an impact on surface character, but contaminants are the major ones.

Moreover, it creates a question about the definition of hydrophilicity because nanocarbon material might be considered hydrophobic or hydrophilic depending on chosen criteria. As it was presented, nanocarbon materials create very stable connections with hydrocarbons. In nearly all applications, these two components are present together, so should they be considered one material in terms of wettability? As water is first adsorbed onto the nanocarbon surface (further replaced by hydrocarbons), is the surface hydrophilic, lipophilic, or maybe amphiphilic? If we use an ideal model, where it is only water, pure air and nanocarbon surface, the WCA value would be so low that the material could be defined as hydrophilic. However, it is nearly impossible to achieve such a condition in real life. To sum up, new models and ways of thinking must be developed to better understand the gained knowledge during the last years and upgrade the surface character definition for the benefit of researchers.

6. Bibliography

[1] D. Janas, G. Stando, Unexpectedly strong hydrophilic character of free-standing thin films from carbon nanotubes, Sci. Rep. 7 (2017). doi:10.1038/s41598-017-12443-y.

[2] G. Stando, D. Łukawski, F. Lisiecki, D. Janas, Intrinsic hydrophilic character of carbon nanotube networks, Appl. Surf. Sci. 463 (2019) 227–233. doi:10.1016/j.apsusc.2018.08.206.

[3] G. Stando, S. Han, B. Kumanek, D. Łukowiec, D. Janas, Tuning wettability and electrical conductivity of single-walled carbon nanotubes by the modified Hummers method, Sci. Rep. 12 (2022) 1–13. doi:10.1038/s41598-022-08343-5.

[4] G. Stando, P.-M. Hannula, B. Kumanek, M. Lundström, D. Janas, Copper recovery from industrial wastewater - Synergistic electrodeposition onto nanocarbon materials, Water Resour. Ind. 26 (2021) 100156. doi:10.1016/J.WRI.2021.100156.

[5] F. Yang, G. Stando, A. Thompson, D. Gundurao, L. Li, H. Liu, Effect of Environmental Contaminants on the Interfacial Properties of Two-Dimensional Materials, Accounts Mater. Res. 3 (2022) 1022–1032. doi:10.1021/accountsmr.2c00114.

[6] G. Stando, P. Stando, M. Sahlman, M. Lundstrom, H. Liu, D. Janas, Synthesis of nanocomposites via electropolymerization of aniline onto hydrophilic films from nanocarbon and investigation of their properties, Electrochim. Acta. 463 (2023) 142842. doi:10.1016/j.electacta.2023.142842.

[7] C. Toumey, Plenty of room, plenty of history, Nat. Nanotechnol. 4 (2009) 783–784. doi:10.1038/nnano.2009.357.

[8] D. Chenthamara, S. Subramaniam, S.G. Ramakrishnan, S. Krishnaswamy, M.M. Essa, F.H. Lin, M.W. Qoronfleh, Therapeutic efficacy of nanoparticles and routes of administration, Biomater. Res. 23 (2019) 1–29. doi:10.1186/s40824-019-0166-x.

[9] D. Guo, G. Xie, J. Luo, Mechanical properties of nanoparticles: Basics and applications, J. Phys. D. Appl. Phys. 47 (2014) 013001. doi:10.1088/0022-3727/47/1/013001.

[10] B. Kumanek, D. Janas, Thermal conductivity of carbon nanotube networks: a review, J. Mater. Sci. 54 (2019) 7397–7427. doi:10.1007/s10853-019-03368-0.

[11] K.L. Kelly, E. Coronado, L.L. Zhao, G.C. Schatz, The optical properties of metal

nanoparticles: The influence of size, shape, and dielectric environment, J. Phys. Chem. B. 107 (2003) 668–677. doi:10.1021/jp026731y.

[12] H.W. Kroto, J.R. Heath, S.C. O'Brien, R.F. Curl, R.E. Smalley, C60: Buckminsterfullerene, Nature. 318 (1985) 162–163. doi:10.1038/318162a0.

[13] S. Iijima, Helical microtubules of graphitic carbon, Nature. 354 (1991) 56–58. doi:10.1038/354056a0.

[14] V.M. Radushkevich, L.V. Lukyanovich, he Structure of Carbon Forming in Thermal Decomposition of Carbon Monoxide on an Iron Catalyst, Russ. J. Phys. Chem. 26 (1952) 88–95.

[15] K.S. Novoselov, A.K. Geim, S. V Morozov, D. Jiang, Y. Zhang, S. V Dubonos, I. V Grigorieva, A.A. Firsov, Electric field effect in atomically thin carbon films., Science. 306 (2004) 666–9. doi:10.1126/science.1102896.

[16] D. Roy, M. Chhowalla, H. Wang, N. Sano, I. Alexandrou, T.W. Clyne, G.A.J. Amaratunga, Characterisation of carbon nano-onions using Raman spectroscopy, Chem. Phys. Lett. 373 (2003) 52–56. doi:10.1016/S0009-2614(03)00523-2.

[17] S.Y. Lim, W. Shen, Z. Gao, Carbon quantum dots and their applications, Chem. Soc. Rev. 44 (2015) 362–381. doi:10.1039/c4cs00269e.

[18] K. Turcheniuk, V.N. Mochalin, Biomedical applications of nanodiamond (Review), Nanotechnology. 28 (2017) 252001.

[19] S. Furmaniak, P.A. Gauden, A. Patrykiejew, R. Mi, P. Kowalczyk, Carbon Nanohorns as Reaction Nanochambers – a Systematic Monte Carlo Study, Sci. Rep. (2018) 1–9. doi:10.1038/s41598-018-33725-z.

[20] J. Ren, F. Li, J. Lau, S. Licht, One-Pot Synthesis of Carbon Nanofibers from CO2, Nano Lett. 15 (2015) 6142–6148. doi:10.1021/acs.nanolett.5b02427.

[21] J.N. Coleman, U. Khan, W.J. Blau, Y.K. Gun'ko, Small but strong: A review of the mechanical properties of carbon nanotube-polymer composites, Carbon N. Y. 44 (2006) 1624–1652. doi:10.1016/j.carbon.2006.02.038.

[22] F. Mansoori Mosleh, Y. Mortazavi, N. Hosseinpour, A.A. Khodadadi, Asphaltene Adsorption onto Carbonaceous Nanostructures, Energy and Fuels. 34 (2020) 211–224.

doi:10.1021/acs.energyfuels.9b03466.

[23] S. Pei, J. Zhao, J. Du, W. Ren, H.M. Cheng, Direct reduction of graphene oxide films into highly conductive and flexible graphene films by hydrohalic acids, Carbon N. Y. 48 (2010) 4466–4474. doi:10.1016/j.carbon.2010.08.006.

[24] C. Soldano, A. Mahmood, E. Dujardin, Production, properties and potential of graphene, Carbon N. Y. 48 (2010) 2127–2150. doi:10.1016/J.CARBON.2010.01.058.

[25] B. Kumanek, D. Janas, Thermal conductivity of carbon nanotube networks: a review, J. Mater. Sci. 54 (2019) 7397–7427. doi:10.1007/s10853-019-03368-0.

[26] J. Salvetat, J. Bonard, N.H. Thomson, A.J. Kulik, L. Forr, Mechanical Properties of Carbon Nanotubes, Appl. Phys. A Mater. Sci. Process. 69 (1999) 255–260. doi:10.1007/978-3-540-36807-6.

[27] C. Lee, X. Wei, J.W. Kysar, J. Hone, Measurement of the Elastic Properties and Intrinsic Strength of Monolayer Graphene, 321 (2008) 385–389.

[28] F. Cesano, M.J. Uddin, K. Lozano, M. Zanetti, D. Scarano, All-Carbon Conductors for Electronic and Electrical Wiring Applications, Front. Mater. 7 (2020). doi:10.3389/fmats.2020.00219.

[29] B. Kumanek, K. Milowska, L. Przypis, G. Stando, K. Matuszek, D. Macfarlane, M. Payne, D. Janas, Doping Engineering of Single-Walled Carbon Nanotubes by Nitrogen Compounds Using Basicity and Alignment, ACS Appl. Mater. Interfaces. 14 (n.d.) 25861–25877. doi:10.1021/acsami.2c00970.

[30] R. Graupner, J. Abraham, A. Vencelová, T. Seyller, F. Hennrich, M.M. Kappes, A. Hirsch, L. Ley, Doping of single-walled carbon nanotube bundles by Brønsted acids, Phys. Chem. Chem. Phys. 5 (2003) 5472–5476. doi:10.1039/b311016h.

[31] L. Wang, Z. Sofer, M. Pumera, Will Any Crap We Put into Graphene Increase, ACS Nano. 14 (2020) 21–25. doi:10.1021/acsnano.9b00184.

[32] S.G. Kim, G.M. Choi, H.D. Jeong, D. Lee, S. Kim, K.H. Ryu, S. Lee, J. Kim, J.Y. Hwang, N.D. Kim, D.Y. Kim, H.S. Lee, B.C. Ku, Hierarchical structure control in solution spinning for strong and multifunctional carbon nanotube fibers, Carbon N. Y. 196 (2022) 59–69. doi:10.1016/j.carbon.2022.04.040.

[33] M. Siahkouhi, G. Razaqpur, N.A. Hoult, M. Hajmohammadian, G. Jing, Utilization of carbon nanotubes (CNTs) in concrete for structural health monitoring (SHM) purposes : A review, Constr. Build. Mater. 309 (2021) 125137. doi:10.1016/j.conbuildmat.2021.125137.

[34] R. Alwafi, A. Saeed, Single - Walled Carbon Nanotubes in Nanosized Basalts as Nanocomposites : The Electrical / Dielectric Properties and Electromagnetic Interference Shielding Performance, J. Inorg. Organomet. Polym. Mater. 32 (2022) 4340–4358. doi:10.1007/s10904-022-02450-6.

[35] K.Z. Donato, H.L. Tan, V.S. Marangoni, M.V.S. Martins, P.R. Ng, M.C.F. Costa, P. Jain, S.J. Lee, G.K.W. Koon, R.K. Donato, A.H.C. Neto, Graphene oxide classification and standardization, Sci. Rep. 13 (2023) 6064. doi:10.1038/s41598-023-33350-5.

[36] Yano Research Institute Ltd., 2019, Global CNT (Carbon Nanotube) Market: Key Research Findings 2018 https://www.yanoresearch.com/en/press-release/show/press_id/2081-2019, (access 10.04.2023).

[37] Grand View Reaserch, 2015, Carbon Nanotubes Market Size, Share & Trends Analysis Report By Product (SWNT, MWNT), By Application (Polymers, Energy, Electrical & Electronics), And Segment Forecasts, 2015 - 2022 https://www.grandviewresearch.com/industry-analysis/carbon-nanotubes-cnt-market, (access 10.04.2023).

[38] Statista, 2015, Market size of carbon nanotubes worldwide from 2012 to 2022, by application (in tons) https://www.statista.com/statistics/714708/carbon-nanotube-global-market-size-by-application/, (access 10.04.2023).

[39] Market and market, 2022, Carbon Nanotubes Market https://www.marketsandmarkets.com/Market-Reports/carbon-nanotubes-139.html?gclid=CjwKCAjwue6hBhBVEiwA9YTx8BZ3HNIimKNZZcHb8PXli6ye8iF-OwiT5fqEr86TiZNDYsZiYnUEmhoCaAEQAvD_BwE, (access 10.04.2023).

[40] Graphene-info, 2017, NanoXplore plans a 10,000 ton graphene powder facility https://www.graphene-info.com/nanoxplore-plans-10000-ton-graphene-powder-facility, (access 10.04.2023).

[41] Grand View Reaserch, 2022, Graphene Market Size, Share & Trends Analysis Report By Product (Graphene Oxide, Graphene Nanoplatelets), By Application (Electronics,

Composites, Energy), By Region, And Segment Forecasts, 2023 - 2030, https://www.grandviewresearch.com/industry-analysis/graphene-industry, (access 10.04.2023).

[42] J.-F. Dai, G.-J. Wang, L. Ma, C.-K. Wu Rev, SURFACE PROPERTIES OF GRAPHENE: RELATIONSHIP TO GRAPHENE-POLYMER COMPOSITES, 2015.

[43] W. Bauhofer, J.Z. Kovacs, A review and analysis of electrical percolation in carbon nanotube polymer composites, Compos. Sci. Technol. 69 (2009) 1486–1498. doi:10.1016/j.compscitech.2008.06.018.

[44] V. Datsyuk, M. Kalyva, K. Papagelis, J. Parthenios, D. Tasis, A. Siokou, I. Kallitsis, C. Galiotis, Chemical oxidation of multiwalled carbon nanotubes, Carbon N. Y. 46 (2008) 833–840. doi:10.1016/j.carbon.2008.02.012.

[45] L. Wang, S. Feng, J. Zhao, J. Zheng, Z. Wang, L. Li, Z. Zhu, A facile method to modify carbon nanotubes with nitro/amino groups, Appl. Surf. Sci. 256 (2010) 6060–6064. doi:10.1016/J.APSUSC.2010.03.120.

[46] A. Kolanowska, P. Wasik, W. Zięba, A.P. Terzyk, Selective carboxylation: Versus layer-by-layer unsheathing of multi-walled carbon nanotubes: New insights from the reaction with boiling nitrating mixture, RSC Adv. 9 (2019) 37608–37613. doi:10.1039/c9ra08300f.

[47] N. Zhang, J. Xie, V.K. Varadan, Functionalization of carbon nanotubes by potassium permanganate assisted with phase transfer catalyst, Smart Mater. Struct. 11 (2002) 962. doi:10.1088/0964-1726/11/6/318.

[48] A. Zniszczoł, A.P. Herman, K. Szymańska, J. Mrowiec-Białoń, K.Z. Walczak, A. Jarzebski, S. Boncel, Covalently immobilized lipase on aminoalkyl-, carboxy- and hydroxy-multi-wall carbon nanotubes in the enantioselective synthesis of Solketal esters, Enzyme Microb. Technol. 87–88 (2016) 61–69. doi:10.1016/j.enzmictec.2016.02.015.

[49] Y. Peng, H. Liu, Effects of oxidation by hydrogen peroxide on the structures of multiwalled carbon nanotubes, Ind. Eng. Chem. Res. 45 (2006) 6483–6488. doi:10.1021/ie0604627.

[50] D. Janas, S. Boncel, A.A. Marek, K.K. Koziol, A facile method to tune electronic properties of carbon nanotube films, Mater. Lett. 106 (2013) 137–140.

doi:10.1016/J.MATLET.2013.04.111.

[51] I.D. Rosca, F. Watari, M. Uo, T. Akasaka, Oxidation of multiwalled carbon nanotubes by nitric acid, Carbon N. Y. 43 (2005) 3124–3131. doi:10.1016/j.carbon.2005.06.019.

[52] H. Kitamura, M. Sekido, H. Takeuchi, M. Ohno, The method for surface functionalization of single-walled carbon nanotubes with fuming nitric acid, Carbon N. Y. 49 (2011) 3851–3856. doi:10.1016/j.carbon.2011.05.020.

[53] K.A. Wepasnick, B.A. Smith, K.E. Schrote, H.K. Wilson, S.R. Diegelmann, D.H. Fairbrother, Surface and structural characterization of multi-walled carbon nanotubes following different oxidative treatments, Carbon N. Y. 49 (2011) 24–36. doi:10.1016/j.carbon.2010.08.034.

[54] I. Gerber, M. Oubenali, R. Bacsa, J. Durand, A. Gonçalves, M.F.R. Pereira, F. Jolibois, L. Perrin, R. Poteau, P. Serp, Theoretical and Experimental Studies on the Carbon-Nanotube Surface Oxidation by Nitric Acid: Interplay between Functionalization and Vacancy Enlargement, Chem. - A Eur. J. 17 (2011) 11467–11477. doi:10.1002/chem.201101438.

[55] N.F. Andrade, D.S.T. Martinez, A.J. Paula, J. V. Silveira, O.L. Alves, A.G. Souza Filho, Temperature effects on the nitric acid oxidation of industrial grade multiwalled carbon nanotubes, J. Nanoparticle Res. 15 (2013) 1–11. doi:10.1007/s11051-013-1761-8.

[56] Y.C. Chiang, W.H. Lin, Y.C. Chang, The influence of treatment duration on multi-walled carbon nanotubes functionalized by H2SO4/HNO3 oxidation, Appl. Surf. Sci. 257 (2011) 2401–2410. doi:10.1016/j.apsusc.2010.09.110.

[57] N. Yao, V. Lordi, S.X.C. Ma, E. Dujardin, A. Krishnan, M.M.J. Treacy, T.W. Ebbesen, Structure and oxidation patterns of carbon nanotubes, J. Mater. Res. 13 (1998) 2432–2437. doi:10.1557/JMR.1998.0338.

[58] G.A. Forrest, A.J. Alexander, A model for the dependence of carbon nanotube length on acid oxidation time, J. Phys. Chem. C. 111 (2007) 10792–10798. doi:10.1021/jp0716839.

[59] D. V. Kosynkin, A.L. Higginbotham, A. Sinitskii, J.R. Lomeda, A. Dimiev, B.K. Price, J.M. Tour, Longitudinal unzipping of carbon nanotubes to form graphene nanoribbons, Nature. 458 (2009) 872–876. doi:10.1038/nature07872.

[60] C.I. Chang, K.H. Chang, H.H. Shen, C.C. Hu, A unique two-step Hummers method for fabricating low-defect graphene oxide nanoribbons through exfoliating multiwalled carbon nanotubes, J. Taiwan Inst. Chem. Eng. 45 (2014) 2762–2769. doi:10.1016/j.jtice.2014.05.030.

[61] K.H. Wu, D.W. Wang, I.R. Gentle, Revisiting oxygen reduction reaction on oxidized and unzipped carbon nanotubes, Carbon N. Y. 81 (2015) 295–304. doi:10.1016/j.carbon.2014.09.060.

[62] A.M. Dimiev, A. Khannanov, I. Vakhitov, A. Kiiamov, K. Shukhina, J.M. Tour, Revisiting the Mechanism of Oxidative Unzipping of Multiwall Carbon Nanotubes to Graphene Nanoribbons, ACS Nano. 12 (2018) 3985–3993. doi:10.1021/acsnano.8b01617.

[63] F. Cataldo, G. Compagnini, G. Patané, O. Ursini, G. Angelini, P.R. Ribic, G. Margaritondo, A. Cricenti, G. Palleschi, F. Valentini, Graphene nanoribbons produced by the oxidative unzipping of single-wall carbon nanotubes, Carbon N. Y. 48 (2010) 2596–2602. doi:10.1016/j.carbon.2010.03.063.

[64] B.M. Maciejewska, M. Jasiurkowska-Delaporte, A.I. Vasylenko, K.K. Kozioł, S. Jurga, Experimental and theoretical studies on the mechanism for chemical oxidation of multiwalled carbon nanotubes, RSC Adv. 4 (2014) 28826–28831. doi:10.1039/c4ra03881a.

[65] N.L. Rangel, J.C. Sotelo, J.M. Seminario, Mechanism of carbon nanotubes unzipping into graphene ribbons, J. Chem. Phys. 131 (2009) 031105. doi:10.1063/1.3170926.

[66] B.B. Parekh, G. Fanchini, G. Eda, M. Chhowalla, Improved conductivity of transparent single-wall carbon nanotube thin films via stable postdeposition functionalization, Appl. Phys. Lett. 90 (2007). doi:10.1063/1.2715027.

[67] H.Z. Geng, K.K. Ki, P.S. Kang, S.L. Young, Y. Chang, H.L. Young, Effect of acid treatment on carbon nanotube-based flexible transparent conducting films, J. Am. Chem. Soc. 129 (2007) 7758–7759. doi:10.1021/ja0722224.

[68] W.S. Hummers, R.E. Offeman, Preparation of Graphitic Oxide, J. Am. Chem. Soc. 80 (1958) 1339–1339. doi:10.1021/ja01539a017.

[69] U. Von Hofmann, E. König, Untersuchungen uber Graphitoxyd, Zeitschrift Für Anorg.

Und Allg. Chemie. 234 (1937) 311–326.

[70] B.C. Brodie, On the Atomic Weight o f Graphite, R. Soc. 149 (1859) 249–259.

[71] L. Staudenmaier, Verfahren zur Darstellung der Graphitslure., Berichte Der Dtsch. Chem. Gesellschaft. 31 (1898) 1481–1487.

[72] M. Pedrosa, E.S. Da, L.M. Pastrana-martínez, G. Drazic, P. Falaras, J.L. Faria, J.L. Figueiredo, A.M.T. Silva, Hummers ' and Brodie ' s graphene oxides as photocatalysts for phenol degradation, J. Colloid Interface Sci. 567 (2020) 243–255. doi:10.1016/j.jcis.2020.01.093.

[73] H.L. Poh, F. Sanek, A. Ambrosi, G. Zhao, Z. Sofer, M. Pumera, Graphenes prepared by Staudenmaier , Hofmann and Hummers methods with consequent thermal exfoliation exhibit very different electrochemical, Nanoscale. 4 (2012) 3515–3522. doi:10.1039/c2nr30490b.

[74] S. Pei, H.-M. Cheng, The reduction of graphene oxide, Carbon N. Y. 50 (2012) 3210–3228. doi:10.1016/J.CARBON.2011.11.010.

[75] R. Jakhar, J.E. Yap, R. Joshi, Microwave reduction of graphene oxide, Carbon N. Y. 170 (2020) 277–293. doi:10.1016/j.carbon.2020.08.034.

[76] Z. Sofer, O. Jankovský, P. Šimek, L. Soferová, D. Sedmidubský, M. Pumera, Highly hydrogenated graphene via active hydrogen reduction of graphene oxide in the aqueous phase at room temperature, Nanoscale. 6 (2014) 2153–2160. doi:10.1039/c3nr05407a.

[77] M.J. Fernández-Merino, L. Guardia, J.I. Paredes, S. Villar-Rodil, P. Solís-Fernández, A. Martínez-Alonso, J.M.D. Tascón, Vitamin C is an ideal substitute for hydrazine in the reduction of graphene oxide suspensions, J. Phys. Chem. C. 114 (2010) 6426–6432. doi:10.1021/jp100603h.

[78] C.K. Chua, M. Pumera, The reduction of graphene oxide with hydrazine: elucidating its reductive capability based on a reaction-model approach, Chem. Commun. 52 (2016) 72–75. doi:10.1039/c5cc08170j.

[79] S. Grimm, M. Schweiger, S. Eigler, J. Zaumseil, High-Quality Reduced Graphene Oxide by CVD-Assisted Annealing, J. Phys. Chem. C. 120 (2016) 3036–3041. doi:10.1021/acs.jpcc.5b11598.

[80] X. Li, H. Qiu, X. Liu, J. Yin, W. Guo, Wettability of Supported Monolayer Hexagonal Boron Nitride in Air, Adv. Funct. Mater. 27 (2017). doi:10.1002/adfm.201603181.

[81] M. Salim, J. Hurst, M. Montgomery, N. Tolman, H. Liu, Airborne contamination of graphite as analyzed by ultra-violet photoelectron spectroscopy, J. Electron Spectros. Relat. Phenomena. 235 (2019) 8–15. doi:10.1016/j.elspec.2019.06.001.

[82] F. Perrozzi, S. Croce, E. Treossi, V. Palermo, S. Santucci, G. Fioravanti, L. Ottaviano, Reduction dependent wetting properties of graphene oxide, Carbon N. Y. 77 (2014) 473–480. doi:10.1016/j.carbon.2014.05.052.

[83] K.Y. Law, Definitions for hydrophilicity, hydrophobicity, and superhydrophobicity: Getting the basics right, J. Phys. Chem. Lett. 5 (2014) 686–688. doi:10.1021/jz402762h.

[84] K.Y. Law, Contact Angle Hysteresis on Smooth/Flat and Rough Surfaces. Interpretation, Mechanism, and Origin, Accounts Mater. Res. 3 (2022) 1–7. doi:10.1021/accountsmr.1c00051.

[85] I. Kopova, L. Bacakova, V. Lavrentiev, J. Vacik, Growth and potential damage of human bone-derived cells on fresh and aged fullerene C60 films, Int. J. Mol. Sci. 14 (2013) 9182–9204. doi:10.3390/ijms14059182.

[86] H. Liu, J. Zhai, L. Jiang, Wetting and anti-wetting on aligned carbon nanotube films, Soft Matter. 2 (2006) 811–821. doi:10.1039/b606654b.

[87] A. Kozbial, Z. Li, J. Sun, X. Gong, F. Zhou, Y. Wang, H. Xu, H. Liu, L. Li, Understanding the intrinsic water wettability of graphite, Carbon N. Y. 74 (2014) 218–225. doi:10.1016/J.CARBON.2014.03.025.

[88] Z. Li, Y. Wang, A. Kozbial, G. Shenoy, F. Zhou, R. McGinley, P. Ireland, B. Morganstein, A. Kunkel, S.P. Surwade, L. Li, H. Liu, Effect of airborne contaminants on the wettability of supported graphene and graphite, Nat. Mater. 12 (2013) 925–931. doi:10.1038/nmat3709.

[89] H. Liu, L. Li, Graphitic materials: Intrinsic hydrophilicity and its implications, Extrem. Mech. Lett. 14 (2017) 44–50. doi:10.1016/j.eml.2017.01.010.

[90] A. Kozbial, X. Gong, H. Liu, L. Li, Understanding the Intrinsic Water Wettability of Molybdenum Disulfide (MoS2), Langmuir. 31 (2015) 8429–8435. doi:10.1021/acs.langmuir.5b02057.

[91] L.A. Belyaeva, G.F. Schneider, Wettability of graphene, Surf. Sci. Rep. (2020). doi:10.1016/j.surfrep.2020.100482.

[92] A.W. Blacha, K.Z. Milowska, M.C. Payne, H.F. Greer, A.P. Terzyk, E. Korczeniewski, A. Cyganiuk, S. Boncel, The Origin of Amphipathic Nature of Short and Thin Pristine Carbon Nanotubes—Fully Recyclable 1D Water-in-Oil Emulsion Stabilizers, Adv. Mater. Interfaces. 10 (2023). doi:10.1002/admi.202202407.

[93] A.W. Kuziel, K.Z. Milowska, P. Chau, S. Boncel, K.K. Koziol, N. Yahya, M.C. Payne, The True Amphipathic Nature of Graphene Flakes : A Versatile 2D Stabilizer, Adv. Mater. 2000608 (2020) 1–7. doi:10.1002/adma.202000608.

[94] P. Topolovsek, F. Lamberti, T. Gatti, A. Cito, J.M. Ball, E. Menna, C. Gadermaier, A. Petrozza, Functionalization of transparent conductive oxide electrode for TiO2-free perovskite solar cells, J. Mater. Chem. A. 5 (2017) 11882–11893. doi:10.1039/c7ta02405c.

[95] A.H. Barber, S.R. Cohen, H. Daniel Wagner, Static and dynamic wetting measurements of single carbon nanotubes, Phys. Rev. Lett. 92 (2004) 5–8. doi:10.1103/PhysRevLett.92.186103.

[96] K.K.S. Lau, J. Bico, K.B.K. Teo, M. Chhowalla, G.A.J. Amaratunga, W.I. Milne, G.H. McKinley, K.K. Gleason, Superhydrophobic Carbon Nanotube Forests, Nano Lett. 3 (2003) 1701–1705. doi:10.1021/nl034704t.

[97] F. De Nicola, P. Castrucci, M. Scarselli, F. Nanni, I. Cacciotti, M. De Crescenzi, Exploiting the hierarchical morphology of single-walled and multi-walled carbon nanotube films for highly hydrophobic coatings, Beilstein J. Nanotechnol. 6 (2015) 353–360. doi:10.3762/bjnano.6.34.

[98] Z. Zhou, T. Gao, S. McCarthy, A. Kozbial, S. Tan, D. Pekker, L. Li, P.W. Leu, Parahydrophobicity and stick-slip wetting dynamics of vertically aligned carbon nanotube forests, Carbon N. Y. 152 (2019) 474–481. doi:10.1016/J.CARBON.2019.06.012.

[99] L.A. Belyaeva, P.M.G. van Deursen, K.I. Barbetsea, G.F. Schneider, Hydrophilicity of Graphene in Water through Transparency to Polar and Dispersive Interactions, Adv. Mater. 30 (2018) 1703274. doi:10.1002/adma.201703274.

[100] G. Hong, Y. Han, T.M. Schutzius, Y. Wang, Y. Pan, M. Hu, J. Jie, C.S. Sharma, U. Mü, D. Poulikakos, On the Mechanism of Hydrophilicity of Graphene, (2016). doi:10.1021/acs.nanolett.6b01594.

[101] J. Rafiee, X. Mi, H. Gullapalli, A. V. Thomas, F. Yavari, Y. Shi, P.M. Ajayan, N.A. Koratkar, Wetting transparency of graphene, Nat. Mater. 11 (2012) 217–222. doi:10.1038/nmat3228.

[102] Z. Li, Y. Wang, A. Kozbial, G. Shenoy, F. Zhou, R. McGinley, P. Ireland, B. Morganstein, A. Kunkel, S.P. Surwade, L. Li, H. Liu, Effect of airborne contaminants on the wettability of supported graphene and graphite, Nat. Mater. 12 (2013) 925–931. doi:10.1038/nmat3709.

[103] A. Longo, M. Palomba, G. Carotenuto, Green Solid-State Chemical Reduction of Graphene, Coatings. 10 (2020).

[104] A. V. Prydatko, L.A. Belyaeva, L. Jiang, L.M.C. Lima, G.F. Schneider, Contact angle measurement of free-standing square-millimeter single-layer graphene, Nat. Commun. 9 (2018) 1–7. doi:10.1038/s41467-018-06608-0.

[105] H. Zhu, H. Wang, S. Jing, Y. Wang, T. Cheng, S. Tao, S. Lou, L. Qiao, L. Li, J. Chen, Characteristics and sources of atmospheric volatile organic compounds (VOCs) along the mid-lower Yangtze River in China, Atmos. Environ. 190 (2018) 232–240. doi:10.1016/j.atmosenv.2018.07.026.

[106] Y.M. Kim, S. Harrad, R.M. Harrison, Concentrations and sources of VOCs in urban domestic and public microenvironments, Environ. Sci. Technol. 35 (2001) 997–1004. doi:10.1021/es000192y.

[107] X. Lyu, H. Guo, Y. Wang, F. Zhang, K. Nie, J. Dang, Z. Liang, S. Dong, Y. Zeren, B. Zhou, W. Gao, S. Zhao, G. Zhang, Hazardous volatile organic compounds in ambient air of China, Chemosphere. 246 (2020) 125731. doi:10.1016/j.chemosphere.2019.125731.

[108] Z. Zhang, X. Wang, Y. Zhang, S. Lü, Z. Huang, X. Huang, Y. Wang, Ambient air benzene at background sites in China's most developed coastal regions: Exposure levels, source implications and health risks, Sci. Total Environ. 511 (2015) 792–800. doi:10.1016/j.scitotenv.2015.01.003.

[109] R.L. Cordell, R. Panchal, E. Bernard, M. Gatari, E. Waiguru, M. Ng'ang'a, J. Nyang'aya,

M. Ogot, M.J. Wilde, K.P. Wyche, A.A. Abayomi, R. Alani, P.S. Monks, J.D. Vande Hey, Volatile organic compound composition of urban air in nairobi, kenya and lagos, nigeria, Atmosphere (Basel). 12 (2021) 1–26. doi:10.3390/atmos12101329.

[110] H. Zhang, C. Chen, W. Yan, N. Wu, Y. Bo, Q. Zhang, K. He, Characteristics and sources of non-methane VOCs and their roles in SOA formation during autumn in a central Chinese city, Sci. Total Environ. 782 (2021). doi:10.1016/j.scitotenv.2021.146802.

[111] E.C. Alexopoulos, C. Chatzis, A. Linos, An analysis of factors that influence personal exposure to toluene and xylene in residents of Athens, Greece, BMC Public Health. 6 (2006) 1–9. doi:10.1186/1471-2458-6-50.

[112] C. Jia, X. Fu, B. Chauhan, Z. Xue, R.J. Kedia, C.S. Mishra, Exposure to volatile organic compounds (VOCs) at gas stations: a probabilistic analysis, Air Qual. Atmos. Heal. 15 (2022) 465–477. doi:10.1007/s11869-021-01124-5.

[113] A. Kozbial, Z. Li, J. Sun, X. Gong, F. Zhou, Y. Wang, H. Xu, H. Liu, L. Li, Understanding the intrinsic water wettability of graphite, Carbon N. Y. 74 (2014) 218–225. doi:10.1016/j.carbon.2014.03.025.

[114] X. Gong, A. Kozbial, L. Li, What causes extended layering of ionic liquids on the mica surface?, Chem. Sci. 6 (2015) 3478–3482. doi:10.1039/c5sc00832h.

[115] J.M. Hurst, L. Li, H. Liu, Adventitious hydrocarbons and the graphite-water interface, Carbon N. Y. 134 (2018) 464–469. doi:10.1016/j.carbon.2018.04.020.

[116] A. Kozbial, F. Zhou, Z. Li, H. Liu, L. Li, Are Graphitic Surfaces Hydrophobic?, Acc. Chem. Res. 49 (2016) 2765–2773. doi:10.1021/acs.accounts.6b00447.

[117] A. Kozbial, Z. Li, C. Conaway, R. McGinley, S. Dhingra, V. Vahdat, F. Zhou, B. Durso, H. Liu, L. Li, Study on the surface energy of graphene by contact angle measurements, Langmuir. 30 (2014) 8598–8606. doi:10.1021/la5018328.

[118] Z. Li, A. Kozbial, N. Nioradze, D. Parobek, G.J. Shenoy, M. Salim, S. Amemiya, L. Li, H. Liu, Water protects graphitic surface from airborne hydrocarbon contamination, ACS Nano. 10 (2016) 349–359. doi:10.1021/acsnano.5b04843.

[119] A. Veligura, P.J. Zomer, I.J. Vera-Marun, C. Józsa, P.I. Gordiichuk, B.J. Van Wees, Relating hysteresis and electrochemistry in graphene field effect transistors, J. Appl. Phys. 110 (2011). doi:10.1063/1.3665196.

[120] A. Ashraf, Y. Wu, M.C. Wang, K. Yong, T. Sun, Y. Jing, R.T. Haasch, N.R. Aluru, S. Nam, Doping-induced tunable wettability and adhesion of graphene, Nano Lett. 16 (2016) 4708–4712. doi:10.1021/acs.nanolett.6b02228.

[121] Y. Wang, C.J. Hansen, C.C. Wu, E.J. Robinette, A.M. Peterson, Effect of surface wettability on the interfacial adhesion of a thermosetting elastomer on glass, RSC Adv. 11 (2021) 31142–31151. doi:10.1039/d1ra05916e.

[122] M. Malaki, A.F. Tehrani, B. Niroumand, M. Gupta, Wettability in metal matrix composites, Metals (Basel). 11 (2021) 1–24. doi:10.3390/met11071034.

[123] J. Rafiee, X. Mi, H. Gullapalli, A. V. Thomas, F. Yavari, Y. Shi, P.M. Ajayan, N.A. Koratkar, Wetting transparency of graphene, Nat. Mater. 11 (2012) 217–222. doi:10.1038/nmat3228.

[124] L. Makkonen, Young's equation revisited, J. Phys. Condens. Matter. 28 (2016). doi:10.1088/0953-8984/28/13/135001.

[125] R. N. Wenzel, RESISTANCE OF SOLID SURFACES TO WETTING BY WATER, Ind. & Eng. Chem. 28 (1936) 988–994. doi:10.1021/ie50320a024.

[126] A.B.D. Cassie, S. Baxter, Wettability of porous surfaces, Trans. Faraday Soc. 40 (1944) 546–551. doi:10.1039/tf9444000546.

[127] D. Murakami, H. Jinnai, A. Takahara, Wetting transition from the cassie-baxter state to the wenzel state on textured polymer surfaces, Langmuir. 30 (2014) 2061–2067. doi:10.1021/la4049067.

[128] A.W. Neumann, R.J. Good, C.J. Hope, M. Sejpal, An equation-of-state approach to determine surface tensions of low-energy solids from contact angles, J. Colloid Interface Sci. 49 (1974) 291–304. doi:10.1016/0021-9797(74)90365-8.

[129] F.M. Fowkes, W.D. Harkins, The State of Monolayers Adsorbed at the Interface Solid-Aqueous Solution, J. Am. Chem. Soc. 62 (1940) 3377–3386. doi:10.1021/ja01869a029.

[130] D.K. Owens, R.C. Wendt, Estimation of the surface free energy of polymers, J. Appl. Polym. Sci. 13 (1969) 1741–1747. doi:10.1002/app.1969.070130815.

[131] N.M. Nurazzi, M.R.M. Asyraf, A. Khalina, N. Abdullah, C.L. Lee, H.A. Aisyah, M. Nor, F. Norrrahim, R.A. Ilyas, M.M. Harussani, M.R. Ishak, Nanotube-Reinforced Polymer

Composite : An Overview, Polymers (Basel). 13 (2021) 1047.

[132] M. Bhattacharya, Polymer nanocomposites-A comparison between carbon nanotubes, graphene, and clay as nanofillers, Materials (Basel). 9 (2016) 1–35. doi:10.3390/ma9040262.

[133] F.G. Granados-Martínez, J.J. Contreras-Navarrete, D.L. García-Ruiz, C.J. Gutiérrez-García, A. Durán-Navarro, E.E. Gama-Ortega, N. Flores-Ramírez, E. Huipe-Nava, L. García-González, M. de L. Mondragón-Sánchez, L. Domratcheva-Lvova, Carbon Nanotubes Synthesis from Four Different Organic Precursors by CVD, MRS Proc. 1817 (2016) imrc2015abs070-abs308. doi:10.1557/opl.2016.53.

[134] R. Wu, H. Yuan, C. Liu, J. Le Lan, X. Yang, Y.H. Lin, Flexible PANI/SWCNT thermoelectric films with ultrahigh electrical conductivity, RSC Adv. 8 (2018) 26011–26019. doi:10.1039/c8ra04863k.

[135] S.B. Yoon, E.H. Yoon, K.B. Kim, Electrochemical properties of leucoemeraldine, emeraldine, and pernigraniline forms of polyaniline/multi-wall carbon nanotube nanocomposites for supercapacitor applications, J. Power Sources. 196 (2011) 10791–10797. doi:10.1016/J.JPOWSOUR.2011.08.107.

[136] J. Chen, B. Liu, X. Gao, Results in Physics Thermal properties of graphene-based polymer composite materials : A molecular dynamics study, Results Phys. 16 (2020) 102974. doi:10.1016/j.rinp.2020.102974.

[137] D.G. Papageorgiou, I.A. Kinloch, R.J. Young, Mechanical properties of graphene and graphene-based nanocomposites, Prog. Mater. Sci. 90 (2017) 75–127. doi:10.1016/J.PMATSCI.2017.07.004.

[138] Q. Meng, K. Cai, Y. Du, L. Chen, Preparation and thermoelectric properties of SWCNT/PEDOT:PSS coated tellurium nanorod composite films, J. Alloys Compd. 778 (2019) 163–169. doi:10.1016/j.jallcom.2018.10.381.

[139] S.I. Voicu, V.K. Thakur, Graphene-based composite membranes for nanofiltration: performances and future perspectives, Emergent Mater. 5 (2022) 1429–1441. doi:10.1007/s42247-021-00291-6.

[140] J.L. Blackburn, A.J. Ferguson, C. Cho, J.C. Grunlan, Carbon-Nanotube-Based Thermoelectric Materials and Devices, Adv. Mater. 30 (2018) 1704386.

doi:10.1002/adma.201704386.

[141] A. Kolanowska, D. Janas, A.P. Herman, R.G. Jędrysiak, T. Giżewski, S. Boncel, From blackness to invisibility – Carbon nanotubes role in the attenuation of and shielding from radio waves for stealth technology, Carbon N. Y. 126 (2018) 31–52. doi:10.1016/j.carbon.2017.09.078.

[142] B. Che, H. Li, D. Zhou, Y. Zhang, Z. Zeng, C. Zhao, C. He, E. Liu, X. Lu, Porous polyaniline / carbon nanotube composite electrode for supercapacitors with outstanding rate capability and cyclic stability, Compos. Part B. 165 (2019) 671–678. doi:10.1016/j.compositesb.2019.02.026.

[143] S.C. Rasmussen, The Early History of Polyaniline: Discovery and Origins, An Int. J. Hist. Chem. Subst. 1 (2017) 99–109. doi:10.13128/substantia-30.

[144] P. Chulkin, M. Łapkowski, An Insight into Ionic Conductivity of Polyaniline Thin Films, Mater. 13 (2020) 2877. doi:10.3390/ma13122877.

[145] S. Bhadra, D. Khastgir, N.K. Singha, J.H. Lee, Progress in preparation, processing and applications of polyaniline, Prog. Polym. Sci. 34 (2009) 783–810. doi:https://doi.org/10.1016/j.progpolymsci.2009.04.003.

[146] H. Valentová, J. Stejskal, Mechanical properties of polyaniline, Synth. Met. 160 (2010) 832–834. doi:10.1016/j.synthmet.2010.01.007.

[147] S.N. Beesabathuni, J.G. Stockham, J.H. Kim, H.B. Lee, J.H. Chung, A.Q. Shen, Fabrication of conducting polyaniline microspheres using droplet microfluidics, RSC Adv. 3 (2013) 24423–24429. doi:10.1039/c3ra44808h.

[148] N.P.S. Chauhan, R. Ameta, R. Ameta, S.C. Ameta, Thermal and conducting behaviour of emeraldine base (EB) form of polyaniline (PANI), Indian J. Chem. Technol. 18 (2011) 118–122.

[149] Q. Qin, Y. Guo, Preparation and Characterization of Nano-Polyaniline Film on ITO Conductive Glass by Electrochemical Polymerization, J. Nanomater. 2012 (2012) 519674. doi:10.1155/2012/519674.

[150] W. Lu, Q. Luo, S. Yin, X. Wu, C.Y. Guo, Aniline-pyrrole Copolymer/SWCNT thermoelectric composites from electrochemical polymerization, Compos. Commun. 27 (2021) 1–5. doi:10.1016/j.coco.2021.100860.

[151] J.W. Kim, E.J. Siochi, J. Carpena-Núñez, K.E. Wise, J.W. Connell, Y. Lin, R.A. Wincheski, Polyaniline/carbon nanotube sheet nanocomposites: Fabrication and characterization, ACS Appl. Mater. Interfaces. 5 (2013) 8597–8606. doi:10.1021/am402077d.

[152] P.C. Ramamurthy, W.R. Harell, R.V. Gregory, B. Sadanadan, A.M. Rao, Mechanical Properties Of Polyaniline / Multi-walled Carbon Nanotube Composite Films, Mater. Res. Soc. 791 (2004) 1–6.

[153] C. Oueiny, S. Berlioz, F.X. Perrin, Carbon nanotube–polyaniline composites, Prog. Polym. Sci. 39 (2014) 707–748. doi:10.1016/J.PROGPOLYMSCI.2013.08.009.

[154] J.M. Chem, D. Antiohos, G. Folkes, P. Sherrell, S. Ashraf, G.G. Wallace, P. Aitchison, A.T. Harris, A.I. Minett, Compositional effects of PEDOT-PSS / single walled carbon nanotube films on supercapacitor device performance, (2011) 15987–15994. doi:10.1039/c1jm12986d.

[155] J. Liu, J. Sun, L. Gao, A Promising Way To Enhance the Electrochemical Behavior of Flexible Single-Walled Carbon Nanotube / Polyaniline Composite Films, J. Phys. Chem. C. 114 (2010) 19614–19620.

[156] Z. Spitalsky, D. Tasis, K. Papagelis, C. Galiotis, Progress in Polymer Science Carbon nanotube – polymer composites : Chemistry , processing , mechanical and electrical properties, Prog. Polym. Sci. 35 (2010) 357–401. doi:10.1016/j.progpolymsci.2009.09.003.

[157] V. Balaji, K. Lau, D. Hui, D. Bhattacharyya, Graphene-based materials and their composites : A review on production , applications and product limitations, Compos. Part B. 142 (2018) 200–220. doi:10.1016/j.compositesb.2018.01.013.

[158] A.M. Díez-Pascual, Chemical Functionalization of Carbon Nanotubes with Polymers: A Brief Overview, Macromol. 1 (2021) 64–83. doi:10.3390/macromol1020006.

[159] Q. Zhang, S. Huang, F. Yu, H. Fu, L. Li, G. Yan, Synthesis and Characterization of Ester Bond-Containing Polyethyleneimine Functionalized Carbon Nanotubes, IOP Conf. Ser. Mater. Sci. Eng. 472 (2019) 0–6. doi:10.1088/1757-899X/472/1/012002.

[160] G. Wang, Z. Qu, L. Liu, Q. Shi, J. Guo, Study of SMA graft modified MWNT/PVC composite materials, Mater. Sci. Eng. A. 472 (2008) 136–139.

doi:10.1016/j.msea.2007.03.017.

[161] S. Qin, D. Qin, W.T. Ford, D.E. Resasco, J.E. Herrera, Functionalization of single-walled carbon nanotubes with polystyrene via grafting to and grafting from methods, Macromolecules. 37 (2004) 752–757. doi:10.1021/ma035214q.

[162] A. Koshio, M. Yudasaka, M. Zhang, S. Iijima, A Simple Way to Chemically React Single-Wall Carbon Nanotubes with Organic Materials Using Ultrasonication, Nano Lett. 1 (2001) 361–363. doi:10.1021/nl0155431.

[163] J.L. Bahr, J.M. Tour, Highly functionalized carbon nanotubes using in situ generated diazonium compounds, Chem. Mater. 13 (2001) 3823–3824. doi:10.1021/cm0109903.

[164] D. Tasis, K. Papagelis, M. Prato, I. Kallitsis, C. Galiotis, Water-soluble carbon nanotubes by redox radical polymerization, Macromol. Rapid Commun. 28 (2007) 1553–1558. doi:10.1002/marc.200700235.

[165] A. Funck, W. Kaminsky, Polypropylene carbon nanotube composites by in situ polymerization, Compos. Sci. Technol. 67 (2007) 906–915. doi:10.1016/j.compscitech.2006.01.034.

[166] D. Janas, M. Rdest, K.K.K. Koziol, Free-standing films from chirality-controlled carbon nanotubes, Mater. Des. 121 (2017) 119–125. doi:10.1016/j.matdes.2017.02.062.

[167] B.J. Kim, S.H. Han, J.S. Park, Properties of CNTs coated by PEDOT: PSS films via spin-coating and electrophoretic deposition methods for flexible transparent electrodes, Surf. Coatings Technol. 271 (2015) 22–26. doi:10.1016/j.surfcoat.2015.01.045.

[168] Z. Xia, R. Wang, B. Qu, Q. Wu, D. Zhuo, Y. Zheng, Microwave absorbing properties of polyaniline coated Buckypaper reinforced epoxy resin composites, J. Appl. Polym. Sci. 139 (2022) 1–15. doi:10.1002/app.53154.

[169] S. Ghose, K.A. Watson, K.J. Sun, J.M. Criss, E.J. Siochi, J.W. Connell, High temperature resin/carbon nanotube composite fabrication, Compos. Sci. Technol. 66 (2006) 1995–2002. doi:10.1016/j.compscitech.2006.01.008.

[170] H. Xia, Q. Wang, K. Li, G.H. Hu, Preparation of polypropylene/carbon nanotube composite powder with a solid-state mechanochemical pulverization process, J. Appl. Polym. Sci. 93 (2004) 378–386. doi:10.1002/app.20435.

[171] A. Ikeda, K. Hayashi, T. Konishi, J.I. Kikuchi, Solubilization and debundling of purified single-walled carbon nanotubes using solubilizing agents in an aqueous solution by high-speed vibration milling technique, Chem. Commun. 4 (2004) 1334–1335. doi:10.1039/b402042a.

[172] P. Song, Z. Cao, Y. Cai, L. Zhao, Z. Fang, S. Fu, Fabrication of exfoliated graphene-based polypropylene nanocomposites with enhanced mechanical and thermal properties, Polymer (Guildf). 52 (2011) 4001–4010. doi:10.1016/j.polymer.2011.06.045.

[173] C. Bartholome, P. Miaudet, A. Derré, M. Maugey, O. Roubeau, C. Zakri, P. Poulin, Influence of surface functionalization on the thermal and electrical properties of nanotube-PVA composites, Compos. Sci. Technol. 68 (2008) 2568–2573. doi:10.1016/j.compscitech.2008.05.021.

[174] C. Tang, H.-F. Wang, X. Chen, B.-Q. Li, T.-Z. Hou, B. Zhang, Q. Zhang, M.-M. Titirici, F. Wei, Topological Defects in Metal-Free Nanocarbon for Oxygen Electrocatalysis, Adv. Mater. 28 (2016) 6845–6851. doi:10.1002/adma.201601406.

[175] A. Singh, T. Ram Prabhu, A.R. Sanjay, V. Koti, An Overview of Processing and Properties of CU/CNT Nano Composites, Mater. Today Proc. 4 (2017) 3872–3881. doi:10.1016/J.MATPR.2017.02.286.

[176] C. Subramaniam, T. Yamada, K. Kobashi, A. Sekiguchi, D.N. Futaba, M. Yumura, K. Hata, One hundred fold increase in current carrying capacity in a carbon nanotube-copper composite, Nat. Commun. 4 (2013). doi:10.1038/ncomms3202.

[177] D. Janas, B. Liszka, Copper matrix nanocomposites based on carbon nanotubes or graphene, Mater. Chem. Front. 2 (2018) 22–35. doi:10.1039/c7qm00316a.

[178] R.K. Khisamov, K.S. Nazarov, L.R. Zubairov, A.A. Nazarov, R.R. Mulyukov, I.M. Safarov, S.N. Sergeev, I.I. Musabirov, D.D. Phuong, P. V. Trinh, N. V. Luan, P.N. Minh, N.Q. Huan, Fabrication, microstructure, and microhardness of copper composites reinforced by carbon nanotubes, Phys. Solid State. 57 (2015) 1206–1212. doi:10.1134/S1063783415060177.

[179] C. Arnaud, F. Lecouturier, D. Mesguich, N. Ferreira, G. Chevallier, C. Estournès, A. Weibel, C. Laurent, High strength - High conductivity double-walled carbon nanotube - Copper composite wires, Carbon N. Y. 96 (2016) 212–215. doi:10.1016/j.carbon.2015.09.061.

[180] R. Jiang, X. Zhou, Q. Fang, Z. Liu, Copper-graphene bulk composites with homogeneous graphene dispersion and enhanced mechanical properties, Mater. Sci. Eng. A. 654 (2016) 124–130. doi:10.1016/j.msea.2015.12.039.

[181] M. Ciszewski, D. Janas, K.K. Koziol, Copper-Decorated CNTs as a Possible Electrode Material in Supercapacitors, Batteries. 5 (2019) 60. doi:10.3390/batteries5030060.

[182] W.A.D.M. Jayathilaka, A. Chinnappan, S. Ramakrishna, A review of properties influencing the conductivity of CNT/Cu composites and their applications in wearable/flexible electronics, J. Mater. Chem. C. 5 (2017) 9209–9237. doi:10.1039/C7TC02965A.

[183] B. Bajaj, H.I. Joh, S.M. Jo, G. Kaur, A. Sharma, M. Tomar, V. Gupta, S. Lee, Controllable one step copper coating on carbon nanofibers for flexible cholesterol biosensor substrates, J. Mater. Chem. B. 4 (2016) 229–236. doi:10.1039/C5TB01781E.

[184] R.M. Sundaram, A. Sekiguchi, M. Sekiya, T. Yamada, K. Hata, Copper/carbon nanotube composites: research trends and outlook, R. Soc. Open Sci. 5 (2018) 180814. doi:10.1098/rsos.180814.

[185] S.J. Yoo, S.H. Han, W.J. Kim, A combination of ball milling and high-ratio differential speed rolling for synthesizing carbon nanotube/copper composites, Carbon N. Y. 61 (2013) 487–500. doi:10.1016/j.carbon.2013.04.105.

[186] Z. Huang, Z. Zheng, S. Zhao, S. Dong, P. Luo, L. Chen, Copper matrix composites reinforced by aligned carbon nanotubes: Mechanical and tribological properties, Mater. Des. 133 (2017) 570–578. doi:10.1016/j.matdes.2016.08.021.

[187] W. Li, D. Li, Q. Fu, C. Pan, Conductive enhancement of copper/graphene composites based on high-quality graphene, RSC Adv. 5 (2015) 80428–80433. doi:10.1039/c5ra15189a.

[188] S. Zhao, Z. Zheng, Z. Huang, S. Dong, P. Luo, Z. Zhang, Y. Wang, Cu matrix composites reinforced with aligned carbon nanotubes: Mechanical, electrical and thermal properties, Mater. Sci. Eng. A. 675 (2016) 82–91. doi:10.1016/j.msea.2016.08.044.

[189] N. Nayan, A.K. Shukla, P. Chandran, S.R. Bakshi, S.V.S.N. Murty, B. Pant, P. V. Venkitakrishnan, Processing and characterization of spark plasma sintered copper/carbon nanotube composites, Mater. Sci. Eng. A. 682 (2017) 229–237.

doi:10.1016/j.msea.2016.10.114.

[190] C. Arnaud, F. Lecouturier, D. Mesguich, N. Ferreira, G. Chevallier, C. Estournès, A. Weibel, C. Laurent, High strength - High conductivity double-walled carbon nanotube - Copper composite wires, Carbon N. Y. 96 (2016) 212–215. doi:10.1016/j.carbon.2015.09.061.

[191] C. Guiderdoni, E. Pavlenko, V. Turq, A. Weibel, P. Puech, C. Estournès, A. Peigney, W. Bacsa, C. Laurent, The preparation of carbon nanotube (CNT)/copper composites and the effect of the number of CNT walls on their hardness, friction and wear properties, Carbon N. Y. 58 (2013) 185–197. doi:10.1016/j.carbon.2013.02.049.

[192] A. Saboori, M. Pavese, C. Badini, P. Fino, A Novel Approach to Enhance the Mechanical Strength and Electrical and Thermal Conductivity of Cu-GNP Nanocomposites, Metall. Mater. Trans. A Phys. Metall. Mater. Sci. 49 (2018) 333–345. doi:10.1007/s11661-017-4409-y.

[193] A.K. Shukla, N. Nayan, S.V.S.N. Murty, S.C. Sharma, P. Chandran, S.R. Bakshi, K.M. George, Processing of copper-carbon nanotube composites by vacuum hot pressing technique, Mater. Sci. Eng. A. 560 (2013) 365–371. doi:10.1016/j.msea.2012.09.080.

[194] L. Wang, Y. Cui, B. Li, S. Yang, R. Li, Z. Liu, R. Vajtai, W. Fei, High apparent strengthening efficiency for reduced graphene oxide in copper matrix composites produced by molecule-lever mixing and high-shear mixing, RSC Adv. 5 (2015) 51193–51200. doi:10.1039/c5ra04782j.

[195] K. Chu, F. Wang, X. hu Wang, D. jian Huang, Anisotropic mechanical properties of graphene/copper composites with aligned graphene, Mater. Sci. Eng. A. 713 (2018) 269–277. doi:10.1016/j.msea.2017.12.080.

[196] P. Hidalgo-Manrique, X. Lei, R. Xu, M. Zhou, I.A. Kinloch, R.J. Young, Copper/graphene composites: a review, J. Mater. Sci. 54 (2019) 12236–12289. doi:10.1007/s10853-019-03703-5.

[197] C. Subramaniam, Y. Yasuda, S. Takeya, S. Ata, A. Nishizawa, D. Futaba, T. Yamada, K. Hata, Carbon nanotube-copper exhibiting metal-like thermal conductivity and silicon-like thermal expansion for efficient cooling of electronics, Nanoscale. 6 (2014) 2669–2674. doi:10.1039/c3nr05290g.

[198] G. Song, Q. Fu, C. Pan, Copper-Graphene Composite Foils via Electro-Deposition: A Mini Review, MRS Adv. 3 (2018) 37–44. doi:10.1557/adv.2018.28.

[199] D. Grujicic, B. Pesic, Electrodeposition of copper: the nucleation mechanisms, Electrochim. Acta. 47 (2002) 2901–2912. doi:10.1016/S0013-4686(02)00161-5.

[200] S. Arai, T. Osaki, M. Hirota, M. Uejima, Fabrication of copper/single-walled carbon nanotube composite film with homogeneously dispersed nanotubes by electroless deposition, Mater. Today Commun. 7 (2016) 101–107. doi:10.1016/j.mtcomm.2016.04.009.

[201] Y. Chai, K. Zhang, M. Zhang, P.C.H. Chan, M.M.F. Yuen, Carbon nanotube/copper composites for via filling and thermal management, in: Proc. - Electron. Components Technol. Conf., 2007: pp. 1224–1229. doi:10.1109/ECTC.2007.373950.

[202] G. Otero, G. Biddau, C. Sánchez-Sánchez, R. Caillard, M.F. López, C. Rogero, F.J. Palomares, N. Cabello, M.A. Basanta, J. Ortega, J. Méndez, A.M. Echavarren, R. Pérez, B. Gómez-Lor, J.A. Martín-Gago, Fullerenes from aromatic precursors by surface-catalysed cyclodehydrogenation, Nature. 454 (2008) 865–868. doi:10.1038/nature07193.

[203] O.A. Gurova, V.E. Arhipov, V.O. Koroteev, T.Y. Guselnikova, I.P. Asanov, O. V. Sedelnikova, A. V. Okotrub, Purification of Single-Walled Carbon Nanotubes Using Acid Treatment and Magnetic Separation, Phys. Status Solidi Basic Res. 256 (2019) 1–6. doi:10.1002/pssb.201800742.

[204] D. Janas, M. Rdest, K.K.K. Koziol, Free-standing films from chirality-controlled carbon nanotubes, Mater. Des. 121 (2017) 119–125. doi:10.1016/j.matdes.2017.02.062.

[205] D.C. Marcano, D. V. Kosynkin, J.M. Berlin, A. Sinitskii, Z. Sun, A. Slesarev, L.B. Alemany, W. Lu, J.M. Tour, Improved synthesis of graphene oxide, ACS Nano. 4 (2010) 4806–4814. doi:10.1021/nn1006368.

[206] M.A. Kim, D.C. Sorescu, S. Amemiya, K.D. Jordan, H. Liu, Real-Time Modulation of Hydrogen Evolution Activity of Graphene Electrodes Using Mechanical Strain, ACS Appl. Mater. Interfaces. 14 (2022) 10691–10700. doi:10.1021/acsami.1c21821.

[207] I. Langmuir, THE ADSORPTION OF GASES ON PLANE SURFACES OF GLASS, MICA AND PLATINUM., J. Am. Chem. Soc. 40 (1918) 1361–1403.

[208] R.A. Said, Microfabrication by localized electrochemical deposition: experimental investigation and theoretical modelling, Nanotechnology. 14 (2003) 523–531. doi:10.1088/0957-4484/14/5/308.

[209] E. Chassaing, K. Vu Quang, R. Wiart, Kinetics of copper electrodeposition in citrate electrolytes, J. Appl. Electrochem. 16 (1986) 591–604. doi:10.1007/BF01006854.

[210] X. Hu, X. Lin, Z. Ling, Y. Li, X. Fu, Fabrication and Characteristics of Galvanostatic Electrodeposited MnO2 on Porous Nickel from Etched Aluminium, Electrochim. Acta. 138 (2014) 132–138. doi:https://doi.org/10.1016/j.electacta.2014.06.109.

[211] R.G. Ehl, A.J. Ihde, Faraday's electrochemical laws and the determination of equivalent weights, J. Chem. Educ. 31 (1954) 226–232. doi:10.1021/ed031p226.

[212] B. Kumanek, T. Wasiak, G. Stando, P. Stando, D. Łukowiec, D. Janas, Simple method to improve electrical conductivity of films made from single-walled carbon nanotubes, Nanomaterials. 9 (2019). doi:10.3390/nano9081113.

[213] D. Janas, G. Stando, Unexpectedly strong hydrophilic character of free-standing thin films from carbon nanotubes, Sci. Rep. 7 (2017) 12274. doi:10.1038/s41598-017-12443-y.

[214] B. Kumanek, G. Stando, P.S. Wróbel, M. Krzywiecki, D. Janas, Thermoelectric properties of composite films from multi-walled carbon nanotubes and ethyl cellulose doped with heteroatoms, Synth. Met. 257 (2019) 116190. doi:10.1016/j.synthmet.2019.116190.

[215] G. Dutra, J. Canning, W. Padden, C. Martelli, S. Dligatch, Large area optical mapping of surface contact angle, Opt. Express. 25 (2017) 21127. doi:10.1364/oe.25.021127.

[216] A.C. Ferrari, D.M. Basko, Raman spectroscopy as a versatile tool for studying the properties of graphene, Nat. Nanotechnol. 2013 84. 8 (2013) 235–246. doi:10.1038/nnano.2013.46.

[217] A.C. Ferrari, Raman spectroscopy of graphene and graphite: Disorder, electron-phonon coupling, doping and nonadiabatic effects, Solid State Commun. 143 (2007) 47–57. doi:10.1016/j.ssc.2007.03.052.

[218] N.L. Tolman, J.M. Mukai, S. Wang, A. Zito, T. Luo, H. Liu, The effect of physical adsorption on the capacitance of activated carbon electrodes, Carbon N. Y. 150 (2019)

334–339. doi:10.1016/J.CARBON.2019.05.005.

[219] G.G. Amatucci, F. Badway, A. Du Pasquier, T. Zheng, An Asymmetric Hybrid Nonaqueous Energy Storage Cell, J. Electrochem. Soc. 148 (2001) A930. doi:10.1149/1.1383553.

[220] F. Cataldo, Raman spectra of C60 fullerene photopolymers prepared in solution, Eur. Polym. J. 36 (2000) 653–656. doi:10.1016/S0014-3057(99)00083-X.

[221] K. Kobashi, Y. Iizumi, K. Hirota, N. Shinomori, K. Shimamoto, Y. Koga, T. Morimoto, T. Okazaki, Quantitative Surface Characterization of As-Grown and Acid-Treated Single-Walled Carbon Nanotubes: Implications for Functional Materials, ACS Appl. Nano Mater. 4 (2021) 5273–5284. doi:10.1021/acsanm.1c00631.

[222] N.B. Trung, T. Van Tam, H.R. Kim, S.H. Hur, E.J. Kim, W.M. Choi, Three-dimensional hollow balls of graphene–polyaniline hybrids for supercapacitor applications, Chem. Eng. J. 255 (2014) 89–96. doi:10.1016/J.CEJ.2014.06.028.

[223] D.G.F. David, M.A. Pinault-Thaury, D. Ballutaud, C. Godet, Sensitivity of photoelectron energy loss spectroscopy to surface reconstruction of microcrystalline diamond films, Appl. Surf. Sci. 273 (2013) 607–612. doi:10.1016/j.apsusc.2013.02.087.

[224] A. Hasanzadeh, A. Khataee, M. Zarei, Y. Zhang, Two-electron oxygen reduction on fullerene C60-carbon nanotubes covalent hybrid as a metal-free electrocatalyst, Sci. Rep. 9 (2019) 1–13. doi:10.1038/s41598-019-50155-7.

[225] W. Lv, L. Li, Q. Meng, X. Zhang, Molybdenum-doped CuO nanosheets on Ni foams with extraordinary specific capacitance for advanced hybrid supercapacitors, J. Mater. Sci. 55 (2020) 2492–2502. doi:10.1007/s10853-019-04129-9.

[226] C. Ammon, A. Bayer, H.P. Steinrück, G. Held, Low-temperature partial dissociation of water on Cu(1 1 0), Chem. Phys. Lett. 377 (2003) 163–169. doi:10.1016/S0009-2614(03)01127-8.

[227] T.N. Bell, E.L. Cussler, K.R. Harris, C.N. Pepela, P.J. Dunlop, An apparatus for degassing liquids by vacuum sublimation, J. Phys. Chem. 72 (1968) 4693–4695. doi:https://doi.org/10.1021/j100859a059.

[228] E. Díaz, S. Ordóñez, A. Vega, Adsorption of volatile organic compounds onto carbon nanotubes, carbon nanofibers, and high-surface-area graphites, J. Colloid Interface Sci.

305 (2007) 7–16. doi:10.1016/j.jcis.2006.09.036.

[229] P. Lazar, F. Karlický, P. Jurecka, M. Kocman, E. Otyepková, K. Šafářová, M. Otyepka, Adsorption of small organic molecules on graphene, J. Am. Chem. Soc. 135 (2013) 6372–6377. doi:10.1021/ja403162r.

[230] V. Mehmeti, M. Sadiku, A Comprehensive DFT Investigation of the Adsorption of Polycyclic Aromatic Hydrocarbons onto Graphene, Computation. 10 (2022) 1–9. doi:10.3390/computation10050068.

[231] X. Yang, J. Li, T. Wen, X. Ren, Y. Huang, X. Wang, Adsorption of naphthalene and its derivatives on magnetic graphene composites and the mechanism investigation, Colloids Surfaces A Physicochem. Eng. Asp. 422 (2013) 118–125. doi:10.1016/j.colsurfa.2012.11.063.

[232] A. Kozbial, Z. Li, C. Conaway, R. McGinley, S. Dhingra, V. Vahdat, F. Zhou, B. Durso, H. Liu, L. Li, Study on the surface energy of graphene by contact angle measurements, Langmuir. 30 (2014) 8598–8606. doi:10.1021/la5018328.

[233] A. Kozbial, C. Trouba, H. Liu, L. Li, Characterization of the intrinsic water wettability of graphite using contact angle measurements: Effect of defects on static and dynamic contact angles, Langmuir. 33 (2017) 959–967. doi:10.1021/acs.langmuir.6b04193.

[234] A. Montellano López, A. Mateo-Alonso, M. Prato, Materials chemistry of fullerene C60 derivatives, J. Mater. Chem. 21 (2011) 1305–1318. doi:10.1039/c0jm02386h.

[235] Z. Spitalsky, D. Tasis, K. Papagelis, C. Galiotis, Carbon nanotube–polymer composites: Chemistry, processing, mechanical and electrical properties, Prog. Polym. Sci. 35 (2010) 357–401. doi:10.1016/J.PROGPOLYMSCI.2009.09.003.

[236] H. Takahashi, D. Suzuoka, A. Morita, Why is benzene soluble in water? Role of OH/π interaction in solvation, J. Chem. Theory Comput. 11 (2015) 1181–1194. doi:10.1021/ct501133u.

[237] B. Kozielska, Concentration of benzene and its alkyl derivatives in Gliwice air, Arch. Waste Manag. Environ. Prot. 15 (2013) 81–88.

[238] N. Selvakumar, H.C. Barshilia, K.S. Rajam, Effect of substrate roughness on the apparent surface free energy of sputter deposited superhydrophobic polytetrafluoroethylene coatings: A comparison of experimental data with different

theoretical models, J. Appl. Phys. 108 (2010). doi:10.1063/1.3456165.

[239] S. Osswald, M. Havel, Y. Gogotsi, Monitoring oxidation of multiwalled carbon nanotubes by Raman spectroscopy, J. Raman Spectrosc. 38 (2007) 728–736. doi:10.1002/jrs.1686.

[240] I.N. Salamatov, D.A. Yatsenko, A.A. Khasin, DETERMINATION OF THE DIAMETER DISTRIBUTION FUNCTION OF SINGLE-WALL CARBON NANOTUBES BY THE X-RAY DIFFRACTION DATA, J. Struct. Chem. 60 (2019) 2089–2096. doi:10.1134/S0022476619120175.

[241] A. Merlen, J.G. Buijnsters, C. Pardanaud, A guide to and review of the use of multiwavelength Raman spectroscopy for characterizing defective aromatic carbon solids: From graphene to amorphous carbons, Coatings. 7 (2017) 153. doi:10.3390/coatings7100153.

[242] S. Reich, C. Thomsen, P. Ordejón, Phonon eigenvectors of chiral nanotubes, Phys. Rev. B. 64 (2001) 195416. doi:10.1103/PhysRevB.64.195416.

[243] V. Le Borgne, L.A. Gautier, P. Castrucci, S. Del Gobbo, M. De Crescenzi, M.A. El Khakani, Enhanced UV photoresponse of KrF-laser-synthesized single-wall carbon nanotubes/n-silicon hybrid photovoltaic devices, Nanotechnology. 23 (2012) 215206. doi:10.1088/0957-4484/23/21/215206.

[244] D. Janas, Powerful doping of chirality-sorted carbon nanotube films, Vacuum. 149 (2018) 48–52. doi:10.1016/J.VACUUM.2017.12.013.

[245] K.A. Worsley, I. Kalinina, E. Bekyarova, R.C. Haddon, Functionalization and dissolution of nitric acid treated single-walled carbon nanotubes, J. Am. Chem. Soc. 131 (2009) 18153–18158. doi:10.1021/ja906267g.

[246] A. Lekawa-Raus, L. Kurzepa, G. Kozlowski, S.C. Hopkins, M. Wozniak, D. Lukawski, B.A. Glowacki, K.K. Koziol, Influence of atmospheric water vapour on electrical performance of carbon nanotube fibres, Carbon N. Y. 87 (2015) 18–28. doi:10.1016/J.CARBON.2015.02.018.

[247] D. Janas, A.C. Vilatela, K.K.K. Koziol, Performance of carbon nanotube wires in extreme conditions, Carbon N. Y. 62 (2013) 438–446. doi:10.1016/J.CARBON.2013.06.029.

[248] J.S. Bulmer, A. Lekawa-Raus, D.G. Rickel, F.F. Balakirev, K.K. Koziol, Extreme Magneto-transport of Bulk Carbon Nanotubes in Sorted Electronic Concentrations and Aligned High Performance Fiber, Sci. Rep. 7 (2017) 1–13. doi:10.1038/s41598-017-12546-6.

[249] J.-E. Um, C.-H. Chung, D.C. Lee, P.J. Yoo, W.-J. Kim, Restoration of the genuine electronic properties of functionalized single-walled carbon nanotubes, RSC Adv. 4 (2014) 42930–42935. doi:10.1039/C4RA07171A.

[250] Y. Mishima, Y. Kimura, S. Wng Kim, Enhancement of Thermoelectric Figure of Merit through Nanostructural Control on Intermetallic Semiconductors toward High-Temperature Applications, Nanomaterials. (2006) 383–418. doi:10.1016/B978-008044964-7/50013-3.

[251] B. Pan, B. Xing, Adsorption mechanisms of organic chemicals on carbon nanotubes, Environ. Sci. Technol. 42 (2008) 9005–9013. doi:10.1021/es801777n.

[252] V. Skákalová, U. Dettlaff-Weglikowska, S. Roth, Electrical and mechanical properties of nanocomposites of single wall carbon nanotubes with PMMA, Synth. Met. 152 (2005) 349–352. doi:10.1016/j.synthmet.2005.07.291.

[253] T. Yamamoto, Y. Makino, K. Uematsu, Improved mechanical properties of PMMA composites: Dispersion, diffusion and surface adhesion of recycled carbon fiber fillers from CFRP with adsorbed particulate PMMA, Adv. Powder Technol. 28 (2017) 2774–2778. doi:10.1016/j.apt.2017.08.003.

[254] K.D. Hammond, W.C. Conner, Analysis of catalyst surface structure by physical sorption, 2013. doi:10.1016/B978-0-12-420173-6.00001-2.

[255] M. Cochet, W.K. Maser, A.M. Benito, M.A. Callejas, M.T. Martínez, J.M. Benoit, J. Schreiber, O. Chauvet, Synthesis of a new polyaniline/nanotube composite: “In-situ” polymerisation and charge transfer through site-selective interaction, Chem. Commun. 1 (2001) 1450–1451. doi:10.1039/b104009j.

[256] H. Zengin, W. Zhou, J. Jin, R. Czerw, D.W. Smith, L. Echegoyen, D.L. Carroll, S.H. Foulger, J. Ballato, Carbon nanotube doped polyaniline, Adv. Mater. 14 (2002) 1480–1483. doi:10.1002/1521-4095(20021016)14:20<1480::AID-ADMA1480>3.0.CO;2-O.

[257] W. Feng, X.D. Bai, Y.Q. Lian, J. Liang, X.G. Wang, K. Yoshino, Well-aligned

polyaniline/carbon-nanotube composite films grown by in-situ aniline polymerization, Carbon N. Y. 41 (2003) 1551–1557. doi:10.1016/S0008-6223(03)00078-2.

[258] M. Łapkowski, Electrochemical synthesis of linear polyaniline in aqueous solutions, Synth. Met. 35 (1990) 169–182. doi:10.1016/0379-6779(90)90041-I.

[259] N. V Blinova, J. Stejskal, M. Trchova, J. Prokes, Control of polyaniline conductivity and contact angles by partial protonation, Polym. Int. 57 (2007) 61–69. doi:10.1002/pi.

[260] Y. Xing, L. Li, C.C. Chusuei, R. V. Hull, Sonochemical oxidation of multiwalled carbon nanotubes, Langmuir. 21 (2005) 4185–4190. doi:10.1021/la047268e.

[261] M. Ohira, T. Sakai, M. Takeuchi, Y. Kobayashi, M. Tsuji, Raman and infrared spectra of polyaniline, Synth. Met. 18 (1987) 347–352. doi:10.1016/0379-6779(87)90903-9.

[262] F. Liu, S. Luo, D. Liu, W. Chen, Y. Huang, L. Dong, L. Wang, Facile processing of free-standing polyaniline/SWCNT film as an integrated electrode for flexible supercapacitor application, ACS Appl. Mater. Interfaces. 9 (2017) 33791–33801. doi:10.1021/acsami.7b08382.

[263] D. Ouis, A. El Kebir, I. Moulefera, L. Sabantina, B. Abdelghani, Synthesis, Characterization and Adsorption of Bisphenol A Using Novel Hybrid Materiel Produced from PANI Matrix Reinforced by Kieselguhr, J. Inorg. Organomet. Polym. Mater. 32 (2022) 1092–1102. doi:10.1007/s10904-021-02151-6.

[264] S. Civiš, A. Knížek, P.B. Rimmer, M. Ferus, P. Kubelík, M. Zukalová, L. Kavan, E. Chatzitheodoridis, Formation of methane and (Per)chlorates on mars, ACS Earth Sp. Chem. 3 (2019) 221–232. doi:10.1021/acsearthspacechem.8b00104.

[265] B. Rajagopalan, S.H. Hur, J.S. Chung, Surfactant-treated graphene covered polyaniline nanowires for supercapacitor electrode, Nanoscale Res. Lett. 10 (2015) 1–9. doi:10.1186/s11671-015-0888-1.

[266] Z. Cai, L. Li, J. Ren, L. Qiu, H. Lin, H. Peng, Flexible, weavable and efficient microsupercapacitor wires based on polyaniline composite fibers incorporated with aligned carbon nanotubes, J. Mater. Chem. A. 1 (2013) 258–261. doi:10.1039/c2ta00274d.

[267] B.C. Beard, Sodium Salts of Chlorine Oxyacid Anions, Cl(+7), Perchlorate, XPS Comparison Spectra, Surf. Sci. Spectra. 2 (1993) 97–103. doi:10.1116/1.1247738.

[268] C.S. Kam, T.L. Leung, F. Liu, A.B. Djurišić, M.H. Xie, W.K. Chan, Y. Zhou, K. Shih, Lead removal from water-dependence on the form of carbon and surface functionalization, RSC Adv. 8 (2018) 18355–18362. doi:10.1039/c8ra02264j.

[269] W.W. Focke, G.E. Wnek, Conduction mechanisms in polyaniline (emeraldine salt), J. Electroanal. Chem. Interfacial Electrochem. 256 (1988) 343–352. doi:https://doi.org/10.1016/0022-0728(88)87008-6.

[270] B. Kumanek, G. Stando, P. Stando, K. Matuszek, K.Z. Milowska, M. Krzywiecki, M. Gryglas-Borysiewicz, Z. Ogorzałek, M.C. Payne, D. MacFarlane, D. Janas, Enhancing thermoelectric properties of single-walled carbon nanotubes using halide compounds at room temperature and above, Sci. Rep. 11 (2021) 1–18. doi:10.1038/s41598-021-88079-w.

[271] A. Kolanowska, A. Kuziel, Y. Li, S. Jurczyk, S. Boncel, Rieche formylation of carbon nanotubes – one-step and versatile functionalization route, RSC Adv. 7 (2017) 51374–51381. doi:10.1039/C7RA10525H.

[272] S. Saravanan, C. Joseph Mathai, M.R. Anantharaman, S. Venkatachalam, P. V. Prabhakaran, Investigations on the electrical and structural properties of polyaniline doped with camphor sulphonic acid, J. Phys. Chem. Solids. 67 (2006) 1496–1501. doi:10.1016/J.JPCS.2006.01.100.

[273] A.D. Mulliken, M.C. Boyce, Mechanics of the rate-dependent elastic-plastic deformation of glassy polymers from low to high strain rates, Int. J. Solids Struct. 43 (2006) 1331–1356. doi:10.1016/j.ijsolstr.2005.04.016.

[274] P. Sirisinudomkit, E. Senokos, N. Rubio, M.S.P. Shaffer, Reductive processing of single walled carbon nanotubes for high volumetric performance supercapacitors, Mater. Adv. 2 (2021) 1981–1992. doi:10.1039/d0ma00898b.

[275] S. Kumagai, K. Mukaiyachi, D. Tashima, Rate and cycle performances of supercapacitors with different electrode thickness using non-aqueous electrolyte, J. Energy Storage. 3 (2015) 10–17. doi:10.1016/j.est.2015.08.002.

[276] Q. Zhu, D. Zhao, M. Cheng, J. Zhou, K.A. Owusu, L. Mai, Y. Yu, A New View of Supercapacitors: Integrated Supercapacitors, Adv. Energy Mater. 9 (2019) 1–11. doi:10.1002/aenm.201901081.

[277] C. Xia, M. Leng, W. Tao, Q. Wang, Y. Gao, Q. Zhang, Polyaniline/carbon nanotube core–shell hybrid and redox active electrolyte for high-performance flexible supercapacitor, J. Mater. Sci. Mater. Electron. 30 (2019) 4427–4436. doi:10.1007/s10854-019-00731-4.

[278] T.A. Yemata, Y. Zheng, A.K.K. Kyaw, X. Wang, J. Song, W.S. Chin, J. Xu, Modulation of the doping level of PEDOT:PSS film by treatment with hydrazine to improve the Seebeck coefficient, RSC Adv. 10 (2020) 1786–1792. doi:10.1039/c9ra07648d.

[279] J.S. Kim, W. Jang, D.H. Wang, The investigation of the seebeck effect of the poly(3,4-ethylenedioxythiophene)-tosylate with the various concentrations of an oxidant, Polymers (Basel). 11 (2019). doi:10.3390/polym11010021.

[280] C.H. Teh, R. Rasid, R. Daik, S.H. Ahmad, DGEBA-Grafted Polyaniline: Synthesis, Characterization and Thermal Properties, J. Appl. Polym. Sci. 121 (2011) 49–58. doi:https://doi.org/10.1002/app.33221.

[281] P.C. Rodrigues, G.P. De Souza, J.D. Da Motta Neto, L. Akcelrud, Thermal treatment and dynamic mechanical thermal properties of polyaniline, Polymer (Guildf). 43 (2002) 5493–5499. doi:10.1016/S0032-3861(02)00401-9.

[282] A.K. Mishra, P. Tandon, DFT study and heat capacity of polyaniline pernigraniline base, J. Phys. Chem. B. 113 (2009) 9702–9707. doi:10.1021/jp901143m.

[283] C.H. Chen, Thermal and morphological studies of chemically prepared emeraldine-base-form polyaniline powder, J. Appl. Polym. Sci. 89 (2003) 2142–2148. doi:10.1002/app.12361.

[284] L.R. de Oliveira, L. Manzato, Y.P. Mascarenhas, E.A. Sanches, The influence of heat treatment on the semi-crystalline structure of polyaniline Emeraldine-salt form, J. Mol. Struct. 1128 (2017) 707–717. doi:10.1016/j.molstruc.2016.09.044.

[285] A. Hachimi, B. Merzougui, A. Hakeem, T. Laoui, G.M. Swain, Q. Chang, M. Shao, M. Ali Atieh, Synthesis of Nitrogen-Doped Carbon Nanotubes Using Injection-Vertical Chemical Vapor Deposition: Effects of Synthesis Parameters on the Nitrogen Content, (2015). doi:10.1155/2015/453725.

[286] M. He, S. Zhou, J. Zhang, Z. Liu, C. Robinson, CVD growth of N-doped carbon nanotubes on silicon substrates and its mechanism, J. Phys. Chem. B. 109 (2005) 9275–

9279. doi:10.1021/jp044868d.

[287] R. Saito, M. Hofmann, G. Dresselhaus, A. Jorio, M.S. Dresselhaus, Raman spectroscopy of graphene and carbon nanotubes, Adv. Phys. 60 (2011) 413–550. doi:10.1080/00018732.2011.582251.

[288] V.T. Nguyen, H.D. Le, V.C. Nguyen, T.T. Tam Ngo, D.Q. Le, X.N. Nguyen, N.M. Phan, Synthesis of multi-layer graphene films on copper tape by atmospheric pressure chemical vapor deposition method, Adv. Nat. Sci. Nanosci. Nanotechnol. 4 (2013) 035012. doi:10.1088/2043-6262/4/3/035012.

[289] A. Castan, S. Forel, F. Fossard, J. Defillet, A. Ghedjatti, D. Levshov, W. Wenseleers, S. Cambré, A. Loiseau, Assessing the reliability of the Raman peak counting method for the characterization of SWCNT diameter distributions: a cross-characterization with TEM, Carbon N. Y. (2020). doi:10.1016/j.carbon.2020.09.012.

[290] A. Augustin, K. Rajendra Udupa, K. Udaya Bhat, Effect of coating current density on the wettability of electrodeposited copper thin film on aluminum substrate, Perspect. Sci. 8 (2016) 472–474. doi:10.1016/j.pisc.2016.06.003.

[291] C.-W. Liu, J.-C. Tsao, M.-S. Tsai, Y.-L. Wang, Effects of wetting ability of plating electrolyte on Cu seed layer for electroplated copper film, J. Vac. Sci. Technol. A Vacuum, Surfaces, Film. 22 (2004) 2315–2320. doi:10.1116/1.1795831.

[292] G. Stando, D. Łukawski, F. Lisiecki, D. Janas, Intrinsic hydrophilic character of carbon nanotube networks, Appl. Surf. Sci. 463 (2019). doi:10.1016/j.apsusc.2018.08.206.

[293] H. Liu, J. Zhai, L. Jiang, Wetting and anti-wetting on aligned carbon nanotube films, Soft Matter. 2 (2006) 811–821. doi:10.1039/b606654b.

[294] J. Wang, Y. Wu, Y. Cao, G. Li, Y. Liao, Influence of surface roughness on contact angle hysteresis and spreading work, Colloid Polym. Sci. 298 (2020) 1107–1112. doi:10.1007/s00396-020-04680-x.

[295] B. Kumanek, G. Stando, P.S. Wróbel, D. Janas, Impact of synthesis parameters of multi-walled carbon nanotubes on their thermoelectric properties, Materials (Basel). 12 (2019). doi:10.3390/ma12213567.

[296] P.R. Bandaru, Electrical properties and applications of carbon nanotube structures, J. Nanosci. Nanotechnol. 7 (2007) 1239–1267. doi:10.1166/jnn.2007.307.

[297] P.M. Hannula, J. Aromaa, B.P. Wilson, D. Janas, K. Koziol, O. Forsén, M. Lundström, Observations of copper deposition on functionalized carbon nanotube films, Electrochim. Acta. 232 (2017) 495–504. doi:10.1016/j.electacta.2017.03.006.

7. Supplement

Synthesis of PANI-SWCNTs composites

The procedure of synthesis of different PANI oxidation states and the chosen range was taken from the Paweł Stando Bachelor thesis, which title was "*Study of synthesis of nanocarbon polyaniline composites by electropolymerizing.*" The whole thesis is available in the archives of the chemical department.

PANI was electropolymerized using cyclic voltammetry (CV) onto nanocarbon films immediately submerged in the synthetic solution after electrode preparation to minimize exposure to airborne hydrocarbons[1]. The reaction setup included an Ag/AgCl reference electrode (ET069/ET072, eDAQ, Australia), a potentiostat (Ossial, T2006B1-EU, Holland), a nitrogen dispenser, a working electrode (SWCNTs or G+SWCNTs. O-SWCNTs film), a counter electrode (corresponding nanocarbon film, the same kind as the working electrode). A glass panel isolated each electrode to guarantee that there were no connections. The synthesized PANI solution contained 1.5 M aniline and 1.7 M $HClO_4$. A solution was prepared and then purged with argon gas for 10 minutes. The electrodes were then dipped into the synthesis solution for nanocomposites. The samples were washed with deionized water (AFS-16, Merck Millipore, Germany) for 1 minute after the reaction was finished in order to get rid of the reaction's byproducts and solution. By increasing the washing duration to five minutes, emeraldine-based (EB) nanocomposites were created. ClO_4^- ions were only partially eliminated from the nanocomposite of ES and SWCNTs (ES+SWCNTs washed) in the case of the samples that were washed for one minute. The final step was drying the product at 40 ºC until it reached a consistent mass, which was then determined using an analytical scale (VWR Digital Analytical Balance, VWR, USA). A voltage range was [0 V) - (1.2 V) vs. Ag/AgCl] was used, and the initial voltage was 0.0 V and 0.4 V, respectively. The operation was carried out using the specified sweep values (50 mV/s) and cycle counts (5, 20, and 50).

8. Academic achievements

Publications

1. Janas, D., **Stando, G.** Unexpectedly strong hydrophilic character of free-standing thin films from carbon nanotubes. *Sci. Rep.* **7**, 12274 (2017). doi: 10.1038/s41598-017-12443-y **(IF=4.122; 140 pkt)**
2. Turek, E., Wasiak, T., **Stando, G.**, Janas, D. Probing the mechanics of aqueous two-phase extraction using large diameter single-walled carbon nanotubes. *Nanotechnology* **29** (40)*,* 405704 (2018). doi: 10.1088/1361-6528/aad359 **(IF=3.399; 100 pkt)**
3. **Stando, G.**, Łukawski, D., Lisiecki, F., Janas. D. Intrinsic hydrophilic character of carbon nanotube networks. *Appl. Surf. Sci.* **463**, 227-233 (2019). doi: 10.1016/j.apsusc.2018.08.206
   (IF=6.182; 140 pkt)
4. Kumanek, B., **Stando, G.**, Wróblewski, P.S., Janas, D. Impact of Synthesis Parameters of Multi-Walled Carbon Nanotubes on their Thermoelectric Properties. *Materials (Basel)* **12** (21), 3567 (2019). doi: 10.3390/ma12213567 **(IF=3.057; 140 pkt)**
5. Kumanek, B., Wasiak, T., **Stando, G.**, Stando, P., Łukowiec, D., Janas, D. Simple Method to Improve Electrical Conductivity of Films Made from Single-Walled Carbon Nanotubes. *Nanomaterials **9** (8), 1113 (2019).* doi: 10.3390/nano9081113 **(IF= 4.324; 100 pkt)**
6. Kumanek, B., **Stando, G.**, Wróbel, P.S., Krzywiecki, M., Janas, D. Thermoelectric properties of composite films from multi-walled carbon nanotubes and ethyl cellulose doped with heteroatoms. *Synth. Met.* **257**, 116190 (2019). doi: 10.1016/j.synthmet.2019.116190 **(IF=3.286; 70 pkt)**
7. Kumanek, B., **Stando, G.**, Stando, P., Matuszek, K., Milowska, K.Z., Krzywiecki, M., Gryglas-Borysiewicz, M., Ogorzałek, Z., Payne, M.C., MacFarlane, D., Janas, D. Enhancing thermoelectric properties of single-walled carbon nanotubes using halide compounds at room temperature and above. *Sci. Rep.* **11**, 8649 (2021). doi: 10.1038/s41598-021-88079-w **(IF=4.996; 140 pkt)**
8. **Stando, G.**, Hannula, P.M., Kumanek, B., Lundström, M., Janas, D. Copper recovery from industrial wastewater - Synergistic electrodeposition onto nanocarbon materials. *Water Resour. Ind.* **26**, 100156 (2021). doi: 10.1016/j.wri.2021.100156 **(IF= 4.206; 200 pkt)**
9. **Stando, G.**, Han, S., Kumanek, B., Łukowiec, D., Janas, D. Tuning wettability and electrical conductivity of single-walled carbon nanotubes by the modified Hummers method. *Sci. Rep.* **12**, 4358 (2022). doi: 10.1038/s41598-022-08343-5 (**IF=4.996; 140 pkt**)
10. Taborowska, P., **Stando, G.**, Sahlman, M., Krzywiecki, M., Lundström, M., Janas, D. Doping of carbon nanotubes by halogenated solvents. *Sci. Rep.* **12**, 7004 (2022). doi:10.1038/s41598-022-11162-3 (**IF=4.996; 140 pkt**)
11. Kumanek, B., Milowska, K.Z., Przypis, Ł., **Stando, G.**, Matuszek, K., MacFarlane, D., Payne, M.C., Janas, D. Doping Engineering of Single-Walled Carbon Nanotubes by

Nitrogen Compounds Using Basicity and Alignment. *Appl. Mater. Interfaces* **14** (22), 25861–25877 (2022). doi: 10.1021/acsami.2c00970 (**IF=10.383; 200 pkt**)

12. Yang, F.*, **Stando, G.***, Thompson, A., Gundurao, D., Li, L., Liu, H. Effect of Environmental Contaminants on the Interfacial Properties of Two-Dimensional Materials. *Acc. Mater. Res.* **3** (10), 1022–1032 (2022). doi: 10.1021/accountsmr.2c00114 (**IF=-; 20 pkt**)
    * – authors contributed equally to this article.
13. **Stando, G.**, Stando, P., Sahlman, M., Lundström, M., M., Liu, H. ‚Janas, D. Synthesis of nanocomposites via electropolymerization of aniline onto hydrophilic films from nanocarbon and investigation of their properties, *Electrochim. Acta* **463**, 142842 (2023), https://doi.org/10.1016/j.electacta.2023.142842, **(IF=7.336, 100 pkt)**
14. **Stando, G.**, Li, L., Liu, H., Janas, D. Are nanocarbon materials hydrophilic or hydrophobic? – toward mechanism of hydrophobization of their surface – in preparation

$\sum_{IF}$= 61.283
$\sum_{MNiSW}$= 1630
h-index = 7 (Scopus); 8 (Google Scholar)

Research projects

10.2019 – up-to-date	Principal Investigator of project “Neat carbon nanostructures with hydrophilic character of the surface and their potential application in composite materials” (0036/DIA/2019/48), Diamond Grant 2019, Source of funding: Ministry of Education and Science, Amount of funding: 56 000 $
04.2018 – 09.2019	Co-Investigator in the project “Nanohybr1Ds: Hybrids composed of carbon nanotubes and metallic nanowires for harvesting energy from waste heat” (LIDER/0001/L-8/16/NCBR/2017), LIDER 9, Principal Investigator: Dawid Janas Ph.D. DSc, source of funding: National Center of Research and Developments, amount of funding: 306 000 $
10.2016 – 03.2018	Co-Investigator in project „Fundamentals of electrical properties of chirality-defined carbon nanotube macroassemblies” (UMO-2015/19/P/ST5/03799) POLONEZ 1, Principal Investigator: Dawid Janas Ph.D. DSc, Source of funding: National Center of Science, Amount of funding: 227 740 $

Internships

30.09.2021 – 29.09.2022	Research scholar, University of Pittsburgh (USA), founded by the Polish National Agency for Academic Exchange (under the Iwanowska program) 30 860 USD
4.08 – 30.08.2019	Visiting research, Aalto University in Espoo (Finland)
3.08 – 30.09.2017	Industrial apprenticeship, a lab technician in the development and production support laboratory PPG Polifarb Cieszyn, Poland

Conference participation

28.05-02.06.2023	243rd ECS meeting, Boston, USA, „Wettability of Carbon Nanostructures – Hydrophobic or Hydrophilic?” **G. Stando**, H. Liu, L. Li, D. Janas – digital presentation
03-07.05.2023	Zjazd Wiosenny Sekcji Młodych Polskiego Towarzystwa Chemicznego, Chęciny, Polska, „Nanostruktury węglowe hydrofilowe czy hydrofobowe?” **G. Stando**, H. Liu, L. Li, D. Janas – poster session
10.12.2022	Winter meeting of Student Young of Polish Chemical Society, Opole, Poland „Synteza polimerów przewodzących na hydrofilowych arkuszach z nanowęgla”, **G. Stando**, P. Stando, H. Liu, D. Janas – poster session
21-25.08.2022	ACS fall meeting, Chicago, USA „Synthesis and properties of single-walled carbon nanotubes-polyaniline nanocomposites”

	G. Stando, P. Stando, M. Sahlaman, M. Lundström, H. Liu, D. Janas – poster session
2.05-2.06.2022	ECS spring meeting, Vancouver, Kanada
	"Electrical properties of nanocarbon-polyaniline nanocomposites"
	G. Stando, P. Stando, P. Chulkin, M. Sahlaman, M. Lundström, H. Liu, D. Janas – digital presentation
	„Recovery of copper from wastewater by electrodeposition onto nanocarbon composites"
	G.Stando, P.-M. Hannula, B. Kumanek, M. Lundström, H. Liu, D. Janas – digital presentation
20.09-23.09.2021	E-MRS fall meeting, online,
	"The impact of the modified Hummers reaction on the properties of single-walled carbon nanotubes"
	G. Stando, S. Han, B. Kumanek, D. Łukowiec, D. Janas. – digital presentation
6.06 – 11.06.2021	NT21: International Conference on the Science and Application of Nanotubes and Low-Dimensional Materials, Online
	"Electrodeposition of copper from wastewater onto nanocarbon networks"
	G. Stando, P.-M. Hannula, B. Kumanek, M. Lundström, D. Janas – poster session
27.05 – 29.05.2021	Spring E-Meeting of Student Section of Polish Chemical Society,
	"Synteza nanokompozytów poprzez elektroosadzanie miedzi z odpadów przemysłowych na arkuszach z nanomateriałów węglowych"

	G. Stando, P.-M. Hannula, B. Kumanek, M. Lundström, D. Janas – oral presentation
14.04 – 15.04.2021	International Conference InterNanoPoland 2021, Online
	"Oxidation of single-walled carbon nanotubes by modified hummers method",
	G. Stando, S. Han, B. Kumanek, D. Łukowiec, D. Janas – poster session
10.09 – 12.09.2020	I Nationwide Online Conference Student Section of Polish Chemical Society, Online
	"Utlenianie jednościennych nanorurek węglowych za pomocą metody hummersa"
	G. Stando, S. Han, B. Kumanek, D. Łukowiec, D. Janas – poster session
29.10 – 30.10.2019	III International Conference on Innovations in Chemical Industry, Gliwice, Poland
	„Arkusze z nanowęgla do odzysku odpadowego ciepła"
	G. Stando, B. Kumanek, D. Janas – poster presentation
27.05 – 31.05.2019	2019 European MRS Spring Meeting, Nice, Franch
	"Unexpectedly strong hydrophilic character of nanocarbon materials"
	G. Stando, D. Janas – poster session
10.04 – 14.04.2019	Spring Meeting of Student Section of Polish Chemical Society, Ustroń, Poland
	"Wpływ doboru warunków syntezy na właściwości termoelektryczne wielościennych nanorurek węglowych"
	G. Stando, B. Kumanek, P. S. Wróbel, D. Janas – oral presentation

25.11 – 30.11.2018	2018 MRS Fall Meeting, Boston, USA
	"Are Carbon Nanotubes Intrinsically Hydrophilic?"
	G. Stando, D. Lukawski, F. Lisiecki, D. Janas – poster session
17.09 – 20.09.2018	2018 European MRS Fall Meeting, Warsaw, Poland
	"Hydrophilic films from carbon nanotubes"
	G. Stando, D. Lukawski, F. Lisiecki, D. Janas – poster session
25.04 – 29.04.2018	Spring meeting of Student Section of Polish Chemical Society, Skorzęcin, Poland
	"Hydrofilowe filmy z nanorurek węglowych"
	G. Stando, D. Janas – poster session
22.06 – 23.06.2017	II International Conference InterNanoPoland 2017, Katowice, Poland
	"Towards multifunctional carbon nanotube macrostructures",
	D. Janas, **G. Stando**, T. Wasiak – poster session